

To the Graduate Council:

I am submitting herewith a dissertation written by Donald Eric Hornback entitled "A measurement of open charm using single muons at forward angles for p+p collisions at center of mass energy 200 GeV". I have examined the final paper copy of this dissertation for form and content and recommend that it be accepted in partial fulfillment of the requirements for the degree of Doctor of Philosophy, with a major in Physics.

---

Kenneth F. Read, Major Professor

We have read this dissertation  
and recommend its acceptance:

---

Soren P. Sorensen

---

Vince Cianciolo

---

Ted Barnes

---

Robert Compton

Accepted for the Council:

---

Vice Provost and Dean of  
the Graduate School

**A measurement of open charm using  
single muons at forward angles for  
p+p collisions at center of mass  
energy 200 GeV**

A Dissertation  
Presented for the  
Doctor of Philosophy  
Degree  
The University of Tennessee, Knoxville

Donald Eric Hornback  
August 2008

# Acknowledgments

Completing a physics Ph.D. is not just about one person, rather, it is a collective effort to help one person reach a point of self-sufficiency in research. This is especially true in high-energy physics with its large collaborations (PHENIX having  $\sim 500$  people) and complicated experiments. Through the ups and downs, my advisor Ken Read maintained the firm vision needed for the successful completion of my doctoral research, and for that I will always be appreciative. While during my tenure in the group Soren Sorensen was primarily focused on teaching and heading the University of Tennessee physics department, he always made the time to talk, advise, and help me to become better. I am also thankful for the friendship of the next generation of graduate students in the group, Dwayne John and Irakli Martashvili, as well as the UT and ORNL groups' post-docs Josh Hamblen (Go Cardinals!) and Akitomo Enokizono.

And I know that I am especially lucky to have had Irakli Garishvili as my fellow graduate student and great friend through nearly my entire tenure at UT. It is impossible to have had a kinder more generous person to discuss the ins and outs of single muons over a plate of curry basil fried rice. The two graduate students that preceded me in the group, Jason Newby and Andrew Glenn helped me in many important ways in first few semesters as a graduate student. Having been abandoned by these experienced graduate students so early on would have been a great disaster, but for two people. Youngil Kwon, the godfather of single muons in PHENIX, in his special way, patiently taught me the ways of the Force... I mean his approach to measuring single muons. At the same time, David Silvermyr exhibited great patience in explaining how to do just about everything I needed to know to successfully operate within PHENIX, enabling me at the point where the "rubber meets the road." Thank you David. You left for CERN to soon.

Maybe every physicist in graduate school meets one person he or she would most like to emulate. For me, that person is Vince Cianciolo. Ultimately though, matching his tirelessly

energetic approach to everything may be impossible. Simply put, this research would not have been completed without his invaluable ideas and guidance.

I would like to also thank all of my PHENIX collaborators for making PHENIX an enjoyable collaboration to work in. It is a testament to our combined efforts, especially given the diverse backgrounds, personalities, and skill sets, that PHENIX operates at the high (frenetic) level that it does. This work benefited especially from the incisive questions and suggestions posed by Yasuyuki Akiba. The software and data used in this research resided on the local computing cluster at Oak Ridge National Laboratory, which greatly facilitated the completion of this work. Both Charles Thomas and Martin Purschke donated their time and skills to help us keep this machine useful. I would also like to thank my two dissertation committee members from outside of the field, Ted Barnes and Bob Compton for their helpful comments and questions.

It just so happens that my parents have lived nearby throughout my time in graduate school, and their support and encouragement has meant a great deal to me. Most importantly, my best friend and wife, Dodie has provided unwavering love and support. Graduate school is long and challenging, and without her it would have not been possible or even worth it. Lastly, our two sons, Colin and Eliot, have changed the way I look at the world and have helped me to realize what is truly important in this temporary life we live.

# Abstract

This dissertation presents the measurement of single muons from the semi-leptonic decay of heavy quark mesons (charm and bottom) in  $\sqrt{s}=200$  GeV  $p + p$  collisions at the Relativistic Heavy Ion Collider at Brookhaven National Lab. The data were recorded in 2005 by the PHENIX experiment. The PHENIX muon spectrometer measures particles at forward angles from approximately  $15^\circ$  to  $33^\circ$  relative to the beam line in both forward and backward directions.

A new analysis technique was developed to estimate and subtract backgrounds from light hadrons in a statistical fashion to reveal the yield of heavy flavor single muons. The yield of single muons is measured as a function of transverse momentum and is used to estimate the charm quark production cross section over the measured region. As heavy quark production is a true prediction of perturbative quantum chromo-dynamic calculations, the measured single muon yield and estimated charm quark cross section are compared to theoretical calculations. These comparisons show that the measured yield of single muons exceeds the existing theoretical expectations by a varying degree, from a factor of four at the lowest measured transverse momentum to a factor of two at the largest measured transverse momentum. The integrated charm quark production estimate also exceeds existing theoretical estimates for charm at forward angles. However, the sizable uncertainties present in both the measured and calculated quantities prohibit a definitive statement concerning charm production at forward angles. In addition to theoretical comparisons, this measurement of single muons in  $p + p$  serves as a springboard to further heavy quark results in both the RHIC spin and heavy-ion programs.

# Contents

<b>1</b>	<b>An Introduction</b>	<b>1</b>
1.1	Content and organization of the thesis . . . . .	2
1.2	RHIC as a QGP and QCD machine . . . . .	3
1.3	QCD and “hard” collisions . . . . .	6
1.4	Particle production and “hard” probes . . . . .	8
1.5	Heavy quark production at RHIC and its role as a probe for both QCD and the QGP . . . . .	10
1.6	Heavy flavor measurements in PHENIX . . . . .	17
1.7	The PHENIX central arm heavy flavor measurement . . . . .	20
1.8	General detector methods for measuring single muons . . . . .	21
1.9	How PHENIX measures single-muons at forward angles . . . . .	24
<b>2</b>	<b>Theoretical and phenomenological issues in heavy quark production</b>	<b>31</b>
2.1	Implementations of the factorization theorem . . . . .	39
2.2	Calculations of heavy quark production . . . . .	42
2.2.1	Heavy flavor cross section from NLO total partonic cross sections . . . . .	43
2.2.2	Heavy flavor cross sections using FONLL . . . . .	45
2.2.3	PYTHIA . . . . .	52
<b>3</b>	<b>Experimental Survey of Heavy Quark Single Lepton Measurements</b>	<b>56</b>
<b>4</b>	<b>The PHENIX Experiment</b>	<b>70</b>
4.1	RHIC . . . . .	70
4.2	The PHENIX detector . . . . .	74
4.3	The PHENIX central arms and global detectors . . . . .	78
4.4	The Muon Arms . . . . .	80
4.4.1	The Muon Magnets . . . . .	82

4.4.2	The Muon Tracker (MuTr) . . . . .	82
4.4.3	The Muon Identifier (MuID) . . . . .	85
4.5	Event triggering . . . . .	92
4.5.1	LVL1 triggers . . . . .	93
4.5.2	Local Level-1 Muon trigger implementation . . . . .	94
4.5.3	Level-1 triggers used in this analysis . . . . .	96
4.5.4	LL1 muon trigger rejection factors . . . . .	96
4.5.5	How biased is the Minimum Bias Trigger? . . . . .	97
4.5.6	Trigger emulation and the need of a “pseudo-emulator” . . . . .	98
4.6	PHENIX data acquisition system . . . . .	100
4.7	PHENIX software and computing . . . . .	101
4.8	Muon spectrometer track reconstruction . . . . .	102
4.8.1	Road finding in the MuID . . . . .	102
4.8.2	Track finding in the MuTr . . . . .	104
4.9	MuID efficiencies . . . . .	105
<b>5</b>	<b>The Single Muon Analysis</b>	<b>108</b>
5.1	Analysis overview . . . . .	108
5.2	Raw data analysis . . . . .	113
5.2.1	PHENIX data flow overview: from collisions to analysis files . . . . .	113
5.2.2	Local analysis software framework . . . . .	114
5.2.3	Data selection and QA . . . . .	114
5.2.4	Forming inclusive muon candidate distributions, $N_I$ . . . . .	115
5.2.5	Track selection and acceptance . . . . .	116
5.2.6	Matching MC and data response by restricting acceptance . . . . .	122
5.3	The hadron cocktail background estimate . . . . .	126
5.3.1	Method for “tuning” the hadron cocktail to match data . . . . .	129
5.3.2	Generating hadron cocktail input . . . . .	131
5.3.3	$\chi^2$ /NDF evaluation of the hadron cocktail . . . . .	141
5.4	<i>Non</i> -hadron cocktail high $p_T$ background estimate . . . . .	142
5.5	Acceptance $\times$ Efficiency corrections . . . . .	147
5.6	Methodology for signal extraction . . . . .	152
5.6.1	Subtraction of backgrounds to obtain yield of single muons, $N_\mu$ . . . . .	152
5.6.2	Extracting the central values of the single muon yield . . . . .	155
5.6.3	Signal to background . . . . .	158

5.6.4	Comparison of north and south arm results . . . . .	161
5.6.5	Combining the arms into a single $p_T$ spectrum . . . . .	163
5.7	Systematic uncertainties in the $p_T$ spectra . . . . .	165
5.7.1	Uncertainty on the yield of single muons, $N_\mu$ . . . . .	165
5.7.2	Uncertainty on the single muon differential cross section . . . . .	167
5.8	Integrating single lepton spectra for $p_T > 1.0$ GeV/c . . . . .	168
5.8.1	General notes on the integration of the $p_T$ lepton spectra . . . . .	168
5.8.2	How much of the integrated cross section is sampled for $p_T > 1.0$ GeV/c? . . . . .	169
5.8.3	Integration of the lepton spectra . . . . .	169
5.8.4	Statistical errors on the integrated lepton spectra . . . . .	171
5.8.5	Systematic uncertainties of the $p_T > 1.0$ GeV/c integrated lepton spectra . . . . .	172
5.9	Methodology for the extraction of $d\sigma_{c\bar{c}}/dy _{y=1.65}$ . . . . .	172
5.9.1	Extrapolating the measurement for $p_T < 1.0$ GeV/c . . . . .	173
5.9.2	Procedure for determination of $d\sigma_{c\bar{c}}/dy$ at $y=1.65$ . . . . .	173
5.9.3	The rapidity broadening of leptons from D mesons . . . . .	175
5.10	Systematic uncertainties on $d\sigma_{c\bar{c}}/dy$ . . . . .	177
5.10.1	Data systematic uncertainties . . . . .	177
5.10.2	Theoretical systematic uncertainties . . . . .	177
5.10.3	Total systematic uncertainty of $d\sigma_{c\bar{c}}/dy$ at $y=1.65$ . . . . .	177
5.10.4	Exploring the theoretical systematic uncertainty by variations in FONLL parameters . . . . .	178
<b>6</b>	<b>Results and Discussion</b>	<b>186</b>
6.1	Single muon $p_T$ spectra in p+p collisions . . . . .	188
6.2	Integrated cross section . . . . .	198
<b>7</b>	<b>Epilogue</b>	<b>207</b>
	<b>Bibliography</b>	<b>210</b>
	<b>Appendix</b>	<b>218</b>
<b>A</b>	<b>Glossary of selected terms</b>	<b>219</b>
<b>B</b>	<b>Additional comparison of results</b>	<b>221</b>

<b>C</b>	<b>Derivation of systematic uncertainties</b>	<b>227</b>
C.1	From which the errors spring . . . . .	227
C.2	Uncertainty on the yield of single muons assuming an error on $N_I$ . . . . .	228
C.3	Uncertainty on the yield of single muons assuming no error on $N_I$ . . . . .	229
C.4	Uncertainty on the single muon differential cross section . . . . .	229
C.5	Combining North and South muon arm systematic uncertainties with correlated and uncorrelated errors . . . . .	230
<b>D</b>	<b>Notes concerning yields and cross section expressions, and how to convert from one to the other</b>	<b>231</b>
<b>E</b>	<b>Bin shift corrections</b>	<b>234</b>
<b>F</b>	<b>Details on the modification of the hadronic package cross sections in the CERN libs</b>	<b>237</b>
<b>G</b>	<b>Run 5 MuID efficiency plots</b>	<b>240</b>
<b>H</b>	<b>Design specifications and performance of the PHENIX muon spectrometer</b>	<b>243</b>
<b>I</b>	<b>Optimal muon acceptance in <math>(p_T, \eta)</math></b>	<b>247</b>
<b>Vita</b>		<b>251</b>

# List of Tables

1.1	Theoretical and experimental heavy quark cross section estimates for $\sqrt{s}=200$ GeV $p + p$ collisions . . . . .	14
4.1	MuTr gap positions . . . . .	85
4.2	MuID gap positions . . . . .	87
4.3	Pseudo-trigger emulator efficiencies . . . . .	101
5.1	Hadron packages settings for the hadron cocktail . . . . .	141
5.2	Additional two-component background fraction, $N_{2c}$ . . . . .	147
5.3	Acceptance $\times$ efficiency as a function of $p_T$ . . . . .	152
5.4	Combining north and south arm $p_T$ spectra systematic uncertainties . . . . .	162
5.5	PHENIX Preliminary heavy flavor single muon $p_T$ spectra . . . . .	165
5.6	Uncertainties in $N_c$ and $N_{2c}$ . . . . .	166
5.7	Uncertainties in the single muon differential cross section . . . . .	167
5.8	Uncertainties in the acceptance and efficiency corrections . . . . .	168
5.9	FONLL normalization scales . . . . .	175
5.10	Modifiable parameters in FONLL . . . . .	179
5.11	Values for different FONLL “cases” at $y=1.65$ . . . . .	180
6.1	Integrated lepton cross section . . . . .	199
6.2	Integrated charm quark cross section results . . . . .	200
B.1	PYTHIA tuning parameters, Case 1 . . . . .	223
E.1	Bin-shift correction factors for Single muon spectra . . . . .	236

# List of Figures

1.1	Conjectured QCD phase diagram . . . . .	5
1.2	Schematic heavy-ion collision timeline . . . . .	6
1.3	Leading order production diagrams for $Q\bar{Q}$ . . . . .	10
1.4	Pictorial representation of the charm decay . . . . .	11
1.5	Schematic p+p and Heavy Ion Collision diagrams . . . . .	13
1.6	Nuclear modification factor for light and heavy quarks . . . . .	15
1.7	Particle decay likelihood over distance . . . . .	23
1.8	Integrated interaction length of the muon steel as a function of distance from the interaction point . . . . .	26
1.9	Single muon background and signal levels . . . . .	29
2.1	Schematic deep inelastic scattering diagram . . . . .	33
2.2	Proton structure function . . . . .	35
2.3	CTEQ6.5M PDF uncertainties . . . . .	37
2.4	Schematic diagram of the leading-order gluon fusion in hadron-hadron collisions	40
2.5	NLO total charm cross sections compared to measurements from the ISR and RHIC . . . . .	44
2.6	FONLL differential cross section compared to RHIC data . . . . .	48
2.7	Estimated uncertainties in NLO and FONLL charmed hadrons vs. $p_T$ . . . . .	49
2.8	FONLL $d\sigma_{c\bar{c}}/dy$ and $d\sigma_{b\bar{b}}/dy$ . . . . .	51
2.9	Sources of single muons from PYTHIA . . . . .	54
2.10	Charm, bottom, and light vector meson contributions to the total single muon yield in PYTHIA . . . . .	55
3.1	FNAL 1974 measurement of single muons . . . . .	58
3.2	ISR $e/\pi$ ratios vs. $\sqrt{s}$ . . . . .	59
3.3	Muon flux versus inverse target density, 1976 FNAL experiment . . . . .	60
3.4	Charm and bottom cross sections circa 1995 . . . . .	62

3.5	D0 forward angle single muon bottom measurement. . . . .	64
3.6	CDF charm meson measurement . . . . .	65
3.7	PHENIX and STAR single lepton results . . . . .	67
3.8	Measured total charm cross sections at RHIC . . . . .	67
4.1	RHIC accelerator complex . . . . .	72
4.2	RHIC store luminosity plots . . . . .	73
4.3	RHIC Runs, species, energy, PHENIX sampled luminosity . . . . .	75
4.4	PHENIX detector 2005 . . . . .	77
4.5	PHENIX acceptance . . . . .	78
4.6	Event collision $z$ -vertex distribution . . . . .	79
4.7	PHENIX muon arm $x$ range for $p + p$ collisions at $\sqrt{s} = 200$ GeV . . . . .	81
4.8	MuTR chamber description . . . . .	84
4.9	MuID two-pack . . . . .	88
4.10	MuID sliced . . . . .	90
4.11	Simplified MuID circuit diagram . . . . .	91
4.12	LVL1 readout stream . . . . .	93
4.13	Muon Level-1 trigger logic . . . . .	95
4.14	Muon trigger rejection factors versus run number . . . . .	97
4.15	PHENIX data flow . . . . .	103
4.16	Event display for a single MuTr octant . . . . .	105
4.17	Full muon arm reconstruction event display . . . . .	107
5.1	Depiction of relative particle flux in the muon arm . . . . .	109
5.2	Distributions of average vertex collision and track production per run number. . . . .	115
5.3	Event $z$ -vertex normalization of muon track yields . . . . .	116
5.4	Di-muon invariant mass distribution used for single muon analysis cut optimization . . . . .	117
5.5	$p\delta\theta$ from di-muons compared to single-particle single muon simulations . . . . .	118
5.6	Definition of $p\delta\theta$ . . . . .	119
5.7	“Decay triangle” in the inclusive track yield $z$ distribution . . . . .	121
5.8	Sequential implementation of cuts to inclusive yield. . . . .	123
5.9	Fiducial geometric acceptance cuts . . . . .	125
5.10	North arm $\phi$ distributions . . . . .	127
5.11	North arm radial distribution . . . . .	128
5.12	MuID Gap 3 hadron cocktail $p_T$ spectra normalized to data yield . . . . .	130

5.13	FLUKA and GHEISHA hadron packages compared to RD10-45 data . . . . .	131
5.14	Thrown vs. reconstructed $p_T$ , $p\delta\theta$ cut NOT applied . . . . .	132
5.15	Thrown vs. reconstructed $p_T$ , $p\delta\theta$ cut applied . . . . .	132
5.16	Kaon tuning weights applied to NLO . . . . .	134
5.17	Default NLO K/ $\pi$ ratios for $\eta$ from 1.1 to 2.3 . . . . .	134
5.18	Pion yields and K/ $\pi$ ratio for hadron cocktail and data . . . . .	135
5.19	Stopped particles in shallow MuID gaps . . . . .	136
5.20	MuID Gap 2 $p_T$ spectra comparison of hadron cocktail and data . . . . .	137
5.21	MuID Gap 4 $z$ -vertex distribution comparison of hadron cocktail and data . . . . .	139
5.22	Comparisons of different hadron cocktail package predictions. . . . .	140
5.23	Distributions of event normalized $p\delta\theta$ for inclusive data tracks before and after $\delta z$ cut. . . . .	143
5.24	$\delta z$ distribution for muon track candidates . . . . .	144
5.25	Partial event display of a high occupancy event . . . . .	146
5.26	Two component fit of $p\delta\theta$ distributions . . . . .	148
5.27	$p\delta\theta$ distributions data and hadron cocktail . . . . .	149
5.28	$z$ -vertex dependent Acceptance $\times$ Efficiency, north arm . . . . .	153
5.29	Momentum and pseudorapidity smearing for muons . . . . .	154
5.30	Single package hadron cocktail $\chi^2$ /NDF . . . . .	156
5.31	Comparison of tuned hadron cocktail input spectra with data . . . . .	157
5.32	Two-package averaged hadron cocktail $\chi^2$ /NDF . . . . .	159
5.33	Signal/Background ratio for north and south arms . . . . .	160
5.34	Separate north and south single muon double differential cross section . . . . .	163
5.35	Combined arm single muon spectrum . . . . .	164
5.36	Fractional integral plot for FONLL to $p_T=0$ GeV/c . . . . .	170
5.37	Example integration of $p_T$ spectra . . . . .	171
5.38	Comparison of single muon and FONLL $p_T$ spectra . . . . .	174
5.39	FONLL $lepton/D$ ratio vs. $y$ . . . . .	176
5.40	Variation of the different FONLL $d\sigma^{lepton}/dp_T$ vs. $p_T$ (in units of GeV/c) distributions relative to the central FONLL prediction. . . . .	182
5.41	Eleven FONLL cases matched to data . . . . .	183
5.42	Extracted $d\sigma/dy$ from the 11 different FONLL calculations. . . . .	184
6.1	J/ $\Psi$ rapidity evolution . . . . .	187
6.2	Run 5 p+p comparison with FONLL charm+bottom . . . . .	190

6.3	PHENIX heavy flavor single electron spectra with comparison to FONLL . . .	192
6.4	$y=1.65/y=0$ ratio of invariant differential cross sections of single muons to single electrons . . . . .	194
6.5	Forward single muon results compared to mid-rapidity PHENIX and STAR spectra . . . . .	197
6.6	PHENIX lepton spectra integrated for $p_T > 1.0$ GeV/c . . . . .	202
6.7	Integrated $d\sigma_{c\bar{c}}/dy$ and $\langle y \rangle=0$ and $\langle y \rangle=1.65$ . . . . .	203
6.8	FONLL scaled to PHENIX $\langle y \rangle=0$ charm measurement . . . . .	204
6.9	Integrated $d\sigma_{c\bar{c}}/dy$ and $\langle y \rangle=0$ and $\langle y \rangle=1.65$ for both STAR and PHENIX . .	206
B.1	Run 5 comparison to the Run 2 single muon measurement. . . . .	222
B.2	Comparison with PYTHIA . . . . .	224
B.3	$d\sigma/dy$ at $y=1.65$ for different FONLL parameter sets . . . . .	225
G.1	MuID efficiencies versus run, north muon arm . . . . .	241
G.2	MuID efficiencies versus run, south muon arm . . . . .	242
H.1	North/South J/ $\Psi$ mass resolution in $p + p$ . . . . .	245
I.1	Tabulated energy loss for a MIP in the PHENIX muon arms. . . . .	248
I.2	Minimum penetration $p_T$ in GeV as a function of $\eta$ for the PHENIX north and south muon arms. . . . .	250

# Chapter 1

## An Introduction

*As an adolescent I aspired to lasting fame, I craved factual certainty, and I thirsted for a meaningful vision of human life - so I became a scientist. This is like becoming an archbishop so you can meet girls.*

*- M. Cartmill*

It is certain that human beings will never fully understand what happens when two nuclei collide. Although a complete understanding will forever lie beyond our grasp, there is much that can still be learned from experiments regarding the nature of the strong nuclear force. In comparison to some disciplines, the overall pace of discovery in nuclear physics is often not rapid. Tempered by the large experimental costs and the incremental nature of both experimental and theoretical advances, the pace of discovery is perhaps best viewed on the timescale of decades. Despite these limitations, much has already been learned.

The year 2008 marks 100 years since Rutherford's seminal work exploring the nuclear structure of matter. That the nuclei of atoms are composed of neutrons and protons, themselves containing point-like constituents referred to as quarks and gluons, dates from experimental and theoretical developments of the 1960's and 70's. Since that time we have further expanded our theoretical understanding of the fundamental interactions of these basic constituents of matter, as well as our ability to create and measure the wide array of observed quark combinations and the gluons that bind them. Measuring the production of these remarkable components of the natural world in the context of a theoretical framework derived from first principles is an essential aspect of high energy and nuclear physics research. Ultimately, we seek answers to a most fundamental question of existence: what is the nature of the force that allows the gluons to bind quarks within nucleons, thus permitting the very

existence of the atoms that comprise our reality?

Through studies of high energy nucleon-nucleon collisions as described here, it is possible to gain glimpses, imperfect though they may be, into this elusive aspect of the universe. This research, undertaken to measure heavy quark production produced in ultra-relativistic nuclear collisions, serves as an incremental step in the grand human program of attempting to better understand the fundamental forces of nature.

## 1.1 Content and organization of the thesis

The work presented in this dissertation describes the measurement of single-muon transverse momentum spectra from the semi-leptonic decay<sup>†</sup> of heavy quark mesons originating in proton-proton ( $p + p$ ) collisions at a center of mass energy, denoted by  $\sqrt{s}$ , of 200 GeV. This measurement is made using the PHENIX detector at the Relativistic Heavy Ion Collider (RHIC) at Brookhaven National Lab (BNL). In this dissertation, the heavy quarks of “flavor” charm and bottom are collectively referred to as heavy flavor<sup>†</sup>. Light quarks are then  $u$ ,  $d$ ,  $s$ , and their anti-particles. A heavy-flavor single-muon measurement in  $p + p$  collisions addresses three physics goals at RHIC: 1) Measurements of heavy flavor in  $p + p$  serve as *the* baseline measurement for heavy-ion heavy-flavor measurements used in the study of the hot, dense partonic medium produced in heavy-ion collisions at RHIC, 2) Heavy quark production cross sections measured in  $p + p$  serve as tests of perturbative quantum chromodynamic calculations, 3) Heavy flavor measurements in polarized  $p + p$  collisions at RHIC provide direct access to gluons in the proton allowing measurements of gluon density and ultimately the fractional contribution of gluonic spin to the total proton spin. For the research presented in this document, experimental conditions do not yet permit a meaningful heavy quark spin measurement in PHENIX. Instead, the first two physics goals provide the primary motivation for this work. The methodology established in this thesis serves as the basis for additional single-muon measurements by PHENIX in different collisions environments ( $Au + Au$ ,  $Cu + Cu$ , and  $d + Au$ ), as well as for future single muon spin analyses.

The remainder of this introductory chapter (Ch. 1) is aimed at providing a general discussion to provide a useful context and motivation for the topic of this thesis research. The final chapter discusses some remaining experimental challenges and the prospects for future

---

<sup>†</sup>Decay through a weak interaction, producing one lepton and neutrino, and one or more hadrons.

<sup>†</sup>The top quark is too heavy to be relevant at the collision energies discussed in this work.

results from single muons in PHENIX. The chapters in between provide some perspective on elements of theory (Ch. 2), a historical perspective on previous experimental efforts (Ch. 3), a description of the collider and detector used (Ch 4.), the actual work done to measure the single-muons (Ch. 5), and the discussion of the results (Ch. 6). There are also a handful of appendices in which various details are provided that do not cleanly fall into any of the aforementioned chapters.

## 1.2 RHIC as a QGP and QCD machine

One of the most celebrated principles of the accepted theory of strong interactions, quantum chromodynamics (QCD), is that of *asymptotic freedom*. This suggests that the effective coupling of the strong force,  $\alpha_s$ , decreases with increasing momentum transfer,  $Q^2$  or, equivalently, with decreasing distance between the interacting particles. High-energy collisions of particles have successfully demonstrated this principle. Directly related to this is the principle of *confinement*, where the strong force coupling becomes progressively stronger at lower energies, which corresponds to longer distances. For this situation, individual quarks and gluons are bound inside hadrons in a condition referred to as “infrared slavery.” Collisions of heavy nuclei at ultra-high energies are thought to produce a state of deconfined, strongly interacting nuclear matter, the *quark gluon plasma* [1]. RHIC was built to produce and study this possible state of matter. To this end, RHIC is capable of colliding the full range of nuclei from  $p + p$  to  $Au + Au$  across a wide range of collision energies, from a minimum center of mass energy *per nucleon-nucleon* (NN) collision of  $\sqrt{s_{NN}}=22$  GeV to a maximum of  $\sqrt{s_{NN}}=200$  GeV<sup>†</sup>. RHIC is also capable of producing asymmetric collisions between different size nuclei, as well as producing polarized proton beams, which serve the parallel and complimentary RHIC physics program to study the spin structure of the proton. This wide variety and range of collision possibilities at RHIC offer a unique technical and experimental challenge, for which the “machine”<sup>‡</sup> people should be greatly complemented.

For a high-temperature and/or high-density thermal medium of nearly massless, strongly interacting particles (such as quarks), the characteristic momentum transfer is of the order of  $T$ , the temperature [4]. For this type of matter, increasing  $T$  corresponds to a decreasing

---

<sup>†</sup>maximum of  $\sqrt{s}=500$  GeV for  $p+p$ , the minimum  $\sqrt{s_{NN}}$  for all ions which may in the future be reduced to  $\sqrt{s_{NN}} \approx 5$  GeV to permit search for the QCD critical point. See Figure 1.1.

<sup>‡</sup>the colloquial name for collider physicists used by detector physicists, who are called “*users*”

effective coupling between the particles. Figure 1.1 shows a schematic of a possible phase diagram for nuclear matter over a range of temperature and baryon chemical potential,  $\mu_B$  [2,3]. Theoretical arguments and experimental data [5] suggest that nucleus-nucleus collisions at RHIC are characterized by low net baryon density, depicted in the left half of the phase diagram. In this region, and at low temperatures, strongly interacting quarks and gluons are confined within nucleons. For increased temperatures, this strongly interacting material is thought to exist as a hadron gas. Lattice QCD calculations suggest that at even higher temperatures a phase transition with a critical temperature of about 175 MeV [6,7] may occur. This phase transition may lead to a state of matter where quarks and gluons are deconfined, such as may have existed a few microseconds after the (most recent) Big Bang.

Whether there is actually a phase transition, the order of the phase transition if it exists, and the possible existence of a critical point all complicate the discussion of the properties of the strongly interacting matter in the high temperature, low baryon density region of the phase diagram. However, what *is* much clearer is the possibility of using high-energy nucleus-nucleus collisions, such as those produced at RHIC to explore this region of the phase diagram. The collision of two nuclei has a short-lived overlap region with a *total* momentum of zero that is roughly the size of a nucleus, permitting a meaningful estimate of an energy density within the overlap region. In head-on  $Au + Au$  collisions at RHIC, energy densities are conservatively estimated to be at least 5 GeV/fm<sup>3</sup> [5]. By comparison, existing theoretical calculations estimate the required energy density for a QCD phase transition to be on the order of 1 GeV/fm<sup>3</sup> [5,8], suggesting that RHIC collisions produce conditions sufficient to explore the possible formation of this new state of matter.

Collisions of heavy ions are described using the standard notion of impact parameter,  $b$ . For nuclei,  $b$  describes the transverse distance between the centers of two colliding nuclei. Collisions with small  $b$  and large overlap are referred to as *central collisions*, while collisions with large  $b$  and small overlap are referred to as *peripheral collisions*. Nuclear matter in the collision overlap region of heavy-ion events is initially heated and compressed to form a hot, dense matter of deconfined quarks and gluons (known collectively as partons) that is thought to quickly reach *local* chemical and thermal equilibrium. Defining a “fire-ball” of produced particles from a relativistic heavy-ion collision as being in any sort of equilibrium is, perhaps, counterintuitive. However, measured particle yields at RHIC can be described by a thermal-statistical model using only the parameters  $T$  and  $\mu_B$  that assumes chemical

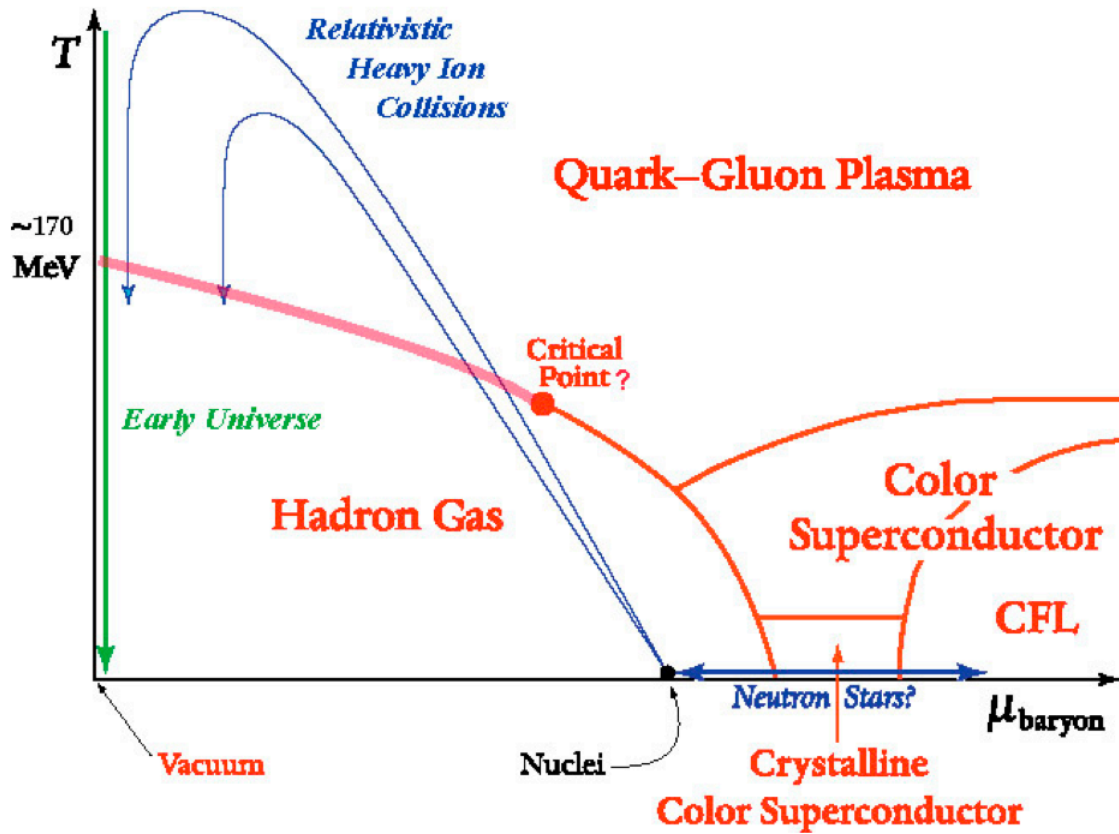


Figure 1.1: Conjectured QCD phase diagram as a function of Temperature  $T$  and baryon chemical potential,  $\mu_{\text{baryon}}$  [2, 3]. The early universe is thought to have been filled with quark-gluon plasma (QGP) during the first microseconds after the big bang. The QGP is also thought to be created in heavy-ion collisions at RHIC. A first order phase transition may occur for  $\mu_{\text{baryon}}$  above the possible critical point.

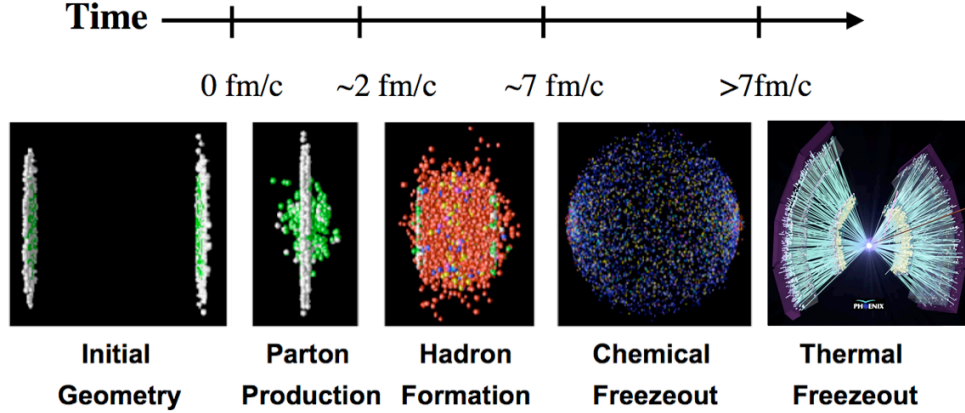


Figure 1.2: Schematic heavy-ion collision timeline. The thermal freeze-out image is an event display from a central  $Au + Au$  collision event measured in the PHENIX central arm. Figure adapted from [11].

equilibrium [9, 10]. Once a state of equilibrium is achieved, regardless of its macroscopic duration, thermodynamic quantities such as pressure, temperature, entropy, etc. can be used to characterize the system.

As depicted in Figure 1.2, after the initial collision of heavy ions, parton production is expected within a time of  $\sim 1$  fm/c <sup>†</sup>. Pressure drives the system to expand and cool, returning the local energy density below the threshold for a phase transition, and according to QCD the partons become confined within hadrons. This “hadron gas” continues to expand and interact until *chemical freeze-out*, which fixes the experimentally observed composition of matter [12]. After further expansion and cooling, the hadrons undergo their last collisions and *thermal freeze-out* occurs. The hadrons then follow known modes of decay, which can be detected experimentally.

### 1.3 QCD and “hard” collisions

In addition to the role of heavy-ion baseline, measurements made in  $p + p$  collisions, including those of heavy quarks, provide tests of QCD that can be directly compared with theoretical calculations. The established framework for the interaction and production of particles is the Standard Model, which possesses three symmetries, written as  $SU(3) \times SU(2) \times U(1)$ , that are necessary and sufficient to describe the interactions of known particles [13]. Despite

<sup>†</sup> $(1 \times 10^{-15} \text{m}) / (3 \times 10^8 \text{m/s}) \sim 3 \times 10^{-8}$  sec.

the spectacular success of the Standard Model, a few lingering, less-than-desirable features exist, such as the *ad hoc* way in which fermion masses, parity/CP violation enter the theory, and the absence of direct observation of the Higgs boson [14]. Despite the overwhelming success of the Standard Model to describe particle interactions, the discovery of the Higgs boson, possibly at the Large Hadron Collider at CERN, will be a crowning experimental achievement in physics.

The gauge field theory Quantum Chromodynamics (QCD) is the SU(3) component of the Standard Model and describes the strong interaction between two kinds of particles with color charge, quarks and gluons, the latter being the gauge bosons of the theory which mediate the strong force. The property of asymptotic freedom states, rather remarkably, that the strong interaction is effectively weak at short distances or high energies. In this regime where QCD is effectively a weakly interacting theory, perturbation theory may be applied. In this case, a typical perturbative cross section in QCD can be written as a power series in terms of the effective (and renormalized) QCD coupling,  $\alpha_s$  [15]:

$$\sigma = A_1 \alpha_s + A_2 \alpha_s^2 + \dots, \quad (1.1)$$

where  $A_i$  are calculated from appropriate diagrams according to the Feynman rules. Calculations up to  $\alpha_s$  are generally referred to as lowest (or leading) order (LO); calculations up to  $\alpha_s^2$  are referred to as next-to-leading order (NLO), and so on. Skirting around the details of renormalization for the moment, the strength of the QCD interaction,  $\alpha_s$ , which is expressed in several different forms in the literature, can be written at lowest order in terms of renormalization energy scale parameter,  $\mu_R^2$  (which will be discussed in more depth in Chapter 2):

$$\alpha_s(\mu_R) = \frac{4\pi}{\beta_0 \ln(\mu_R^2/\Lambda_{QCD}^2)}, \quad (1.2)$$

where  $\Lambda_{QCD}$  is a measure of the scale at which  $\alpha_s$  really does become “strong” [16], and  $\beta_0$  is the lowest order power series expansion of the  $\beta$ -function used in renormalization to determine the coupling  $\alpha_s(\mu_R)$  [15]. The exact details of the  $\beta$ -function are neglected for this discussion. Higher order terms in the expansion of  $\alpha_s$  are expressed in inverse powers of  $\ln(\mu_R^2/\Lambda_{QCD}^2)$ . For the relevant high-energy, heavy-quark calculations to be discussed in this dissertation, the renormalization scale,  $\mu_R$ , approximately coincides with the physical energy scale,  $E$ , of the interaction, and for the purpose of this discussion the physical energy

scale is equated with the transverse momentum of the detected particle,  $E \sim p_T$ . The value for  $\Lambda_{QCD}$  varies depending on the number of “active” quark flavors<sup>†</sup>, but it is generally of the order 200 MeV, which is close to the mass of a typical hadron [17]. Ultimately, faith in QCD as the theory of the strong interaction is based primarily on the ability of perturbative QCD (pQCD) to successfully match the large body of experimental data that has been accumulated.

Equation 1.2 is formulated in such a way to nicely highlight some important properties of QCD. The property of confinement, that only color-singlet (color neutral) combinations of quarks, anti-quarks, and gluons of the size  $\sim 1$  fm exist as independent particles able to propagate over distances greater  $\gg 1$  fm, is readily seen for  $\mu_R \sim \Lambda_{QCD}$ . In this case  $\alpha_s(\mu_R)$  is large, indicating strong coupling. On the other hand, as the energy scale becomes large,  $\mu_R \gg \Lambda_{QCD}$ , the effective coupling becomes very small, justifying a quasi-free (i.e. perturbative) treatment of partons within the nucleus.

The crossover between the dominance of non-perturbative and perturbative effects in a particular high-energy collision is often denoted by referring to processes as either *hard* (perturbative) or *soft* (non-perturbative). Experimentally, the crossover from the dominance of one regime to the other is usually taken to be  $p_T \sim 2.0$  GeV/c. In terms of Equation 1.2, the crossover takes place at distances  $\Lambda_{QCD}^{-1} \sim 1$  fm [16]. This is the point where quarks are bound to form hadrons and where perturbation theory is no longer applicable. Lattice QCD approaches, which implement discrete lattice spacings to remain ultraviolet finite (non-divergent) are used to explore this non-perturbative regime. This work, however, is concerned with an inherently hard process, heavy quark production.

## 1.4 Particle production and “hard” probes

Generally speaking, the interaction of two particles can be described as either elastic or inelastic. Elastic collisions conserve the identity of the original particles and conserve kinetic energy. In high-energy physics, inelastic collisions are characterized by the production of “new” particles and often result in the obliteration of the original particles. Three general types of facilities exist to provide these high-energy inelastic collisions for study: fixed-target

---

<sup>†</sup>this is discussed in Chapter 2

accelerators, lepton (such as  $e^+e^-$ ) colliders, and hadron colliders. In point-like  $e^+e^-$  annihilation “collisions” all of the center of mass energy contributes to particle production. The situation is different in fixed-target hadron-hadron collisions and hadron-hadron colliders due to the fact that hadrons are composite particles with the center-of-mass energy distributed over the nuclear constituents, generally referred to as partons, which include valence quarks, “virtual” quark/anti-quark ( $q\bar{q}$ ) pairs, and gluons. In hadron-hadron collisions, inelastic collisions result in the dissipation of incident parton longitudinal energy which is then transferred into particle production. In  $p + p$  collisions, the subject of this research, colliding protons retain on average about half of their initial momentum after the collision, suggesting that only about half of the center-of-mass energy is used in particle production [18].

The likelihood, in terms of interaction cross sections, for both elastic and inelastic collisions have been measured for  $p + p$  collisions at several different facilities and indicate at  $\sqrt{s} = 200$  GeV, such as at RHIC, protons interact four times as often inelastically as elastically. The average total charged particle multiplicity at this energy from inelastic collisions is six [18]. These produced particles can be plotted in terms of the kinetic variable transverse momentum,  $p_T$ , which is defined as the component of momentum perpendicular to the beam axis. Particle yields measured over a limited solid angle are denoted by  $dN/dp_T$  and exhibit an approximately exponential drop with increasing  $p_T$ . Invariant yields or cross sections extrapolate  $dN/dp_T$  over the full  $4\pi$  phase-space and are written as  $E \frac{dN}{d^3p}$  or  $E \frac{d\sigma}{d^3p}$ , respectively<sup>†</sup>.

Hard processes are important for particles produced with  $p_T \gtrsim 2.0$  GeV/ $c$ . In these hard reactions the incident partons that undergo a hard scattering reaction can produce particles with large  $p_T$  which are said to serve as “hard probes” of the collision. Hard probes play a vital role in the study of nuclear matter and QCD, for they permit the study of particle production processes that are both theoretically calculable and experimentally accessible. Light quarks with  $p_T > 2.0$  GeV/ $c$  depend on a single hard scale,  $\mu$  and therefore provide a straightforward application of pQCD. Existing NLO pQCD calculations for light quark production for  $p_T > 2.0$  GeV/ $c$  are in good agreement with experimental measurements [19]. Because of their large mass, which also provides an additional hard scale in the perturbative calculation, heavy quarks are by definition hard probes. In the following section heavy quark production and its utility as a probe of QCD and QGP is explored further.

---

<sup>†</sup>Invariant yields are discussed in Appendix D.

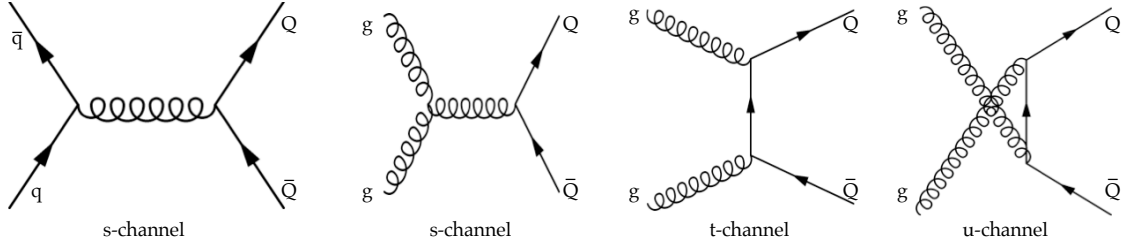


Figure 1.3: Leading order production diagrams for heavy quark pairs,  $Q\bar{Q}$ . Diagrams adapted from [21] and [22].

## 1.5 Heavy quark production at RHIC and its role as a probe for both QCD and the QGP

Of the three *flavors* of “heavy” quarks, charm, bottom, and top, the energy available at RHIC to produce heavy quark pairs,  $Q\bar{Q}$ , is sufficient, statistically speaking, primarily for charm production. Bottom production is also relevant but significantly below charm in total production; the total bottom cross section is estimated to be 1-2% that of charm (for specific values see Table 1.1). With a mass of  $174 \text{ GeV}/c^2$ , the energy required for top quark pair production is above the obtainable threshold at RHIC. Therefore, for the purpose of this dissertation the term heavy flavor is taken to mean some admixture consisting primarily of charm quarks with a small contribution of bottom quarks. In  $\sqrt{s}=200 \text{ GeV}$   $p + p$  collisions, pQCD calculations indicate that the charm cross section exceeds the bottom cross section until  $p_T \sim 4.0 \text{ GeV}/c$ , above which bottom then dominates [20].

At leading order the primary heavy quark production mechanism at RHIC energies is gluon fusion,  $g + g \rightarrow Q + \bar{Q}$ <sup>†</sup>, with suppressed LO contributions from the process  $q + \bar{q} \rightarrow Q + \bar{Q}$  since it requires an anti-quark in the initial state [23]. At next-to-leading order some contributing processes are i)  $q + \bar{q} \rightarrow Q + \bar{Q} + g$ , ii)  $g + q \rightarrow Q + \bar{Q} + g$ , iii)  $g + \bar{q} \rightarrow Q + \bar{Q} + \bar{q}$ , and iv)  $g + g \rightarrow Q + \bar{Q} + g$  [21]. In these LO and NLO processes, heavy flavor is produced symmetrically, with equal numbers of quark and anti-quarks. It is also worth mentioning that in terms of the “typical” pQCD cross section expressed in Equation 1.1, these LO diagrams for heavy quark production are proportional to  $\alpha_s^2$  not  $\alpha_s$ . NLO processes are then of order  $\alpha_s^3$ . This can be explained examining the diagrams in Figure 1.3. Every vertex contributes a

<sup>†</sup>concerning notation:  $q$  ( $\bar{q}$ ) refers to an initial quark (anti-quark),  $g$  for gluons,  $Q$  ( $\bar{Q}$ ) for final state quark (anti-quark)

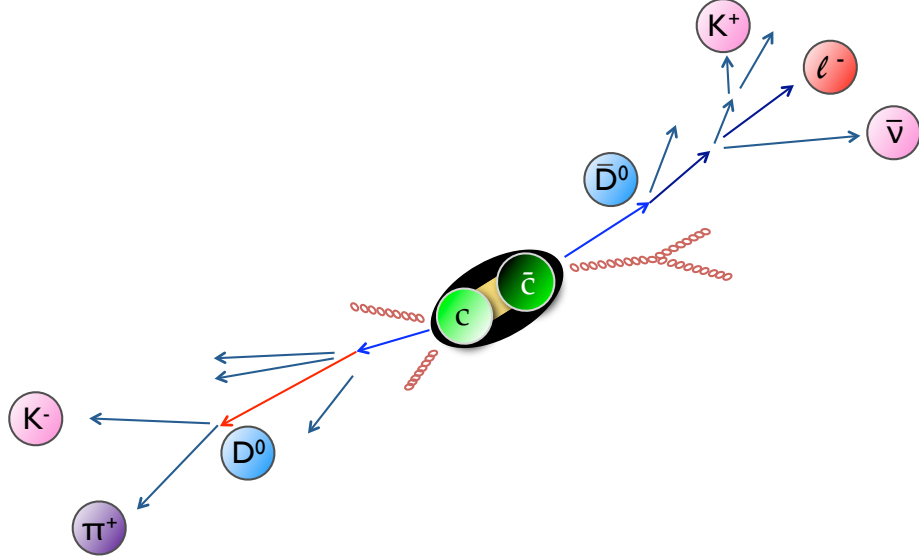


Figure 1.4: Pictorial representation of the fragmentation of a charm quark and the semi-leptonic decay of a charm meson. The measurement of the lepton depicted on the right-hand side of the figure is *the* primary focus of this dissertation.

single factor of  $g_s$  to the amplitude,  $\mathcal{M}$ , where  $g_s$  is the QCD coupling before renormalization and is related to  $\alpha_s$  in the following way:  $\alpha_s = g_s^2/4\pi$  [15]. The two vertices in each of the LO diagrams in Figure 1.3 have an amplitude of  $\mathcal{M} \sim g_s^2 \sim \alpha_s$ , according to the Feynman rules [24]. The cross section,  $\sigma$ , is related to the amplitude by  $\sigma \sim |\mathcal{M}|^2$ , and the overall cross section from these LO diagrams is therefore  $\sigma \sim \alpha_s^2$ .

At the center of Figure 1.4 is a charm/anti-charm quark pair produced in an initial inelastic hard collision. This cartoon diagram represents the central phenomena of interest of this dissertation, and will be referenced indirectly throughout the rest of this work. The host of  $c\bar{c}$  resonances ( $J/\Psi, \Psi$ , etc.), referred to collectively as charmonia, are of huge historical and experimental importance. However, these resonances comprise just a tiny fraction of the total charm cross section  $< 1\%$ . Most of the charm cross section results in the production of the family of charm mesons, referred to as  $D$ 's. Two decay processes of experimental interest at PHENIX (having large branching ratios) are shown in Figure 1.4. The  $D^0$  meson decay on the left shows the hadronic decay to  $K^-\pi^+$ . The study of this hadron decay mode is used at RHIC to measure charm production but is not the focus of this work. The decay illustrated on the right of Figure 1.4 shows the semi-leptonic decay of  $\bar{D}^0$  to a lepton, the lepton's anti-neutrino, and a  $K^+$ . The detection of these “single” leptons, either electrons or muons

in this context, is the central focus of this dissertation. The decay mode shown here is just for the  $\bar{D}^0$ . In reality, there are multiple  $D$  mesons that decay semi-leptonically. Measuring the inclusive yield of single leptons from  $D$  meson decay and knowing the appropriate mix of types of  $D$  mesons and their branching ratios to single leptons, the total production of charm can be estimated. Provided that this is experimentally possible, it is worth discussing the motivations for doing so.

Heavy quark production is of considerable and ongoing experimental and theoretical interest, due in part to the fact that current understanding is incomplete on both fronts. Contrary to light quark flavors ( $u, d, s$ ) the large mass of heavy quarks permits the calculation of total and differential ( $p_T$  spectra) production cross sections over all  $p_T$ . That means that heavy quark production provides a direct test of QCD (or more precisely, pQCD). However, consideration of heavy quarks introduces the additional hard scale of mass,  $m_{HQ}$ , into the perturbative series that requires a reorganizational scheme that reduces the two scale problem to an effective single scale problem which takes into account the relative sizes of  $p_T$  and  $m_{HQ}$  [17]. Multiple effective single scale calculation schemes exist and are further discussed in Chapter 2. While pQCD calculations for light quarks are restricted to  $p_T \gtrsim 2.0$  GeV/c, for heavy quarks the large mass provides a hard scale for  $p_T \lesssim 2.0$  GeV/c allowing pQCD calculations in this low  $p_T$  region. However, in this region large theoretical uncertainties arise from an incomplete knowledge of several key inputs: the effective mass of the heavy quark, uncertainties in the parton distribution functions (PDF's) and fragmentation functions measured in  $e^+e^-$  annihilations, and most importantly, the choice of renormalization and factorization scales in the perturbative series. All of these issues are discussed in Chapter 2.

While there have been several experimental heavy quark measurements, higher precision measurements are required to better constrain existing pQCD calculations which contain these large uncertainties. This is especially true for charm production, where the relative “lightness” of charm introduces significantly larger uncertainties into calculations as compared to bottom. Current experimental and theoretical measurements and uncertainties for the total heavy quark production cross sections for  $\sqrt{s}=200$  GeV  $p + p$  collisions are listed in Table 1.1.

As illustrated in Figure 1.5, processes with large momentum transfers, referred to as “hard” processes, between partonic constituents within colliding nuclei can produce particles with large  $p_T$ . These “hard” collisions are the dominant processes for particles produced with  $p_T$

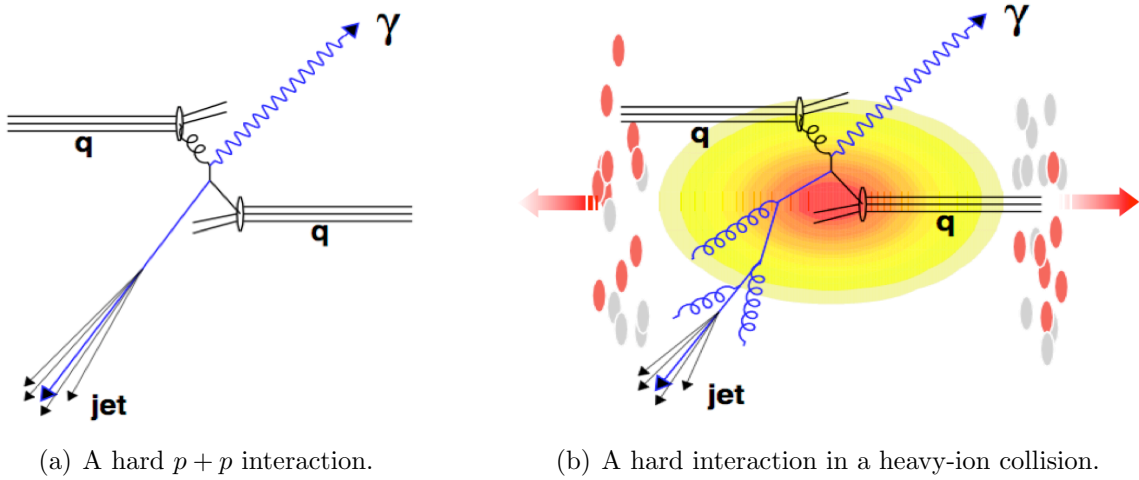


Figure 1.5: Illustration of interactions  $p+p$  and heavy ion collisions. Particles produced in a QGP-like medium will pass through the medium before being detected. The effect of the medium on these hard collision probes can be studied relative to control interactions in  $p + p$  collisions through quantities such as,  $R_{AB}$  (Equation 1.5). Figure adapted from [30]

above about  $2 \text{ GeV}/c$ . In  $p + p$  collisions, where a QCD phase transition is not expected, measured particle production serves as a baseline to heavy ion collisions. In a QGP-like medium produced in, for example,  $Au + Au$  collisions, energetic partons (large  $p_T$ ) produced in hard scattering events passing through the medium can lose energy and momentum, either through gluon radiation (bremsstrahlung) or in elastic or inelastic interactions with the medium [4].

In heavy collisions, the nuclear modification factor,  $R_{AB}$ ,

$$R_{AB} = \frac{dN_{A+B}}{\langle N_{coll} \rangle \times dN_{p+p}} \quad (1.3)$$

is one of the quantifiers of medium effects on particle yields.  $R_{AB}$  is defined as the ratio of particle yields in a particular heavy-ion collision environment,  $dN_{A+B}$ , and particle yields measured in “binary” nucleon-nucleon collisions,  $dN_{p+p}$ , scaled by the expected number of point-like binary nucleon-nucleon collisions,  $\langle N_{coll} \rangle^\dagger$ , for the centrality class of heavy-ion collisions being considered. A distinction is made between “initial” state effects, which result from the physics of the incoming nuclei prior to the collision, and “final state” effects that include the effects of the produced medium on particle yields. Neglecting initial

<sup>†</sup> $\langle N_{coll} \rangle$  is determined from Glauber model calculations [31].

Table 1.1: Theoretical and experimental heavy quark cross section estimates for  $\sqrt{s}=200$  GeV  $p+p$  collisions. The STAR result is obtained from a  $d+Au$  measurement.

Quark	Mass (GeV)	$\sigma_{total}$ (mb)	Uncertainty on $\sigma$	Source
charm	$1.25\pm 0.09$	0.256	+0.400 / -0.146	FONLL [20]
charm		0.244	+0.381 / -0.134	NLO [25]
charm		0.567	$\pm 0.057^{stat} \pm 0.224^{sys}$	PHENIX [26]
charm		1.3	$\pm 0.2^{stat} \pm 0.4^{sys}$	STAR [27]
bottom	$4.2-4.7\pm 0.07$	0.00187	+0.00099 / -0.00067	FONLL [20]
bottom		0.0046	$\pm 0.0013^{stat} +0.0026/-0.0022^{sys}$	PHENIX [28]
bottom		0.0039	$\pm 0.0025^{stat} +0.003/-0.002^{sys}$	PHENIX [29]
top	$174.2\pm 3.3$	$\sim 0$	N/A	N/A

state effects (e.g. Cronin broadening [32]) and assuming binary scaling of point-like QCD nucleon-nucleon processes, we should find  $R_{AB}=1$ . Ignoring these effects, deviation of  $R_{AB}$  from unity in heavy-ion collisions is equivalent to deviation from simple QCD expectations for particle yields, presumably due to QGP-like medium effects.

The applicability of binary-scaling of QCD processes in heavy-ion collisions has been demonstrated (within experimental uncertainties) by two measurements at RHIC. The first is made using “direct” photons produced in initial hard collisions via the process  $g+q\rightarrow\gamma+q$ . As photons interact electromagnetically, a strongly interacting medium should be transparent to photons, thus their production reflects only the properties of the initial state [5]. PHENIX reported in 2005 that direct photon yields in  $Au+Au$  collisions measured over different centrality classes do show  $R_{AA}=1$  ( $R_{AA}$  for  $Au+Au$  instead of the generic  $R_{AB}$ ), exhibiting binary scaling relative to a  $p+p$  pQCD calculation [33]. The binary scaling of total heavy quark production has also been demonstrated [34] and is taken as another experimental confirmation of the binary scaling of point-like QCD processes in heavy ion collisions.

One of the most striking experimental results at RHIC is that of the significant energy loss of light quarks observed in the QGP-like medium. In this case, light quarks are “observed” through light meson measurements, such as  $\pi^0$ , while heavy quarks are “observed” through single leptons as already discussed. Figure 1.6 shows the nuclear modification factor,  $R_{AA}$  (subscript  $AA$  for  $Au+Au$ ), plotted for both light (via  $\pi^0$ ) and heavy quarks (via  $e^\pm$ 's from  $D$ 's) for selected  $p_T$  bins as a function of  $N_{part}$ .  $N_{part}$  is the number of participant nucleons in a given heavy-ion collisions and is a measure of collision centrality, where  $N_{part}$  increases

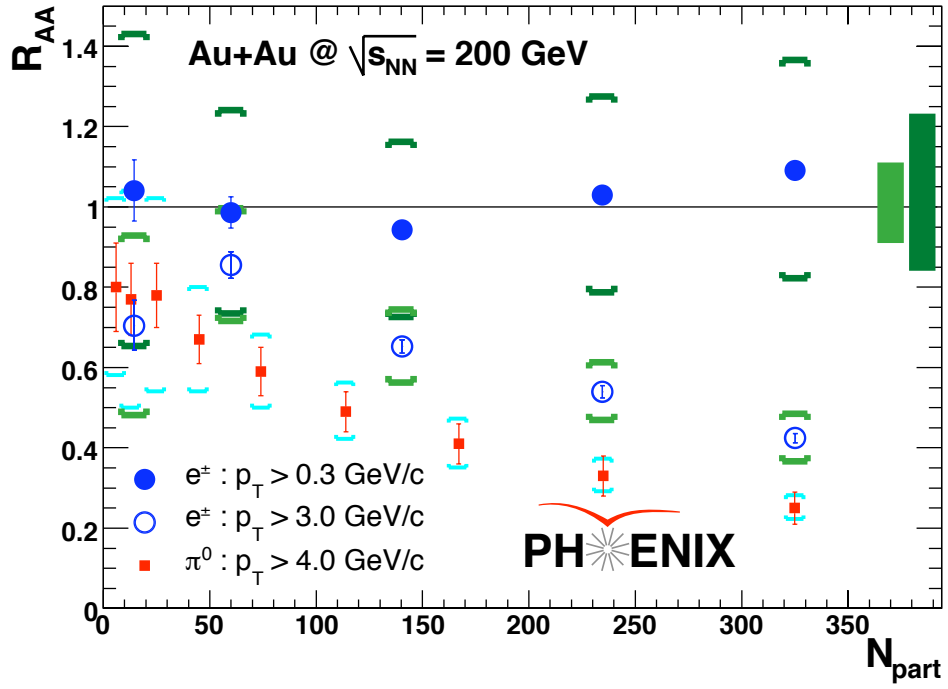


Figure 1.6: Nuclear modification factor for light and heavy quarks as a function of the number of participants,  $N_{part}$ . See text for additional details.

for more central events. Light quark energy loss is exhibited for  $\pi^0$  of  $p_T > 4.0$  GeV/c (solid (red) squares) where  $R_{AA}$  shows clear and increasing suppression with increasing collision centrality up to a *factor of five* in particle yields ( $R_{AA} \sim 0.2$  at higher  $p_T$ ) relative to the appropriately scaled  $p + p$  baseline. Quark energy loss in the medium is understood through gluon radiation and elastic and inelastic scattering of quarks within the medium. For a specified value of  $p_T$ , suppression in  $R_{AA}$  vs.  $N_{part}$  is a direct result of this energy loss that reduces the original particles'  $p_T$  values (effectively shifting the  $p_T$  spectra to the left on a plot of  $p_T$ ).

Heavy quarks also have a valuable role to play in studying energy loss in the QGP-like medium. As previously discussed, photon production in a heavy-ion collisions has demonstrated the binary scaling of point-like QCD nucleon-nucleon collisions indicated by  $R_{AA}=1$  (Equation 1.5). As opposed to photons that only interact electromagnetically, heavy quarks are color charged objects and are expected to interact with a medium of deconfined quarks and gluons. Heavy quarks are produced primarily through initial hard processes with a timescale of  $\tau \propto 1/2m_{HQ}$  for  $Q\bar{Q}$  pairs and subsequent thermal production processes are strongly suppressed [35]. The weak decay of heavy quarks means that their lifetime is longer than the produced medium. This allows heavy quarks to also serve as probes of phenomena of color-screening and color charge density of the medium [4]. Energy loss in the medium for heavy quarks through gluon radiation was expected to be strongly suppressed relative to light quarks at forward angles, the so-called “dead cone effect” [36].

A plot of particle production over all  $p_T$  and  $N_{part}$  showing no suppression ( $R_{AA}=1$ ) would provide some reassurance that the observed suppression is not due to other, non-medium effects. In Figure 1.6 the solid (blue) circles show  $R_{AA}$  for heavy flavor single electrons (described in the next section) for  $p_T > 0.3$  GeV/c, which contains more than half of heavy-flavor single electrons above this lower experimental  $p_T$  bound.  $R_{AA}$  for the integrated heavy-flavor yield is consistent with unity and indicates the applicability of binary scaling of QCD processes for heavy flavor production for all  $Au + Au$  collision centralities. The open (blue) circles in Figure 1.6 show heavy flavor single electrons for  $p_T > 3.0$  GeV/c. Suppression as a function of  $N_{part}$  is also observed for heavy quarks. The single electron  $p_T > 3.0$  GeV/c bin is equivalent to the  $p_T > 4.0$  GeV/c bin for  $\pi^0$  since heavy flavor single electrons result from charm mesons with  $p_T > 4.0$  GeV/c<sup>†</sup>. This apples-to-apples comparison between light and heavy quarks indicate that heavy quark energy loss is less than that for light quarks, but the energy loss is still greater than originally expected when considering the anticipated

---

<sup>†</sup>The inherent momentum degradation in the process  $D \rightarrow$  lepton.

dead cone effect. This observed energy loss is not fully understood, but this observation along with hydrodynamic calculations for  $Au + Au$  data suggest that the QGP-like medium is behaving like a strongly interacting fluid rather than a quark-gluon “plasma” [34]. Our understanding of the medium produced at RHIC is evolving, and heavy quarks are playing a vital role in driving this evolution.

## 1.6 Heavy flavor measurements in PHENIX

As free quarks are not observable in nature, charm quarks produced in the initial hard scattering processes between partons will hadronize primarily into the family of “open” charm  $D$  mesons, which are combinations of rare  $c$  or  $\bar{c}$  quarks with one of the ubiquitous light quarks. The energy distribution of a final state  $D$  meson is described by its corresponding fragmentation function, which describes the fraction of energy inherited from the original  $c$ -quark. Both hadronization and fragmentation are examples of primarily soft QCD processes which cannot be calculated perturbatively but can be measured experimentally. The charm quantum number is preserved in strong but not weak interactions, so the single charm quark  $D$ ’s decay weakly with corresponding lifetimes of  $\tau \sim 10^{-15}$  seconds. An example of the weak, semi-leptonic decay of a  $D$  meson has been shown in Figure 1.4, where the resulting “single” lepton,  $l$ , is either an electron or muon.

Direct lepton production through weak and electromagnetic interactions are suppressed relative to the strong interaction by twelve and four orders of magnitude respectively [24], so experimentally speaking, essentially no leptons are directly produced in nucleon-nucleon collisions. This relative dearth of “early” leptons suggests that they may be useful probes for charm detection; however, electrons and muons are by no means scarce particles, for they are produced abundantly in light hadron decays that must be successfully accounted for and eliminated through experimental techniques.

As prescribed by the weak interaction theory, certain decay modes of  $D$  mesons are more highly favored than others. The single lepton semi-leptonic decay has already been mentioned. Other prominent decay modes such as  $D^0 \rightarrow K^- \pi^+$  and  $D^+ \rightarrow K^- \pi^+ \pi^-$  result in light hadron daughters. Both the semi-leptonic and hadron decay channels represent experimentally convenient methods for measuring heavy quark production from heavy flavor mesons. The semi-leptonic decay mode amounts to an *indirect* measurement since only the leptons are measured and used to infer the  $D$  meson and by extension the charm quark. A

*direct* measurement of  $D$  mesons using hadron daughters forms an invariant mass from the expected hadron decay combinations, permitting “direct” observation of  $D$ ’s as a peak in the invariant mass spectrum. An overview of both direct and indirect methods is now discussed.

One such direct measurement of charm is the reconstruction of a  $K^-\pi^+$  resulting from the decay of a  $D^0$  meson. Once the invariant mass<sup>†</sup> distribution is formed, and the  $D$  peak is observed, the background level represented by the invariant mass continuum beneath the peak is statistically subtracted to provide the yield of  $D$  mesons. The proper decay length, denoted by  $c\tau$ , for  $D^\pm$  is  $311.8 \mu m$  and for  $D^0$  is  $122.9 \mu m$ . In simulations using the PHENIX detector, the mean detected vertex of  $D^\pm$ ’s is about  $800 \mu m$  from the primary collision vertex, with the additional factor of 2.5 due to the Lorentz boost. The charm/anti-charm quark pairs decay essentially at the collision vertex, while heavy flavor mesons will decay from a secondary vertex offset by the boosted lifetime of the particle. Precise vertex determination and identification of these secondary charm decay vertices could permit the reduction of the large amounts  $K^-\pi^+$  pairs not arising from charm meson decay but has not *yet* been implemented.

Identification of these displaced vertices permits the tagging of likely heavy flavor decay events, reducing the overall background to a level that allows direct measurements with a high degree of significance. This is done at the B-factories [37] and the Tevatron [38] where the detectors possess these capabilities. However, neither of the large detectors at RHIC, STAR and PHENIX, currently possess displaced vertex measurement capabilities, hampering efforts to make direct measurements. The inability to tag likely C or B events using a secondary vertex dramatically increases the backgrounds prohibiting precision measurements [27]. Without precision vertex information these analyses, especially in heavy-ion collisions, face very low signal to background levels (1/100’s) but do benefit somewhat from the ability to calculate backgrounds from the invariant mass continuum below the mass peak. Efforts to install high resolution vertex tracking permitting the identification of these secondary heavy flavor vertices are underway in both STAR and PHENIX and have the possibility of revolutionizing heavy quark measurements at RHIC.

The indirect method of heavy flavor measurement, which is the method employed in this dissertation work, is made is through the measurement of single leptons from the semi-leptonic decay of  $D$  mesons. The basic analysis methodologies to measure both single electrons and

---

<sup>†</sup>frame invariant mass,  $M$ , defined as:  $M^2 = E^2 - |P|^2$ , where  $E$  is the particle’s energy and  $P$  is its momentum.

single-muons have been employed since the early 1970's [39]. The measurement is statistical in that estimates of all “backgrounds” are subtracted from all single lepton candidate tracks identified in the detector. If the primary sources of backgrounds are well understood and subtracted, the remaining excess of particle tracks is then attributed to the heavy flavor signal. In this method, no individual reconstructed particle or track is identifiable as being either signal or background. It is only through the statistical (numerical) estimation and subtraction of quantities that any physics message is obtained. While this methodology does not characterize individual events, clear kinematic differences between the “prompt” or “direct” leptons from heavy flavor decay and the various sources of background that originate from the copiously produced hadrons do exist. Characterization of the backgrounds through these indirect means is the key to this methodology and serves as the primary limitation to precision for measurements made using this approach.

The two lightest mesons, pions and kaons, represent a dominant fraction of the total inelastic cross section for  $p + p$  collisions. An approximate ratio of light hadrons to muons from charm can be obtained by approximating the light hadron ( $\pi$ ,  $K$ ) production cross section as the full  $p + p$  inelastic cross section of 30 mb. The total charm quark production cross section has been measured by the PHENIX collaboration to be about 0.5 mb. The Particle Data Group quotes a global fractional value of charm quark decay to single leptons at 9.6%. For the indirect method, PHENIX measures this inclusive set of single leptons resulting from all  $D$  meson decay, which is primarily  $D^0$  and  $D^\pm$ . About 3.2% of the  $D^0$ 's have muons in the decay chain ( $\sim 3.5\%$  for electrons). The values for  $D^\pm$ 's are  $\sim 9.5\%$  for muons and  $\sim 8.6\%$  for electrons. Assuming that nearly all measured charm in the single-muon channel results from  $D^\pm$  and  $D^0$  semi-leptonic decay, and assuming a  $D$  chemistry of 70%  $D^0$  and 30%  $D^\pm$ , the branching fraction for charm to single-muon is approximately 5%. This suggests a ratio of light hadron to heavy flavor single-muon of:  $30 \text{ mb} / (0.5 \text{ mb} \cdot 0.05) = 1200$ . Fortunately, with the existing PHENIX detector design the ratio of total background to signal in the muon channel is reduced to an overall level of 2:1 or 3:1 depending on  $p_T$ . The situation for the single electron measurement in PHENIX is a bit rosier, with the background to signal ratio less than 1 for all of the acceptance except at the lowest values of  $p_T$ .

As opposed to the direct method, which can easily distinguish between charm and bottom through the use of invariant mass distributions, the charm and bottom components are not easily separable with the indirect measurement approach, although recent results are able to provide a first look at separating the charm and bottom components [28]. As

mentioned, for heavy flavor single leptons, charm is the dominant component below a  $p_T$  of about 4.0 GeV/c, with bottom believed to dominate above that [20]. The heavy flavor single-muon measurement presented in this work covers the  $p_T$  range from 1.0-5.0 GeV/c, so the term heavy flavor is nearly synonymous with charm.

## 1.7 The PHENIX central arm heavy flavor measurement

The PHENIX detector (Chapter 4), which is used for this dissertation measurement, does not possess full  $4\pi$  solid angle coverage. Rather, the detector is designed to make measurements in two primary kinematic regions. With the convention of angles measured relative to the longitudinal beam axis, the two regions are: 1) mid-rapidity<sup>†</sup>, with  $\pi/2$  acceptance centered at  $90^\circ$  polar angle in the “central arm”, and 2) forward rapidity, from about  $10^\circ$  to  $30^\circ$  polar angle in both forward and backward directions with full azimuthal coverage.

The heavy flavor single electron result previously discussed (Figure 1.6) is a PHENIX central arm single electron measurement. The central arms have very little material within their acceptance, enabling them to focus on the measurement of electrons [26, 34]. Using particle identification detectors, a clean sample of electrons can be collected. However, there exist several sources for electrons apart from that of heavy flavor decay. The largest source of background electrons result from  $\pi^0 \rightarrow \gamma\gamma$  decay and the subsequent photon conversion (a.k.a. pair production  $\gamma \rightarrow e^+e^-$ ) in the limited material (mostly air) between the collision vertex and the PHENIX central arm detector. Dalitz decay,  $\pi^0 \rightarrow e^+e^-\gamma$ , also contributes significantly. Other less important sources of background electrons arise from direct photons, weak kaon decay, and vector meson decay. Most of these backgrounds, namely  $\pi^0$  and  $\eta$ , have been independently measured by PHENIX [19] and provide excellent input into Monte Carlo detector simulations which only have to deal with well understood electromagnetic processes. The level of photon conversion background is essentially measured by adding additional conversion material in the PHENIX acceptance for a portion of the collision period. The additional material increases the level of photon conversion by a well determined factor. These various details all combine to allow PHENIX to make the most precise heavy flavor charm quark cross section measurements at RHIC [26, 34].

---

<sup>†</sup>Rapidity is defined in Appendix A. It is related approximately to polar angle, with mid-rapidity corresponding to  $\theta=90^\circ$ .

## 1.8 General detector methods for measuring single muons

This section introduces two important details of experimental detector design when measuring single muons. The next section (Section 1.9) then discusses these details in terms of the existing PHENIX muon detector. The standard technique for muon identification employs large amounts of dense material (e.g. steel) which interacts with and absorbs hadrons. Unlike electrons, which due to their light mass readily interact in absorber, high momentum muons possess significant penetrating power. To optimize an experiment to measure muons, there are two simple, though immensely important details to consider: 1) the location of the closest absorber to the collision vertex, and 2) the total amount of available absorber and how it is allocated before the muon detection equipment.

### Location of closest absorber to the collision vertex

Placement of absorber material as close as possible to the collision vertex maximizes the number of hadrons absorbed before they can decay into muons. Once a hadron decays into a muon, it will likely penetrate the absorber material and reach the muon detection layer as a background track. Since primarily just two types of particles are at play in the single-muon analysis, heavy flavor muons and light hadrons, represented primarily by  $\pi^\pm$  and  $K^\pm$ , it is instructive to consider the decay of both types of particles in the muon arm acceptance. The dominant decay channel for charged pions is  $\pi^\pm \rightarrow \mu^\pm \nu_\mu$  (99.99%). The neutrino passes undetected through the detector and, to a large extent, the muon possesses the energy and direction of the parent pion.

Once a hadron decays into a muon the likelihood that it will penetrate to the deepest layer of the detector entering the pool of muon candidates dramatically increases since muons will not be absorbed in the steel. The dominant source of energy loss for muons is ionization energy loss in the steel. Depending on the location of the closest absorber material, with an average decay length,  $c\tau$  of 7.8 m, a small but meaningful fraction of the total number of pions will decay into muons. The fraction of pions that do decay as a function of decay length (cm) is given by [15]:

$$P(z) = 1 - e^{-Mz/|\mathbf{p}|c\tau},$$

where  $P(z)$  is the probability that an unstable particle decays before a distance  $z$ ,  $M$  and  $|\mathbf{p}|$  is the particle's mass and momentum, and  $c\tau$  is the mean proper lifetime in meters. The  $c\tau$

for muons is 658.7 meters and for kaons is 3.7 m. The large  $c\tau$  for muons indicates that their decay is irrelevant for the current analysis. Using these values the decay likelihood can be plotted (Figure 1.7) as a function of the distance traversed for a  $p_T=1.0$  GeV/c and  $p_T=5.0$  GeV/c, which is the range over which single-muons have been measured. The figure shows that the likelihood for a pion to decay before reaching absorber material is about two orders of magnitude above the muon decay likelihood (not visible in the figure), while the kaon decay probability is more than a factor of 3 to 4 larger than that for pions for the same  $p_T$ . This plot includes the 99.9% and 63.4% branching ratio for  $\pi$ 's and  $K$ 's to muons, respectively. Although the overall yield of kaons produced in collisions is significantly less than that of pions (Figure 5.18 shows the  $K/\pi$  ratio as a function of  $p_T$ ), due to the increased decay probability before reaching absorber material, kaons contribute nearly equally as a source of muon backgrounds from hadron decay.

### Depth and allocation of absorber material

It is illustrative to examine a “traditional” fixed-target muon experiment, such as the Fermilab experiments with 300 GeV proton beams incident on fixed uranium targets [40]. Fixed-target collisions produce muons boosted in the direction of the incident beam, while particles produced in the center-of-mass of colliding beams do not receive the same momentum boost in the forward/backward direction of the beams. The Fermilab fixed-target experiment measured muons with momenta between 90 and 150 GeV/c, while typical muon momenta at RHIC ranges from as low as 3 GeV/c to approximately 25 GeV/c. The degree of multiple scattering a particle undergoes scales inversely with the particles momentum,  $\theta \sim 1/p$ , so a comparison of the lower bound of muon momenta indicates that for the same amount of material muons in PHENIX would experience a factor of  $30\times$  more multiple scattering. The extent of angular straggling directly impacts particle tracking resolution, which by extension directly degrades momentum determination. The Fermilab experiments used 3 m of steel immediately following the target for hadron absorption. An additional 5 m of steel was used in the muon apparatus down stream of the beam. The total of 8 m of steel absorber can be compared to the  $\sim 1.5$  m of steel in the PHENIX muon arm. The amount of total steel directly sets the hadron contamination level in the measured muon tracks.

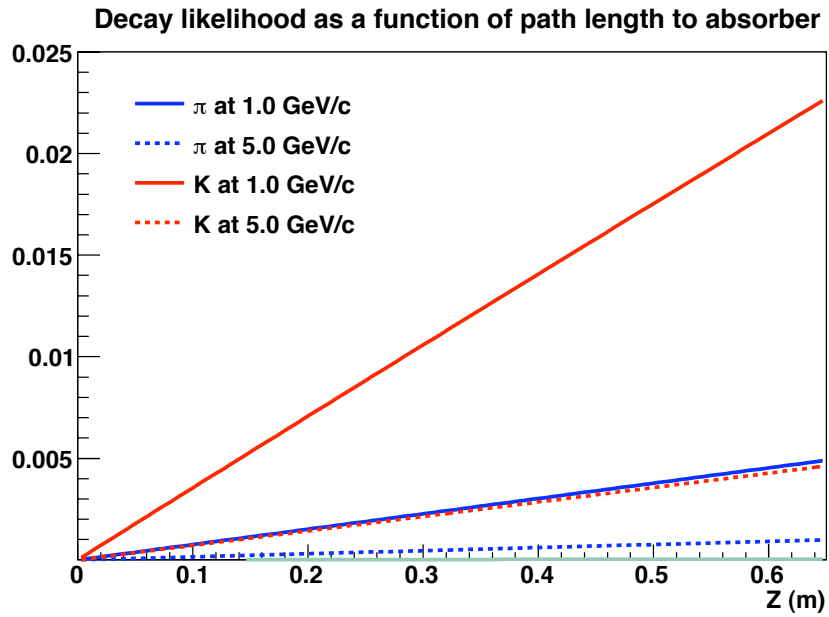


Figure 1.7: Particle decay likelihood as a function of flight path of  $\pi$  (blue),  $K$  (red), and  $\mu$  (green, but not visible) for  $p_T$  1.0 and 5.0 GeV/c. Typical muon decay likelihood is below  $10^{-3}$ . The typical  $z$ -vertex acceptance for the single muon analysis includes the range  $20 \leq z \leq 60$  cm of *total* decay path length since the closest absorber is at  $|z| < 41$  cm accepted collisions have a range of  $-20 \leq z \leq 20$  cm.

## 1.9 How PHENIX measures single-muons at forward angles

Compared to the mid-rapidity central arm measurements, the experimental situation is less sanguine for forward rapidity heavy flavor measurements in the single-muon channel. The presence of steel in the PHENIX forward angle muon spectrometers removes all of the backgrounds that arise from electromagnetic processes that play a crucial role in the PHENIX central arm single electron analysis, although other important sources of muon backgrounds remain. The two PHENIX “muon” spectrometers, also referred to as muon “arms”, at forward and backward rapidity are optimized primarily for the measurement of dimuons resulting from charmonium decay. So, a measurement of single-muons with the PHENIX detector must be able to successfully estimate and eliminate large backgrounds using a detector that was never designed for that explicit purpose. The key issues of the location of first absorber material and the total amount and allocation of the absorber material have been discussed for optimal muon detection. These two issues are now considered for the PHENIX muon arms.

### Location of closest absorber to the collision vertex *in PHENIX*

The PHENIX experiment possesses a interaction region that is free of instrumentation or other material over a region  $\pm 41$  cm along the direction of the beam pipe ( $z$ -direction). Figure 1.7 illustrates that a non-negligible fraction of pions and kaons will decay into muons in this region. The probability for a hadron to decay over a given distance (in the lab frame) decreases with increased momentum. This can be seen in Figure 1.7 as the  $p_T=5.0$  GeV/ $c$  probability lines (dashed) lie a factor of more than three below the  $p_T=1.0$  GeV/ $c$  lines (solid).

Unlike at fixed-target experiments where the interaction point is well known by the location of the target material, at RHIC, where protons and heavy ions are circulated in bunches within two beams moving in opposite directions, the timing of the delivery of different bunches is not accomplished exactly at the interaction point at  $z=0$ . Instead, collisions between the two beams occurs over a wide swath in  $z$  that extends  $\pm 30$  cm of  $z=0$ . Given this, ideally the placement of the nearest absorber material would be at  $\pm 30$  cm from the vertex; however, this wide collision region also serves as the event vertex for the PHENIX central arm acceptance. In order to prevent backgrounds from originating in absorber material

and entering the central arm detector acceptance, the nearest absorber material in the muon arm begins at  $z = \pm 41$  cm, roughly 10 cm beyond its optimal placement for muon detection.

The schematic location of the sensitive detector layers and the amount of steel hadron absorber in a particular PHENIX muon arm are represented in Figure 1.8. On the left side of Figure 1.8 the first absorber material is comprised of copper “nose cone” and steel of the central magnet that totals about 80 cm of contiguous absorber material. The combination of the wide event vertex and the extra decay path to the first absorber material means that above the minimum  $p_T$  cutoff of the muon arm acceptance, essentially *all* of the light hadrons that decay into muons will enter as background tracks into the pool of inclusive muon candidates. Since light hadrons have been estimated to outnumber heavy flavor single-muons by a factor of more than 1000, the integrated yield of the non-negligible fraction of light hadrons that decay to muons easily outnumbers the integrated yields of heavy flavor single-muons. This effect is most pronounced at low values of  $p_T$  (less than 3.0 GeV/c).

### **Depth and allocation of absorber material *in PHENIX***

The integrated nuclear interaction length is plotted on the vertical axis of Figure 1.8. By definition, muon candidates penetrate to the deepest sensitive layer in the muon arm, which is the Muon Identifier (MuID) gap 4 located at approximately 870 cm from the interaction point. The total amount of steel absorber between the event collision vertex and the deepest layers of the MuID is roughly 150 cm. Hadron interaction in material can be approximated by a simple exponential model described by  $e^{-L/\lambda_I}$ , where  $L$  is the integrated depth of absorber material and  $\lambda_I$  is the nuclear interaction length at a particular momentum for a particular hadron in a given material. For our purposes it is useful to assume the hadron is a pion which has a momentum averaged  $\lambda_I$  of roughly 16 cm in steel. Using these assumptions, the  $9.5\lambda_I$  of steel in the PHENIX muon arms naively provides a total hadron rejection of  $e^{-9.5} \approx 10^{-4}$ . However, the likelihood for nuclear interaction is not equivalent to the likelihood for nuclear absorption, which is the key to muon-hadron separation.

In a research and development effort spanning 1989 to 1992 [41, 42] for what eventually evolved into the PHENIX muon spectrometer, range measurements in absorber for different types of beams ( $p, \pi, \mu$ ) were studied. Hadrons that interact in absorber material can shower, producing soft particles that are readily absorbed. But at larger momentum, hadrons are shown to increasingly interact in a way that produces “knock-on” particles that can carry

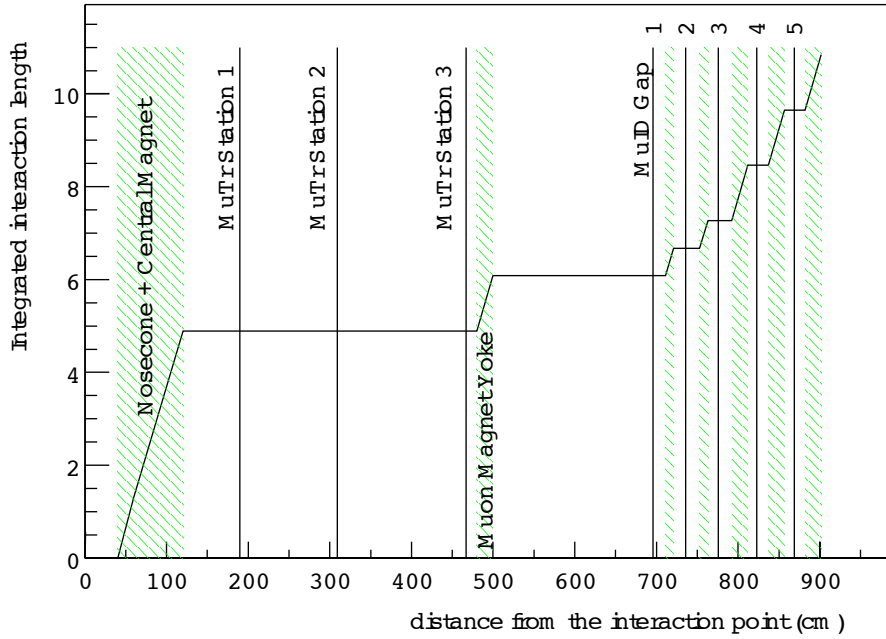


Figure 1.8: Depiction of a PHENIX muon spectrometer including distances from the interaction point (0,0,0) of detector layers and absorber material. The green indicates the regions of absorber material.

nearly the same momentum as the interacting particle, thereby penetrating more deeply into absorber material than expected in the simple exponential interaction model. The fraction of events with hits as a function of nuclear interaction lengths was measured for pions of 8 GeV/c total momentum, which is equivalent to a pion with a  $p_T$  of about 2.0 GeV/c in the middle of the muon arm acceptance. Roughly half of the events produced a hit in the calorimeter at a depth of 3.5 to  $4\lambda_I$ . Pions of larger momentum are observed to produce deeper penetrating particles. The results also show (see Figure 5.13) that after the initial range of 3.5 to  $4\lambda_I$  a more exponential-like trend is observed, and after  $8\lambda_I$  only 3% of the events showed hits. Extending the range measurement to  $10\lambda_I$  for the same 8 GeV/c pion, it is reasonable to expect a hadron absorption level of about 200. This indicates that for the amount of total absorber in the muon arm, and given that the overall production of light hadrons exceeds that for heavy flavor muons, the expected yield of “punch-through” hadrons (or a high momentum interaction remnant) that pass through the absorber material to enter the inclusive muon candidate pool is expected to be roughly the same order of magnitude than the signal heavy flavor muons. A natural question to ask is then, why not add more absorber material to provide further hadron absorption?

Due to the relative softness of the muon momenta in PHENIX, the placement of absorber material before the muon tracking chambers located at  $50 < z < 500$  cm in Figure 1.8 must be balanced by the extent of tolerable tracking resolution degradation. Given this constraint, the desire to additional absorber material to reduce hadron contamination in the muon sample runs up against a muon arm physics design goal. The MuID two shallowest absorber layers located at large  $z$  ( $z > 600$  cm) are intentionally thin to enhance the measurement of light vector mesons with a typical  $p_T < 2.0$  GeV/c, which is at the low end of the momentum acceptance muon arm. Any additional steel within the MuID volume cannot simultaneously accommodate this physics goal and still fit within the space of the experimental hall; therefore, the extent of hadronic backgrounds described in both this section and the previous section provide unavoidable challenges to making a single-muon measurement. Thankfully, analysis techniques are available to identify and measure the yields of muons from hadron decay as well as that of punch-through hadrons.

## Background estimation and subtraction

An indirect single lepton measurement of charm, as previously described, takes all properly reconstructed tracks to the deepest layer of the MuID and subtracts statistical estimates of

the backgrounds in the last MuID layer to obtain the signal. Since the production of light hadrons dominates the production of heavy flavor, this measurement technique requires an accurate estimate of measured tracks originating from  $\pi^\pm$ 's and  $K^\pm$ 's, with significantly smaller contributions from other hadrons such as  $K_L^0$ ,  $K_s^0$ ,  $p$ , and  $\bar{p}$ . As discussed, the primary muon backgrounds can be categorized as either originating from hadron decay or originating from hadrons “punching-through” that are misidentified as muons.

The combined hadron decay and hadron punch-through backgrounds in the single-muon analysis presented in this work are estimated using an integrated background Monte Carlo estimate that is benchmarked and constrained by the muon detector’s ability to indirectly identify both background types. Estimation of the muons from hadron decay exploits the measured collision vertex dependence of these “decay” muons (Figure 1.7). The shallow MuID absorber layers permit the measurement of unidentified hadron yields in the detector layers at lower  $z$  ( $700 \leq z \leq 800$  cm in Figure 1.8) since hadrons interacting and showering in the steel will stop. Ideally, these two measurements would constrain a standard detector GEANT based hadron Monte Carlo (MC) and permit a precise estimate of the backgrounds in the last MuID layer, but there is one more wrinkle. The simulation of hadron interactions for large amounts of steel is not well constrained. For thin absorbers the default hadron shower MC code works well, but for large amounts of steel (such as  $>1$  m), the differences between the two standard hadron shower packages are of the order of 50% due to amplification of small differences in the interaction cross section and in the reaction products [42]. By adjusting the overall interaction cross section in the MC hadron shower code, the input hadron spectra can be “tuned” to simultaneously match the measured stopped hadron distributions in the shallow MuID gaps and the measured hadron decay collision vertex dependence.

Figure 1.9 summarizes the work performed in this dissertation. The inclusive track yield (closed circles) is measured in the PHENIX muon spectrometer. The analysis undertaken to measure heavy flavor single muons determines a series of track quality selection criteria, dubbed “analysis cuts” which are optimized retain heavy flavor single muons and reject backgrounds. The application of these analysis cuts removes backgrounds and results in the  $p_T$  spectrum represented by the open circles. The remaining background is estimated and subtracted to determine the yield of heavy flavor single muons (blue stars). The final ratio of signal/background for this analysis ranges from  $\sim 0.3$  to  $\sim 0.5$ , which when combined with a 10% uncertainty in the background estimates gives a minimum attainable systematic

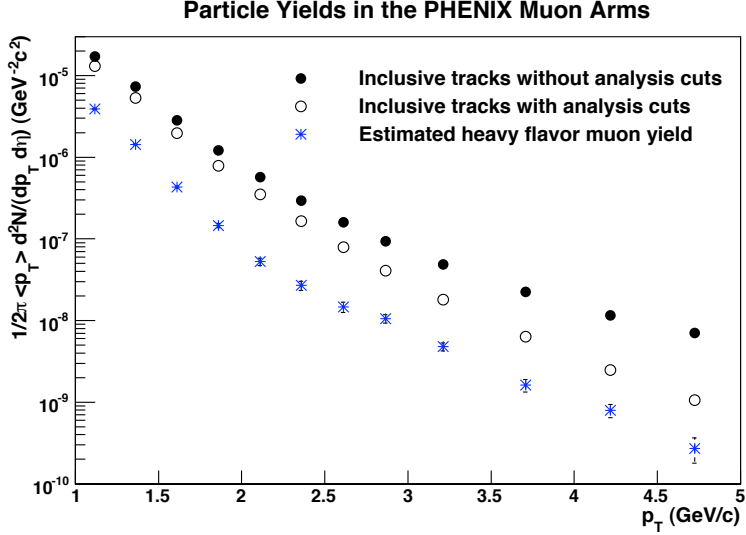


Figure 1.9: Plots of event normalized inclusive track yields versus  $p_T$  along with the estimated heavy flavor single-muon yield (stars). The application of analysis cuts reduces the total track sample by about 50% at low  $p_T$  and an order of magnitude at high  $p_T$  (from solid to open circles). Details are discussed in Chapter 5.

uncertainty of  $\sim 30\%$  on the final extracted cross section. In terms of invariant yields, the analysis effort can be summarized by the following simple equation:

$$N_{H.F.\mu}(p_T) = N_{total}(p_T) - N_{hadrons}(p_T) - N_{other}(p_T),$$

where  $N_{total}$  is the invariant yield of inclusive muon candidates,  $N_{hadrons}$  is the estimated yield of tracks originating from hadrons estimated by a tuned MC,  $N_{other}$  is some “other” background source attributable to non-hadronic sources. The  $N_{other}$  component, which is discussed later (Chapter 5.4), is small when compared to the hadronic background level and is included here for completeness. The subtracted quantity,  $N_{H.F.\mu}$ , represents the sample of single-muons attributable to heavy flavor decay. This subtraction takes a surprisingly long time to compute: hundreds and hundreds of man hours, thousands and thousands of computer hours, and two calendar years.

After the subtraction, there are two final steps. The yield of single muons is then converted into an invariant yield and/or cross section. The yield of single muons over the measured  $p_T$  region is then compared to pQCD calculations. A particular pQCD calculation is used to extrapolate from the minimum measured  $p_T$  of 1.0 GeV/c to  $p_T=0.0$  GeV/c. Using

estimates of branching ratios and  $D$  meson chemistry, an integrated charm quark production cross section,  $d\sigma_{c\bar{c}}/dy$ , over the measured slice of rapidity can be extracted for comparison purposes.

# Chapter 2

## Theoretical and phenomenological issues in heavy quark production

This dissertation presents a measurement of heavy quark production in high-energy hadron-hadron ( $p+p$ ) collisions. Since the theory describing this physics is QCD, interpreted through the quark-parton model, these results are compared to pQCD calculations as a test of both theoretical and experimental understanding. The phenomenological connection between QCD and the quark-parton model is the assumption of *factorization*. Factorization permits the separation of perturbatively calculable hard collision processes between hadronic constituents from universal, experimentally measurable, non-perturbative parton densities, which provide a description of the internal structure of the colliding hadrons. For hadron production cross sections, such as for  $D$  charm mesons, the additional process of *fragmentation* of quarks into hadrons must be included in the analysis. This process is described by fragmentation functions, which are measured experimentally and describe the decay probabilities of the heavy quarks into daughter hadrons (e.g.  $\pi$ 's,  $K$ 's, and  $D$ 's). In calculations that facilitate direct comparisons between experiment and theory, the additional step of describing the non-perturbative hadron-to-lepton decay spectrum and the branching ratio from the parent hadrons must also be considered. In  $p+p$  collisions this entire process can be schematically represented as [43]:

$$pp \xrightarrow{pQCD} Q \xrightarrow{N.P. frag.} H_Q \xrightarrow{decay} lepton \quad (2.1)$$

where  $Q$  is the heavy quark, *N.P. frag* stands for non-perturbative fragmentation process,  $H_Q$  is the heavy-quark hadron, and *lepton* represents the final-state observable. This chapter discusses these ingredients in heavy quark production cross sections, with an emphasis

on charm and to a lesser extent bottom production. Specific calculations relevant to this experimental work are discussed.

## Structure functions and parton distribution functions

Information concerning the internal structure of hadrons is an essential input into many pQCD calculations and is especially relevant in the calculation of heavy quark production in hadron-hadron collisions. The uncertainties in the parton distribution functions remain an important source of uncertainty in present day charm quark production calculations. For this reason a short discussion of the development of parton distribution functions is presented here.

This topic has its origins in the deep-inelastic scattering experiments of the 1960s. In the course of roughly a decade, quarks were first proposed as mathematical objects [44], deep-inelastic scattering results indicated that quarks might actually be the fundamental constituents of protons, the parton model was proposed by Feynman [45], and the existence of the charm quark was verified. The initial quark model proposed by Gell-Mann, Zweig, and Ne'eman a description of hadrons as being composed of combinations of quarks and anti-quarks. The early quark model included three quarks,  $u$ ,  $d$ , and  $s$ , but experimental results quickly pushed the development of the quark model beyond that stage. High-energy lepton-nucleon scattering experiments conducted beginning in 1968 (also referred to as deep-inelastic scattering, or DIS), played an essential role in the development of the quark-parton model.

In lepton-nucleon scattering, the incoming lepton exchanges a virtual photon (i.e. Coulomb interaction) with the target nucleon (as depicted for deep inelastic scattering in Figure 2.1). The effective spatial resolution of the photon goes as  $\sim 1/Q^2$ , where  $Q^2$  is the square of the four-momentum transfer. For lower energy (smaller  $Q^2$ ) interactions with a target nucleon, the virtual photon resolves a single point charge, the nucleon in this case, and the transferred energy induces excited states, or resonances. These resonances such as the  $\Delta$ , with an invariant mass of 1232 MeV/ $c^2$ , are short lived with typical widths of  $\Gamma \approx 100$  MeV, corresponding to  $\sim 7 \cdot 10^{-24}$  seconds [46].

Increasing the  $Q^2$  of the photon improves the spatial resolution. For larger  $Q^2$ , the nucleon will break apart into a number of secondaries. At sufficiently large  $Q^2$ , the photon

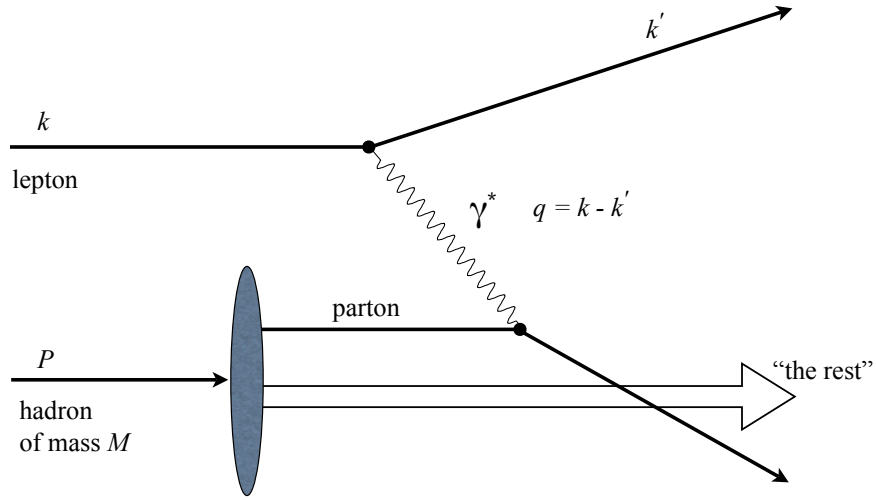


Figure 2.1: Schematic deep inelastic scattering diagram, adapted from [46].  $\gamma^*$  in the figure represents the virtual photon, which acts as a probe.

is capable of resolving structure within the nucleon, which is referred to as *deep* inelastic scattering. Figure 2.1 schematically depicts a typical deep inelastic lepton-hadron scattering process. A few of the other variables used to describe the DIS processes are  $\nu$ , the energy transferred from the lepton to the nucleon in the initial nucleon’s rest frame, and  $x$  (the “Bjorken  $x$ ”), which in the infinite momentum frame corresponds to the dimensionless fraction of the proton’s momentum carried by the parton [13]:

$$x = \frac{Q^2}{2Pq} = \frac{Q^2}{2M\nu} \quad (2.2)$$

where  $q$  is the virtual photon four-momentum,  $P$  is the proton four-momentum, and  $M$  is the invariant mass of the nucleon [46].

In the simple case of measuring the elastic scattering cross section of a lepton from a single point charge, such as a nucleon for sufficiently low  $Q^2$ , the scattering can be described in terms of form factors,  $F$ , of one parameter,  $Q^2$ . For inelastic scattering with large  $Q^2$  and secondary hadron production, another degree of freedom is needed to describe the cross section. In this case the form factors, referred to in this context as structure functions,  $F_1$  and  $F_2$ , are expressed in terms of two parameters,  $x$  and  $Q^2$ . Measurements of the inelastic cross section permit these structure functions to be extracted, and in the regime  $Q^2 \rightarrow \infty$  and  $\nu \rightarrow \infty$

(Bjorken limit) and for a given  $x$  over a large range of  $Q^2$ , the total inelastic cross section of leptons scattering from nucleons has been shown to be approximately independent of the  $Q^2$  of the collisions;  $F_i(x, Q^2) \approx F_i(x)$ . This phenomenon, that the scattering is expressible in terms of functions of the single variable  $x$ , is called Bjorken scaling. That the structure functions are approximately independent of  $Q^2$  for a given  $x$ , means that the photon is resolving single point charges *within* the nucleon. This is analogous to the single variable form factors used to describe low  $Q^2$  elastic scattering cross sections. The observation of Bjorken scaling, before the advent of QCD, was an important step toward the eventual adoption of the quark-parton model [13].

If quarks were non-interacting, no additional structure would be observed as  $Q^2$  is increased further, and exact Bjorken scaling would hold for all  $Q^2$  and  $x$  [24]. However this is not the case, as is suggested by QCD phenomenology. With increasing  $Q^2$ , the number of partons resolved by the virtual photon increases. Since quarks are electrically charged and gluons are not, the use of the photon to probe the structure of a nucleon in DIS experiments is limited to the quarks, but it is understood that in addition to valence quarks and sea quarks, gluons also contribute significantly to the internal structure of nucleons. The sea quarks, born out of fluctuations in the QCD vacuum, have observable effects on the measured structure functions. As a result, the scaling of structure functions in  $x$  and  $Q^2$  is, in fact, observed not to hold.

In Figure 2.2 the structure function,  $F_2$ , of the proton is shown versus  $Q^2$  for many values of  $x$ . As discussed in [24], there is an increased probability of finding a quark at smaller  $x$  because high-momentum quarks tend to lose momentum through gluon radiation. Two distinct trends can be observed in the functions shown in Figure 2.2: 1) for small fixed  $x$  (toward the top of the figure) the structure function *increases* with  $Q^2$ , and 2) at large fixed  $x$  the structure function *decreases* with increasing  $Q^2$  [15].

At low  $x$  and with increasing  $Q^2$ , the increased spatial resolution of the virtual photon allows one to observe the effects of the sea quarks that originate from the QCD vacuum as quark/anti-quark pairs with lifetimes governed by the uncertainty principle. At low  $x$ , with increasing  $Q^2$  the structure function increases because the number of partons sharing the momentum of the nucleon increases. Due to the ephemeral nature of the sea quark contribution their effective quantum numbers average to zero, and they carry only a small fraction of the nucleon's momentum [46]. This effect is reversed at larger  $x$ , with decreasing

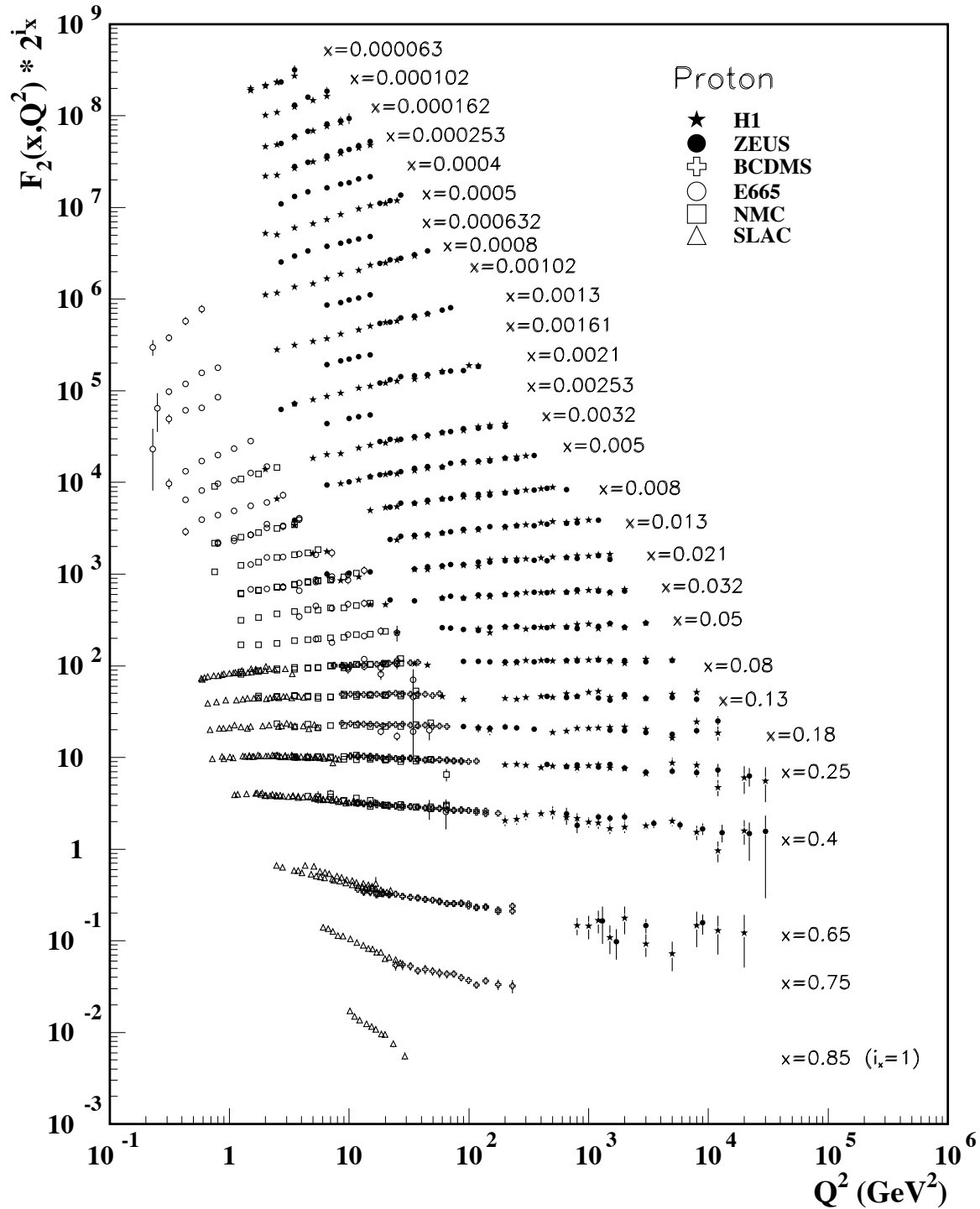


Figure 2.2: Structure function,  $F_2$ , of the proton measured in electromagnetic scattering [15]. For clarity in plotting,  $F_2$  is multiplied by a factor  $2^{i_x}$ , where  $i_x$  is the number of the  $x$  bin, ranging from  $i_x=1$  ( $x=0.85$ ) to 28 ( $x=0.000063$ ).

$Q^2$ . At large  $x$  there is an increased probability of observing softer “valence” quarks whose momentum has been degraded by gluon emission [24].

Although the structure functions themselves are process dependent, process-independent parton distribution functions (PDF’s) may be extracted from the structure functions measured in DIS experiments. These PDF’s can then be used in proton-proton collision calculations that are ultimately compared to measured particle spectra. A fundamental set of perturbative QCD relations known as the DGLAP\* or the Altarelli-Parisi equations can be used to infer some properties of the structure functions. Although perturbation theory cannot be used to calculate the structure functions directly, the DGLAP equation permits the calculation of the *evolution* of the structure function in  $Q^2$  once the function is known (measured) at a specific  $x$  and  $Q^2$ . The origin and utility of these equations are discussed in [16,24]. In one application, the structure functions in various processes measured at lower energies can be evolved to higher energies such as those seen at RHIC. The set of CTEQ<sup>†</sup> parton distribution functions that result from a global fit to data and evolved in this manner [50–52] are used as input to the heavy quark calculations of relevance to this work.

Uncertainties in the parton densities extrapolated from measured (HERA, see [15] for citations) to unmeasured regions (RHIC and LHC) are an important source of uncertainties in the calculated cross sections at RHIC energies. Figure 2.3 shows the CTEQ6.5M  $u$ -quark,  $d$ -quark, and  $g$  (gluon) distributions at the scale  $\mu = 2$  GeV normalized to the CTEQ6.1M PDF’s [52]. The shaded areas represent an estimated uncertainty band from the CTEQ6.1M analysis, and in the region of interest in the PHENIX muon arms (Figure 4.7),  $x \sim 10^{-1}$  to  $10^{-2}$ , the uncertainties are  $\approx 10$ -20%. For precision measurements these uncertainties could be considered rather large, especially for the gluon distribution. For the charm measurements at RHIC, other non PDF uncertainties dominate the current theoretical uncertainties. All sources of uncertainties in heavy quark calculations are summarized in Section 2.2.2.

### The renormalization and factorization scales

The concept of renormalization in QCD is especially relevant to this experimental dissertation because the choice of the renormalization scale,  $\mu_R$ , in heavy-quark pQCD calculations is one of the largest sources of uncertainty encountered when comparing these calculations to experiment. The goal of the section is not to attempt a grand summary of the details of

---

\*Dokshitzer-Gribov-Lipatov-Altarelli-Parisi [47–49]

†Coordinated Theoretical-Experimental Project on QCD, [www.phys.psu.edu/~cteq](http://www.phys.psu.edu/~cteq)

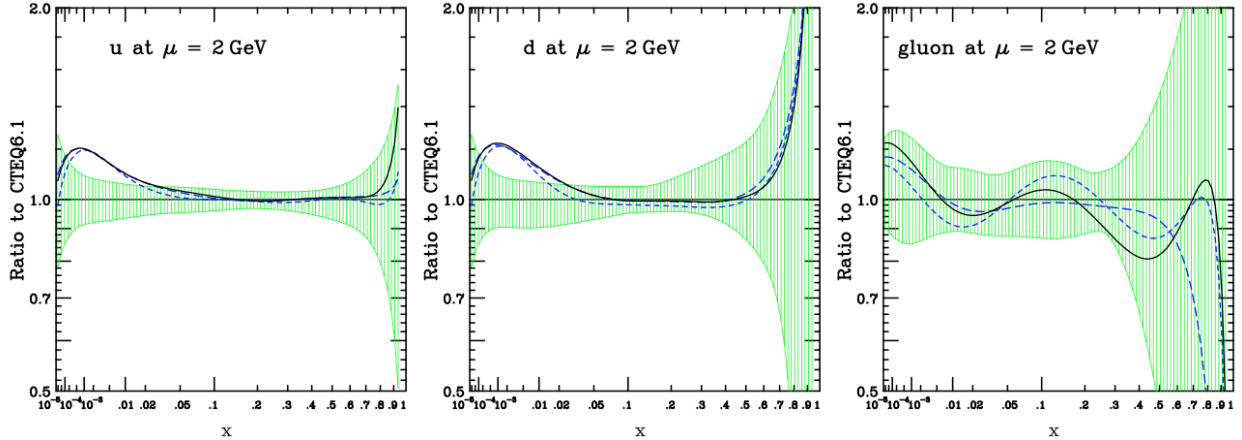


Figure 2.3: CTEQ6.5M PDF uncertainties for  $u$ ,  $d$ , and  $g$  as a function of  $x$  for the scale choice,  $\mu = 2$  GeV [52]. The  $x$  range measured for charm in PHENIX is in the range  $0.01 \lesssim x \lesssim 0.1$ .

renormalization in QCD, but rather to provide sufficient context to understand the origin and significance of  $\mu_R$  and the related factorization scale,  $\mu_F$ .

Renormalization in both QED and QCD refers to a re-parameterization of the interaction strength through the introduction of a quasi-arbitrary parameter,  $\mu_R$ , the renormalization scale. This parameter determines how the perturbative series is expanded. The choice of the renormalization scale is arbitrary in the sense that the final observed cross sections (or  $|\mathcal{M}|^2$ ) are physical observables and must therefore be independent of  $\mu_R$ . In the following discussion of heavy quark production, the common convention is followed relating  $\mu_R$  to the characteristic scale of the process [53], which in this case is  $m_{HQ}$ . For additional, introductory reference to renormalization and the renormalization group equation please see [16, 24].

The separation of the non-perturbative and perturbative components of a pQCD scattering amplitude calculation is implemented through the “convenient” choice of the factorization scale. This can be demonstrated by consideration of a generic pQCD expansion, which will typically contain logarithmic terms such as  $\ln(Q^2/\Lambda_{QCD}^2)$ . Note that:

$$\ln(Q^2/\Lambda_{QCD}^2) = \ln(Q^2/\mu_F^2) + \ln(\mu_F^2/\Lambda_{QCD}^2), \quad (2.3)$$

where the arbitrary scale  $\mu_F$  is the factorization scale, and  $\Lambda_{QCD}$  is the perturbative cut-off [16]. For this particular example, partons with  $p_T < \mu_F$  may be considered part of the

hadron structure and absorbed into the PDF, where as partons with  $p_T > \mu_F$  are considered part of the perturbative component of the calculation.

The choice of the values of  $\mu_R$  and  $\mu_F$  has the single largest impact on the uncertainties associated with the current set of heavy quark calculations of any parameter, especially in the predictions of charm production amplitudes. This fact will be revisited several times in the remainder of this dissertation. Concerning the exact choice of the factorization scale, as long as  $\mu_F$  is comparable to the hard scattering scale, e.g.  $\mu_F \approx p_T$ , differences in the calculated cross sections due to the variation of  $\mu_F$  reflect differences at the next order in the perturbation series [52]. Thus, variation of this parameter (and  $\mu_R$  as well) in a next-to-leading order calculation explores the uncertainty associated with the next-to-next-to-leading order contributions. In practice,  $\mu_F$  is conveniently chosen to be the same as  $\mu_R$ .

## Heavy quark fragmentation

Fragmentation functions are dimensionless functions that describe the inherently non-perturbative (i.e. non-calculable) momentum degradation that occurs in the hadronization process of quarks into hadrons. They describe the final state energy distribution of hadrons resulting from initial partonic hard scattering processes. Relative to light quarks, heavy flavor mesons retain a large portion of the original heavy quark momentum. In practice, heavy quark fragmentation functions are implemented by convolving non-perturbative effects using the Peterson or Kartvelishvili parameterizations [15] with a perturbative fragmentation calculation. For heavy quarks produced at large momentum relative to their mass, perturbative effects in the form large logarithms such as  $\alpha_s \log(m_{HQ}/p_T)$  play an important role in modifying the shape of the heavy quark fragmentation. Schemes that resum these logarithmic terms provide the perturbative component of the hadronization process [20], and the non-perturbative component is extracted phenomenologically from  $e^+e^-$  data. The non-perturbative fragmentation function is expected to scale roughly as  $\mathcal{O}(\Lambda/m_{HQ})$ , where  $\Lambda$  is a hadronic scale of a few hundred MeV. Because of this, the non-perturbative component will have non-negligible effects without degrading the accuracy of the factorized pQCD cross section (as claimed in [43]). The particular fragmentation function implementation and subsequent hadron decay to leptons used by the primary calculation referenced in this dissertation, referred to as FONLL, is discussed further in Section 2.2.2.

## 2.1 Implementations of the factorization theorem

QCD’s utility as the theory of the strong interaction is largely rooted in predictions made using the quark-parton model. In the original, pre-QCD parton model, hadrons are envisioned as extended objects consisting of partons held together by their mutual interactions. In the language of QCD and the improved quark-parton model, quarks and gluons are referred to collectively as partons that are asymptotically free at short distances. Within this phenomenology, the internal structure of hadrons due to the long-distance mutual interactions cannot be calculated. By neglecting parton-parton interactions, at high-energy/short distances the scattering amplitudes of “free” partons can be calculated. The short-distance and long-distance phenomena may be brought together into a single theoretical prediction by asserting the **factorization theorem** [54].

Factorization refers to the ability to separate, or factorize, the short-distance (perturbative, or hard) and long-distance (non-perturbative, or soft) components of the inclusive partonic cross sections [17]. Long distance, non-calculable effects can be factorized into functions describing the distribution of partons in a hadron (using PDF’s) or hadrons in a parton for final-state hadrons (using fragmentation functions) [54]. These two non-perturbative functions are measurable and are universal in the sense that when measured in one process, such as in DIS or  $e^+e^-$  scattering, they can be applied to a different process, such as the hadron-hadron collisions considered in this work. Once the non-perturbative effects have been factored out, the remaining cross section is a short distance, perturbatively calculable scattering of partons.

### “Classic” leading-order heavy quark factorization

The primary mechanism for heavy quark production in hadron-hadron collisions is the hard collision of one parton from each hadron. For hadron-hadron collisions at RHIC energies the dominant leading-order process is gluon fusion. Other LO contributions are suppressed because they require an anti-quark in the initial state [23]. LO gluon fusion, depicted in Figure 2.4, is used to demonstrate the factorization theorem, as was first applied to heavy quark production by Collins *et al.* in 1986 [55]. The cross section for hadrons  $A + B \rightarrow$  heavy quarks  $C + D +$  anything can be expressed as

$$\frac{d\sigma}{dy_C dy_D} \sim \sum_{i,j} \int dx_A f_{i/A}(x_A) \int dx_B f_{j/B}(x_B) H_{ij}(s, m_{HQ}, x_A, x_B, y_C - Y, y_D - Y) \quad (2.4)$$

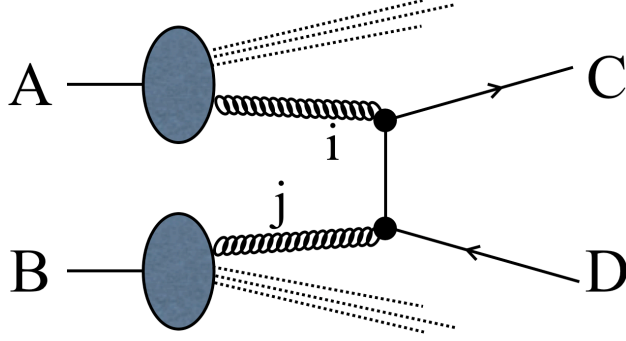


Figure 2.4: Schematic diagram of the leading-order ( $\alpha_s^2$ ) process of gluon fusion in hadron-hadron collisions. Additional details can be found in the text.

where  $x$  is the Bjorken  $x$ , the sum runs over the partons  $i$  and  $j$ , and  $Y$  is the rapidity of the parton center of mass frame<sup>†</sup>. The functions  $f$  are the PDF's, and  $H_{ij}$  is the partonic hard scattering cross section for the production of a heavy quark pair (plus anything else).

In [55] it is stated that the calculation of the cross section in Equation 2.4 relies on one basic assumption—that the mass of the heavy quark is sufficiently heavy to justify perturbative treatment. In the center of mass of the produced heavy quark system the intermediate virtual quark state is of order  $1/m_{HQ}$ , so if  $m_{HQ}$  is sufficiently large, the process is dominated by short-distance effects and is calculable in pQCD.

Two corollary details to this assumption play out in the calculation of the perturbation series expanded in terms of  $\alpha_s$ . First, in the factorized cross section in Equation 2.4, contributions suppressed by powers of the typical hadron mass scale,  $m_{hadron}$  relative to  $m_{HQ}$  are ignored. Second, the partonic cross section,  $H_{ij}$ , is expanded in powers of  $\alpha_s(m_{HQ})$ , which again requires  $m_{HQ}$  to be large. As noted in Chapter 1, diagrams such as Figure 2.4 lead to LO cross sections of the order of the *square* of the amplitude,  $|\mathcal{M}|^2$ , hence of order  $\alpha_s^2$ , and the NLO terms are of order  $\alpha_s^3$  [56]. The coupling  $\alpha_s$  is evaluated at the scale of the heavy-quark mass, which is  $\approx 0.3$ - $0.5$  for charm,  $\approx 0.2$  for bottom, and  $\approx 0.1$  for top [57].

---

<sup>†</sup> $Y = \frac{1}{2} \ln(x_A/x_B)$

## Heavy quark factorization at general order

Rather than express the cross section as originally written in Equation 2.4 [55], the most common form in current literature for the cross section of a heavy-quark pair ( $Q\bar{Q}$ ) is written as:

$$\sigma_{Q\bar{Q}} = \int dx_1 dx_2 f_i^{H1}(x_2, \mu_F) f_j^{H2}(x_1, \mu_F) \hat{\sigma}_{ij}(x_1 p_1, x_2 p_2, m_Q, \mu_F, \alpha_s) \quad (2.5)$$

where the  $f$ 's are the parton distribution functions,  $\hat{\sigma}$  is the short-distance partonic cross section (which is calculable order-by-order in pQCD [57]), and  $\mu_F$  is the renormalization scale. In calculations of total cross sections to NLO (order  $\alpha_s^3$ ), an increase relative to the LO result of about a factor of three is found [56]. Given the increase in the cross section due to NLO terms, the size of the next-to-next-to-leading order (NNLO) terms should clearly also be addressed. This is discussed in Section 2.2.1.

A general proof of the factorization theorem for heavy quarks in deep inelastic scattering, order by order for all orders of perturbation theory, was given by Collins in 1998 [58]. Two important features of the heavy quark factorization method are notable. First, the heavy quark masses are retained in the calculations if they are non-negligible with respect to the scale of the hard scattering. Second, in the calculation of the strong coupling,  $\alpha_s$ , the assumed number of “active” light quark flavors,  $n_{lf}$ , varies according to the physical scale (such as momentum). This can be viewed as a mass-dependent application of the factorization theorem.

As discussed in [58], the use of different numbers of  $n_{lf}$  have overlapping ranges of validity with threshold or switching-points between the schemes, which for the case of charm switches from  $n_{lf}=3$  to  $n_{lf}=4$ . The active light quarks are treated as partons with zero mass, and the inactive quarks are considered to be massive and non-partonic, so their contributions are not included. The matching between the  $n_{lf}$  and  $n_{lf}+1$  schemes is done using the renormalization and factorization scales set (approximately) to the the mass of the  $(n_{lf}+1)^{th}$  quark. In the variation of the physical scale of the process, such as  $Q$  in DIS or  $p_T$  in this work, the number of active quarks is varied accordingly. For the case of charm, charm is treated as non-partonic (i.e. massive) and  $n_{lf} = 3$  for  $p_T < m_{charm}$ . For  $p_T > m_{charm}$ , charm is treated as an active partonic flavor, and  $n_{lf} = 4$ .

## 2.2 Calculations of heavy quark production

Unlike light quark flavors ( $u, d, s$ ), “hard” processes are responsible for the production of heavy quarks ( $c, b, t$ ) which have masses,  $m_{HQ}$ , greater than about 1.3-1.5 GeV/c<sup>2</sup> (and hence a  $Q\bar{Q}$  creation threshold of  $\sim 3.0$  GeV/c<sup>2</sup>). The large masses of the heavy quarks motivates pQCD calculations of total  $Q\bar{Q}$  cross section calculations, while is not justified for light quarks. The consideration of heavy quarks introduces the additional quark mass scale,  $m_{HQ}$ , in addition to the basic energy scale ( $p_T$  in this context), which requires a different organization of the perturbative series depending on the relative magnitudes of  $m_Q$  and  $p_T$ . There are essentially two cases to consider,  $m_{HQ} \sim p_T$  and  $p_T \gg m_{HQ}$  [59]. The mass of the bottom quark is sufficiently large so as to preclude some of the ambiguities associated with calculations of charm quark production. This dissertation is concerned primarily with charm production, so “charm quark” is used nearly synonymously with “heavy quark” in the following discussion.

The first case,  $m_{HQ} \sim p_T$ , sometimes referred to as the Fixed-Flavor Scheme (FFN) for heavy flavor production, is calculated from hard processes initiated by light quarks and gluons, with the number of active light “partonic” flavors set to  $n_{lf}=3$  for charm. The number  $n_{lf}$  used in the calculation scheme determines how  $\alpha_s$  is calculated. This scheme is robust at threshold,  $m_{HQ} \sim p_T$ , but for  $p_T \gg m_{HQ}$  becomes unreliable since the perturbation series contains terms of the form  $\alpha_s^n \log^n(p_T^2/m_{HQ}^2)$ , which does not have good convergence properties for large  $n$  [59].

For the second case,  $p_T \gg m_{HQ}$ , sometimes referred to as the *zero mass scheme*, in which the heavy quark is included as an active flavor,  $n_{lf}=4$  for charm, in the calculation which serves to re-sum the logarithmic terms mentioned in the previous case. However, this scheme becomes unreliable as  $p_T \rightarrow m_{HQ}$ . This is the approach taken by global QCD analyses of parton distributions (e.g. MRS, CTEQ) and Monte Carlo programs (e.g. PYTHIA, HERWIG) [17]. Since many of the experimental measurements are at the interface between these two regimes, a heavy quark calculation spanning the full energy range must incorporate the physics of both the zero-mass and FFN schemes. For charm production this means seamlessly combining the  $n_{lf}=3$  (FFN) and  $n_{lf}=4$  ( $m_{HQ}$ ) schemes over the full energy range. The same idea holds for bottom production, in which the  $n_{lf}=4$  (FFN) and  $n_{lf}=5$  ( $m_{HQ}$ ) schemes are combined.

For the purpose of comparisons to measurements at RHIC, production cross sections for

heavy quarks are calculated with two basic approaches: 1) starting from total partonic cross sections calculated to NLO with  $n_{lf}=3$  using standard proton PDF's [60]. 2) integration of  $p_T$  and  $y$  distributions in the Fixed-Order Next-to-Leading-Log calculation which effectively merges the  $n_{lf}=3$  and  $n_{lf}=4$  schemes as described above [20]. These two approaches are discussed in the next two sections.

## 2.2.1 Heavy flavor cross section from NLO total partonic cross sections

Reconsidering the schematic equation (Equation 2.1):

$$pp \xrightarrow{pQCD} Q \xrightarrow{N.P.frag.} H_Q \xrightarrow{decay} lepton$$

The partonic cross section,  $\hat{\sigma}_{ij}$  (the first step from  $pp$  to  $Q$  in the scheme above) can be written in an  $\mathcal{O}(\alpha_s^3)$  (NLO) form [60],

$$\begin{aligned} \hat{\sigma}_{ij}(s, m, \mu_F^2, \mu_R^2) = & \frac{\alpha_s^2(\mu_R^2)}{m^2} \{f_{ij}^{(0,0)}(\rho)\} \\ & + 4\pi\alpha(\mu_R^2)[f_{ij}^{(1,0)}(\rho) + f_{ij}^{(1,1)}(\rho) \ln(\frac{\mu_F^2}{m^2})] + \mathcal{O}(\alpha_s^2)\}, \end{aligned} \quad (2.6)$$

where the  $f_{ij}^{k,l}$  are partonic scaling functions that depend only on  $\rho=4m^2/s$ , calculated to NLO [61]. According to the factorization theorem, the hadronic p+p cross section for charm production, written in terms of  $\hat{\sigma}_{ij}$ , is:

$$\sigma_{Q\bar{Q}}(s, m^2) = \sum_{i,j=q\bar{q},g} \int dx_1 dx_2 f_i^p(x_1, \mu_F^2) f_j^p(x_2, \mu_F^2) \hat{\sigma}_{ij}(s, m, \mu_F^2, \mu_R^2) \quad (2.7)$$

where  $x_1$  and  $x_2$  are the fractional momenta carried by the colliding partons, and  $f_i^p$  are the proton PDF's. The total cross section depends only on the quark mass and the renormalization scales  $\mu_R$  and  $\mu_F$  but not the kinematical quantity  $p_T$ . The heavy quark is considered massive in this calculation and is therefore not an active flavor. Using  $m=1.5$  GeV, fixed scales of  $\mu_F=\mu_R=m$ , and  $n_{lf}$  light flavors, the predicted NLO total charm cross section at the RHIC energy of  $\sqrt{s}=200$  GeV is [60]

$$\sigma_{c\bar{c}}^{NLO_{n_{lf}}} = 301_{-210}^{+1000} \mu b. \quad (2.8)$$

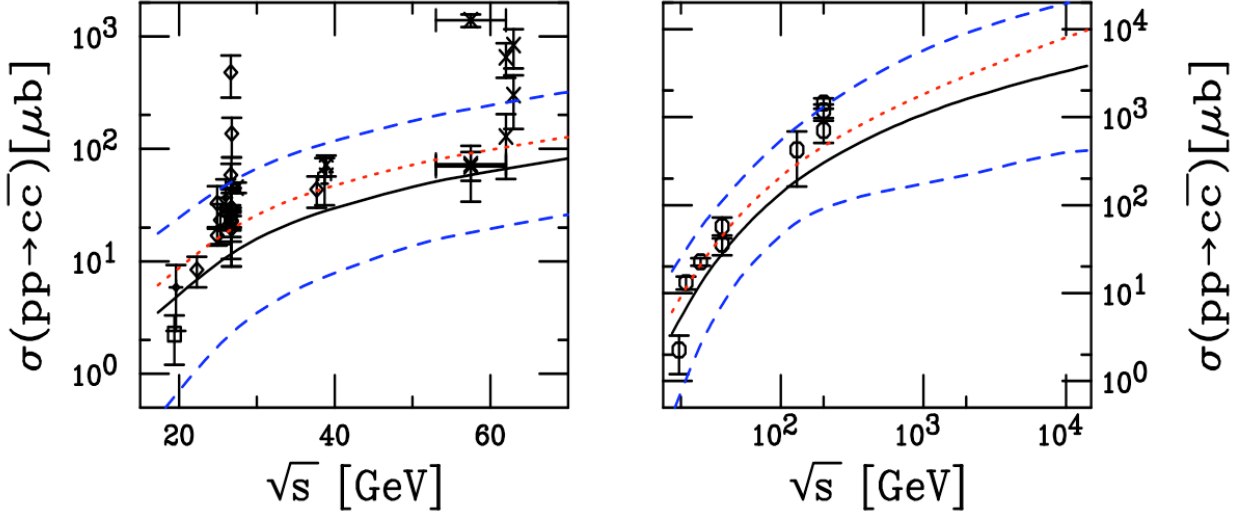


Figure 2.5: NLO total charm cross sections [60] calculated with CTEQ6M parton densities, compared to measurements from the ISR and RHIC. The dashed lines are the upper and lower edges of the calculation’s band of uncertainty, as determined in Section 2.2.2. The dotted line is a separate cross section calculation using  $m=1.2 \text{ GeV}/c^2$  and  $\mu_R=\mu_F=m$ .

Figure 2.5 shows the energy dependence of the total charm quark cross section. Details are provided in the figure caption.

### Uncertainties in the total partonic charm cross section

Several factors contribute to the large charm cross section uncertainties evident in Equation 2.8 and Figure 2.5. The right panel of Figure 2.5 shows that the uncertainty band in the total cross section grows broader with increasing  $\sqrt{s}$ , which corresponds to decreasing  $x$  and increasing gluon contributions which are less well determined. Also, the relatively small charm quark mass (compared to bottom) leads to a sizable factorization scale dependence for the total cross section. For charm, it is also true that the strong coupling constant is changes rapidly with the renormalization scale, as discussed in [60].

The same procedure has been adopted for evaluating uncertainties in both this FO NLO calculation and the FONLL calculation (Section 2.2.2). By varying the parameters in the calculation, an uncertainty band is established that is meant to encompass with a large probability the “true” theoretical prediction [20]. This procedure for evaluating the uncertainty in the calculations is discussed in Section 2.2.2.

## The effect of higher order corrections on the partonic cross sections

It is notable that NLO corrections to LO calculations increase the total cross section by a factor of 2 to 3, depending on the scales, mass, and parton densities, i.e.  $\sigma_{NLO}/\sigma_{LO} \sim 2$  to 3. The NNLO terms have been estimated to be of similar size to the NLO corrections, but are diminished to a factor of less than 1 with the inclusion of next-to-leading log terms [62].

### 2.2.2 Heavy flavor cross sections using FONLL

The state-of-the-art (*circa* 2008) charm cross section calculation used for comparison to experimental heavy flavor results in the field is the Fixed-Order plus Next-to-Leading-Log (FONLL) result [20]. FONLL provides the heavy flavor single lepton  $p_T$  spectrum,  $\frac{Ed^3\sigma_l}{dp^3}$ , that can be directly compared to measurements, as well as the total production cross section  $\sigma_{c\bar{c}}$ . The authors write the factorized lepton production cross section schematically as

$$\frac{Ed^3\sigma_l}{dp^3} = \frac{E_Q d^3\sigma_Q}{dp_Q^3} \otimes D(Q \rightarrow H_Q) \otimes f(H_Q \rightarrow l). \quad (2.9)$$

Here  $\otimes$  denotes a generic convolution,  $D(Q \rightarrow H_Q)$  corresponds to the measured non-perturbative hadronic fragmentation functions of heavy quarks ( $Q$ ) into heavy hadrons ( $H_Q$ ) as extracted from  $e^+e^-$  data, and  $f(H_Q \rightarrow l)$  involves the lepton decay spectrum, which implicitly accounts for the branching fraction of hadrons to leptons. FONLL includes a fixed-order NLO result [61,63] and also the resummation of larger perturbative terms proportional to  $\alpha_s^n \log^k(p_T/m_{HQ})$ . Since FONLL is the principle theoretical calculation used for direct comparison to the experimental work of this dissertation, as well as the model used to convert the single muon spectra to a charm quark cross section, further details of the implementation of FONLL will be discussed here.

### Implementation of FONLL

The discussion has previously alluded to the fact that for heavy quark production in pQCD, an additional scale, namely the mass  $m_{HQ}$  of the heavy quark alters the perturbative series organized around a single scale expansion. The fixed-order NLO calculation [61, 63] that has been available now for 20 years uses the fact that the mass of a heavy quark acts as an infrared cutoff on collinear singularities [55]. This permits one to express the cross section as a power series in the strong coupling constant evaluated at a renormalization scale close to the heavy quark mass. This works well when the quark mass is the only relevant scale for

the problem, as for the total heavy quark production cross section in Section 2.2.1.

However, for larger momenta ( $p_T \gtrsim m$ ), there is no single characteristic scale for the problem, and the perturbative series no longer converges with the use of either  $m$  or  $p_T$  as the value of the renormalization scale,  $\mu_R$ , and factorization scale  $\mu_F$ . For these larger  $p_T$  values convergence of the series is spoiled by the emergence of large logarithms of the ratio  $p_T/m$  at all orders in the perturbative expansion [64]. The logarithmic terms in the  $p_T$  expansion are classified as either  $\alpha_s^2(\alpha_s \log p_T/m)^k$ , which is referred to as leading-logarithmic or LL, and  $\alpha_s^3(\alpha_s \log p_T/m)^k$ , which is referred to as next-to-leading logarithmic, or NLL.

The FONLL calculation is a formalism that combines the existing fixed-order NLO calculations, referred to as FO, and all logarithmic terms summed to NLL, i.e. FO + NLL = FONLL. An explanation of the sundry details of the FONLL approach can be found in [64], but there is one important theoretical detail to outline here that is crucial to the successful combination of the different FO and NLL calculations. The FO approach uses the  $\overline{MS}$  renormalization scheme, which treats the heavy quark as massive. This means that for charm quark calculations there are three light flavors ( $n_{lf}=3$ ) for the running  $\alpha_s$  coupling, and charm should not be used in the PDF evolution. The NLL resummed calculation (for  $p_T \gg m_{HQ}$ ) makes use of a different renormalization scheme in which the heavy quark is included as an active flavor,  $n_{lf}=4$ . In order to combine the FO and NLL calculations, a change of scheme is implemented in the FO calculation that changes  $n_{lf}=3$  to  $n_{lf}=4$  to match the NLL calculation. Once this is done the FO and NLL match exactly to order  $\alpha_s^3$ .

### Parameters in the FONLL calculation

The FONLL calculation has as physical parameters the heavy quark mass and the coupling  $\alpha_s$ , as well as the unphysical renormalization and factorization scales  $\mu_R$  and  $\mu_F$ . The central values used for the scales are  $\mu_R=\mu_F=\mu_0=m_T=\sqrt{p_T^2+m^2}$ . The parton densities are included as a non-perturbative input. The QCD scale for five flavors,  $\Lambda^{(5)}$ , is 0.226 GeV, which is the value taken from the CTEQ6M parton densities. The central value for the heavy quark masses are 1.5 GeV/c<sup>2</sup> for charm and 4.75 GeV/c<sup>2</sup> for bottom.

### Fragmentation and lepton decay spectra in FONLL

Heavy quark fragmentation is implemented within the FONLL formalism that merges the FO + NLL calculations [65]. The NLL formalism is used to extract the non-perturbative

fragmentation effects from  $e^+e^-$  data. The decay of the  $D$  and  $B$  mesons to leptons uses spectra measured by CLEO at the Cornell Electron-positron Storage ring [66] at  $\sqrt{s}=10.5$  GeV. The  $p_T$  spectrum from this measurement is fit and used to represent all charm hadrons. The final FONLL lepton spectra is obtained by convoluting this  $D \rightarrow e$  spectra and the calculated parton-model  $b \rightarrow c$  spectra. The resulting spectrum is normalized using averaged  $D$  meson branching ratios, namely  $\text{BR}(D \rightarrow e) = 10.3 \pm 1.2\%$ .<sup>§</sup> This value is calculated for electrons but is used for the muon spectra. The averaged BR difference between electrons and muons is not expected to be large and is certainly small when compared to other uncertainties in both the calculated and measured lepton  $p_T$  spectra.

## Results from FONLL

Figure 2.6 from [20] plots the  $p_T$  spectrum for experimental results from the PHENIX and STAR collaborations *circa* 2004-2005 along with the uncertainty band of the FONLL calculation. The FONLL bands include contributions from  $D \rightarrow e$ ,  $B \rightarrow e$ , and  $B \rightarrow D \rightarrow e$ .

The total  $c\bar{c}$  cross section from FONLL is:

$$\sigma_{c\bar{c}}^{FONLL} = 256_{-146}^{+400} \mu b. \quad (2.10)$$

## Systematic evaluation of the theoretical uncertainties

Uncertainties in the FONLL calculation at RHIC energies originate from five sources [67]:

1. The effect of higher order terms is estimated through the variation of the scales  $\mu_R$  and  $\mu_F$  as described previously. For charm this effect is the dominant uncertainty, contributing a factor of  $\approx 3$  at low  $p_T$ , decreasing to  $\approx 50\%$  at higher  $p_T$ .
2. Variation in the mass of the heavy quark. For charm, the contribution to the total uncertainty is only relevant for  $p_T \leq 2-3$  GeV/ $c^2$ . Figure 2.7 shows the uncertainty bands as functions of  $p_T$  derived from variations in the scales, mass, and combined variation of scales and quark mass.
3. Non-perturbative fragmentation has effects of  $\approx 10-20\%$  at low  $p_T$  with smaller effects at larger  $p_T$ . If properly implemented, fragmentation should not be a large source of uncertainty relative to other sources.

---

<sup>§</sup>using a  $D$  chemistry of 30%  $\text{BR}(D^\pm \rightarrow e) = 17.2\%$  and 70%  $\text{BR}(D^0 \rightarrow e) = 6.9\%$

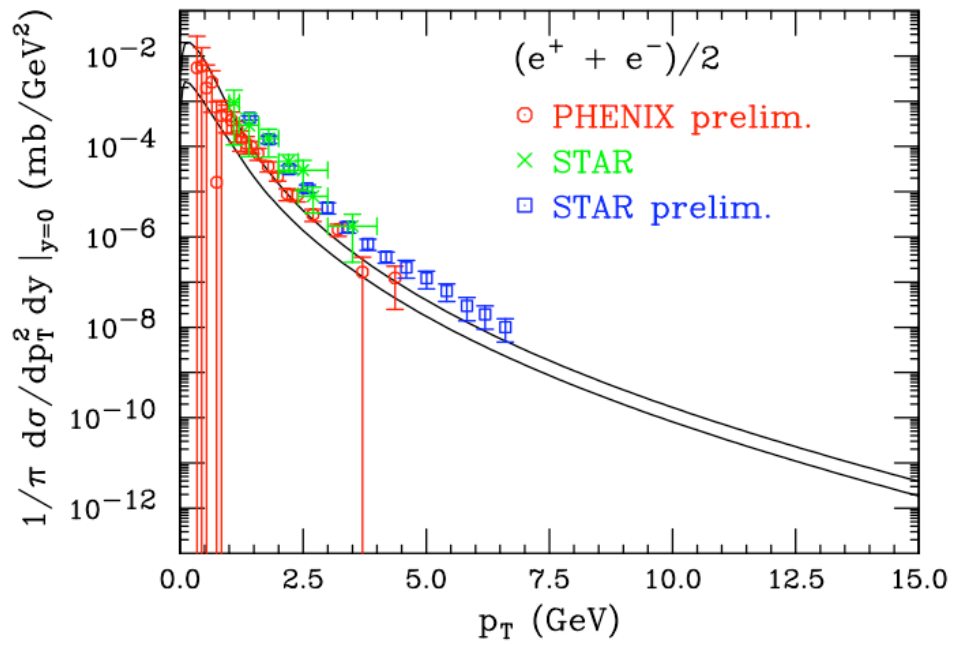


Figure 2.6: FONLL differential cross section compared to RHIC data [20] (2004-2005 experimental results).

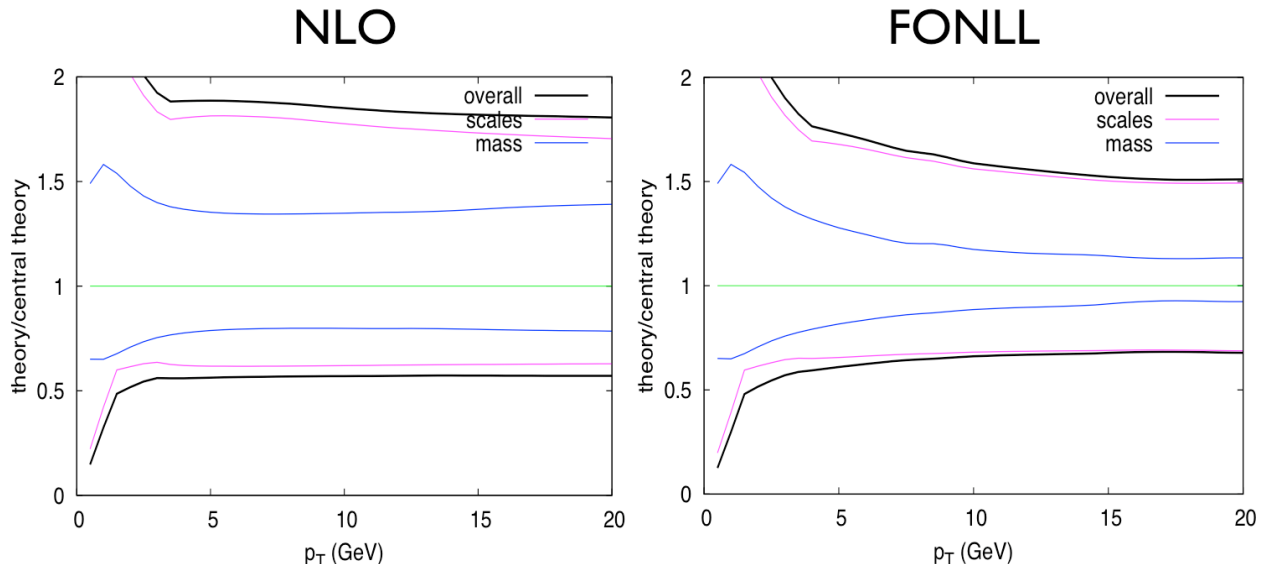


Figure 2.7: Uncertainties in NLO and FONLL charmed hadrons vs.  $p_T$  by variation of quark mass and normalization/factorization scale values [67].

4. Uncertainties in the parton distributions, as shown in Figure 2.3, are  $\approx 10\text{-}20\%$ , based on the global fit analysis performed by the CTEQ group [52].
5. Uncertainty in the FONLL calculation of lepton spectra. The uncertainty in the decay of  $D$ 's to leptons is not directly addressed. Tests in B production by the FONLL author show that the uncertainty of the lepton decay is “fairly negligible” [68]. It likely that even in  $D$  production the lepton decay uncertainty is probably washed out by other, much larger uncertainties, since in this case the D decay spectra are fairly well measured experimentally [66].

Extensive efforts are taken by the FONLL authors to estimate the theoretical uncertainties associated with the calculation. Based on the discussion in the previous list, the largest two sources of uncertainty are used in establishing a theoretical uncertainty band, while smaller uncertainties estimated from the heavy-quark fragmentation and PDF's are not explicitly used as estimators. While a central value is predicted for both the total and differential cross section, emphasis for comparisons to measurements is placed on the uncertainty band obtained from the calculation as in Figure 2.7.

The sensitivity of the cross section to variation in the scales  $\mu_R$ ,  $\mu_F$ , the mass  $m$ , and the PDF's can be used to estimate the uncertainty in the cross section due to the absence

of higher order terms. Using the definition  $\mu_{R,F} = \xi_{R,F} \mu_0 = \xi_{R,F} m_T$ , the scales are varied independently using seven sets:  $\{(\xi_R, \xi_F)\} = \{(0.5,0.5), (0.5,1), (1,0.5), (1,1), (1,2), (2,1), (2,2)\}$ , and the mass is varied from  $m=1.3$  GeV for the upper bound to  $m=1.7$  GeV for the lower bound. Because of the strong variation on the lepton  $p_T$  spectrum for different scale choices (see Figure 5.41), the envelope of all variations is used to define the upper and lower uncertainty band. The uncertainties for each of the seven sets of scale choices is added in quadrature with the upper and lower mass choice in the following way:

$$\frac{d\sigma_{max/min}}{dp_T} = \frac{d\sigma_{cent}}{dp_T} + / - \sqrt{\left(\frac{d\sigma_{\mu,max/min}}{dp_T} - \frac{d\sigma_{cent}}{dp_T}\right)^2 + \left(\frac{d\sigma_{m_{HQ},max/min}}{dp_T} - \frac{d\sigma_{cent}}{dp_T}\right)^2} \quad (2.11)$$

The final upper and lower FONLL bounds consist of the total envelope determined in Equation 2.11 for all choices of scales and mass. The uncertainty bands determined by Equation 2.11 are usually plotted when compared to measurements, such as in Figure 2.6. When making FONLL comparisons to data, it is important to keep in mind the *non-gaussian* nature of the uncertainty bands. The central curve only represents the central portion of a nearly flat probability band that contains (estimated from experience [43]) a 80-90% probability of containing the “correct” prediction [60]. While this discussion is primarily focused on charm production, Figure 2.8 shows the rapidity distributions for 200 GeV  $p+p$  FONLL for both bottom and charm. This plot highlights the large uncertainties associated with charm relative to bottom.

### How is FONLL different from NLO?

Comparisons of the total charm cross sections from the FO NLO and FONLL calculations (Equations 2.8 and 2.10) show good agreement within rather large uncertainties. At this point, it is worth summarizing the difference between the two calculation schemes, especially since they both make use of the same NLO partonic cross sections and have adopted a similar procedure to evaluate uncertainties in the calculation. The following list is adopted from [21], which highlights the differences in terms of total cross sections.

1. Total cross sections: FONLL total cross sections are obtained from integrals over the  $p_T$  and  $y$  distributions. The NLO total cross sections are obtained from partonic cross sections.

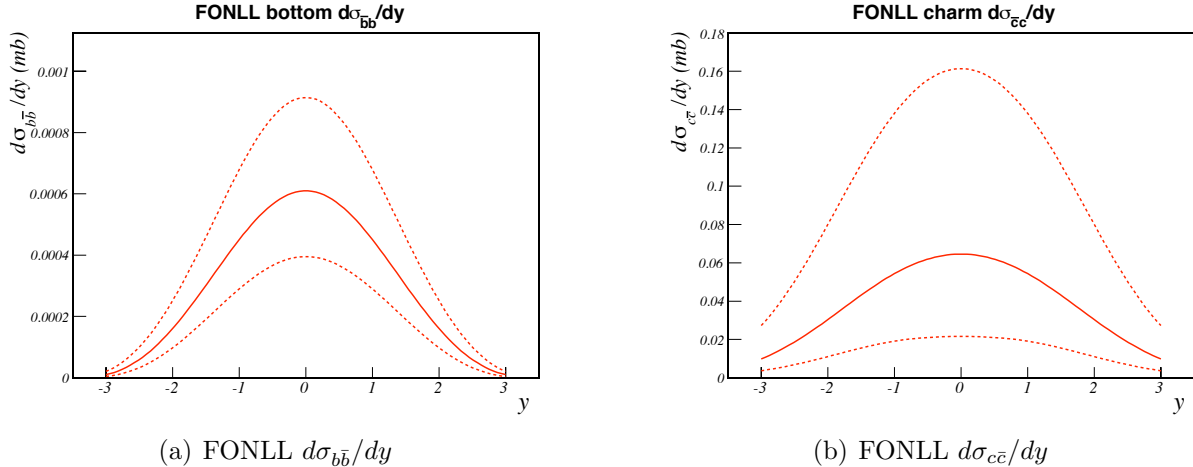


Figure 2.8: FONLL  $d\sigma/dy$  distributions for bottom and charm [20]. The solid curve corresponds to the central FONLL charm prediction. The dashed curves indicate the upper and lower theoretical uncertainty bounds. The much larger theoretical uncertainty associated with the charm cross section is readily evident.

2. Concerning  $\alpha_s$ : In FONLL  $\alpha_s(\xi_R, m_T)$  and  $p_T$  are the relevant scales, with  $\alpha_s$  decreasing with increasing  $p_T$ . In NLO  $\alpha_s(\xi_R, m)$  is fixed ( $m$  not  $m_T$ ), and  $m_{HQ}$  is the relevant scale. Incidentally, fixing  $\alpha_s$  in FONLL increases the total cross section by about 15%.
3. Number of active flavors,  $n_{lf}$ : In FONLL for  $p_T \gg m_{HQ}$ , the heavy quark is considered a light, active flavor. For  $p_T \sim m_{HQ}$  the fixed-order calculation is modified through the use of a different renormalization scheme from  $n_{lf}=3$  to  $n_{lf}=4$  for charm. The fixed-order NLO calculation always treats the heavy quark as heavy, so for charm  $n_{lf}=3$  and for bottom  $n_{lf}=4$ .

Due to the sensitivities to several parameters in the calculations associated with the “lightness” of the charm quark, there is no single “best” calculation choice for charm production. Rather different approaches work better in different circumstances. In an ideal case where total charm quark production could be measured down to  $p_T=0$ , the NLO calculation based on the total partonic cross section is possess little dependence on unphysical parameters ( $\mu_R, \mu_F$ ). For comparisons to experimental quantities at larger  $p_T \gg m_{HQ}$ , where the quark mass of charm or even bottom is insignificant, the FONLL calculation is the most rigorous calculation available for direct comparison to data. However, for low  $p_T$  (at or below  $m_{HQ}$ ), for comparison to measured  $p_T$  spectra, theoretical uncertainties severely cloud the issue. The single most important choice in the NLO and FONLL calculations is that of  $n_{lf}$ , which

strongly affects the calculation of the value of the coupling,  $\alpha_s$ . Another important unsettled issue is the gluon density at low  $x$ , which is not well constrained.

### How FONLL is used in this dissertation work

Numerous FONLL and NLO calculations have been generously made available by the authors, Matteo Cacciari and Ramona Vogt. Lepton  $p_T$  spectra, rapidity distributions of quarks, mesons, and leptons are all used in the course of this analysis. Calculations using different scale and mass choices were provided, allowing the study of how the variation in the calculation’s parameters affected the central curve prediction (Figure 5.41).

### 2.2.3 PYTHIA

PYTHIA is a Monte Carlo high-energy physics event generator that produces full event collisions from a variety of incoming particles in a wide range of energies. Heavy quark production is implemented through multiple processes in PYTHIA. The leading order processes  $q\bar{q} \rightarrow Q\bar{Q}$  and  $gg \rightarrow Q\bar{Q}$  are included, as are the processes referred to as “flavor excitation” and “gluon splitting” [69]. Heavy quarks present in the initial parton distributions at the  $Q^2$  scale of the hard interaction can lead to flavor excitation processes, such as  $Qg \rightarrow Qg$ . PYTHIA also considers heavy quark production via the process of gluon splitting,  $g \rightarrow Q\bar{Q}$ . It is known that as the center of mass energy,  $\sqrt{s}$  increases the relative size of leading order processes decreases. To account for missing higher order terms, PYTHIA implements a “K-factor” that arbitrarily increases/decreases heavy quark production, effectively allowing PYTHIA to be “tuned”.

PYTHIA is a very useful tool for studying physics processes and fully simulated  $p+p$  events (for example) with the full complement of secondary observed final states. However, rather than use a “tuned” PYTHIA that does not calculate all relevant diagrams, the availability of full NLO calculations (such as FONLL) is preferred when comparing to measured double differential cross sections (i.e.  $p_T$  spectra). The question of PYTHIA vs. NLO pQCD is not simply a question of LO + K-factor versus NLO. PYTHIA organizes its separate heavy flavor production calculations depending on the number of heavy quarks *present at the production vertex*: leading order pair creation has two, flavor excitation has one in the parton distribution, and gluon splitting has none. Alternatively, NLO calculations are organized according to initial state ( $gg$ ,  $gg$ ,  $gq$ ) [21]. Flavor excitation and gluon splitting are subclasses of NLO diagrams for  $gg$  and  $gq$ , but since these diagrams are included but not other interfering NLO

contributions, PYTHIA tends to give larger cross sections.

The previously published PHENIX single muon result [70] made explicit comparisons to PYTHIA and used it to extract the integrated charm cross section,  $d\sigma_{c\bar{c}}/dy$ . While PYTHIA is not used for any explicit comparisons or cross section derivations in this work, comparisons of this dissertation’s result to the previous single muon measurement and PYTHIA 6.2 can be found in Appendix B. When running PYTHIA heavy quark calculations, only one heavy flavor is calculated at a time, MSEL parameter 4 for charm and 5 for bottom. If the relative mix of charm/bottom is to be studied, “minimum bias” PYTHIA is run with the MSEL parameter set to 2. For charm, specifying MSEL=4 produces heavy quarks in every event which is “more efficient” for computer resources, while MSEL=2 calculations produced heavy quarks more infrequently (as in reality) and requires several days of running to acquire equivalent statistics. Comparisons between charm distributions determined in these two different ways showed differences of  $\approx 30\%$  in spectral shape and overall normalization. This is due to processes that result in a heavy quark that are not included in the processes explicitly discussed in this section.

Figure 2.9 shows the results of a  $\sqrt{s}=200$  GeV  $p+p$  PYTHIA simulation examining the sources of single muons at  $\langle y \rangle = 1.65$  with  $p_T > 0.9$  GeV/c, which corresponds to the PHENIX muon arm acceptance. This PYTHIA is “tuned” as in [71] to match previously measured charm results. This simulation shows that charm decays contribute  $\approx 75\%$ , of hard single muons from the collision vertex in the PHENIX muon arm acceptance. Bottom contributes 11%, and all other sources of single muons are negligible except those from light vector mesons (i.e.  $\rho$ ,  $\eta$ ,  $\omega$ , and  $\phi$ ). Figure 2.10 highlights the expected dominance of charm in the total yield of particles at a function of transverse momentum. A separate light vector meson subtraction is not performed on the extracted single muon yield in this work, but based on the calculation in Figure 2.10, it is expected that the overall single muon cross section (and thus also the extracted charm cross section) would be reduced by  $\approx 10\%$ . The subtraction of single muons from light vector meson sources will be performed for the final published single muon spectrum.

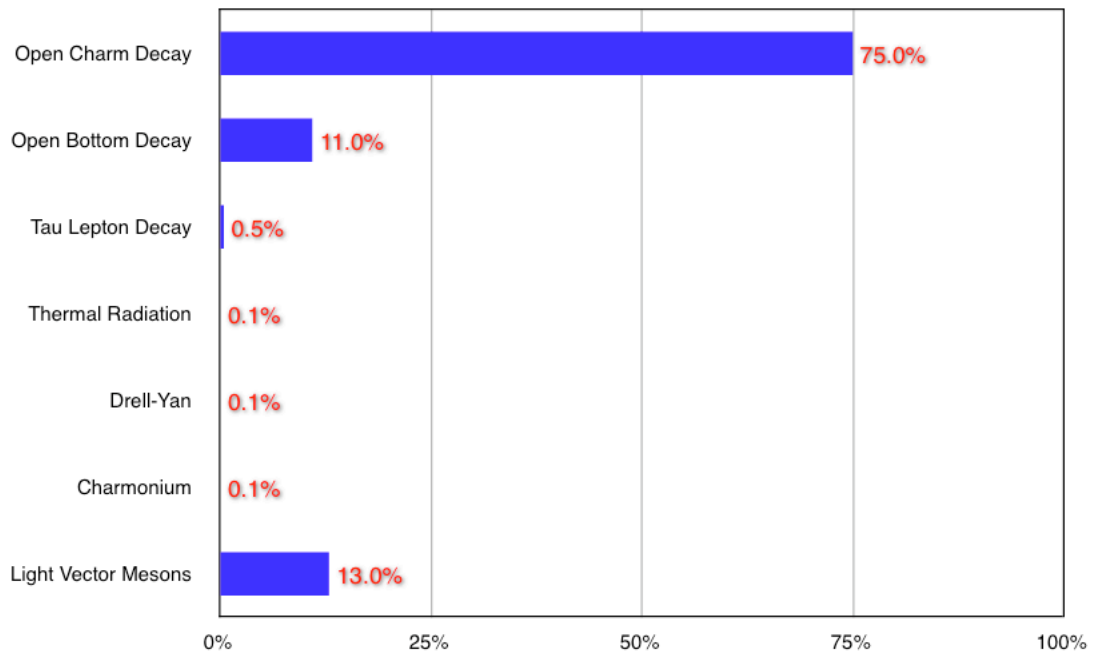


Figure 2.9: Sources of single muons with  $p_T > 0.9$  GeV/ $c$  from PYTHIA for  $p+p$  200 GeV and  $\langle y \rangle = 1.65$ .

*Charm, Bottom, and Light Vector Meson Contributions in PYTHIA*

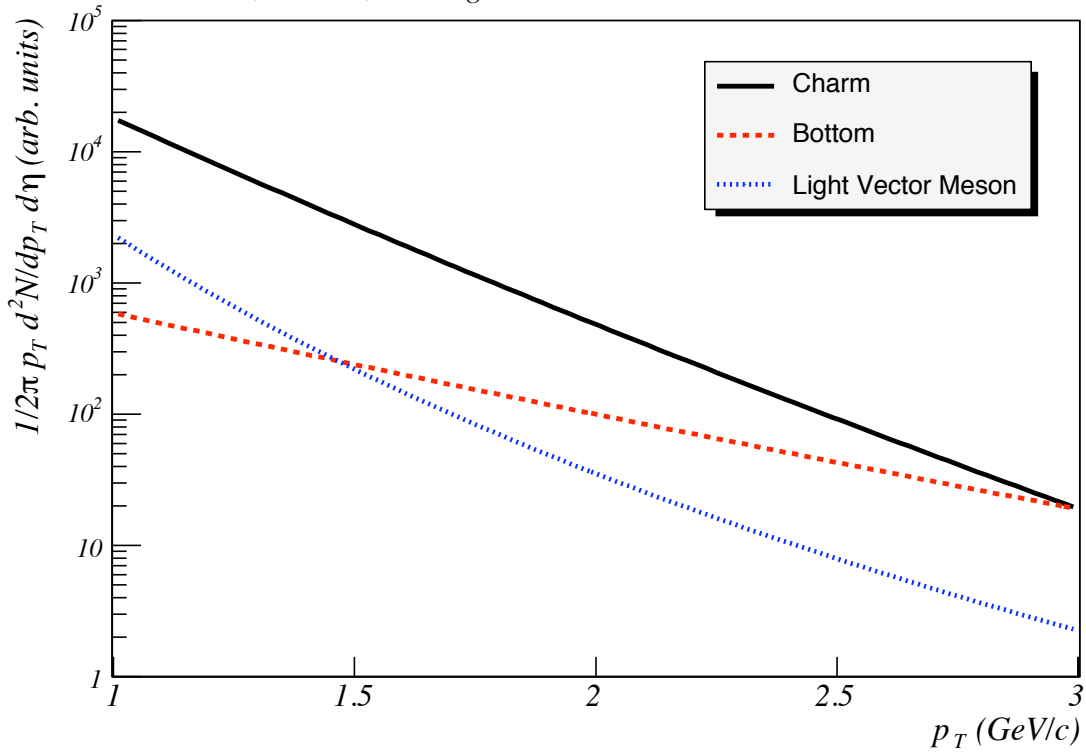


Figure 2.10: Charm, bottom, and light vector meson contributions to the total single muon yield in PYTHIA as a function of transverse momentum [69, 70].

## Chapter 3

# Experimental Survey of Heavy Quark Single Lepton Measurements

The existence of quarks as mathematical objects had been postulated in 1964 by Murray Gell-Mann and George Zweig [72] and independently by Y. Ne'eman. This initial quark model included three quarks, *up*, *down*, and *strange*, which accounted for most of the strongly interacting particles that had been observed to that date. In a series of deep inelastic scattering experiments in the late 1960s and early 1970s, experimental physicist saw indications that nucleons consisted of point-like constituent particles that could be the postulated quarks. While the possible existence of a fourth quark, dubbed *charm*, had been bandied about for several years, its existence was specifically postulated in 1970 by Glashow, Iliopoulos and Maiani to account for the absence of observed flavor changing neutral currents, which were otherwise anticipated in the theory of the weak interaction [73]. The observed narrow resonance of mass 3.097 GeV/c in 1974 at both BNL and the Stanford Linear Accelerator (SLAC) was quickly recognized as the discovery of the charm quark in a bound charmonium state ( $c\bar{c}$ ). With this convincing confirmation of the quark model, contemporary physicist had witnessed changes in the experimental and theoretical landscape that would guide much of high-energy physics research well into the future.

The history of the charm quark, and then shortly after, the bottom quark, is an extensive subject. The primary focus of this chapter is on measurements of heavy quarks that are related to this work in two ways: 1) through the use of single leptons to measure charm or bottom production, and 2) those measurements of charm or bottom that motivated the development of the heavy quark pQCD calculations discussed in Chapter 2, which have

emerged in the last five years to become *the* state of the art calculations to which nearly all measurements are compared.

The experimental technique and primary assumptions used in the measurement of heavy flavor single leptons, for both electrons and muons, draws upon a long history that dates from the early to mid 1970s. While single leptons have long been used to measure charm quark production, single “direct” leptons were recognized as having interesting origins, even if the exact origins were not clear. As in [56], it is natural to loosely divide the charm and bottom measurements into historical generations in the following way: Generation I, 1974 to  $\sim$ 1985; Generation II 1985-1995; Generation III, 1995-2005, and the current set of measurements at RHIC. Apart from the final “generation” at RHIC (which is not a purely “high-energy” physics collider), this chronological division falls naturally along the advancements in both the collider facilities and detector technologies. This listing is not meant to be entirely comprehensive, but is meant to touch upon highlights from each “era”.

### **Generation I (1974-1985): Early single lepton measurements at Fermilab and CERN**

In the early to mid 1970s Fermilab and CERN pioneered the measurement of single leptons from heavy flavor—even before heavy quarks had been experimentally confirmed. At Fermilab a series of fixed-target experiments were conducted using proton beams on targets such as beryllium. At CERN, the Intersecting Storage Rings (ISR) collided proton beams that provided for a series of single lepton measurements.

In 1974, before the charm quark discovery, a Fermilab experiment [39] that used  $p$ - $Be$  collisions at 300 GeV measured both single “direct” electrons and muons to search for parents of observed “direct” single leptons. Understanding the unknown origin of these direct single leptons served as a primary motivation for the measurement. Possible candidates for the parents of the single leptons were listed as: 1) virtual massive photons, 2) “light” vector mesons ( $\rho$ ,  $\omega$ ,  $\phi$ , ...) produced with large transverse momentum, 3) intermediate bosons ( $W^\pm$ ,  $Z^0$ ), 4) charmed particles, and 5) heavy leptons. Virtual “massive photons” refers to processes in which quarks interact electromagnetically, obtaining large transverse momenta through the exchange of virtual “massive photons”. The quarks possess this large momenta in intermediate states between the absorption and emission of these “massive photons”. The

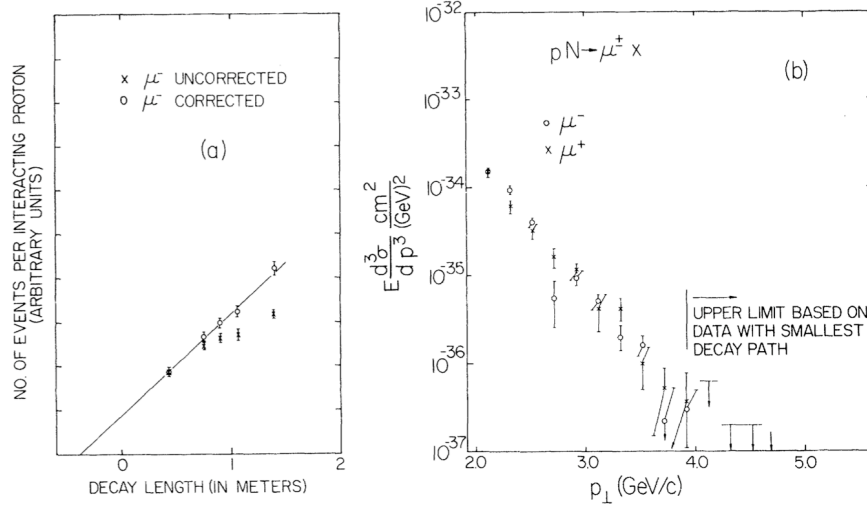


Figure 3.1: 1974 FNAL measurement of single muons [39]. The left figure plots the yield of muons versus decay path and is used to estimate muon contributions from light hadron decay. The right plot is the invariant cross sections as a function of  $p_T$  per nucleon for “direct” muons near  $90^\circ$  in the center of mass system.

light vector mesons had been known since the mid 1960s, and before the advent of the Standard Model they were identified as massive vector bosons that coupled to isospin.

This experiment in 300 GeV  $p$ - $Be$  collisions employed two key experimental methods whose general principles are still being used in single lepton measurements at RHIC *thirty* years later. The left plot of Figure 3.1 shows muon yield versus decay length which identifies contributions from light hadron decays. This plot is a progenitor of the  $z$ -vertex distributions (see Chapter 5) used in this single muon analysis to determine the fraction of tracks that are muons that result from light hadron decay. In the companion measurement of electrons, the two largest background sources from  $\gamma$  conversion in the material and  $\pi^0$  Dalitz decay were experimentally understood and estimated by inserting a series of foils of known thickness into the beam and plotting the yield of electrons as a function of foil thickness. This permits the determination of the electron signal due only to “prompt” sources. This approach is echoed in the current approach in PHENIX to estimate electrons by adding additional converter material. The muon spectra measured from this experiment is shown in the right plot of Figure 3.1.

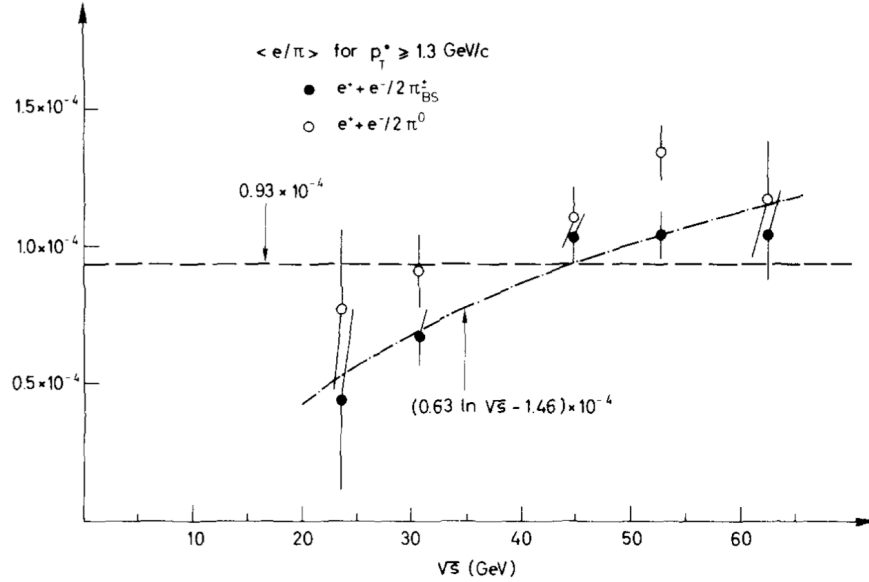


Figure 3.2: ISR  $e/\pi$  ratios vs.  $\sqrt{s}$  [74].

At the ISR single electrons were also measured [74]. This long paper concludes by saying, “the origin of the single electrons is underdetermined and, as such, presents a challenge to both experimentalists and theorists.” They were also (perhaps) hinting at the existence of charmed mesons when they state that based on their findings, the single electron yield can “be explained by a particle of mass  $m > 0.800 \text{ GeV}/c^2$  which decays to  $e^+e^-$  pairs.” The  $e/\pi$  ratios measured in [74] are plotted as a function of  $\sqrt{s}$  are shown in Figure 3.2. Interpreting this plot *a posteriori*, the charm signal from single electrons extrapolated to higher energies indicates an increasing charm cross section that would make electrons at RHIC “a good measure of charm production.” [75].

Four months before the publication of the first charmed meson measurement in August 1976 [76], an April 1976 paper by Buchholz *et al* entitled “Measurement of Direct Muon production in the Forward Direction” [40] highlights some interesting experimental techniques (this is the experiment mentioned in Chapter 1). Building on the ISR results that measured lepton production for  $p_T > 1.0 \text{ GeV}/c$  and  $x \approx 0$  which reported constant yields in the ratio  $\mu/\pi$  of  $10^{-4}$ , this Fermilab result extended the ISR results to intermediate  $x$  ( $\approx 0.3$ ) and low  $p_T$  ( $< 0.4 \text{ GeV}/c$ ).

This experiment determined the ratio of direct muons to pions by varying the effective

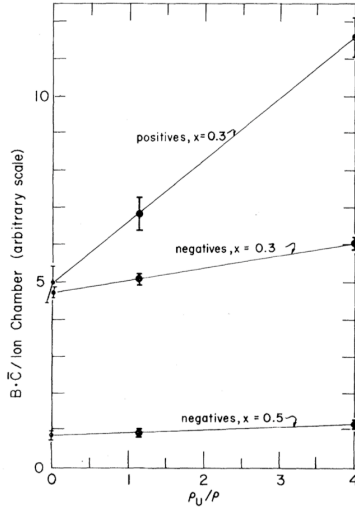


Figure 3.3: Corrected (muon flux/ion chamber) versus inverse target density. The intercept corresponds to the direct-muon (i.e. from charm) signal per incident proton. Additional details are found in the text [40].

density of the uranium target. As shown previously in Figure 1.7 in Chapter 1, pions produced in the initial collisions will decay into muons with the property that the decay muons will travel an average distance that is inversely proportional to the density of the target. Figure 3.3 shows the corrected muon flux versus inverse target density. By knowing the shape of the hadron  $p_T$  yield, the slope of the muon yield versus density is used to determine the pion flux. The vertical intercept in Figure 3.3 corresponds to an extrapolation to infinite density target which would remove the  $\pi, K \rightarrow \mu$  decay daughter contamination and provides the direct-muon signal per incident proton.

The ratio of  $\mu/\pi$  at very small  $p_T$  was observed to be comparable ( $10^{-4}$ ) to that observed at the ISR at larger  $p_T$ . Since the  $\pi$  cross section was known to grow at low  $p_T$ , the constant  $\mu/\pi$  ratio indicates a similarly large total cross section for direct muons—regardless of their ultimate source. With a successful technique in hand to remove the muons resulting from light hadron decay, the next largest background component contemplated in this experiment was due to light vector meson decay ( $\rho, \omega, \phi$ ) and was estimated from 1970s contemporary sources to be less than 10% of the observed muon yield. Present day (after 2002) estimates of “direct” muons from light vector mesons are estimated to be of comparable size [71]. Positive flux was not measured due to the use of an incident proton beam which made the separation of  $\pi^+$ ’s from the abundant secondary protons impossible.

Beginning in 1976, a slew of additional charm measurements at the ISR at CERN with  $\sqrt{s}=52\text{-}63$  GeV ushered in a brief era of confusion concerning charm production cross sections. Using a variety of beams, targets, energies, and observed final states, many experiments measured conflicting charm cross sections that varied wildly by more than a factor of five. In the 1987 review of heavy flavor production in hadron-hadron interactions [77], the author states:

With these conflicting data it is impossible to draw any precise conclusion on the charm cross section at ISR energies. Let me just point out that these experiments were performed several years ago and a number of aspects of charm production are now better understood... It is unlikely that this question will ever be settled at the ISR since the accelerator is now closed down. Fortunately, we can soon expect reliable measurements from several experiments at the FNAL accelerator...

Meanwhile, as a side note, the bottom quark was discovered in 1977 at Fermilab by the E288 experiment [78].

### **Generation II (1985-1994): heavy flavor at the SPS and fixed-target at FNAL**

After the rush of charm measurements in the late 1970s and early to mid 1980s, some of which have been mentioned here, increasing attention was paid to bottom quark production due to the increased energies of new accelerators at the SPS and the Tevatron and also the realization that bottom, not charm, with its larger mass, would provide more precise tests of QCD predictions. Figure 3.4 is meant to serve as a summary plot for several measurements made during this period. Measured cross sections for charm (top points) and bottom (lower points) are placed with NLO pQCD calculations bands [57,61] for different mass settings. The UA1 collaboration measured bottom production in the late 1980s and early 1990s [79, 80] at the CERN SPS ( $p\bar{p}$  collisions) at  $\sqrt{s}=546$  and 630 GeV that were in good agreement with the then recently completed NLO ( $\alpha_s^3$ ) calculations [81]. The particulars of these measurements made in this period is not entirely relevant for the purpose of this dissertation, so we proceed directly to the minor saga of bottom production in  $p\bar{p}$  collisions.

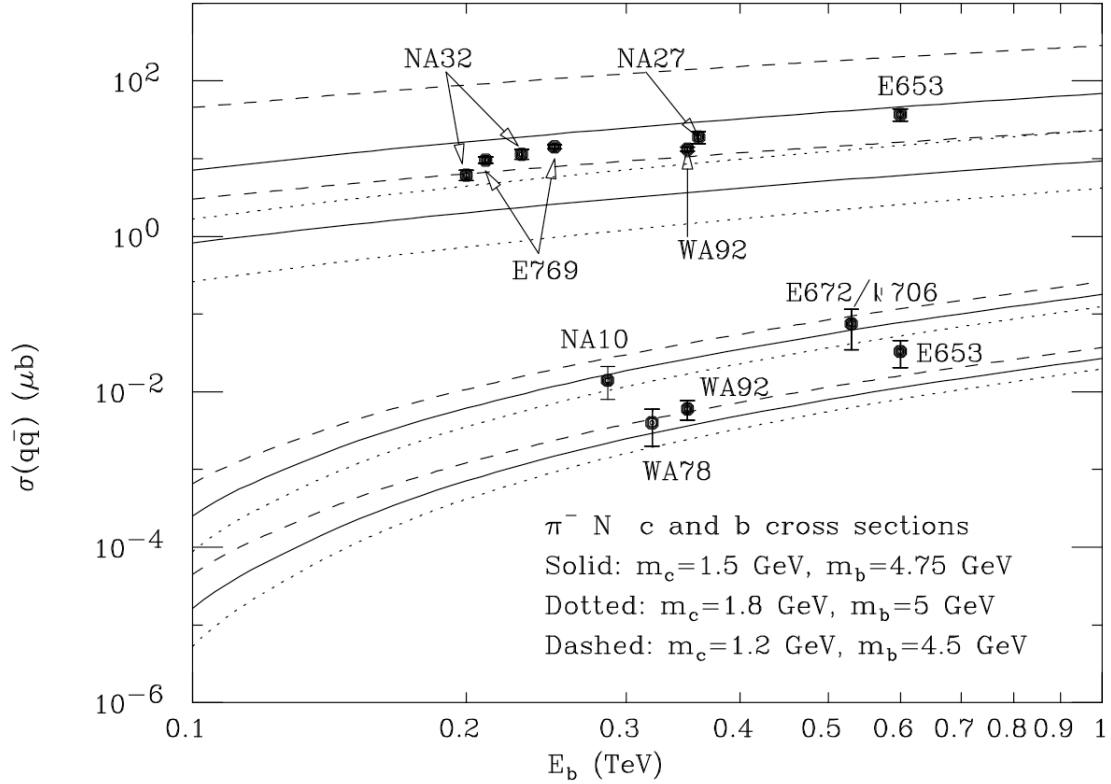


Figure 3.4: Charm and Bottom cross sections *circa* 1995 [82]. Despite the obscuring effect of the logarithmic vertical axis, the measured cross sections for both charm and bottom can be seen to agree with theoretical expectations, within the sizable theoretical uncertainty bands from NLO pQCD calculations. The relative size of the theoretical uncertainty band for charm is significantly larger than for bottom.

### Generation III (1995-2005): Selected charm and bottom measurements at the Tevatron

Beginning in 1992 early bottom measurements by both D0 and CDF at the Tevatron ranged from tenuous agreement with theory to large disagreements. As discussed in [81] and [83], these measurements were in apparent disagreement with the existing UA1 results. Probably spurred by the Tevatron Run I D0 and CDF results, fixed target charm meson and baryon cross sections measurements at FNAL were published in 1996 from data taken in 1988. These measured cross sections are reported to be larger than with existing pQCD calculations but in agreement with existing experimental and theoretical uncertainties [84].

By the year 2000, the reports of an experimental excess in bottom production were well known. Adding to this, in June 2000 D0 published forward rapidity measurements in bottom production in the range  $2.4 \leq y \leq 3.2$  (Figure 3.5) [85]. The cross section from  $b$  decay in this region was shown to exceed existing NLO pQCD calculations by a *factor of four*. By 2002 CDF measured the  $B^+$  total and differential cross sections [86] and had found a disagreement of a factor of  $2.9 \pm 0.2 \pm 0.4$  relative to existing NLO calculations. However by the next year, CDF's measurement of charm mesons, Figure 3.6, at  $|y| < 1$  [87] proved to be higher than theoretical calculations by *only* 100% at low  $p_T$  and 50% at high  $p_T$ —a clear improvement. And most importantly they were now compatible within the non-negligible uncertainties on both data and theory. Subsequent measurements in RUN II (2004 and later) at the Tevatron do not contradict the finding that NLO pQCD was adequately describing the data.

What had happened? Three theoretical developments (and one experimental) led to a convergence of the measurements and theory that is observed today concerning heavy flavor production at the Tevatron [65, 81, 83].

- Resummation of logarithmic terms, the birth of the FONLL calculations added 20% to theoretical cross sections.
- New Parton Distribution Functions from improved global fits provide an increase of  $\sim 10$ -20% in theoretical cross sections.
- A change in the treatment of non-perturbative fragmentation also added about 20% to theoretical cross sections.

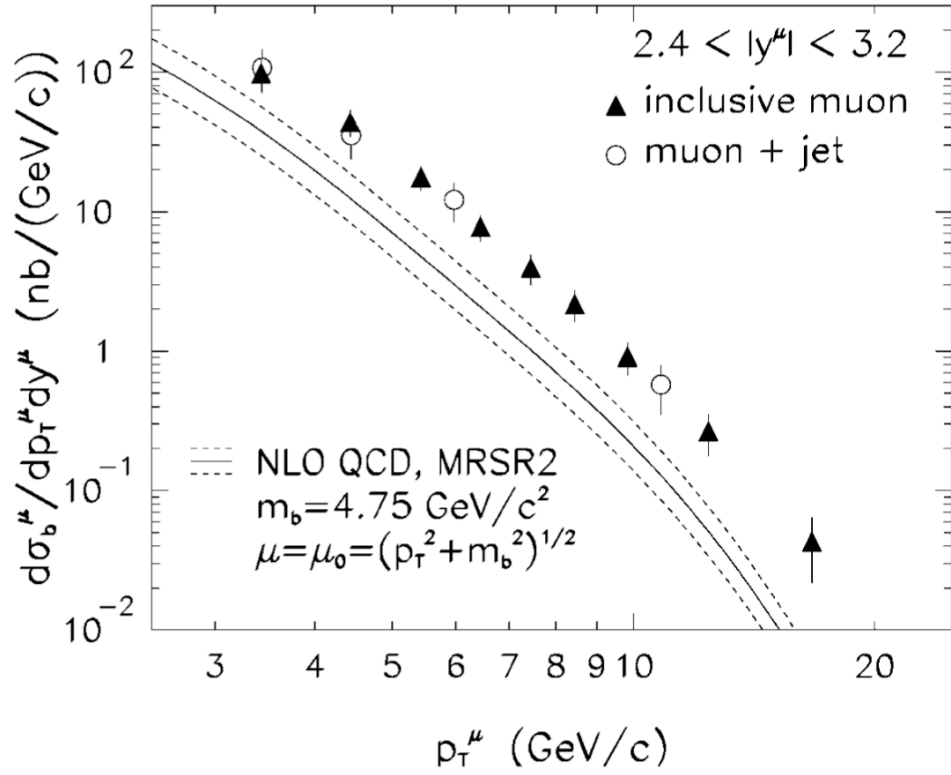


Figure 3.5: D0 forward angle, single muon bottom measurement a factor of  $2.9 \pm 0.2 \pm 0.4$  above then existing NLO calculations [85].

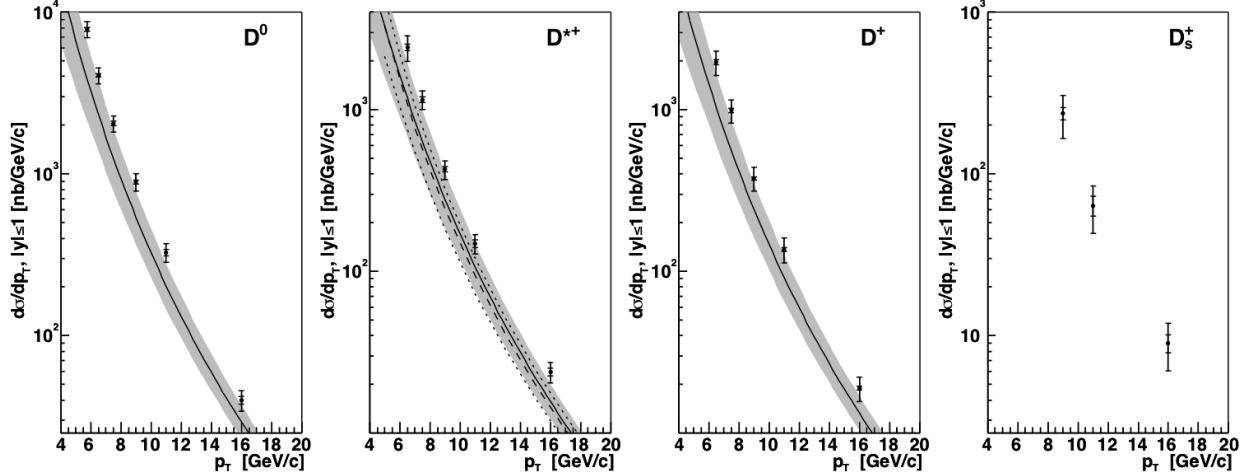


Figure 3.6: CDF charm meson measurement [87]. The dark shaded band is an 2003 version of the FONLL calculation. See text for additional details.

- Although the published Tevatron measurements themselves have not changed, if one were to consider a “renormalization” of the Tevatron Run I using Run II measurements, a reduction of the central data points by  $\approx 25\%$  (within the uncertainties in the Run I results) might be appropriate.

As an aside, the top quark was verified at the Tevatron in 1995.

### Is this what the future was supposed to look like?... The RHIC single lepton charm measurements

The prospects for a charm measurement in heavy-ion collisions at RHIC via single electron measurements were considered several years before the first collision [75]. Experiments in the 1970s had shown that the yield of direct single leptons from the semi-leptonic decays of charm particles were at a level of  $e/\pi$  levels of  $\sim 10^{-4}$  for  $p_T > 1.3$  GeV/c. As shown in the ISR charm data in Figure 3.2, the cross section for charm (or the heavy-flavor  $e/\pi$  ratio) increases with  $\sqrt{s}$ , so the signal/background is expected to improve both for  $p + p$  and heavy-ions at 200 GeV at RHIC. This led to expectations that single electron measurements at RHIC should provide clean charm measurements not only for  $p + p$  collisions, but for heavy-ion collisions such as  $Au + Au$  as well. This prescient statement proved to be mostly true.

Figure 3.7 shows a recent comparison of RHIC single electron results. STAR and PHENIX

disagree by a factor of two, and the STAR  $D$  measurements average a factor of five above FONLL, albeit with large errors. At the time of this writing, this disagreement between the two experiments has not been settled. Within the existing experimental and theoretical uncertainties the PHENIX result is consistent with the FONLL calculation, at a fit to constant ratio of about 1.7 relative to FONLL central values. Comparing just the STAR and PHENIX results and ignoring FONLL, the discrepancy is thought to be a “normalization” issue, since the difference is largely independent of  $p_T$ . Plots of  $R_{AA}$ , where a normalization issue cancels out when dividing the proton reference spectra into the heavy-ion measurement, show agreement between STAR and PHENIX measurements. The possible origin of the normalization difference is not currently understood.

Since the STAR/PHENIX discrepancy will be addressed again in Chapter 6, some experimental details are provided for context. PHENIX measures single electrons with two separate central arms, each with  $90^\circ$  azimuthal acceptance and pseudorapidity coverage of  $|\eta| \leq 0.35$ . Electrons are measured in the central arms using combined information from an electromagnetic calorimeter and a ring imaging Cerenkov detector. The measurement of single electron and muons from heavy flavor is performed through the statistical subtraction of background sources, with the remaining yield attributed to open heavy flavor decays. For single electrons, the primary background sources have been directly measured [19]. A full GEANT based background “cocktail” is generated to estimate all sources of backgrounds. Additionally, the ratio of conversion electrons is altered by the addition of a thin layer of conversion material between the vertex and detector for a portion of the run period. The relative increase in conversions provides a direct measurement of this key background and serves as an independent cross check to the cocktail approach [26]. The Ph.D. dissertations of Yifei Zhang [90] and Xin Dong [91] provide the details of STAR’s methodology for measuring heavy-flavor single electrons.

Figure 3.8 shows the extracted total charm cross sections plotted for different collision environments compared to the NLO total charm cross section discussed in Section 2.2.1. The STAR and PHENIX points are internally self-consistent, while the difference between the experiments remains at approximately a factor of two. The contribution of heavy-flavor single muons measured by PHENIX at forward angles is discussed in terms of these results in Chapter 6. Apart from an unexpected *mea culpa* by either experiment or a striking new result, it is likely that the existing difference in charm results will persist for several more years,

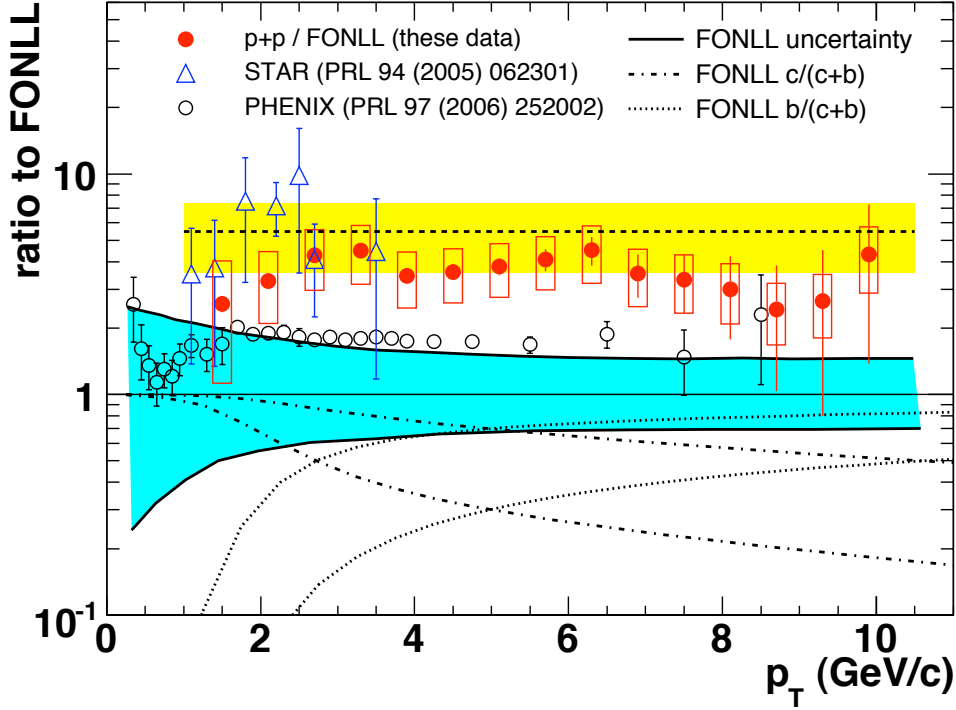


Figure 3.7: Heavy-flavor single lepton results at RHIC *circa* 2007-2008. PHENIX [26] and STAR [88] single lepton and  $D$  meson results [27] results compared to a FONLL calculation (solid blue band).

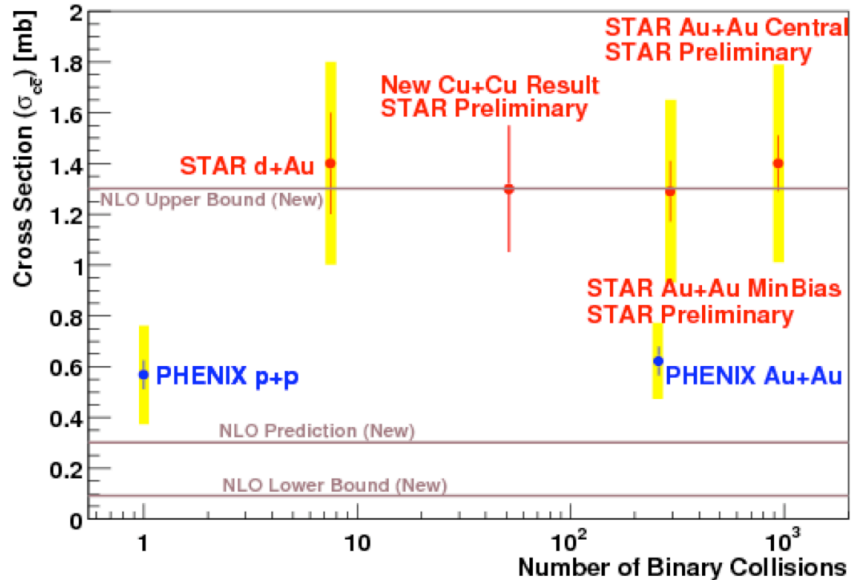


Figure 3.8: Measured total charm cross sections for different collision species at RHIC for both STAR and PHENIX. Plot taken from [89].

until perhaps the installation of upgrade detector capabilities in both STAR and PHENIX sometime after 2011-2012.

### Looking backwards before looking forward again

In the excellent review article by Tavernier in 1987 [77], the motivations for studying charm production (and bottom as well) in hadron-hadron interactions were listed as:

- “Charm production in hadron-hadron interactions is obviously a legitimate research subject in its own right.”
- “It is hoped that the mass of the charmed particle provides the high mass scale that makes perturbative calculations in the framework of QCD meaningful. If this is the case, charm production is a useful probe of the hadron structure and possibly even a useful testing ground for QCD.”
- “Our ability to predict the production of charmed particles will indicate how well we can predict the production of the hypothetical strongly interacting particles which are expected in several recent theories (gluinos, squarks, etc.).”
- “The study of charm has a considerable “practical” importance. Lepton production\* in hadron-hadron interactions is one of the most useful probes of fundamental processes. This was once more dramatically illustrated by the recent [1987] discovery of the intermediate bosons, which were discovered by observing leptonic final states in hadron-hadron interactions. Heavy flavor production is an important source of leptons. A knowledge of the characteristics of heavy flavor production is essential for evaluating the background in many important reactions. In addition, lepton production by charmed particles will be the most important source of charged leptons or neutrinos for secondary beams in the next generation accelerators. Already in the present accelerators  $D_s$  decay is the most important source of  $\tau$  neutrinos.”

Twenty years after this list was written, it is fair to say that charm production measurements have addressed, in part, some of these items. The mass scale provided by the charm quark, as shown in Chapter 2 is considered to provide a sufficiently high mass scale to permit the application of pQCD. However, it is also true that the mass scale is indeed, just “heavy enough”, and as a result there remains sizable uncertainty associated with pQCD predictions

---

\*including single leptons!

of charm. It is certainly true that the larger mass scale provided by the bottom quark permits more precise theoretical calculations that is able to serve as true “precision” tests of QCD. Initial discrepancies in bottom (not charm) production at the Tevatron in the late 1990s where measurements exceeded theory by a factor of 3 to 4 somewhat fed the discussions of “other” physics contributions playing a role in the disagreement [92]. Subsequently, through modifications in the theoretical calculations and re-evaluation of the measurements, the discrepancies decreased significantly, to less than a factor of two and within the uncertainties posted by both experiments and theoretical calculations. So despite precision to a factor of two, the ability of pQCD to describe heavy quark production is not in doubt. Ongoing experimental upgrades at RHIC and with the beginning of the LHC era should provide increasingly precise measurements against which theoretical progress, including the next generation of NNLO calculations, can be benchmarked.

# Chapter 4

## The PHENIX Experiment

This section provides general descriptions of all the experimental apparatuses used in the measurement of single muons, from the Relativistic Heavy Ion Collider (RHIC) which provides the collisions, to the PHENIX detector system which measures the collision products, to a description of the specific PHENIX detector subsystems involved in the measurement of heavy flavor single muons.

### 4.1 RHIC

The purpose and basic goals of RHIC were described in Chapter 1. This section provides some additional details of the accelerator. To measure muons resulting from the decay of heavy flavor quarks, we first need heavy quarks. These are provided in particle beam collisions at RHIC, located at Brookhaven National Laboratory (BNL) on Long Island, New York [93] [94]. RHIC is the world's first high-energy heavy-ion collider, building upon the existing Alternating Gradient Synchrotron (AGS) accelerator complex which now serves as an injector to the RHIC rings. The AGS, which has played a role in three Nobel prizes\*, also separately provides ion beams for other research programs at BNL, such as the NASA Space Radiation Laboratory.

RHIC is capable of accelerating nuclei from hydrogen (e.g. proton) to gold,  $Au$ , with a maximum energy of 100 GeV per nucleon for heavy ions and a maximum of 250 GeV for protons. In the case of  $Au$ , which has 197 nucleons (79 protons and 118 neutrons), the total beam energy per  $Au$  nucleus is 19700 GeV. A quick calculation can put this collision energy

---

\*C.C. Ting 1976 for  $J/\Psi$ ; J. Cronin, V. Fitch 1980 for CP Violation; L. Lederman, M. Schwartz, J. Steinberger 1988 for  $\nu_\mu$ .

in a clear day-to-day context... using mosquitoes. The kinetic energy of two mosquitoes can be calculated using the familiar  $\frac{1}{2}mv^2$  formula:  $(2.5 \text{ mg}) \times (2.5 \text{ km/hr})^2 = 1.2 \mu\text{J}^\dagger$ . An equivalent calculation of the energy in two colliding gold nuclei is then:  $1.6 \times 10^{-19} \frac{\text{J}}{\text{eV}} \times 197 \times 200 \text{ GeV} \sim 6 \mu\text{J}$ , which is the same order of magnitude as the mosquitoes [95]. The head-on collision of just two individual *Au* nuclei has a macroscopically relevant energy; the head-on collision of two such beams of *Au* nuclei produces an large energy density in a finite volume that has an initial temperature roughly equivalent to  $10^{12}$  Kelvin.

RHIC produces these collisions with two independent, super-conducting rings 3.8 km in circumference. Each ring has an independent source of ions, which permits the collisions of unlike ion species. Two separate Van de Graaff generators serve as the first stage of acceleration of heavy ions. Protons are obtained from the proton linear accelerator, referred to as the proton linac. It is instructive to trace the path of both heavy ions and protons from origin to collision. Figure 4.1 depicts the RHIC facility schematically. Gold ions of -1 charge originate in the pulsed sputter ion source in the at the front of the Tandem Van de Graaff, the ions are partially stripped of electrons with a foil, retaining a +32 charge, and are accelerated to an energy of 1 MeV per nucleon by the time they exit the Van de Graaff. The gold beam travels up the transfer line to the Booster Synchrotron which accelerates the ions to an energy of 95 MeV per nucleon. The ions exit the Booster and pass through the stripper achieving a +77 charge state. The ions are injected into the AGS in 24 bunches, which accelerates the ions to 10.8 GeV per nucleon, the RHIC injection energy. The ions are rebunched from 24 to 4 bunches in the AGS and pass through another stripper in the AGS-to-RHIC Beam Transfer Line achieving the fully stripped charge state of +79. The ions are then injected into the RHIC rings one bunch at a time and accelerated to their maximum energy of 100 GeV per nucleon in RHIC's accelerator rings. Since the RHIC magnets are superconducting, they must be cooled to a stable operating temperature of 4.6 Kelvin, or -451° Fahrenheit. The magnets are used to steer the beams around the rings that are brought to collision at the interaction points of the different experiments.

Figure 4.2 shows screen captures from the RHIC beam intensity monitor fastidiously watched by the PHENIX shift crews. These particular screen shots were chosen from this author's shift periods. The upper plot in Figure 4.2 is taken from the 2005 p+p 200 GeV run, and the lower plot is taken from the 2007 Au+Au 200 GeV run period. While the particular details

---

<sup>†</sup>Mosquito speeds have been estimated to be even higher with a tail wind, though of course it is the relative velocity that is relevant to the calculation.

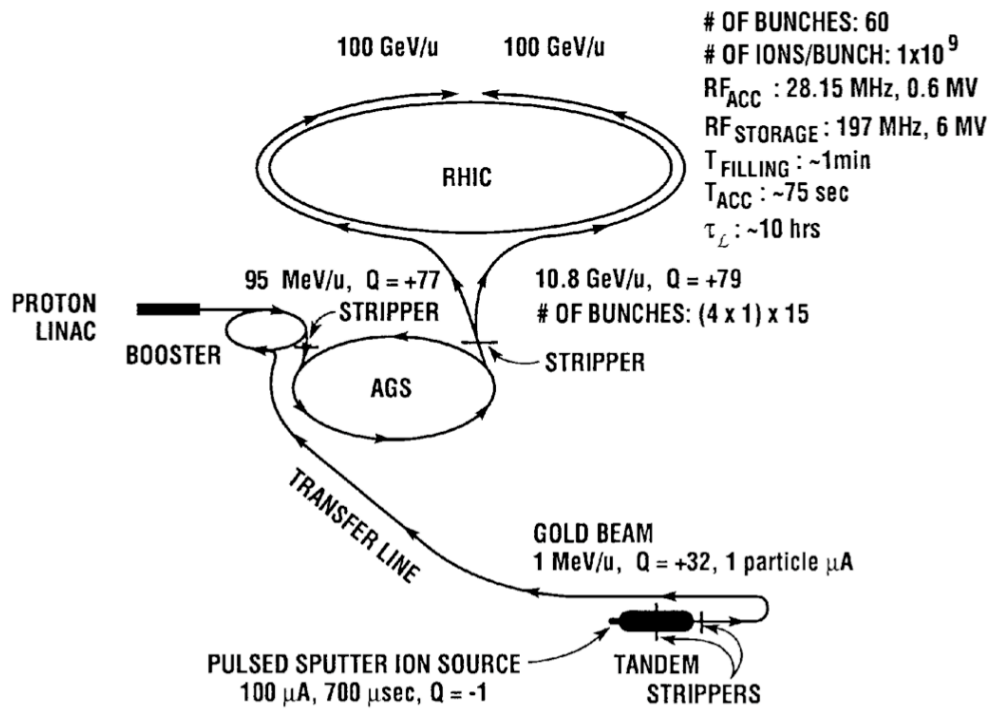


Figure 4.1: RHIC accelerator complex

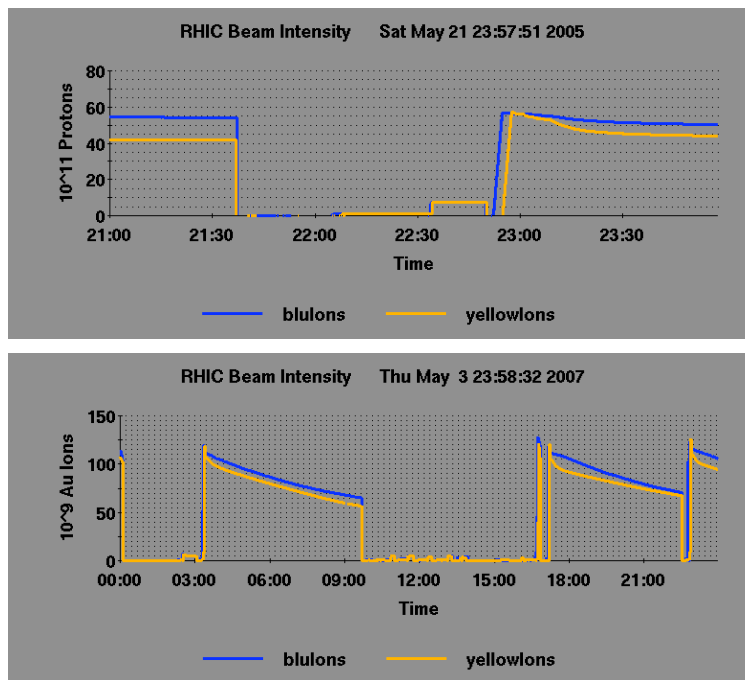


Figure 4.2: Example of time RHIC luminosity time dependence plots. The vertical axes show the RHIC beam intensities for protons (top) and gold ions (bottom) as a function of time. The time axes differ between the two plots obscuring the comparison of the beam lifetime of Au and protons.

of the plots are a little hard to distinguish from these screen shots, some details learned from time spent on shift at PHENIX concerning the behavior of the beams are worth mentioning. First, and of no real surprise, the maximum intensity of a proton beam is significantly higher than that of a gold beam, close to a factor of 50. Second, the decay of the particle beam intensity, which very approximately follow an exponentially falling distribution with an extended tail, is more rapid for the gold beams than for the proton beams due to intra-beam coulomb effects. Third, the implementation of “stochastic” cooling beginning in the 2007 Au+Au run was able to significantly extend the lifetime of a gold ion beam, which amounts to essentially changing the decay constant on the beam’s exponential lifetime and maintains a larger interaction rate for a longer period of time. Figure 4.3 details the RHIC run periods and the PHENIX recorded luminosity and data sets.

In 2000 when RHIC recorded its first collisions, four detectors were operational: BRAHMS, PHENIX, PHOBOS, and STAR. The *Solenoidal Tracker at RHIC* (STAR) detector employs a cylindrical Time-Projection Chamber (TPC) 4m in both diameter and length inside a solenoidal magnet. The TPC provides large acceptance, approaching  $4\pi$  particle tracking capability, and is aided by several other sub-system detectors, including the Silicon Vertex Detector and Barrel Electromagnetic Calorimeter. The Barrel Electromagnetic Calorimeter provides photon and electron identification and energy determination capabilities. [94]

PHOBOS is a near table-top size detector that possesses a two-arm magnetic spectrometer and a central detector and a series of ring detectors. The high-speed and high-resolution micro strip detector elements provide the detection of charged hadrons and leptons in selected solid angles.

The BRAHMS detector measures particles at forward and mid-rapidity with its two-arm magnetic spectrometer that are moveable to different settings. As of 2007 the two smaller detector collaborations BRAHMS and PHOBOS are no longer actively taking data.

## 4.2 The PHENIX detector

The **P**ioneering **H**igh **E**nergy **N**uclear **I**nteraction **eX**periment (PHENIX) [96] was named such since it “rose from the ashes” of four other detector proposals for RHIC. The names of these abandoned PHENIX proto-detectors will someday be lost to history, so they are listed here: TALES, SPARC, OASIS, and DIMUON. It is worth noting that the proposed

	Year	Species	$\sqrt{s}$ [GeV]	$\int L dt$	$N_{\text{tot}}$ (sampled)	Data Size
Run1	2000	Au - Au	130	$1 \mu\text{b}^{-1}$	10 M	3 TB
Run2	2001/02	Au - Au	200	$24 \mu\text{b}^{-1}$	170 M	10 TB
		Au - Au	19		< 1 M	
Run3	2002/03	p - p	200	$0.15 \text{pb}^{-1}$	3.7 B	20 TB
		d - Au	200	$2.74 \text{nb}^{-1}$	5.5 B	46 TB
Run4	2003/04	p - p	200	$0.35 \text{pb}^{-1}$	6.6 B	35 TB
		Au - Au	200	$241 \mu\text{b}^{-1}$	1.5 B	270 TB
Run5	2005	Au - Au	62.4	$9 \mu\text{b}^{-1}$	58 M	10 TB
		Cu - Cu	200	$3 \text{nb}^{-1}$	8.6 B	173 TB
		Cu - Cu	62.4	$0.19 \text{nb}^{-1}$	0.4 B	48 TB
		Cu - Cu	22.4	$2.7 \mu\text{b}^{-1}$	9 M	1 TB
Run-6	2006	p - p	200	$3.8 \text{pb}^{-1}$	85 B	262 TB
		p - p	200	$10.7 \text{pb}^{-1}$	233 B	310 TB
Run-8	2007/08	p - p	62.4	$0.1 \text{pb}^{-1}$	10 B	25 TB
		Au - Au	200	$725 \mu\text{b}^{-1}$	4.6 B	570 TB
Run-8	2007/08	d - Au	200	$81 \text{nb}^{-1}$	160 B	437 TB
		p - p	200	$5.7 \text{pb}^{-1}$	115 B	140 TB
		Au - Au	9.2		few k	

Figure 4.3: RHIC runs, species, energy, PHENIX sampled luminosity. The single muons measured in this analysis correspond to the Run 5, 2005 p-p entry. PHENIX has sampled a factor of four more  $p + p$  collisions since 2005 that are not yet analyzed.

DIMUON experiment and the previously discussed R&D efforts [42] were the progenitors of what became the PHENIX muon arms.

The “mixed” origins of the PHENIX detector (Figure 4.4) explain in part its novel hybrid design consisting of two pairs of “arms”, referred to internally as the central arms and muon arms. There is a collection of global subsystem detectors which provide event characterization, such as collision centrality and vertex information. These detectors also play a vital role in the PHENIX event trigger system which is discussed Section 4.5. The data analyzed in this analysis was recorded in 2005, at the beginning in the fifth year of physics running at RHIC. By this time the PHENIX detector was a fully mature experiment well described in existing literature [96–100]. So, instead of attempting a fully comprehensive description of the PHENIX detector systems, the focus is instead placed on important details of the detectors relevant to the detection of heavy flavor single muons.

## PHENIX coordinates and acceptance

To facilitate subsequent discussions of the detector geometry and details of the single muon analysis, the general layout of the PHENIX detector is described, including two general coordinate systems employed by PHENIX. The PHENIX experimental hall sits at the eight o’clock position on the RHIC ring, where the beam lines cross with approximate headings of north and south (see Figure 4.1). During the summer or other long RHIC shut-down periods, the experimental hall is opened to permit maintenance on the detectors, and one can go down and stand next to the beryllium beam pipe<sup>‡</sup> in the interaction region, also referred to as the interaction point (IP). The IP resides at the origin, (0,0,0), for PHENIX coordinate systems. For both Cartesian and cylindrical coordinate systems the beam line corresponds to the  $z$ -axis with North being the positive direction. The IP is the center of both the upper and lower images in Figure 4.4 (in between the MVD and BB(C) labels). In the lower image of Figure 4.4 the north muon arm is on the right and the South muon arm is to the left. The positive  $x$ -direction points into the page, and the positive  $y$ -direction is up.

Cylindrical coordinates  $(\theta, \phi, z)$  are often used. The polar angle  $\theta$  is defined relative to the beam axis  $z$ , such that  $\theta=90^\circ$  is perpendicular to the  $z$ -axis. The azimuthal angle  $\phi$  is 0 at the  $x$ -axis (west). The descriptions of the detectors that follow will use cylindrical

---

<sup>‡</sup>The beam pipe can easily be punctured by debris thrown from the top of the experimental hall by air conditioner installers

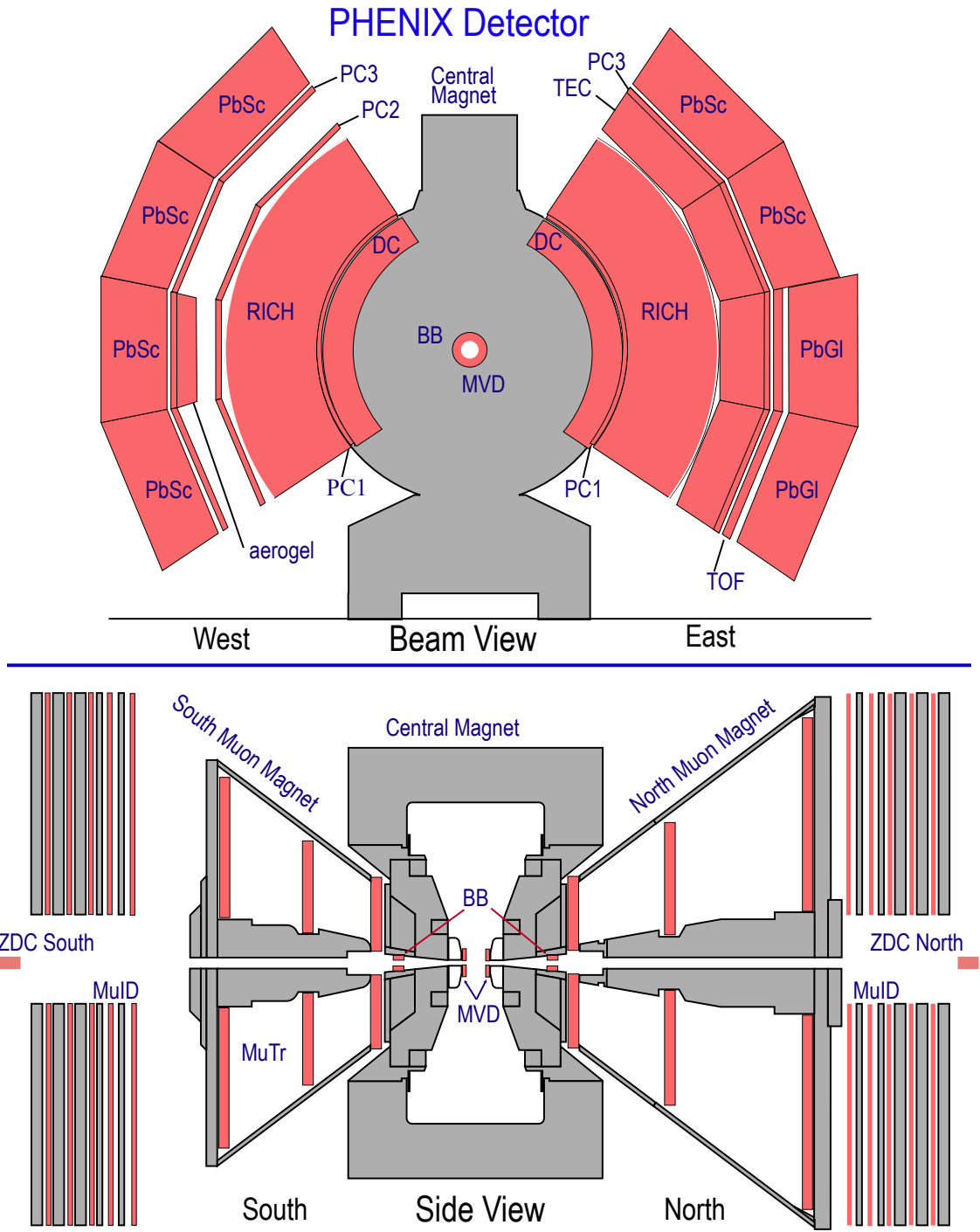


Figure 4.4: The PHENIX detector circa 2005. Details are discussed in the text.

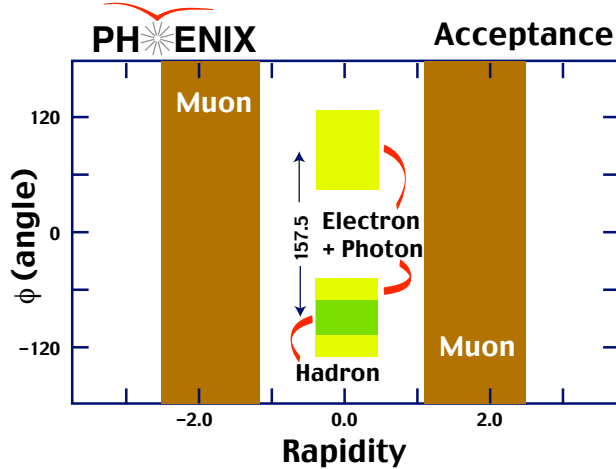


Figure 4.5: PHENIX detector acceptance as a function of rapidity,  $y$ , and azimuthal angle.

coordinates. For the relativistic particles measured in the PHENIX muon arms ( $p_T > 1.0$  GeV/c), the pseudo-rapidity variable  $\eta$  is essentially equivalent to the rapidity variable,  $y$ . For a full definition of the variables  $y$ ,  $\eta$ , and their relationship to the polar angle  $\theta$ , see Appendix A or [18]. Figure 4.5 illustrates the PHENIX acceptance in  $\phi$  and  $y$ . Smaller polar angles correspond to larger  $y$ . The muons arms full azimuthal acceptance at forward (or larger) rapidity is shown, as is the rapidity acceptance of the central arm detectors with partial  $\phi$  acceptance.

### 4.3 The PHENIX central arms and global detectors

The top and bottom images of Figure 4.4 provides two separate perspectives of the PHENIX detector, each highlighting a different arm. The top picture in Figure 4.4 provides a South side beam-line view of the central arm. The central arm consists of an east and west arm that each cover  $90^\circ$  in azimuth. The central arms reside in a magnetic field provided by the central magnet. In this region surrounding the IP, the magnetic field is parallel to the beam. The central arm consists of quasi-concentric layers of various detectors. As of 2005, the detector subsystems in the central arms include the Drift Chamber, Pad Chamber, Time Expansion Chamber for tracking, Ring Imaging Cherenkov detector, Time-of-Flight detector, and the Electromagnetic Calorimeter for particle identification, as well as those sub-systems being added in the upgrades program [94].

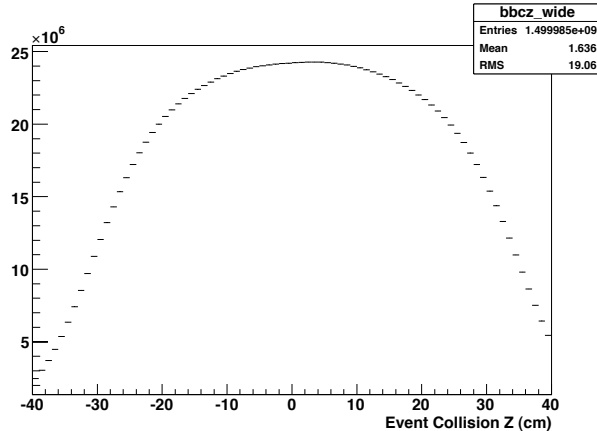


Figure 4.6: 200 GeV  $p + p$  event collision  $z$ -vertex distribution as determined by the BBC (2005).

PHENIX also employs a set of detectors for event characterization, such as the collision vertex, collision centrality, and reaction plane orientation. Determination of the collision centrality and the reaction plane are not relevant for  $p + p$  collisions, though additional information can be found in [97]. However, the determination of the event vertex is extremely important in the single muon analysis, as many of the quantities examined in the course of the analysis are plotted as direct functions of the event  $z$  vertex. The event vertex determined by the BBC for this work is shown in Figure 4.6. As the distribution shows, the range over which the collisions are provided by RHIC is quite large, with an RMS of 19 cm. The Beam-Beam Counter (BBC) serves as PHENIX's vertex detector, as well as the minimum-bias trigger.

The two (North and South) BBC detectors (labeled as BB in Figure 4.4) reside at far forward angles,  $3.0 \leq |\eta| \leq 3.9$ , and detect charged particles with full azimuthal acceptance. The BBC is designed to operate in both  $p + p$  and  $Au + Au$  collision environments. Each BBC is assembled from 64 hexagonally shaped quartz Cherenkov radiators instrumented with a photomultiplier tube (PMT) and arranged in a cylinder coaxial with the beam. The arrival times of particles on either side of the collision vertex are measured with a resolution of about 52 ps, and the average value is used to determine the event start time which then permits the determination of the collision vertex position,  $z_{vtx}$ . For central  $Au + Au$  collisions each PMT will detect about 15 charged particles; for  $p + p$  collisions there are only a few charged particles produced in the total event. Due to differences in the total charge detected in the

BBC for different collision environments, the determined collision vertex resolution varies with collision species. For  $Au + Au$  collisions the vertex resolution is about 0.5 cm, while for  $p+p$  the resolution is approximately 2 cm. The PHENIX Level-1 (LVL1) trigger (Section 4.5) requires a minimum number of fired PMT's in each BBC and  $|z_{vtx}| < 30$  cm [97].

## 4.4 The Muon Arms

The PHENIX Muons Arms [100] consist of two independent spectrometers at both forward and backward directions of the interaction point, corresponding to  $1.1 \leq |\eta| \leq 2.4$  for the North arm and  $1.2 \leq |\eta| \leq 2.2$  for the South arm. Each spectrometer is designed with sufficient geometric acceptance (one steradian), momentum resolution, and muon identification capabilities to permit the study of vector meson production, the Drell-Yan process (via muon pairs), and heavy quark production (through both muon pairs and single muons). The muon arms, augmented with anticipated upgrades, will also play an important role in the RHIC spin program through the detection of single high  $p_T$  muons ( $p_T > 20$  GeV/c) resulting from Z and W particle decays produced in the collision of polarized protons. For the 2005 PHENIX muon arm configuration, Figure 4.7 shows the  $x$  range covered by the muon spectrometer [101]. The North arm with its slightly more forward acceptance can probe down to a  $x$  of about 0.13, while for the south the value is approximately 0.24.

Each muon arm is comprised of a muon magnet and two subsystem detectors that work in concert to measure muons: the muon tracker (MuTr) which resides inside the muon magnet, and the muon identifier (MuID) which is located immediately downstream of the muon magnet backplate (also called yoke). The MuID and MuTr possess separate instrumentation, electronic, and signal readout which are combined later to track particles passing within the acceptance of the PHENIX muon arm and determine the penetration depth for muon/hadron separation. Particles emerging from a collision event at the interaction point ( $z=0$  cm) must first penetrate through about 80 cm ( $\sim 5\lambda_I$ ) of absorber material before entering the region of the muon magnet and reaching the first detector layer of the MuTr. The next three sections provide successive descriptions of the muon magnet, the MuTr subsystem detector, and the MuID subsystem detector.

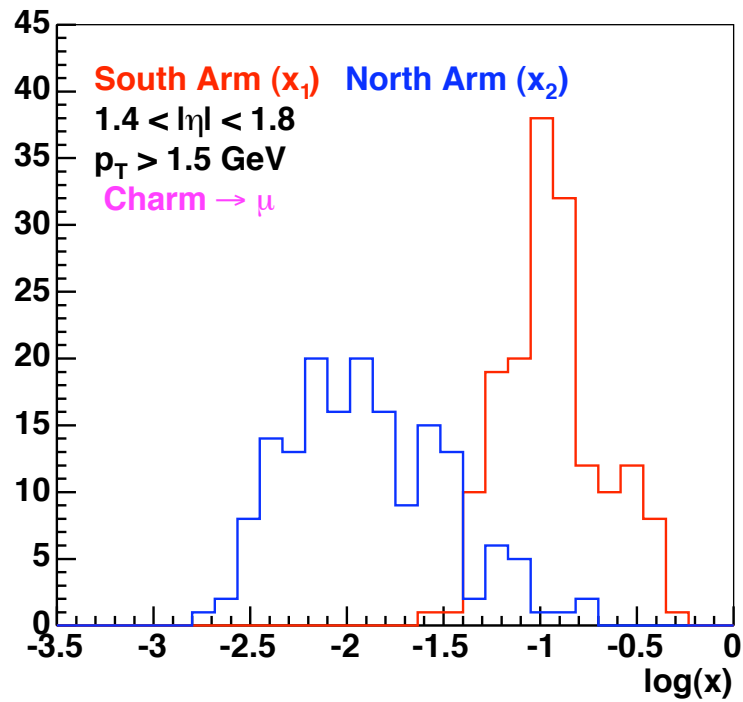


Figure 4.7: PHENIX muon arm  $x$  range for  $p + p$  at  $\sqrt{s} = 200 \text{ GeV}$  [101] corresponding approximately to  $x \sim 10^{-1}$  to  $10^{-2}$ . The difference in  $x$  range is due to the different forward acceptance for the North and South muon arms.

### 4.4.1 The Muon Magnets

The two PHENIX muon magnets house both the north and south Muon Tracker subsystems and use solenoid coils to produce radial magnetic fields. The muon magnets were designed in order to enclose the entire tracking chambers to maximize muon acceptance (full azimuth and  $\sim 25^\circ$  in  $\theta$ ) while simultaneously minimizing the effect on the RHIC circulating beams. The magnetic field is “reasonably” uniform and is mapped to a precision of 1%. The radial magnetic field’s integral is approximately proportional to the polar angle  $\theta$ . Charged particles follow helical trajectories, moving in  $\phi$  with approximately constant  $\theta$ . Both magnets with their unique “lampshade” shape can clearly be seen in Figure 4.4. Also noticeable in the figure is the difference in the north and south muon magnets (and also the MuTr). The north muon magnet’s position is fixed and covers the full length between the PHENIX central arm and the front of the Muon Identifier. The south muon magnet is 1.5 m shorter and can be moved to allow access to the PHENIX central arm detectors. Both arms have similar  $\int B \cdot dl$ , but the additional length and flatter piston angle give the north muon magnet better theoretical acceptance for measurements of  $\phi$  and  $\Upsilon$  mesons. The muon magnet backplates, also referred to as magnet yokes, serve as the first absorber layer of the Muon Identifier and have a thickness of 30 cm in the north arm and 20 cm in the south arm. The front  $z$  locations of the north and south magnet backplates are 630 cm and -480 cm respectively.

Magnetic field maps for both the PHENIX central and muon magnets are conducted using a surface mapping method that provides a calculation of the magnetic field based on measurements performed at points on the surface of the magnet. Hall probes are used to measure several points along radial lines on the magnet’s interior surface. The integrated magnetic field strength ( $\int B \cdot dl$ ) along a line at  $15^\circ$  is 0.75 Tesla-meters in the south magnet and 0.72 Tesla-meters in the north magnet. In both arms the average transverse momentum kick from the magnets is 0.2 GeV/c.

### 4.4.2 The Muon Tracker (MuTr)

The basic layout of the muon tracker is represented in Figure 4.8. Both the north and south Muon tracking chambers consist of three stations of cathode strip chambers for measuring the trajectory of particles in a magnetic field. The strength of the magnetic field is sufficient to permit momentum and charge sign determination. The MuTr stations are in the shape of octants, as seen in Figure 4.8, with the station number (1,2,3) and diameter increasing with distance from the interaction point. The largest tracking station is Station 3 with octant

chambers about 2.4 m wide and long.

The MuTr determines the momentum of charged particles in a standard fashion by combining the bend of a charged particle in a magnetic field and precise trajectory information using the basic principle provided in the Lorentz force law. The magnetic field in the MuTr volume is essentially radial and the particles traverse the volume at relatively low angles relative to the beam line of about  $20^\circ$ . For a charged particle entering the magnetic field the component of the velocity parallel to the magnetic field is unaffected, while the component of the velocity perpendicular to the magnetic field will be affected causing the particles motion to bend in the perpendicular direction. For this perpendicular component, the momentum of the particle is given by:

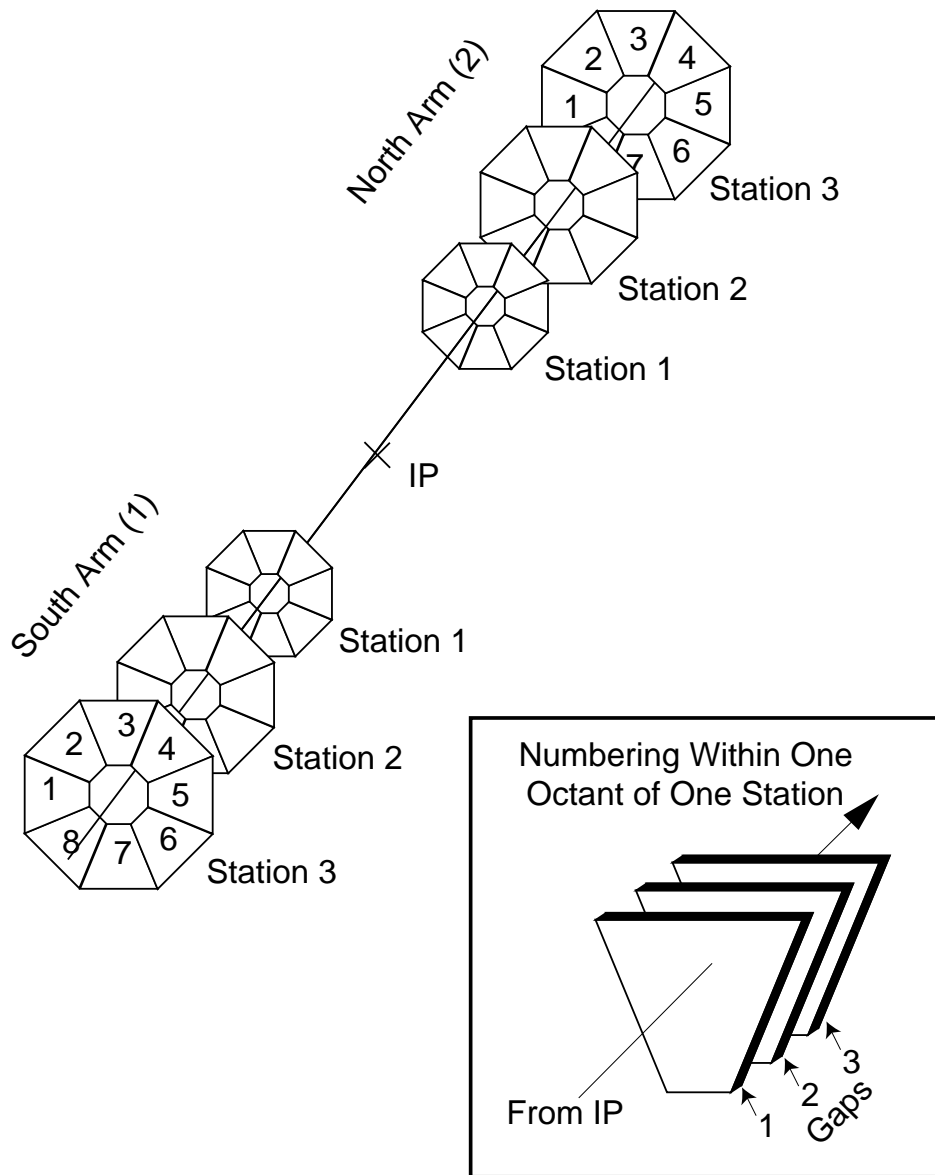
$$p = q \cdot B \cdot R \quad (4.1)$$

where  $q$  its charge,  $B$  the magnetic field strength, and  $R$  is the radius of the induced circular motion. As a charged particle passes through the MuTr volume, each of the tracking stations measures a position point along the particle's arc as it bends. A particle's momentum can be determined to the extent that both  $R$  and  $B$  are known. The MuTr essentially measures  $R$  in 3-dimensions in a high particle multiplicity environment.

Tracking stations 1 and 2 each contain 3 chamber "gaps", and station 3 contains 2 "gaps". Each chamber gap consists of two cathode planes on either side of an anode wire plane. The anode wires are instrumented in each half-octant, each covering a segment of  $\phi$  acceptance. One plane of cathode strips runs radially (perpendicular to the anode wires), while the second plane has cathode strips at stereo angles that range between 0 and  $\pm 11.25$  degrees relative to the perpendicular strips. The perpendicular cathode strips are capable of providing the highest resolution  $\phi$  measurements. Each strip is 1 cm wide, and the distribution of charge is fit across multiple strips, ultimately providing position resolution in the bend plane of about  $100 \mu m$ . The stereo angle cathode strips provide crude two-dimensional resolution which aids in the rejection of false cathode strip hits, generally referred to as "ghost" hits. For the purposes of read out cathode strips serve as the most basic unit of the MuTr. The chambers are operated with a gas mixture that is 50% Ar, 30% CO<sub>2</sub>, and 20% CF<sub>4</sub> and at a typical voltage of 1850 V.

Except for the area lost due to the support structure, the MuTr stations have full azimuthal acceptance ( $\phi$ ), and a  $\theta$  acceptance that ranges from  $10^\circ$  to  $37^\circ$ , which corresponds to

# Muon Tracking Nomenclature



W. Kinnison, 9/13/97

Figure 4.8: MuTR chamber description. Each MuTr station octant is instrumented in half-octants (not depicted).

Table 4.1: MuTr gap positions. Distances are to the front of the gap.

Arm	Station	Number of gaps	$z$ (cm)	Rad. Length % $X_0$
North	1	3	180	< 10
North	2	3	347	< 0.1
North	3	2	612.5	< 10
South	1	3	-180	< 10
South	2	3	-300	< 0.1
South	3	2	-460	< 10

$1.1 \leq |\eta| \leq 2.4$ . This angular acceptance is shown in Figure 4.5. Table 4.1 lists the positions of the different MuTr chambers and their relative radiation lengths. In order to measure the particle bend with maximum resolution, the amount of material in Station 2 is minimized, with  $\leq 0.1\%$  radiation length. The amount of material in all three MuTr stations amounts to about  $0.2 X_0$  (radiation lengths).

The MuTr chambers must contend with secondaries from the collision that can degrade the inherent  $100 \mu\text{m}$  resolution capability or even cause incorrect momentum determination. The impact of likely collision-related backgrounds on momentum determination has direct bearing the measurement of single muons and is discussed further in Chapter 5. Additional information and references concerning the design, construction, and electronics of the MuTr can be found in [100].

### 4.4.3 The Muon Identifier (MuID)

Once a charged particles passes through the Station 3 of the MuTr, it reaches the muon magnet backplate which serves as the first absorber layer of the MuID. Figure 4.4 shows the basic design of the MuID which has five alternating steel absorber (gray) and instrumented sensitive (red) layers that permit the separation of muons from hadrons.

#### MuID absorber allocation

Table 4.2 lists the  $z$ -positions and preceding absorber layer thickness of the different MuID layers. The choice of the total amount of steel absorber and the thickness of the absorber layers in the MuID was determined by two primary designs goals that address 1) restricting hadron contamination in the muon sample, and 2) the desire to measure low momentum

muon pairs, for instance for  $\phi$  meson detection. The logical sequence for the total amount and placement of steel in the muon arm is:

1. The proximity of the first absorber material relative to the collision vertex determines the free-decay path length for hadrons (as in Figure 1.7) which fixes the amount of muons from hadron decay. Ideally, the absorber is placed as close as possible to the collision vertex. In PHENIX the closest absorber is 41 cm from  $z=0$  with a collision point that is distributed according to that in Figure 4.6, which results in an irreducible Gap 4  $\mu/\pi$  ratio of  $1 \times 10^{-3}$ .
2. The total depth of steel in the front absorber, which sits between the collision point and the MuTr stations, is necessarily limited by the tolerable momentum degradation caused by multiple scattering. The balance struck between the two countervailing issues of the required level of hadron rejection and momentum degradation places 79 cm of steel absorber ( $\sim 5\lambda_I$ ) between the vertex and before the first MuTr tracking station.
3. The total remaining amount of steel is determined by choosing a hadron punch-through level that is 1/4 the size of irreducible decay muon level fixed in the first step. The factor of 1/4, or  $2.5 \times 10^{-4}$  provides more than an order of magnitude reduction in the muon pair background ( $J/\Psi$ ). The front absorber provides about  $10^{-2}$   $\pi$  rejection, so the total amount of steel needed to reach  $2.5 \times 10^{-4}$   $\mu/\pi$  separation is 90 cm. Since the muon magnet backplate is 30 cm thick in the north arm (20 cm in the south arm) an additional 60 cm (or more...) of steel is required in the MuID layers.
4. In order to measure low momentum ( $p_T \sim 1 \text{ GeV}/c$ )  $\phi$ ,  $\rho$ , and  $\omega$ 's in the muon arms, MuID Gaps 1 and 2 were allocated 10 cm of preceding absorber.
5. The remaining 40 cm of steel is placed before the remaining two MuID gaps in both arms for  $\mu/\pi$  separation. The total amount of steel in the South arm is 10 cm less than the North arm, which means it will have slightly larger punch-through hadron level. Muons and non-interacting hadrons penetrating the successive layers of steel experience ionization energy loss inside the absorber material. Muons and light hadrons entering the MuID are relativistic and behave essentially as minimum ionizing particles (MIP's) with energy loss described by the Bethe-Bloch parameterization [15]. MIP's undergo approximately 0.15 GeV of energy loss per 10 cm of steel which translates into about 0.9 GeV of energy loss in just the 60 cm of MuID steel.

Table 4.2: MuID gap positions. Front and back are defined relative to the interaction point at (0,0,0). The absorber width is for the *preceding* absorber layer.

Arm	Gap	Front $z$ (cm)	Back $z$ (cm)	Absorber width (cm)
North	0	686.96	704.24	30 (backplate)
North	1	728.46	745.74	10
North	2	768.76	786.04	10
North	3	815.86	833.14	20
North	4	861.36	878.64	20
South	0	-686.96	-704.24	20 (backplate)
South	1	-728.46	-745.74	10
South	2	-768.04	-786.04	10
South	3	-815.86	-833.14	20
South	4	-861.36	-878.64	20

## Additional MuID shielding

Shortly after the first collisions were recorded in PHENIX, the occupancies observed in the MuID were approximately twice that expected from Monte Carlo (GEANT 3) simulations [102]. Investigation uncovered that the simulations were missing material. After this issue was resolved, it was determined that the primary source of the backgrounds observed in the MuID were particles emanating from the beam pipe at nearly perpendicular angles 7 to 9 meters downstream from the collision vertex. In addition to this, another unexpected source of backgrounds was determined to be due to the beam “scraping” on the steering magnets inside the tunnel before entering the interaction region. This phenomenon deposits energy not from the direction of the collision vertex but from *behind* the detector. Improved beam steering and collimation, as well as the addition of steel shielding in the MuID square-hole (after RHIC Run 2) and in the beam tunnel (after RHIC Run 3) have alleviated but not completely removed both of these background sources.

## MuID gap instrumentation and read out

As shown in Figure 4.10 each MuID gap is instrumented with six overlapping panels. Each MuID gap was constructed with the same size panels to reduce total production costs, though in principle the more shallow panels could have been smaller, as seen by the 37° gap 0 ring in Figure 4.10. The detector technology in each of the MuID panels are commercially available plastic streamer tubes operated in proportional mode, referred to as Iarocci tubes. Depicted in Figure 4.9, the Iarocci tubes are 8.4 cm wide,  $\sim 1$  cm thick, and extend the entire width of a segmented MuID panel. The inside of the tubes are circulated with a gas mixture of

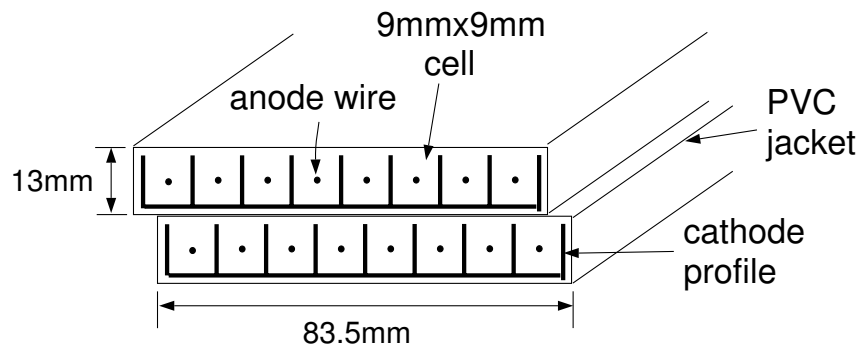


Figure 4.9: MuID two-pack cross section

92% CO<sub>2</sub> and 8% *i*-C<sub>4</sub>H<sub>10</sub> (isobutane).

Isobutane serves to quench electron avalanches in the tubes, allowing operation at higher voltages and gain without sparking. For ideal operations the isobutane level would be even higher except for safety concerns. Limitation of the gas mixture to a maximum of 8% isobutane keeps the gas from being inherently flammable even in the presence of oxygen. However, the possibility of a MuID chamber leak of the heavier-than-air isobutane is a potential safety hazard in the experimental hall. To reduce this hazard a secondary volume of N<sub>2</sub> ( $\sim 40$  m<sup>3</sup>) outside of the tubes but inside the MuID panels is separately circulated to maintain gas below a flammable level near the MuID read-out electronics, as well as providing the secondary benefit of keeping the chamber electronics dry.

As shown in Figure 4.9, a single tube possesses eight channels each with a relatively thick 100  $\mu$ m anode wire strung the length of the tube. For readout all eight wires in a tube are coupled together, and each tube is logically OR'd with a second tube to form a “two-pack”. Two-packs serve as the most basic MuID detector element that is read out and used for track reconstruction. Figure 4.9 also illustrates that the tubes in a two-pack are offset by half a cell. The combination of the half-cell offset and logical OR'ing of the two-pack tubes significantly increases the efficiency of a single layer of Iarocci tubes [102]. A two-pack with one operational tube is approximately 70% efficient and >90% efficient with both tubes operating. Each high-voltage chain serves approximately 20 tubes. A total of 3170 two-packs reside in each of the MuID arms. Each panel in a MuID gap, depicted in Figure 4.10, contains one layer of horizontal and one layer of vertical two-packs, providing 8.4 cm segmentation for both  $x$  and  $y$  positions. When coupled with the MuTr tracking capabilities, this level of segmentation provides the granularity needed to match the MuID information with sufficient background rejection and track reconstruction in both  $p+p$  and heavy ion collisions.

Each tube in a two-pack belongs to a different high-voltage supply chain. In the event that a single high-voltage power supply fails only one tube in a two-pack will be disabled. The expected resistance from a given high-voltage chain is estimated using the setup in Figure 4.11 which depicts the current algebra for a chain of  $N$  tubes with  $n$  broken wires [103]. The expected resistance for one MuID HV chain is:

$$R_n(G\Omega) = \frac{1 G\Omega}{(1 + n \cdot \frac{1.0}{0.4})} \quad (4.2)$$

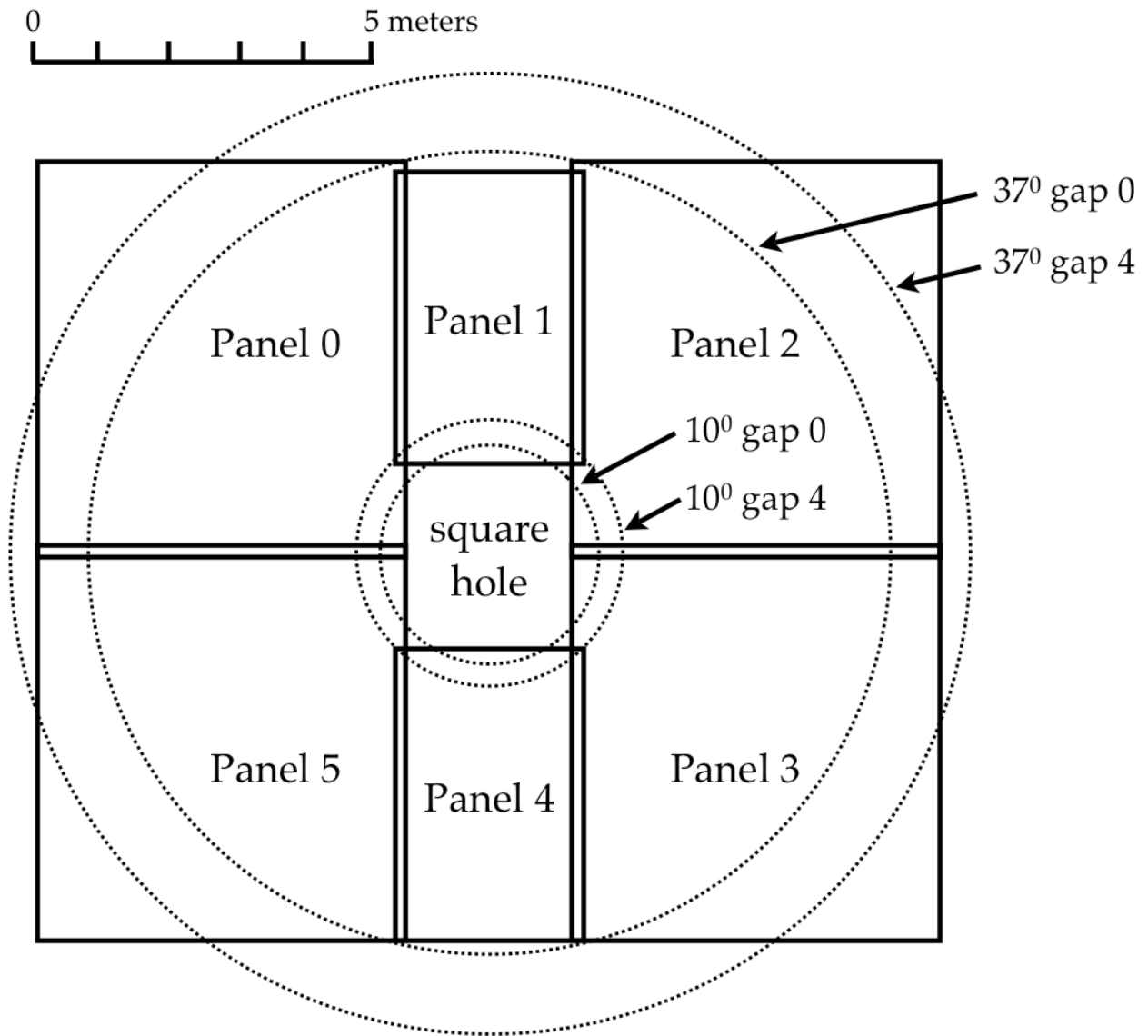


Figure 4.10: Approximate schematic drawing representing both a north and south MuID gap as seen from the South side. The panel numbering progresses clockwise, around the square hole through which the beam pipe passes. The circles describe the angular acceptance from 10 to 37 degrees for the shallowest gap (0) and the deepest gap (4). The massive size of the MuID (more than 10 meters across) is also shown.

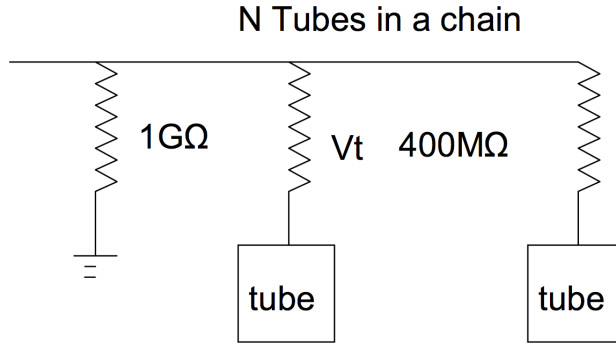


Figure 4.11: Simplified MuID circuit diagram. HV is supplied along the top line. See text for details.

Each MuID tube is connected to a HV chain through a  $400\text{ M}\Omega$  “current limiting” resistor. The tubes themselves can be considered an infinite resistor, unless a wire in a tube breaks which would then short the chain. The  $400\text{ M}\Omega$  resistor prevents multiple wires from disabling an entire HV chain and permits the determination of the number of broken wires by examining the read-out current. The MuID tubes store charge much like a capacitor, so in order to prevent the tubes from holding the current after HV is disabled, the  $1\text{ G}\Omega$  resistor is added in parallel to server as a bleeder resistor. The value of  $1\text{ G}\Omega$  was chosen to be as large as possible while still allowing discharge in an acceptable length of time. The Iarocci tubes are operated at voltages of  $4200\text{-}4500\text{ V}$ . With the reasonable assumption of linearity<sup>§</sup>, the expected current draw from a high-voltage chain can be determined using:

$$I_n(\mu A) = V \cdot (1 + 2.5n) \quad (4.3)$$

where  $V$  is the normal operating voltage of  $4.4\text{ kV}$ . For the case of zero broken wires, this results in an expected current of  $4.4\text{ }\mu\text{A}$ . In practice, especially as the Iarocci tubes age, some number of broken wires is unavoidable. When a tube breaks a wire the reported current will increase by the discrete amounts indicated in Equation 4.3.

A charged particle passing through the gas in the tubes will ionize the gas and deposit charge on the anode wires with some latent drift time that depends on the location in the tube and the operational voltage. Each of the 6140 two-packs must be read out for every

---

<sup>§</sup>Over the entire course of the operational voltage some non-Ohmic effects are observed, but in the operational regime Ohm’s law works reasonably well. The non-ohmic effects are observed as the hit rates get “high” which invalidates the assumption of infinite resistance of the Iarocci tubes.

beam crossing, which occurs at 106 ns intervals. Given the large size of the MuID detector (10m  $\times$  13m cross sectional area) and the large dimensions of the experimental hall requiring signal propagation up to 30 m, timing of the readout presents a challenge. The signals from the two-packs are amplified in-panel and sent to a Readout Card (ROC). The ROC's process the analog signal and digitize each two-pack as either a hit, 1 or no-hit, 0. The ROC's also synchronize the data and provide buffering of the hit information for up to forty beam crossings. All channels are synchronized in a staged process using a series of programmable delays and multiplexers. The MuID hit information is preserved if a trigger condition is met. The MuID is one of just five of the  $\sim$ fourteen PHENIX subsystem detectors to participate in the triggering system. Additional details concerning MuID readout electronics and construction can be found in [100].

## 4.5 Event triggering

The event rate and occupancy of the detector varies greatly in the various colliding systems, from a few tracks per event in  $p + p$  collisions, to 10% of all detector channels in central  $Au + Au$  collisions. In order to operate in these wide ranging conditions, PHENIX possesses two levels of event triggering, denoted as level 1 (LVL1) and level 2 (LVL2).

Figure 4.12 outlines the basic readout process from a collision to the data collection process (see Section 4.6). The PHENIX LVL1 system [99] processes every beam crossing, which occurs every 106 ns (from the 9.4 MHz RHIC beam clock) and generates an *accept/reject* decision within  $\sim$ 40 beam crossings. The LVL1 trigger is useful for rejecting empty beam crossings (non-events) and uninteresting events.

The MuID digitizes the detector response in real-time, while the MuTr stores the analog detector response and digitizes after receipt of a LVL1 trigger *accept*. Once the LVL1 trigger issues an *accept* for an event, the information from the different subsystems is stored in a LVL1 event buffer that can hold up to five events. Depending on the number of events in the LVL1 event buffer, the event is then digitized and transferred from the Read-out-cards (ROC's) to the Front-end-modules (FEM's). The PHENIX standard conversion period is 80 clock-ticks (beam-crossings). Once the data is on the FEM, the readout process to the Data Collection Modules (DCM's) (see Section 4.6) is performed. For those events that satisfy the LVL1 trigger conditions, LVL2 trigger algorithms provide an increased level of event rejection by using fast-reconstructed events to identify potential rare process events. The

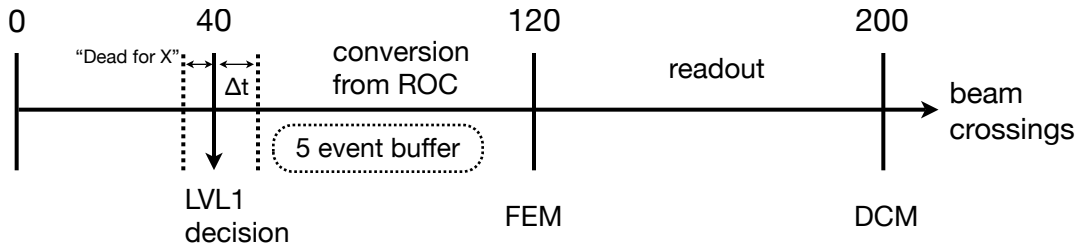


Figure 4.12: LVL1 readout stream schematic depicted on an axis defined by the number of beam crossings. The  $\Delta t$  corresponds to the potential delay in conversion based on the number of LVL1's in the 5 event buffer. The Dead for X period prohibits a second LVL1 *accept* within X number of beam crossings.

single muon analysis makes use of the LVL1 trigger but not LVL2, so additional discussion of LVL1 follows.

### 4.5.1 LVL1 triggers

The LVL1 trigger system consists of two components: Local Level-1 (LL1) and Global Level-1 (GL1). The LL1 communicates directly with the associated subsystem trigger detectors and processes the different trigger algorithms. Five of the  $\sim 14$  PHENIX detector subsystems participate in the LVL1 trigger. The GL1 takes the LL1 information and combines them to generate a LVL1 *accept/reject*. When the LVL1 algorithms issue an *accept* decision, a “dead for X” beam crossings is imposed for trailing events, where X is some number of beam crossings. A second LVL1 *accept* cannot be issued during this period. “Dead for X” has two important effects. Firstly, this allows the tracking chambers (MuTr and Drift Chamber) that take more than one clock-tick to collect their signal fully. Secondly, any “events” due to noise which may have durations of several clock ticks are avoided.

The single muon triggers used in this analysis require a so-called *minimum bias* trigger response from the BBC detector, referred to as the BBCLL1, and some combination of hits in the MuID layers. A programmable combination of subsystem detectors, in this case the BBC and MuID, is referred to as a particular physics trigger. There are on the order of  $\sim 25$  different physics triggers used by PHENIX.

The high event rates at RHIC, especially in  $p + p$  collisions, the limited rejection power of a particular physics trigger, and the maximum data acquisition throughput (or bandwidth)

will in some cases combine to not allow all physics triggers that generate a LVL1 *accept* to be recorded. Rather, the LVL1 triggered events that are actually preserved are referred to as *scaled* trigger events. This “pre-scaling” of events categorizes triggers into three types: raw, live, scaled. Raw triggers are events that satisfy a particular physics trigger condition, such as the combined BBC & MuID trigger. An event that generates a “raw” trigger when the LVL1 is not “dead for four” is said to possess a “live” trigger. The live trigger is compared against a programmable scale-down test that restricts every  $n+1$  live LVL1 triggers, where  $n$  is the so-called pre-scale or scale-down factor.

### 4.5.2 Local Level-1 Muon trigger implementation

Two LL1 *muon* triggers are used in this analysis: the Muon 1-Deep and Muon 1-Shallow. The muon LL1 trigger algorithm, implemented separately for horizontal and vertical MuID layers, employs combinations of MuID hits, called symsets, defined in terms of a MuID Gap 0 hit. The symset logic for the M1D and M1S triggers is depicted in Figure 4.13. For the purpose of the LVL1 trigger and for a given MuID gap and orientation, the various two-packs for the six different MuID panels are logically combined to form a single “logical” tube spanning the length (width or height) of the MuID. A symset is defined for every logical MuID tube at Gap 0 by projecting from a  $z$ -vertex position of (0,0,0) cm through the Gap 0 tube position to the Gap 4 position. The corresponding symset is then those tubes that lie along the ray from Gap 0 to Gap 4 (corresponding to tubes 0-4B in the figure). Due primarily to multiple scattering in absorber material and to a lesser extent  $z$ -vertices differing from  $z=0$ , the symset definition includes those tubes adjacent to the central symset tube row (rows A and C in the figure).

For every event the LL1 algorithm checks the hit pattern of every symset for the entire MuID. If the hits in the MuID satisfy either the 1-Shallow and/or 1-Deep symset logic shown in Figure 4.13, the LL1 will issue an *accept*. The LL1 decisions for both the 1-Shallow and 1-Deep are combined with the BBCLL1 in the GL1 decision for the final event *accept/reject* decision, after which the scale-down test is applied before the event may be recorded. Since the combined Muon and BBC triggers: 1-Deep LL1 & BBCLL1 and 1-Shallow & BBCLL1, are the actual trigger decision for event *accept/reject*, they will be subsequently referred to as simply Muon 1-Deep (M1D) and Muon 1-Shallow (M1S). As implemented for Run 5, the M1D is a subset of the M1S trigger set based on the logic of Figure 4.13.



### 4.5.3 Level-1 triggers used in this analysis

In total there are three triggered data sets are used in this analysis:

- The minimum bias (MB) data set is triggered solely by the BBCLL1. After selection of good runs and a vertex cut of  $|z_{vtx}| < 25$  cm, there are  $1.02 \times 10^9$  ( $1.12 \times 10^9$ ) recorded MB events in the North (South). Correcting for the BBCLL1 trigger pre-scales, there are  $3.76 \times 10^{10}$  ( $4.91 \times 10^{10}$ ) events in the North (South). The scale-down corrected MB distributions are used to normalize the muon track into invariant yields used in single muon analyses.
- The M1D triggers provide a data set of events containing an enriched sample of tracks penetrating to gap 4 of the MuID. The M1D trigger was not scaled down in Run 5.
- The M1S data set contains an enhanced sample of shallow penetrating tracks, defined to be gaps 2 and 3 in the MuID. Study of the flux of stopped hadrons in these shallow gaps allows for the estimation of the number of punch-through hadrons contaminating the sample of muon candidates in gap 4. The M1S trigger was only implemented for a fraction of the total run period. The total number of scaled-down BBC triggers for the M1S data set is  $5.54 \times 10^8$ . For the runs used in this analysis, none of the M1S triggers are scaled down.

### 4.5.4 LL1 muon trigger rejection factors

The purpose of a dedicated physics trigger is to select events of specific physics interest. The effectiveness of a rare process trigger is gauged by its selectivity or rejection factor relative to the minimum bias trigger. The trigger rejection factor (R.F.) is defined as:

$$R.F. = \sum_i \frac{total\ events_i}{triggered\ events_i} \quad (4.4)$$

where  $i$  is a sum over runs, such as shown in Figure 4.14.

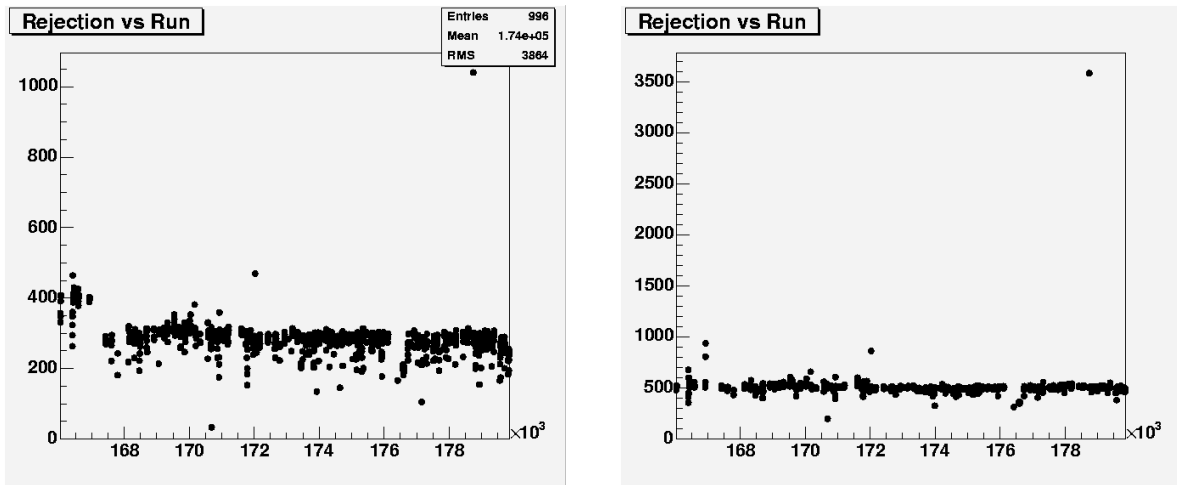
For the charmonium di-muon analysis in Run 5, which has a production cross section of about 1% of that for heavy flavor single muons, the di-muon trigger provided a rejection factor of  $\sim 3000$  in the North arm and  $\sim 13000$  in the South arm. In contrast, the rejection provided by the M1D varied between about 300 in the North arm and 500 in the South arm.

The rejection provided by the M1S triggers was even lower.

The PHENIX data acquisition system possess a finite bandwidth that is shared by the multiple trigger streams. Triggers with low rejection factors will fire more often, and therefore consume more of the total bandwidth. In order to prevent these triggers from reducing the duty-factor of the data acquisition system, referred to as the “live time”, trigger pre-scales are applied that directly scale down the number of triggered events that are recorded for analysis. The low rejection factor of the M1S means that a large scale-down factor is applied to the trigger or even that the trigger is removed altogether from the trigger scheme. The limited number of M1S triggered events available from the Run 5 data is one direct limitation in the analysis’s ability to measure single muons at larger  $p_T$  since the hadron background is estimated by comparison of the data selected with the M1S trigger.

#### 4.5.5 How biased is the Minimum Bias Trigger?

Particle production is discussed in terms of invariant yields ( $N$ ) from inelastic particular collisions, for instance  $p + p$  collisions. Ideally, yields are formed from the true number of produced particles divided by the true number of inelastic reactions. However, experimentally only a fraction of the true number of produced particles are actually measured in just a fraction of the true number of inelastic events. The PHENIX minimum bias trigger, the BBCLL1, has been determined to sample about  $23.0 \pm 2.2$  mb of the total 200 GeV  $p + p$



(a) North M1D trigger rejection factors vs. run

(b) South M1D trigger rejection factors vs. run number

Figure 4.14: Muon trigger rejection factors versus run number.

inelastic cross section of 41.8 mb ( $\sim 55\%$ ). The efficiency, or trigger bias, of the BBC,  $\epsilon_{BBC}$ , was determined by examining events with taken with the non-MB trigger that have tracks. This was done using  $\pi$ 's at mid-rapidity. For these events, the BBC was found to be  $0.79 \pm 0.02$  efficient. To obtain an invariant yield (See Appendix D), the measured yield of particles must be corrected in the following way to obtain the true yield of particles within the PHENIX min-bias acceptance:

$$N^{true} = N^{meas} \cdot \frac{\sigma_{BBC}^{pp}}{\epsilon_{BBC}^{c\bar{c} \rightarrow \mu}} \quad (4.5)$$

where  $\sigma_{BBC}^{pp}$  is 23.0 mb ( $0.55 \times 41.8$  mb) and  $\epsilon_{BBC}^{c\bar{c} \rightarrow \mu}$  is 0.79. Simulations in the muon arm have previously indicated that for charmonium the  $\epsilon_{BBC}$  is the same as that for the central arm. The efficiency  $\epsilon_{BBC}$  has not been explicitly checked for single particles in the muon arm, but the true value for  $\epsilon_{BBC}$  is not expected to vary much from the current value. The BBC trigger bias effect is insignificant for heavy ion collisions due to a larger number of charged particles being produced which increases the overall efficiency of the BBC. Both  $\sigma_{BBC}^{pp}$  and  $\epsilon_{BBC}$  are applied to the measured yield of single muons to convert them to invariant differential cross sections.

## 4.5.6 Trigger emulation and the need of a “pseudo-emulator”

### A swapped trigger fiber causes a problem

It was discovered after Run 5 that a trigger fiber for two MuID HV chains was swapped in the last gap of the North arm, resulting in an “extra” inefficiency in the affected area for the M1D trigger. The region affected is approximately 1/3 of Gap 4’s vertical chains. The MuID gaps possess two sensitive layers, so this suggests that approximately  $1/2 \cdot 1/3 \approx 18\%$  of the North Gap 4 area is subject to this trigger inefficiency. However, this effect is mitigated significantly by the inclusion of Gap 3 in the M1D trigger, as shown in Figure 4.13(a).

The Run 5 p+p di-muon analysis determined the swapped fiber to have caused an additional 6% trigger inefficiency. For single tracks, as opposed to dimuons, the effect should be less pronounced. However, in the implementation of the hadron cocktail we suffer this expected effect triply. In the matching of simulated hadrons to data, the data will have tracks missing in Gap 4 due to the swapped fiber (single effect), and simulation will be biased high relative to data since it does not implement the swapped cable (double effect). Additionally, the acceptance and efficiency corrections applied to the extracted single muon yield, which

are based on simulated muons, will not correct for this effect, leaving the North arm lower than expected (triple effect). This effect is correctable using a properly implemented trigger emulator.

The trigger emulation software available in the offline code is an exact implementation in C++ translated directly from the FPGA code used in the actual LL1 trigger. During data acquisition, the trigger algorithm takes all of the MuID hits and maps them into all possible symsets to test for a trigger condition being met i.e. for a given event the MuID hits satisfy the symset logic shown in Figure 4.13. However, the trigger emulator was regrettably not included in the Run 5 p+p data production.

### **Emulating a trigger emulator**

Since the LL1 trigger emulator information is not directly available at the analysis stage, an analysis software trigger psuedo-emulator was constructed to check the approximate efficiency of both the LL1 M1D and M1S triggers. The pseudo-emulator is implemented using basic hit information in the MuID and the trigger logic in Figure 4.13. The pseudo-emulator is adjusted to match the performance of the true trigger emulator through comparisons with simulations, to include the swapped fiber region in the North arm Gap 4 which affects the M1D triggered data. All tracks used in the analysis of the data and hadron cocktail are then subjected to the psuedo-emulator conditions. The implementation of the trigger emulator allows us to correct for the global trigger inefficiency as well as the specific North arm Gap 4 M1D problem, eliminating it as a source of systematic uncertainty in the analysis. The rest of this section is dedicated to describing the implementation of the pseudo-emulator.

The hit locations for the last gap of the MuID are unfortunately not available for use in the final analysis stage, but they do contain the layer by layer MuID hit information, as well as the road slopes ( $dx/dz$  and  $dy/dz$ ) and the Gap 0 x and y hit positions. The following is a listing in the logical order of the implementation of the pseudo-emulator:

1. Symsets employ a single tube at Gap 0 and three tubes at all subsequent gaps. A ray projected to  $z=0$  from the Gap 4 tube A (or C) through tube 0B defines the maximum amount of deflection tolerated between Gap 0 and Gap 4 for the symset to fire (see Figure 4.13(a)). The offset between 1.5 tube widths in Gap 4 and 0.5 tube widths in Gap 0 account for an 18 cm ( $9.0 \text{ cm} \cdot 1.5 + 9.0 \text{ cm} \cdot 0.5$ ) differential in  $x$  (or  $y$ ) between Gap 4 and Gap 0 (a distance of about 175 cm) . For a given track, the MuID road slope

and Gap 0 ( $x$  or  $y$ ) hit position is used to project to  $z=0$ . The expected maximum differential allowed over the distance from Gap 0 to  $z=0$  (a distance of 675 cm) is 71.4 cm. The  $dx/dz$  and  $dy/dz$  MuID road slopes of a track are used to separately check  $x$  and  $y$  offsets at  $z=0$ . Tracks with extrapolated offsets exceeding 71.4 cm could not have satisfied a symset condition and would not have fired the M1D trigger.

2. In addition to the  $z=0$  offset condition, the reconstructed track must also satisfy the hit requirements described by the logic shown in Figure 4.13(a). There is a maximum of two hits per gap, one for each orientation. The track must have at least 3 out of 5 fired symset layers, including a least one fired symset layer in Gaps 0 or 1 and separately Gaps 3 or 4.
3. For those tracks with a Gap 4 position falling inside the swapped trigger fiber region, the Gap 4 vertical hit is zeroed out. The trigger hit condition for these tracks is still 3 out of 5 gap layers, except that only one sensitive layer (instead of 2) is active at Gap 4, and any existing detector inefficiencies in the horizontal chains will directly result in the trigger conditions not being met. This is the origin of the trigger bias introduced by the swapped trigger fiber.

The efficacy of the described pseudo-trigger emulator is determined through comparison in muon simulations with the actual LL1 trigger emulator performance. In simulations where the true emulator decision is available, the pseudo-emulator demonstrated that it rejects more tracks than the true emulator. At the same time the amount incorrectly accepted by the pseudo-emulator is less than 0.1%. Application of the pseudo-emulator to both the data and hadron cocktail, as well as the acceptance & efficiency muon simulations, eliminates the muon trigger bias as a source of systematic uncertainty and is automatically accounted for in the final corrections.

Table 4.3 details the rejection factor of the pseudo-trigger emulator for both M1D and M1S as a function of arm. As expected, there is an extra loss of efficiency in the North arm Gap 4 due to the swapped trigger cable previously described.

## 4.6 PHENIX data acquisition system

The PHENIX data acquisition system (DAQ) [98, 99] consists of several different components. The DAQ is interfaced through the Run Control (RC) graphical user interface which

Table 4.3: Pseudo-trigger emulator efficiencies for both data and hadron cocktail.

data		
	M1S - Gap 3	M1D - Gap 4
North	99.9	89.9
South	99.8	95.1
hadron cocktail		
North	99.1	88.4
South	98.9	93.3

coordinates the components of the DAQ and allows for the coordinated starting and stopping of data collection. The data collection process is initiated when a LVL1 *accept* is sent to the subsystem front end electronics through the timing system which synchronizes the read-out electronics of various detector subsystems. The RC then instructs the FEM's to send the data to the data collection modules (DCM) which collect, package, and zero-suppress the data to reduce the overall data volume. The Event Builder (EvB) receives several parallel data streams from the DCM's and assembles the various fragments into complete events. LVL2 triggering is performed at this stage. The data is then sent to the data loggers to be recorded onto disk. The data is broken into *run numbers* which are incremented sequentially approximately every hour or when experimental conditions require a start/stop of the DAQ. This allows for correction keyed on run number to be performed at the analysis stage to correct for any changing experimental/detector conditions, such as detector calibrations and efficiencies, gas flow problems, or electronics problems.

## 4.7 PHENIX software and computing

The standard computing environment in PHENIX is LINUX and the *tsh* interactive shell. A standard set of environment variables are provided to link to PHENIX software. PHENIX software is rebuilt continually. There are several build types, of which three are relevant for this analysis: pro, ana, new. The pro build is the gold-standard of PHENIX software that it performed rarely and for the purpose of official data reconstruction or simulation projects. Ana builds are performed nearly weekly and remain available for use over a long term. Since several months can pass in between pro builds, ana builds provide a source of stable PHENIX libraries, especially when compared to new builds. The new builds are attempted daily and incorporate all of the latest versions of code checked into the code repository. New builds

operate on a 4-day cycle: new.1, new.2, new.3, new.4. The new pointer is rotated daily with the oldest of the four new builds being replaced.

PHENIX uses a CERN ROOT [105] based analysis code environment. The data is recorded by the DAQ into runs that consist of several PHENIX Raw Data Files (PRDF's) for a single run. Each PRDF is processed to reconstruct tracks. The reconstructed data is stored in reduced data volume formats for later physics analysis. Figure 4.15 shows a schematic representation of multi-step data flow in PHENIX from collisions to physics measurement.

## 4.8 Muon spectrometer track reconstruction

The current PHENIX muon arm software framework was developed in 2003 after the first two years of PHENIX operation. The tracking algorithm is written entirely in C++ and has been developed to cope with large hit multiplicity environments found in heavy ion collisions. With the reduced particle multiplicity and the corresponding detector occupancy in  $p + p$  collisions, the same tracking algorithm is essentially applied in the  $p + p$  case. The MuID and MuTr combine to form a “reconstructed” track in the muon arm, with composite information on: momentum, spatial position, penetration depth in the MuID steel, and collision vertex position (which also uses BBC information). This combination of hit information from two separate subsystem detectors begins in the MuID.

### 4.8.1 Road finding in the MuID

As previously discussed, the most basic unit of the MuID detector readout used in the track reconstruction algorithm is the two-pack, which for a given event is either on (“hit”) or off (“not hit”). Adjacent hits in the MuID are grouped into clusters, and these clusters can be combined across the MuID gaps for each tube orientation (horizontal or vertical) into one-dimensional linear “roads” that project back toward the collision vertex region. Counting from 0, the algorithm is seeded using Gap 1 hits and attempts to form roads from hits that extend in both directions in the MuID. With the lack of a magnetic field in the MuID, and despite the effects of multiple scattering, the most likely path through the MuID steel layers is a straight line. The one-dimensional roads are fit using a straight line and are then paired with roads of opposite orientation to form a two-dimensional MuID road which contains the position and direction information from the MuID that is included in the track reconstruction process.

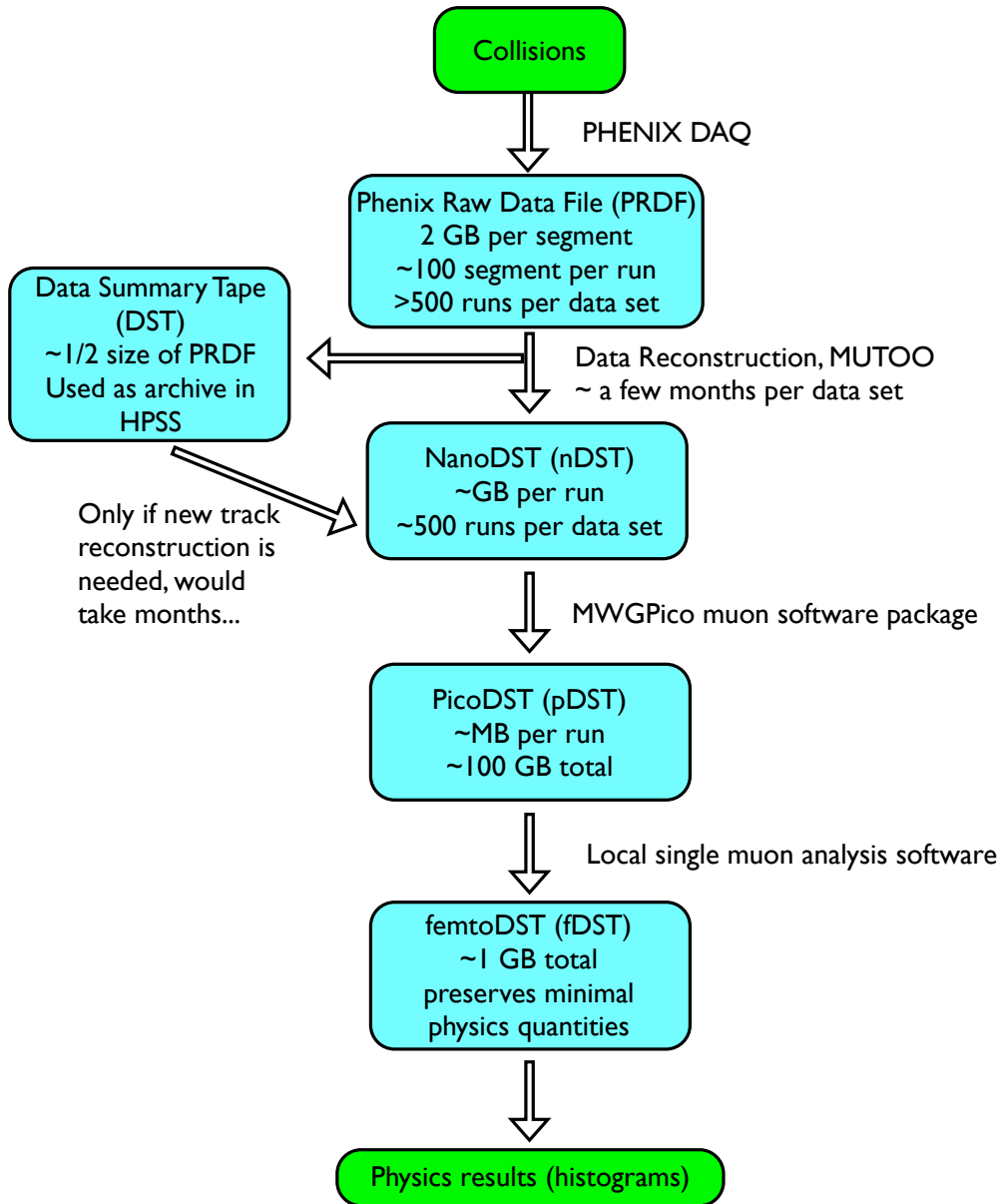


Figure 4.15: PHENIX data flow for the Run 5 PHENIX single muon analysis.

There are various conditions that the paired one-dimensional roads must satisfy. To form a two-dimensional MuID road, the depth of the one-dimensional roads of opposite orientation are not permitted to differ by more than one gap. Each one-dimensional road must contain hits in at least two gaps, and paired one-dimensional roads cannot differ in total hits by more than 2. The minimum depth for a full MuID road is Gap 2 and cannot have more than two gaps that lack hits preceding the final gap in the road. Under these various constraints, the gap depth of a full MuID road is determined by the deepest hit from either paired one-dimensional roads. Further details concerning the MuID road-finder algorithm are discussed in [106]. To reduce the combinatorial background in the next step of the muon arm reconstruction, the MuID roads seed the track finding algorithm for the MuTr.

### 4.8.2 Track finding in the MuTr

The most basic unit of the MuTr is a cathode strip which will “fire” if enough ionization charge is deposited when a charged particle passes through the detector volume. On average a single particle will fire from one to three adjacent cathode strips, which are combined into a MuTr cluster. For high occupancy events it is possible that two particles will fire cathode strips that will lead to overlapping clusters. This particular issue potentially plays an important role in the analysis, particularly at high  $p_T$  (Section 5.4). MuTr gap coordinates are derived from sets of fired cathode strips from a particular MuTr gap. Since the cathode strips are oriented at stereo angles to one another, two cathode strips within a gap can provide a two-dimensional position information. Each MuTr station (1,2, or 3) contains either two or three gaps (Table 4.1) that are separated by just a few centimeters. Coordinates from each gap within a MuTr station corresponding to the two or three space points over the few centimeters of thickness of a particular MuTr station. Once these space points are fit with a straight line they are referred to as MuTr stubs.

A schematic description of the muon arm track finding algorithm is now presented, with additional details available at [107, 108]. The MuTr track finding algorithm begins by attempting to match MuTr Station 3 stubs with all potential roads at the MuID Gap 0. Once a match between a MuID road and Station 3 stub is made, the algorithm then attempts to proceed to Stations 2 and 1. Once the track as been formed from stubs in each of the three Station, the matched MuTr track and MuID road now possess all available information from the muon arm. The MuTr tracks are also projected through the front absorber material to

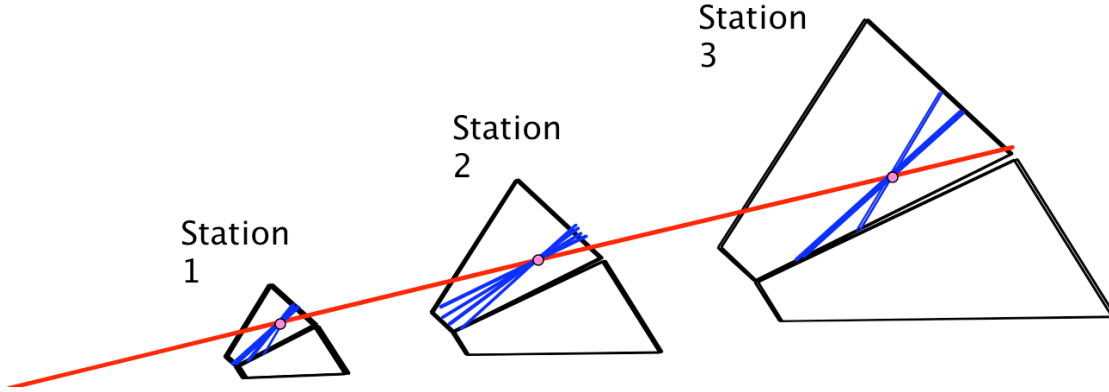


Figure 4.16: An event display for a single MuTr octant showing fired cathode strips in blue, MuTr stubs in pink, and a reconstructed MuTr track in red. As shown, each octant is instrumented as two half-octants.

obtain the position, direction, and momentum of the particle at the collision point [107]. Figure 4.16 is a portion of the muon arm reconstruction event display highlighting fired cathode strips (in blue) and the corresponding MuTr stubs for each station. The individual gaps within a particular MuTr station are too close together to be properly displayed in this figure.

## 4.9 MuID efficiencies

MuID two-pack efficiencies are determined using two different methods, the Data Method, which is the primary method, and the High-Voltage (HV) Method [103] which provides some level of cross check. These efficiencies are implemented for simulations in the GEANT 3 based detector response. The Data Method uses reconstructed roads from collision data that pass certain quality cuts. These roads are used to examine the efficiency for each two-pack orientation. The HV Method examines the high-voltage log files to determine the expected efficiency based on current draw, number of broken wires, etc. The HV method cannot detect problems with the low-voltage supplies that power the electronics or issues with the front end electronics or sagging voltage supplies (a problem experienced due to aging of the power supplies with slow variation of some internal resistors in the HV power supplies).

The performance of the MuID in Run 5 was quite stable (Appendix G). Therefore, for the purpose of simulations the MuID two-pack efficiencies are determined by averaging over

all runs. While this is in large part a valid approximation, the single muon analysis, relative to the di-muon analysis, is especially sensitive to fluctuations in efficiency in the MuID gaps. In the Monte Carlo detector response implemented in simulations for single muon background subtraction and acceptance corrections, additional checks are required to ensure parity between simulation and actual MuID performance. These checks are discussed subsequently in Chapter 5.

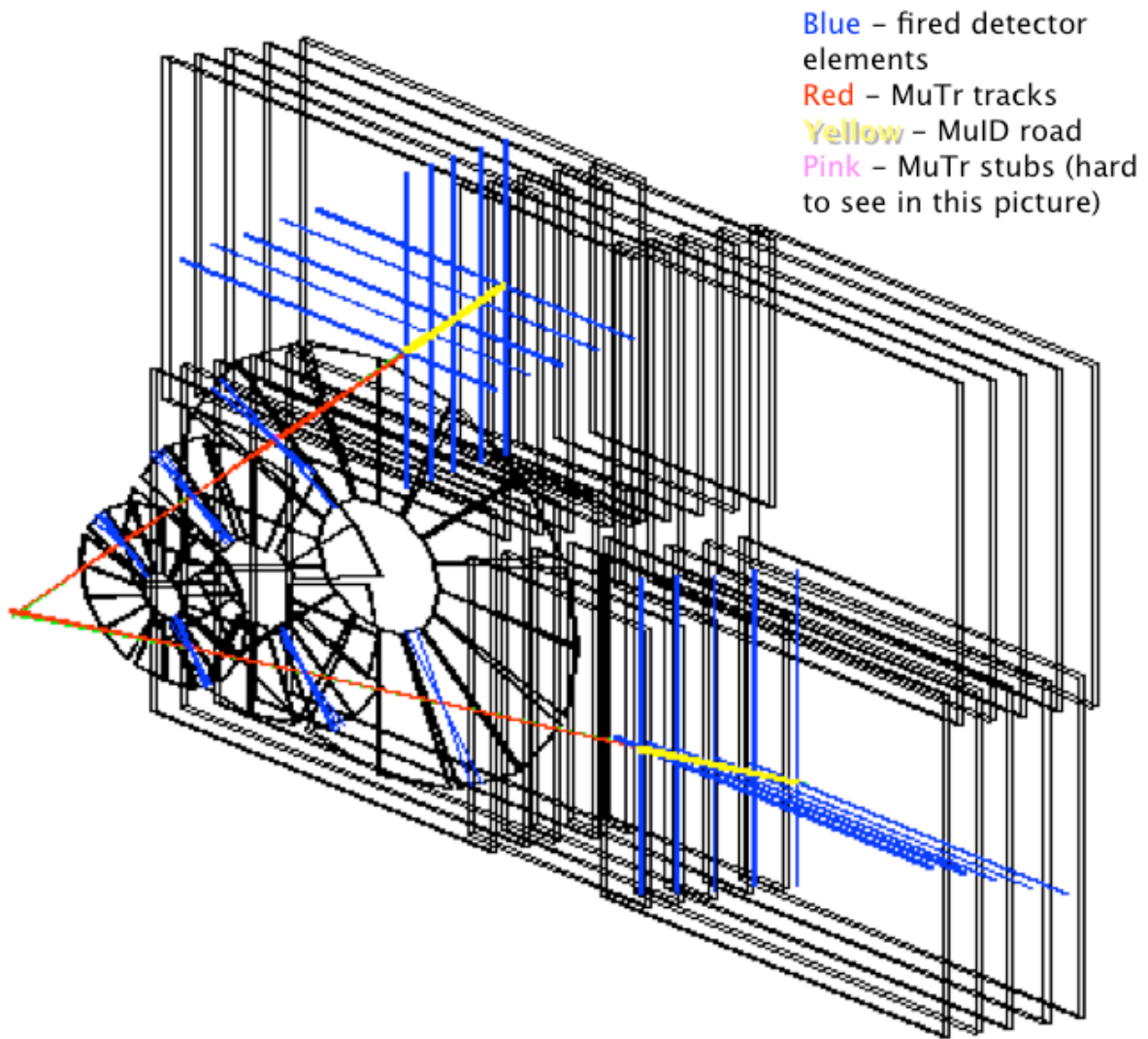


Figure 4.17: Event display of for a full muon arm reconstruction.

# Chapter 5

## The Single Muon Analysis

### 5.1 Analysis overview

The analysis for the measurement of heavy-flavor single muons in PHENIX presented in this chapter establishes what will serve as the standard approach for the measurement of heavy-flavor via single leptons [26,74,88] until future upgrades change the PHENIX muon detection capabilities. An inclusive yield of potential single muons is identified, and estimates of all “background” yields from various sources are statistically subtracted with excess attributed to the semi-leptonic decay of heavy flavor mesons.

The heavy flavor single muon yield is extracted from the sample of inclusive single muon candidates, which are defined as tracks successfully reconstructed to the last gap of the MuID (Gap 4) shown in Figure 5.1. Due to the significant amount of absorber material (pion rejection  $> 250:1$ ) between the vertex and deepest MuID gap (Gap 4), the PHENIX single muon analysis suffers from relatively few independent background sources, namely the light hadrons  $\pi^\pm$ ,  $K^\pm$ , their decay daughters, and to a much lesser extent,  $K_s^0$ ,  $K_L^0$ ,  $p$ , and  $\bar{p}$ . After the application of all track selection cuts optimized for heavy flavor single muons, the fraction of background tracks in the pool of single muon candidates in the MuID Gap 4 remains large, with a background-to-signal ratio of approximately 3:1 over all  $p_T$ . For the purpose of this analysis these physical background sources are categorized in two ways: muons from hadron decay and punch-through hadrons. The relative flux of these particles and heavy-flavor single muons in the PHENIX muon spectrometer is depicted in Figure 5.1, which shows a schematic cross-section of the detector as a function of penetration depth relative to the collision vertex at  $z=0$  cm.

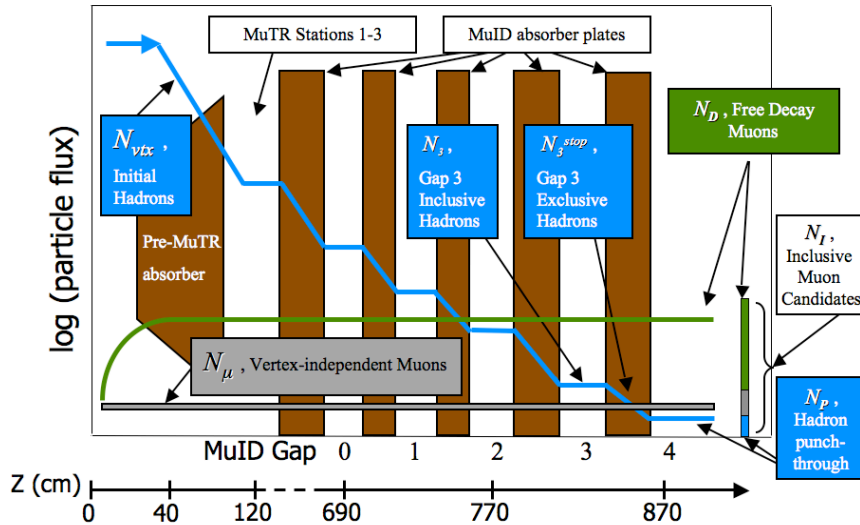


Figure 5.1: Schematic depiction of the relative flux of particles in the muon arm as a function of distance from the collision point [70]. Further details are discussed in the text.

### Muons from hadron decay

As Figure 5.1 shows, the initial flux of light hadrons is the single largest source of particles in the PHENIX muon arm. The decay lengths,  $c\tau$ , for the  $\pi$ 's (780 cm) and  $K$ 's (371 cm)\* are long compared to the flight path from the collision vertex to the first absorber material in the muon arm at  $z=41$  cm (Figures 1.8 and 5.1). More than 99% of these light hadrons reach the first absorber without decaying and are absorbed; however, the initial flux is sufficiently larger than that of heavy-flavor single muons such that this small fraction of hadrons decaying into muons is an important source of background tracks. Having decayed into muons, these particles will penetrate all of the steel absorber layers in the detector and be identified as heavy-flavor single muon candidates. These muons from hadron decay are the single largest integrated background source and statistically dominate all tracks for  $p_T < 3.0$  GeV.

The fraction of  $\pi$ 's and  $K$ 's decaying into muons increases linearly with total flight path (as shown in Figure 1.7). This analysis considers particle tracks originating at  $-25 \leq z \leq 25$  cm, which is a subset of all particles emerging from the relatively wide collision vertex distribution (Figure 4.6) measured by the BBC. For particles entering into the north muon arm ( $z > 0$ ) and for this selected  $z$ -vertex region, hadrons have as little as 16 cm (from  $z = 25$

\*For comparison, the muon decay length is 658.6 meters

cm to 41 cm) and as much as 66 cm (from  $z = -25$  to 41 cm) of “free” flight path. Hadrons are not all immediately absorbed at the front face of the absorber at  $z = 41$  cm, rather they are absorbed with a probability that is approximated by an exponential,  $1 - e^{-\frac{z-41}{\lambda_{Abs}}}$  beginning at  $z = 41$  cm. This extends the average effective flight path a few more centimeters into the front absorber, which is 79 cm thick corresponding to  $\sim 5 \lambda_I$  assuming an average<sup>†</sup>  $\lambda_I = 16$  cm. The number of muons from hadron decay remains relatively constant after this first absorber due to the absorption of the parent hadrons. A negligible background source may be attributable to hadrons that have survived multiple  $\lambda_I$  of absorber material before decaying into a muon (and neutrino) somewhere after the first absorber material; however, this source of background is implicitly handled in the background estimation method used in this analysis. The characteristic linear vertex dependence *measured* in the muon candidate  $z$ -vertex yields can be used to calculate this background component and is used as one constraint to the light-hadron background estimate.

### Punch-through hadrons

Despite the exponential-like probability for hadrons to interact in steel, some small fraction of the total hadron yield will penetrate through the 1.5 m of steel and be detected in the deepest MuID gap [41]. Since these hadrons may have originated at the primary collision  $z$ -vertex, they exhibit no characteristic linear  $z$ -vertex dependence as observed for muons from hadron decay. These punch-through hadrons are indistinguishable from heavy flavor muons originating from  $D$  and  $B$  meson decay with  $c\tau$ 's on the order of  $\sim 120$ - $500 \mu m$  and secondary vertices  $800 \mu m$  from the initial collision vertex [15], which is well below the resolution of the PHENIX vertex detector.

As the PHENIX muon arms possess no direct means for characterizing the hadron punch-through yield in the last MuID gap, Monte Carlo simulations are needed to estimate this background component. The shallow MuID Gaps 2 and 3 assist in the punch-through background estimate since they can be used to select stopped shallow hadrons that have undergone a nuclear interaction and stopped before reaching MuID Gap 4<sup>‡</sup>. The capability to measure unidentified stopped hadrons serves as a crucial secondary constraint in the light-hadron background estimate, which is performed using Monte Carlo so-called “hadron cocktail” simulations.

---

<sup>†</sup>The nominal interaction length for iron and copper are  $\lambda_I^{Fe} = 16.7$  cm and  $\lambda_I^{Cu} = 15.3$  cm [70].

<sup>‡</sup>Additional details of the shallow hadron selection are discussed in Section 5.3.2.

## Implementing a hadron cocktail in the muon arms

The estimation of physical background sources is performed using a data-constrained hadron cocktail GEANT-3 [109] Monte Carlo simulation with the full PHENIX detector geometry. Light hadron measurements do not exist at the muon arm forward rapidity acceptance, leaving these sources of backgrounds not well constrained. The hadron cocktail implemented in this analysis takes a prescribed mix of pions and kaons as input and fully propagates them through GEANT and the muon arm response-reconstruction software chain. The hadron cocktail is normalized to the observed hadron yield in the next-to-last MuID gap (Gap 3). The ability of the hadron cocktail to accurately estimate the hadronic flux observed in the muon arms is verified by a simultaneous comparison of the Gap 2 hadron yields and the Gap 4  $z$ -vertex distributions.

Modification of the input  $p_T$  spectra along with modifications of the steel hadron interaction cross section employed by GEANT provide the sufficient degrees of freedom needed to produce a reliable hadron background estimate. This estimate is judged against three primary conditions which apply to hadron simulations which are normalized to Gap 3 stopped hadron yields observed in data. The three conditions are: 1) the input  $p_T$  spectra for pions and kaons lie in between the measured spectra at  $y=0$  and  $y=3$ , 2) the Gap 2 stopped hadron flux matches that observed in data, and 3) the  $z$ -vertex distributions match between simulation and data for those tracks resulting from the decay of light hadrons in the vertex collision region.

## The single muon twelve-step program

The analysis procedure is now outlined in a step-by-step fashion. The basic procedure is applied independently to each arm using the same software/analysis framework. This procedure is repeated for each individual hadron cocktail estimate that is generated from different FLUKA/GHEISHA cross section settings.

1. Admit we *were* powerless over single muons—that our backgrounds *had* become unmanageable.
2. Determine for data the Gap 2 and Gap 3 stopped hadron yields by applying track selection criteria optimized for shallow gap hadron yields. Determine for data the inclusive yield of Gap 4 muon candidates by applying track selection criteria as described in Section 5.2.5.

3. Run a version of the hadron cocktail. This consists of selecting a particular hadron shower code (FLUKA or GHEISHA) and a particular scale value for the steel hadron interaction cross section. The hadron simulations require several weeks to complete using computer farms at Brookhaven (BNL) and Oak Ridge National Laboratories (ORNL). All hadron cocktail simulation files are then copied to the local ORNL HERANS cluster, aggregated, and reconstructed using standard PHENIX muon reconstruction code to produce simulated single muon data files. These are processed using the same analysis code used to analyze the data.
4. The output from the hadron cocktail is compared at Gaps 2, 3, and 4 to data. These yields are uncorrected yields, meaning no acceptance and efficiency corrections have been applied. However, fiducial acceptance cuts are employed to maximize consistency of response of the detector between data and simulation (as in Figure 5.9). The hadron cocktail  $p_T$  yield is normalized to match data at Gap 3. This is accomplished through an iterative alteration of the input  $p_T$  spectra per  $p_T$ -bin for the hadron cocktail particles until simulation and data match at Gap 3. This is efficiently implemented by modifying the relative “weights” of tracks.
5. Once the Gap 3 yields of hadron cocktail and data are adjusted to match by reweighting (to a ratio of 1), the yields in Gap 2 and Gap 4 are analyzed. The extent of the match between the data and hadron cocktail distributions are quantified using,  $\chi^2/\text{NDF}$  matching values that are calculated for the Gap 2  $p_T$  points and the Gap 4  $z$ -vertex distributions. Details of the  $\chi^2/\text{NDF}$  calculation are described in Section 5.3.3.
6. For a fully tuned hadron cocktail package (matched at Gap 3), the input spectra for kaons and pions determined by tuning to match MuID yields can be checked against measured hadron spectra at  $y=0$  and  $y=3$  (as in Figure 5.18(a)).
7. Once the Gap 2  $p_T$  and Gap 4  $z$ -vertex hadron cocktail yields are considered to successfully match data (determined using a  $\chi^2$  calculation as described below in Section 5.6.2), the resulting Gap 4 hadron flux prediction is used as an estimate of the light hadron backgrounds in the inclusive muon candidate sample.
8. A small background source not fully reproduced by the hadron cocktail but observed in  $p\delta\theta$  distributions (discussed in Section 5.4 is subtracted). The subtraction is made by a two-component fit of both data and simulation  $p\delta\theta$  distributions, with a relatively larger fraction of this background present in data. This background source is referred to as  $N_{2c}$ .

9. The hadron cocktail background estimate,  $N_c$ , and the two-component fit background,  $N_{2c}$ , are subtracted from the inclusive muon candidate yield,  $N_I$  by:  $N_\mu = N_I - N_c - N_{2c}$ .
10. The remaining yields are attributed to an excess of single muons from heavy flavor decay,  $N_\mu$ . This quantity is acceptance and efficiency corrected using values determined from single muon simulations as described in Section 5.5.
11. *Caveat lector*: Since no single hadron package provides adequate matching for both muon arms at all  $p_T$ , multiple hadron cocktail simulations are run using different steel hadron interaction cross sections for either FLUKA or GHEISHA. The results from multiple hadron cocktails are used to extract the final single muon result as described below in Section 5.6.2.
12. Having had a spiritual awakening as the result of these steps, we try to carry this message to other PHENIX single-muoners, and to practice these principles in future single muon analyses.

## 5.2 Raw data analysis

### 5.2.1 PHENIX data flow overview: from collisions to analysis files

The data used in this analysis was collected by PHENIX at RHIC from April 2005 through June 24, 2005. The LVL1 triggered data production including the muon arms was performed in Japan at the RIKEN PHENIX Computing Center, referred to as CCJ. A total of 263.2 TB of raw data was transferred from BNL in New York to CCJ over an 80 day period. The average transfer rate was about 40MB/sec. The track reconstruction from the raw data, referred colloquially to as “The Production”, used the PHENIX “pro.73” libraries. The Production was completed in July 2006 with the transfer of the production files back to BNL completed in August. The data flow from raw data files to the produced nanoDST’s was previously shown in Figure 4.15. The refined data files used for this analysis are created using Muon Working Group (MWG) track reconstruction and response software previously described. The files used for the single muon analysis are derived from the production MWGMuon and MWGMinBias nanoDST’s.

All production nanoDST’s were subsequently transferred back to RCF from Japan and placed in HPSS file storage. The full set of Run 5 “MWG” and “MinBias” nanoDST’s,

corresponding to 426 GB were stored at the ORNL HERANS computing cluster. Single muon picoDST's are produced from the nanoDST's using the MWGpico package in the MUTOO muon arm software framework located in the PHENIX code versioning system (CVS) at: *offline/packages/MWGpico*. The nanoDST's contain final reconstructed track information, as well as other quantities of interest such as trigger information and detector hit information.

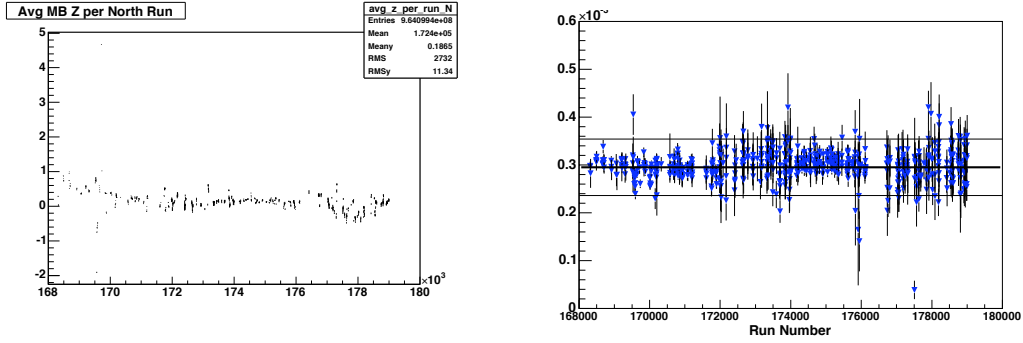
### 5.2.2 Local analysis software framework

The nanoDST is a highly condensed data format but is still prohibitively large for quick access and analysis. Two further steps are taken to condense the data. The MWGpico software package is used to produce so-called picoDST's. The size of just one single muon picoDST file in conjunction with the large size of Run 5 data set containing muon and min bias triggers translates into a set of picoDST's that are  $\sim 100$  GB in size. This set of single muon picoDST's are then filtered in one additional step using locally developed analysis software which preserved the minimal amount of physics information needed to accomplish the analysis.

A single final analysis file, colloquially referred to as a "femtoDST", is produced for the data as well as for background simulations. The filtering step from picoDST to femtoDST also places loose  $z$ -vertex cuts ( $\pm 30$  cm), as well as performing the good run list check. The final condensed femtoDST has a size of  $\sim 1$  GB, per charge sign. It takes approximately 2 minutes to complete a final histogram filling analysis loop. The compiled C++ code used to fill the femtoDST is archived in a code versioning system (CVS) at *offline/analysis/ETSMframework/*.

### 5.2.3 Data selection and QA

This section describes the process taken to arrive at the Run 5  $p+p$  single muon good run list. There are four separate good run lists, M1D and M1S for each arm. Initial checks to remove runs due to various issues such as: magnetic field status, run-control (DAQ) status, nominal hit rates, calibration status, electronics status, shift-crew log status, and high-voltage status. After this initial series of checks, the north di-muon run list consists of 642 runs, and the south arm list contains 822 runs. The entire nanoDST data set for both muon triggers (files labeled "MWG Muon") and min bias (files labeled as "MWG MinBias") are copied and disk resident at the ORNL cluster. Single muon picoDST's (comprised of one event based



(a) Average  $z$ -vertex position per run number

(b) Track production per minimum bias event as a function of run number. The solid lines indicate  $\pm 20\%$  from the mean.

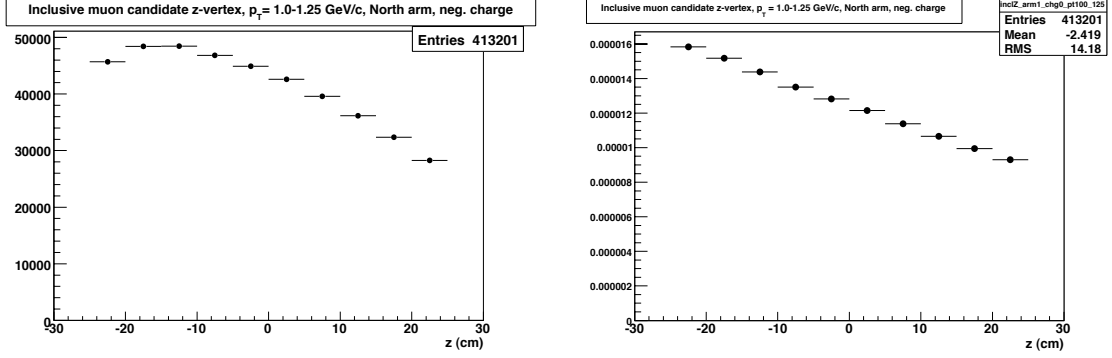
Figure 5.2: Distributions of average vertex collision and track production per run number.

ntuple and one track based ntuple) are then produced using the PHENIX CVS package offline/packages/MWGPico. The single muon picoDST's are filled using the M1D and M1S trigger information.

The M1S triggered data set is included as a subset of the M1D runs, so the good run QA performed is valid for both data sets. The runs including the M1S trigger were taken at the beginning of the run period. The average BBC  $z$ -vertex as a function of run number is shown in Figure 5.2(a). The plots shows that the BBC  $z$ -vertex remained very stable and within a few centimeters of  $z=0$  through for the entire set of runs considered in this analysis. Figure 5.2(b) illustrates the average number of tracks per MB event per run number. Run periods with large variations were excluded from analysis.

#### 5.2.4 Forming inclusive muon candidate distributions, $N_I$

Inclusive muon candidates,  $N_I$ , are tracks reconstructed to the deepest MuID layer, Gap 4. In forming the invariant yields for both  $z$  and  $p_T$  we divide by the BBC  $z$ -vertex event distribution. Figure 5.3 shows the un-normalized and event normalized vertex distributions. Appendix D describes this process.



(a) Unnormalized  $z$ -vertex distribution of muon tracks in the north arm (b) Minimum bias event normalized  $z$ -vertex distribution of muon tracks in the north arm

Figure 5.3: Panel (a) is divided by the measured BBC event vertex distribution (Figure 4.6) to form Panel (b). The distinctive linear  $z$ -vertex dependence from the hadronic decay muons is observed.

## 5.2.5 Track selection and acceptance

### Optimization of analysis cuts using a known heavy flavor muon sample

This analysis optimizes track selection criteria using known heavy flavor single muons from the Run 5 and 6  $p+p$   $J/\Psi$  LVL2 filtered data sets. These data were combined and analyzed by applying the full set of di-muon analysis track cuts [110] on the di-muon invariant mass distributions.

Tracks residing within  $2\sigma$  of a gaussian fit to the di-muon mass peak (shown in Figure 5.4) constitute a known and relatively clean sample of muons resulting from charmonium decay. For tracks within the selected mass region, distributions of all relevant single muon analysis variables are analyzed and compared to single muon simulations. This benchmarks the simulated single-particle distributions against known heavy flavor single muons. As an indicator of the excellent degree of agreement between single muon MC and data, Figure 5.5 illustrates the observed  $p\delta\theta$  distributions for both the di-muon and single particle simulations. Due to statistical limitations, the heavy flavor single muons in the di-muon sample reach a  $p_T$  of only 3.0 GeV/c. Muon track selection criteria is then determined for  $p_T < 3.0$  GeV/c using this data sample. Based on the strong agreement between the single muon simulations and the observed heavy-flavor muons, single muon simulations are used to determine optimized track selection criteria for  $p_T > 3.0$  GeV/c.

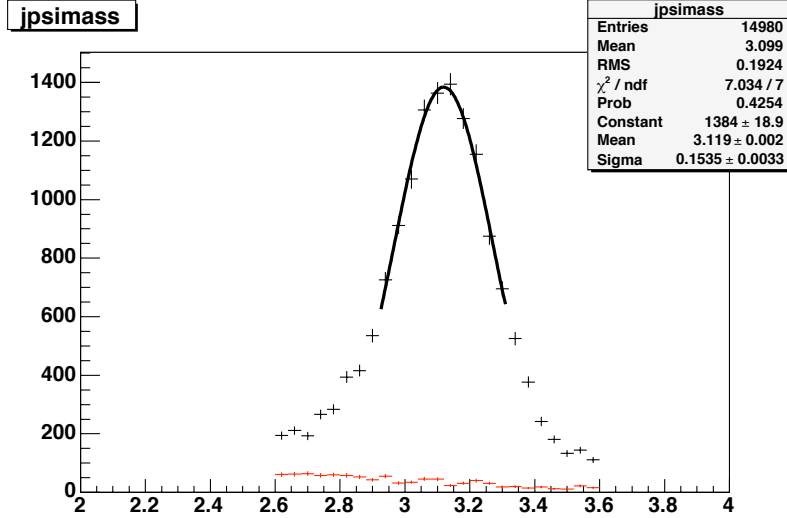


Figure 5.4: Di-muon invariant mass distribution of unlike-sign track pairs (black) and like-sign background (red). Tracks residing in the fitted region (black line) provide a relatively clean sample of heavy flavor single muons (from the  $J/\Psi$ ) and are used for track selection optimization.

### Definition of analysis variables

1. **BBC  $z$ -vertex** -  $z$  vertex of the event collision as determined by the BBC detector.
2. **Number of MuTr hits** - As described in Section 4.4.2, the MuTr consists of three stations per arm, can have up to 16 hits per arm. Stations 1 and 2 each have three layers and Station 3 has two layers. A gap consists of an anode plane sandwiched between two continuous cathode planes. In a gap, one cathode plane is straight and the other is rotated relative to the first at stereo angle. Overlap of the cathode planes in a given station's gap are readout to provide the space point "hits". There are a maximum of six hits each in Stations 1 and 2, while Station 3 has a maximum of four hits.
3. **RefRad** - This variable is the projected radial offset of the track associated MuID road at  $z=0$ . The value is calculated from the separate  $\Delta x$  and  $\Delta y$  offsets at  $z=0$  using  $\sqrt{\Delta x^2 + \Delta y^2}$ . The offsets are obtained by extrapolating to  $z=0$  the one-dimensional slope in either  $x$  or  $y$  of the MuID road through the Gap 0 hit position (n.b. specifically referred to as refX, refY in the software).

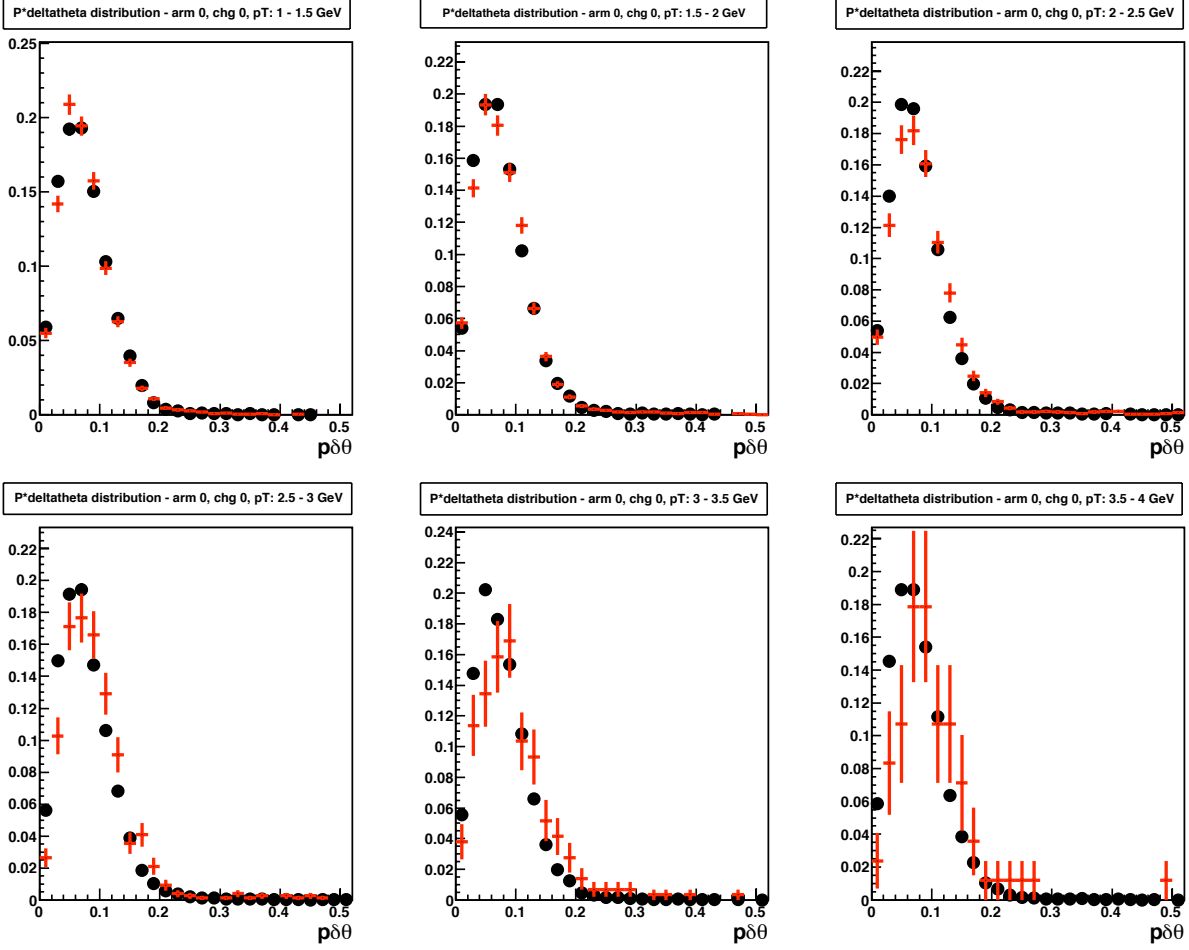


Figure 5.5:  $p\delta\theta$  from di-muons compared to single-particle single muon simulations. Six 500 MeV bins of  $p_T$  up to 4.0 GeV are shown: di-muon data red crosses and single-particle single muon simulations in black circles.

4. **Road Slope** - Slope of the MuID road determined from the 2D-road. A minimum slope is taken to ensure the MuID square hole is avoided.
5. **DG0** - “Distance at Gap 0”, or DG0, is the difference between the MuTr track projection and the MuID road projection at MuID Gap 0. The units of DG0 are centimeters.
6. **DDG0** - DDG0 is the angle between the MuTR track project and the MuID road projection at MuID Gap 0. The units of DDG0 are degrees.
7.  **$p\delta\theta$**  -  $p\delta\theta$  measures the extent of deflection due to multiple scattering that a track undergoes in the pre-MuTr absorber. The 19 cm of copper and 60 cm of steel, which lie at  $41 \text{ cm} \leq z \leq 120 \text{ cm}$  between the collision vertex and the first MuTr station, induce significant radiative energy loss and multiple scattering [111]. See Figure 5.6 for a pictorial representation of the definition. The scattering angle  $\delta\theta$  is defined for this analysis in the muon arms as:

$$\delta\theta_{sta1} = \cos^{-1} \left( \frac{\vec{P}_{sta1} \cdot \vec{R}_{sta1}}{P_{sta1} \cdot R_{sta1}} \right) \quad (5.1)$$

where  $R_{sta1}$  is the position vector and  $P_{sta1}$  is the momentum vector at MuTR Station 1. The  $z$ -component of the position vector is the  $z$  position at station 1 minus the  $z$ -vertex position. The scattering angle,  $\delta\theta$ , is scaled by the average of momentum of the track at Station 1 and the projected momentum at the vertex,  $\bar{P} = \frac{P_{vtx} + P_{sta1}}{2}$ . Scaling the

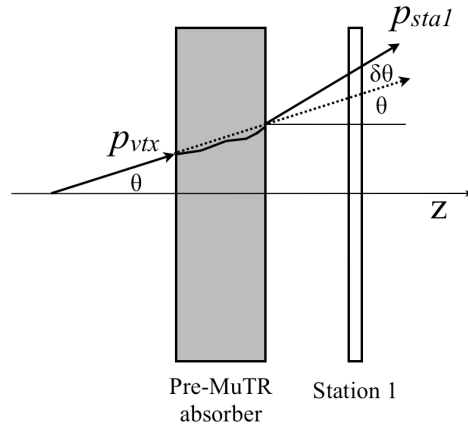


Figure 5.6: Definition of  $p\delta\theta$  analysis variable. The product of a particle’s multiple scattering angle and a momentum should remain constant for all momenta.

scattering angle by the total momentum should ensure that the distribution remains approximately a gaussian with constant width in all  $p_T$  bins, since angular deflections fall as  $1/p$ . The constant gaussian of the  $p\delta\theta$  distribution is useful in characterizing the purity of the single muon track sample. The  $p\delta\theta$  cut is taken from a gaussian fit with a mean  $\mu \approx 0.07$  and  $\sigma \approx 0.05$ . It strongly rejects those tracks which have been assigned an improper momentum due to tracking difficulties associated primarily with high local occupancies in the MuTR stations. Improper momentum assignment to a track manifests itself in  $p\delta\theta$  values outside the expected constant gaussian form (Figure 5.27). This cut also significantly eliminates those tracks that result from the decay of a hadron inside the muon arm, specifically the MuTR, which can result in incorrect momentum association.

It is worth noting, for historical reasons, that  $\bar{P} \cdot \delta\theta$  can be defined in more than one way:  $\bar{P} \cdot \delta\theta_{P_{vtx}}$  was also defined in [70] using not the projected position and momentum vector from the vertex, but the momentum vector at MuTR Station 1 and the momentum vector at the vertex: as  $\bar{P} \cdot \delta\theta_{P_{vtx}} = \cos^{-1} \left( \frac{\vec{P}_{sta1} \cdot \vec{P}_{vtx}}{P_{sta1} \cdot P_{vtx}} \right)$ . Both definitions of the  $p\delta\theta$  variable should be equivalent. Some brief tests established that the cuts did perform similarly in rejecting background, but some level of difference was seen. This difference was not fully explored or documented.

8.  **$\delta z$**  - As the single hadron cocktail cannot exactly reproduce the  $p\delta\theta$  distributions (further discussed in section 5.4) observed in data (Fig. 5.27), this difference between MC and data must be fully understood. The  $\delta Z$  cut originated because it satisfactorily rejects those tracks exhibiting pathological  $p\delta\theta$  values.  $\delta Z$  is defined as the difference between the event vertex, as determined with the BBC with a 2 cm resolution, and vertex provided by the muon reconstruction code track fit. Those tracks which show large differences between the event  $z$ -vertex and the track fit vertex correlate strongly with those tracks possessing the large  $p\delta\theta$  values that the hadron cocktail does exactly reproduce.
9. **Near-side  $z$ -vertex** - Restricting the  $z$ -vertex acceptance to tracks with  $z$ -vertex closer to the arm being considered increases the signal/background at low  $p_T$  by preferentially eliminating muons from hadron decay (Figure 5.7). In Figure 5.7, the inclusive muon track distribution is merged with a cartoon portrayal of the relative background contributions within the accepted  $z$ -vertex region.  $D_1$  and  $D_2$  correspond to the component of tracks due to muons from hadron decay in the  $z$ -vertex acceptance. The

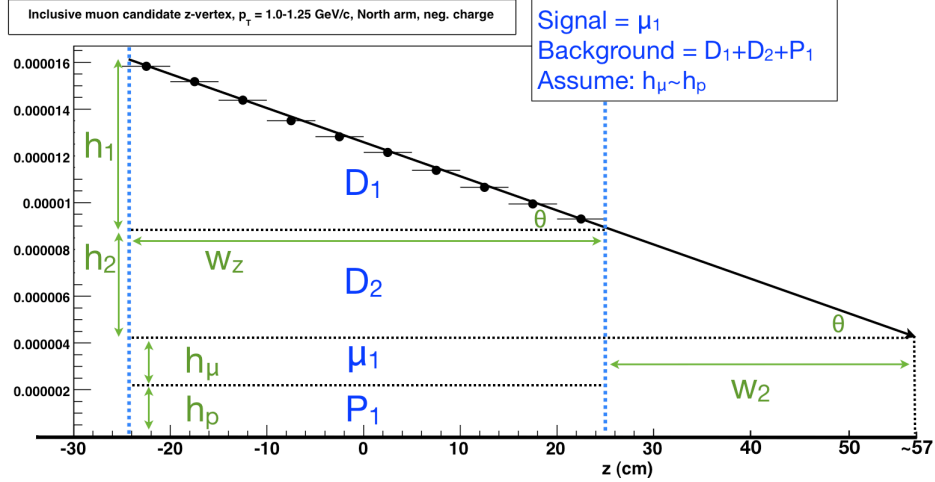


Figure 5.7: Schematic of particle yields, including the “Decay triangle” using the  $z$ -vertex distribution from Figure 5.3(b).

fraction of tracks that result from hadron decay drops to essentially zero after one absorption length,  $\lambda_{abs}$ , in the front steel that begins at  $z = 41$  cm. By fitting the  $z$ -vertex distribution and extrapolating the fit to this point at approximately  $z \approx 57$  cm, the vertex independent components due to punch-through hadrons  $P_1$ , and heavy flavor muons  $\mu_1$  can be estimated. The linear distribution holds relatively well for  $p_T < 2.5$  GeV/c and can be used to estimate the  $D_1 + D_2$  components, as was done in [70]. However, the relative mix of  $\mu_1$  and  $P_1$  is not easily identified and requires a simulation to disentangle each component.

### Application of analysis cuts

Analysis cuts are placed on a track by track basis. The track selection criteria for the accepted  $\eta$  bin  $1.4 \leq |\eta| \leq 1.9$  is discussed below. Some selected criteria are implemented with  $p_T$  dependence. For simplicity of presentation, the exact  $p_T$  dependent values used are not listed here for all variables.

1. **BBC  $z$ -vertex:**  $-25 < z < 25$  cm for all  $p_T$ , except for  $p_T < 1.75$  GeV/c the “near-side”  $z$ -vertex cut using only the 25 cm nearest the arm in question. For the north arm the cut is  $0 < z < 25$ , and for the south arm the cut is  $-25 < z < 0$ . The effect of the near-side cut is to improve the overall signal to background level by reducing the amount of hadron decay muons preferentially to that of heavy flavor muons, since

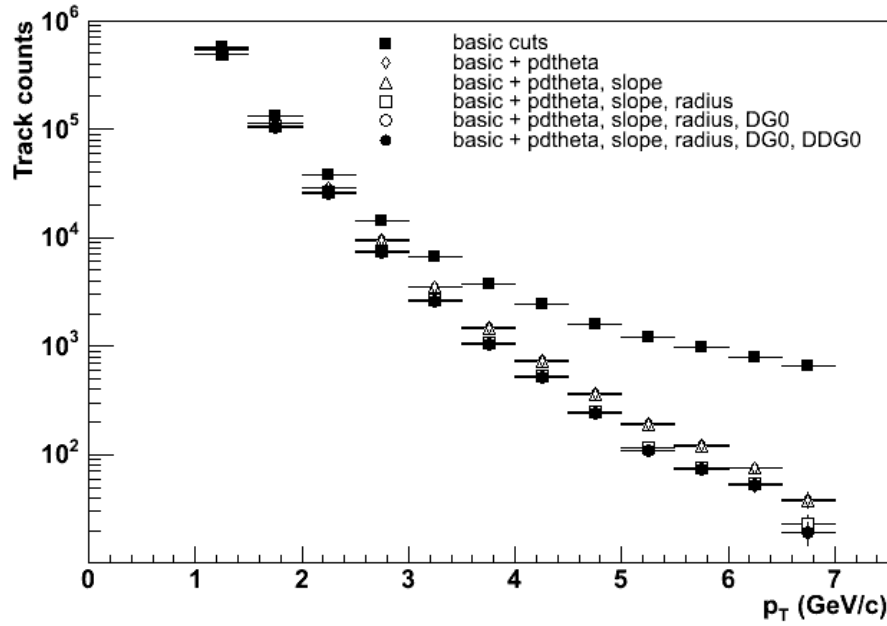
relatively more hadron decay muons occur in the  $z$ -region farther from the detector due to decay kinematics.

2. **Number of MuTR hits:**  $> 12$ .
3. **RefRad:**  $\sqrt{x^2 + y^2} < 100$  cm.
4. **Road Slope:**  $\sqrt{\left(\frac{dx}{dz}\right)^2 + \left(\frac{dy}{dz}\right)^2} > 0.21$ , ensures that the tracks possess a minimal angle.
5. **DG0:** South arm:  $DG0 < 20$  cm. North arm:  $DG0 < 15$  cm.
6. **DDG0:** Angle (in degrees) South arm:  $DDG0 < 10$  degrees. North arm:  $DDG0 < 9$  degrees.
7.  $\bar{p} \cdot \delta\theta_{sta1}$ :  $< 0.2$ , referred to commonly as  $p\delta\theta$ .
8.  $\delta z$ :  $< 2$  cm.
9. Trigger emulator software is run on data and simulations, as described in section 4.5.6
10. Acceptance cuts are also placed using the ROOT class TCutG. This is described in the next section (5.2.6).

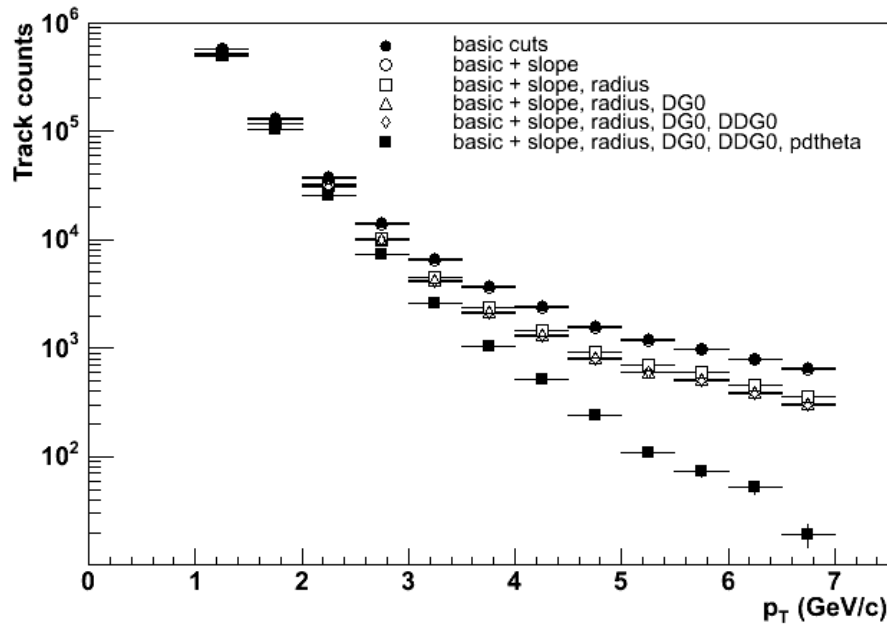
Figure 5.8 shows the inclusive muon spectra with different cuts applied. Basic cuts refers to basic  $\eta$  acceptance cuts and MuTR  $> 12$  hits. The figure illustrates qualitatively that the application of the successive cuts is successful in reducing the overall background levels. The  $p\delta\theta$  cut is demonstrated to have the most dramatic affect at reducing background tracks with increasing  $p_T$ .

## 5.2.6 Matching MC and data response by restricting acceptance

The match between Monte Carlo (MC) and data is of the utmost importance in this analysis. Ultimately, the hadron cocktail Monte Carlo is tuned to match track distributions observed in data is used as a background estimate. The extent to which the MC matches data serves as a direct source of systematic uncertainty in the final result. In running simulations the “true” hardware performance is implemented during the response and reconstruction stages of the simulations. However, differences in detector acceptance remain due to the imperfect implementation of actual hardware conditions during the specified run period in the MC. Another source of difference between MC and data is the use of a single run number for the hadron cocktail estimates. The PHENIX muon code accesses the hardware settings for a



(a) Inclusive muon candidate distribution with an ordered application of track selection cuts.  $p\delta\theta$  applied first.



(b) Inclusive muon candidate distribution with an ordered application of track selection cuts.  $p\delta\theta$  applied last.

Figure 5.8: Sequential implementation of cuts to inclusive yield.

single specified data run (corresponding to about one hour of real data taking). Because of the large hadron rejection provided by the  $10 \lambda_I$  of steel, extended (weeks) of CPU time is required to calculate a single hadron cocktail with the needed Gap 4 statistics out to a  $p_T$  of 5.0 GeV/c. Therefore, a single “good” run is specified for the hadron cocktail reconstruction, since several different (seven in this analysis) hadron package estimates are performed for this analysis.

To minimize the effect of the run to run variation in the detector acceptance in the data that is hard in practice to accomplish in simulations, separate fiducial geometric acceptance cuts are placed on both the data and simulations. To ensure optimal matching, MC simulations are run and the hit patterns in the detector are checked against data. In the MuID, which consists of 5 gaps with 2 sensitive layers per gap, Gap 4, 3, and 2 hit patterns in x,y are examined requiring 10, 8, 6 hits respectively. The requirement of all hits exposes any areas of discrepancy between the MC response and that observed in data. The MuID run performance is very stable, but for one period of runs a high-voltage chain was disabled which affected  $\sim 10\%$  of the total acceptance in x,y. Since the efficiencies implemented in the MuID are done using values averaged over the entire run period, this area is excluded to eliminate any MC/data discrepancy. Likewise, for the MuTr the hit distributions are examined for each MuTr station with full hits required. In addition to small areas of disagreement in the overall response of different MuTr octants, the edges between octants tend to have differences between the response and data. These edge areas are removed for both MC and data using very narrow  $\phi$ -angle restrictions.

Figure 5.9 shows an example of how these fiducial geometric cuts are implemented. The plot is of the x,y hit positions of tracks in the north MuTr Station 3. Similar distributions are studied as described for all MuID and MuTr detector layers. This allows for the maximization of agreement between data and simulation, even if simulation uses very few (even a single) run number to specify the detector response function. The largest negative aspect of this approach is the relatively large reduction in statistics (upwards of 30%) these cuts impose. This analysis is not statistics limited in the specified  $p_T$  region 1.0-5.0 GeV/c, and thus, this loss of statistics is acceptable.

The  $\phi$  and radial hit position distributions are compared using the hadron cocktail. Examine all three MuTr stations and Gaps 2,3,4 of MuID. Acceptance is restricted to specific radial and  $\phi$  regions for both MC and data to maximize agreement in the tracks accepted

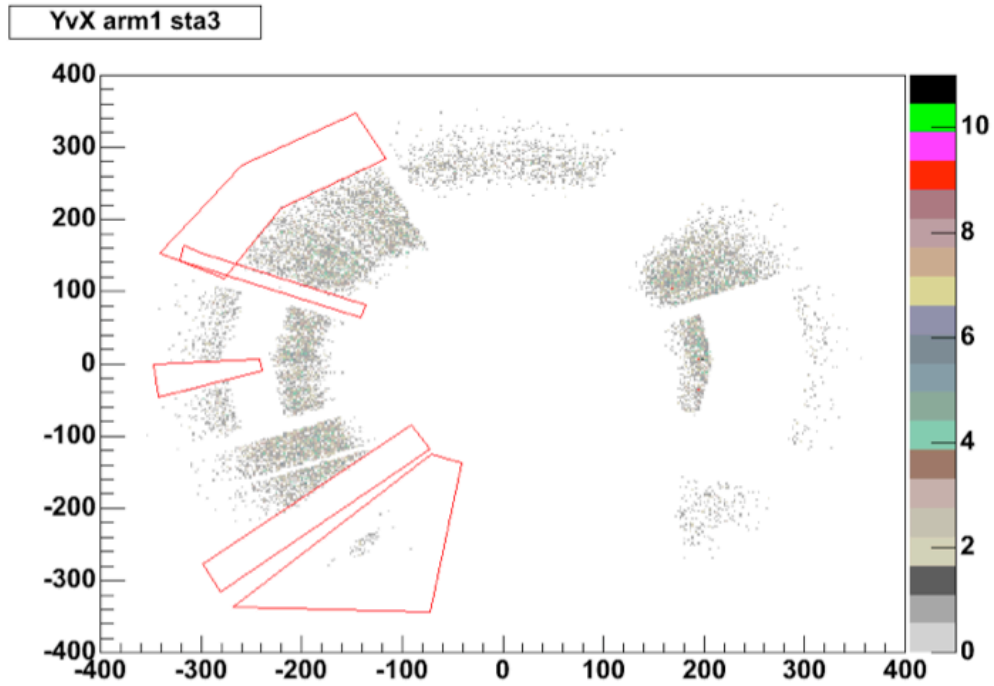


Figure 5.9:  $x,y$  distribution of hits in the MuTr Station 3 requiring 16/16 layers fired MuTr layers. This condition causes the large empty areas. 13/16 hits are used in the analysis and such large areas are not observed for this case. The areas inside the red regions are those rejected by the fiducial cuts to match MC and data hit distributions.

for analysis. Figure 5.10 and Figure 5.11 show comparisons of MC hadron tracks normalized to data in both  $r$  and  $\phi$  based on the hit position in Gap 0 of the MuID. The rms of the ratio of the MC/data for these distributions form one of the components used in the determination of the systematic uncertainty in the Acceptance $\times$ Efficiency correction,  $\sigma_{Ac}$  (Table 5.8).

### 5.3 The hadron cocktail background estimate

Hadrons, predominately pions and kaons, along with their decay daughters dominate the flux of particles from the vertex into the muon spectrometer. As discussed in the analysis overview at the beginning of the chapter, a hadron cocktail consisting of  $\pi$ 's and K's is used to estimate the light hadron decay and punch-through components of the inclusive muon candidates.

Previous efforts at PHENIX single muon analyses used linear fits of the  $z$ -vertex distributions to estimate the yield of muons from light hadron decay. In order to estimate the hadron-punchthrough component, two approaches had been attempted: 1) a data-driven generator calibrated using GEANT simulations as in [70] or, 2) a purely data-driven method using unidentified hadrons measured in the shallow MuID Gaps 2 and 3 in order to extrapolate the hadron punch-through yield to Gap 4. The first method suffers from rather large systematic uncertainties due to the discrepancy of 50% between the two default hadron shower packages FLUKA and GHEISHA. The second purely data-driven method was explored for this analysis but discarded due to its unphysical extrapolated punch-through hadron estimates.

Part of the failure of the purely data-driven approach is attributed to the effects observed in [42], where pions were demonstrated to have substantial penetrating power into steel exceeding the naive expectation of exponential absorption of hadrons in steel. This effect can be seen in Figure 5.13. The right plot is for  $8\lambda_I$  of material. A total momentum of 8 GeV/c corresponds to an equivalent  $p_T$  of  $\sim 3$  GeV/c in the muon arm, which is the approximate  $p_T$  where the punch-through hadron component begins to dominate the total background fraction. For this momentum, the fraction of pion events having hits after  $8\lambda_I$  is 0.07, whereas a naive exponential absorption would provide  $e^{-8} \approx 0.0003$ . This is understood by recalling the difference between nuclear interaction and nuclear absorption, i.e.  $\lambda_I \neq \lambda_{abs}$ . A pion that interacts strongly can have secondaries that inherit a large enough fraction of the initial

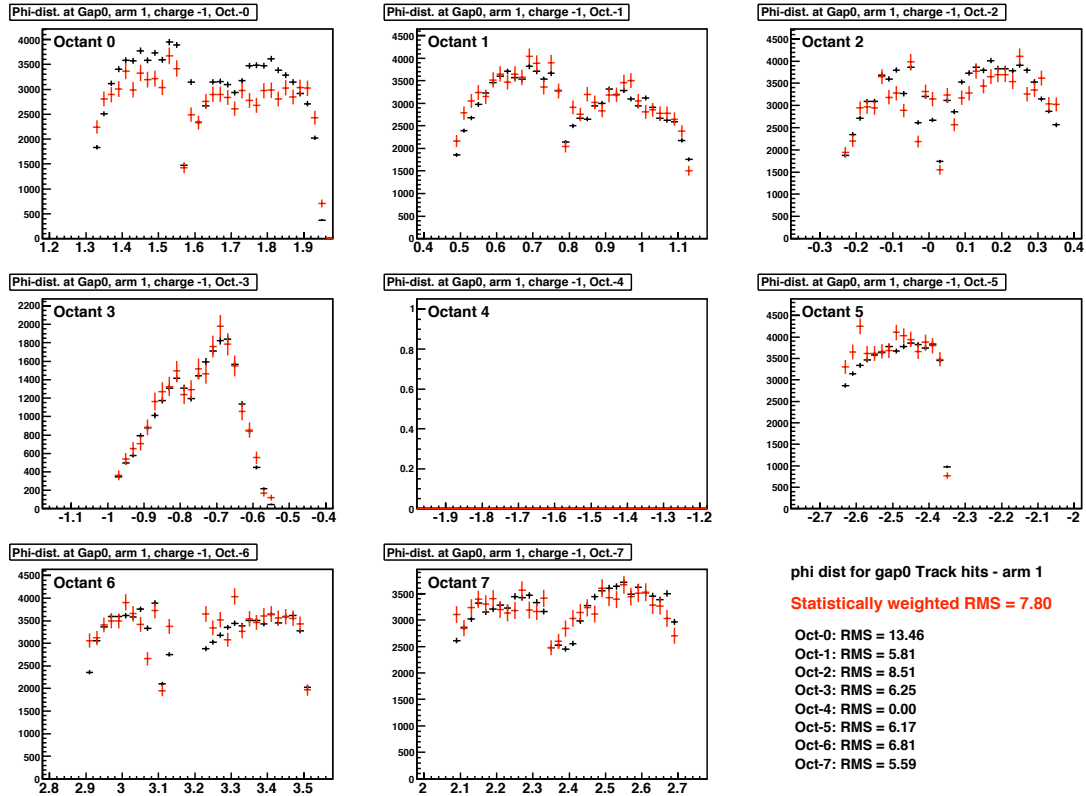


Figure 5.10: North  $\phi$  distributions for data and MC using MuID Gap 0  $x,y$  hit positions. Black points are data and red points are simulation.

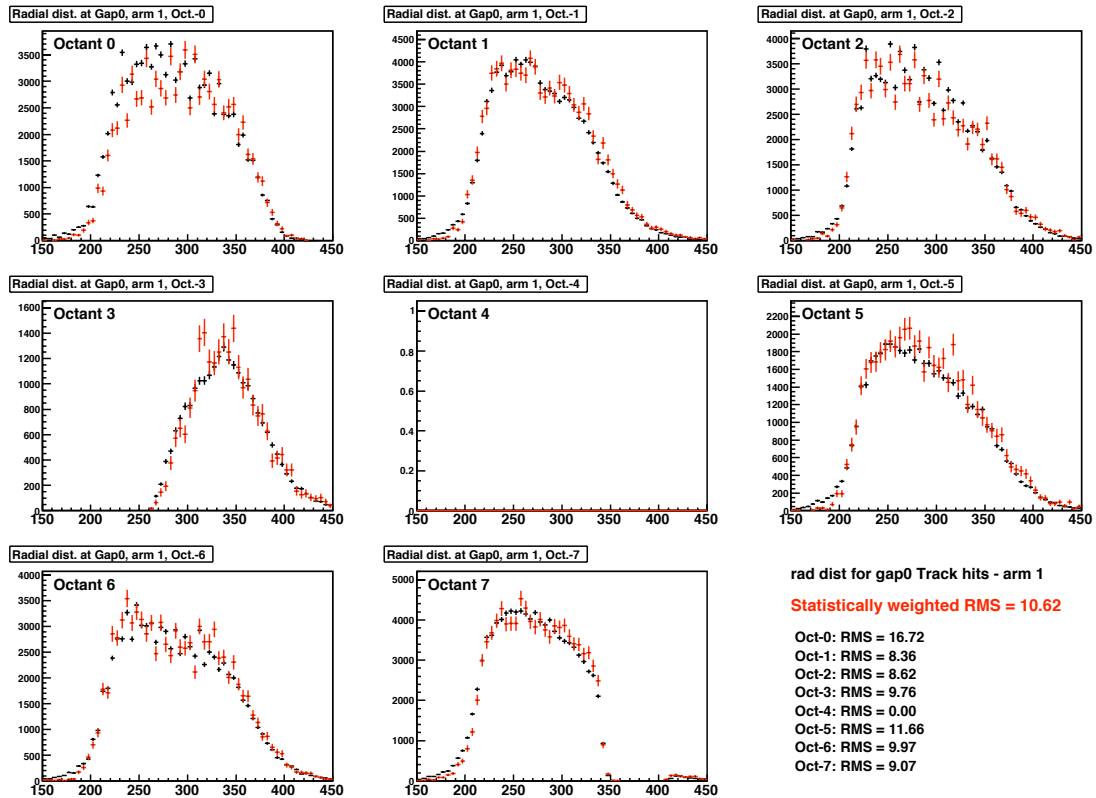


Figure 5.11: North arm radial distance distributions for data and MC using MuID Gap 0  $x,y$  hit positions. Black points are data and red points are simulation.

momentum to continue to penetrate a significant distance into the absorber. This effect invalidates the assumption of extrapolating the hadron yield to Gap 4 assuming exponential absorption based on observed Gap 2 and Gap 3 stopped hadron yields.

### 5.3.1 Method for “tuning” the hadron cocktail to match data

The hadron cocktail originates as a predetermined admixture of single pions and kaons with the prescribed NLO  $p_T$  spectra. These input hadrons are propagated through the entire GEANT/ response/ reconstruction chain for a particular hadron interaction package cross section setting. The resulting reconstructed hadron tracks are then compared to data and are “tuned” to maximally match the stopped hadron  $p_T$  spectrum in the next-to-last MuID gap, Gap 3, as in Figure 5.12. This is accomplished by adjusting both the overall normalization factor and the initial hadron  $p_T$  spectrum per  $p_T$  bin. In essence, the input or “thrown”  $p_T$  shape is adjusted for each hadron package cross section setting so that the reconstructed hadron cocktail match data at Gap 3. Once the hadron cocktail is tuned at Gap 3, the extent of the hadron cocktail match to data is examined in:

1. the preceding MuID gap, Gap 2. A  $\chi^2/\text{NDF}$  is calculated between data and hadron cocktail.
2. the MuID Gap 4  $z$ -vertex distribution. A point-to-point  $\chi^2/\text{NDF}$  is calculated for each  $z$ -point (10 per  $p_T$  bin) between data and hadron cocktail using the mean  $z$  difference between data and hadron cocktail in each  $p_T$  bin.
3. the adjusted input hadron  $p_T$  spectra are compared to existing measurements at mid and far-forward rapidity to ensure that the input hadron spectra falls within expected global values.

Additional details of these items are discussed in the following sub-sections.

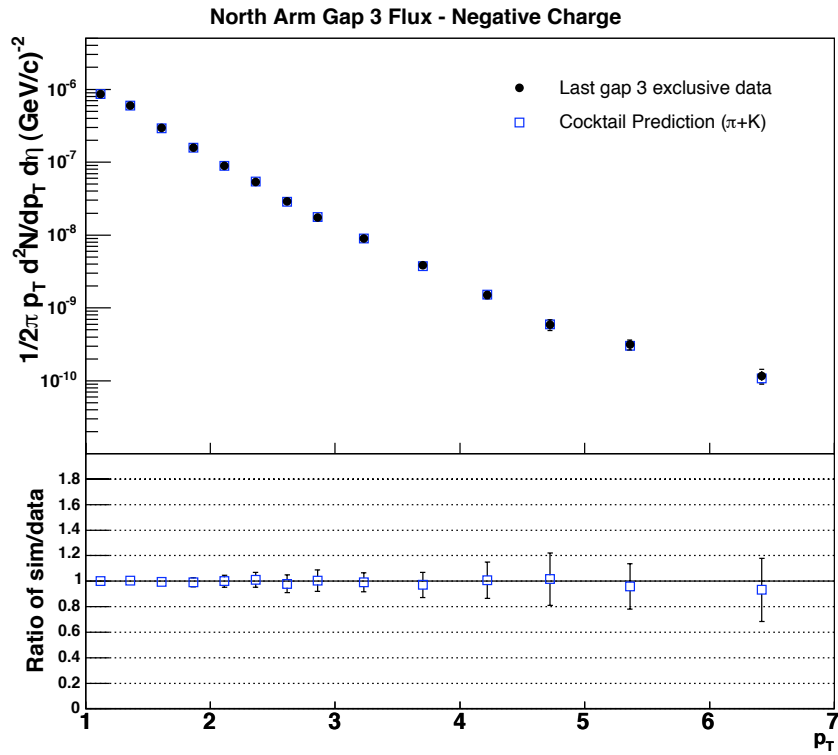


Figure 5.12: MuID Gap 3 hadron cocktail  $p_T$  spectra normalized to data yield. The upper plot shows the uncorrected  $p_T$  yield of data in the north MuID Gap 3 (black points) as well as the hadron cocktail prediction at Gap 3 after normalization to data.

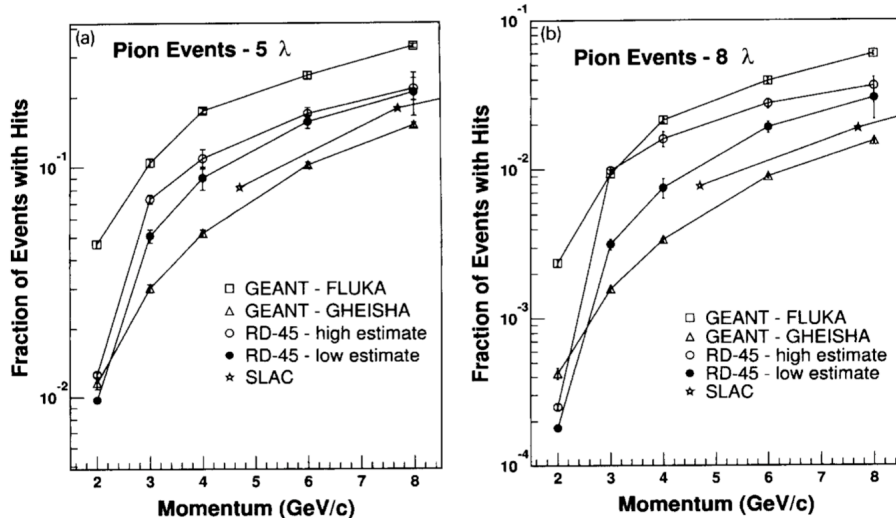


Figure 5.13: FLUKA and GHEISHA hadron packages compared to RD10-45 data [42]. See text for discussion.

### 5.3.2 Generating hadron cocktail input

Formation of a hadron cocktail background estimate faces two immediate problems: 1) the hadronic backgrounds yields are not directly measured in the muon arm rapidity window, 2) the inability of the available GEANT hadron shower packages to properly predict the passage of hadrons through large amounts of steel, with predictions for the muon arm ultimately differing by a factor of 2.

Ultimately, the hadron cocktail is matched to observed yields in the MuID Gap 2, 3, and 4. The simplest approach for an input spectra would be to generate a spectra flat in  $p_T$  and proceed with the re-weighting scheme to match to data. A large amount of steel exists to simulate, and only  $\sim 1$  per 1000 thrown tracks survives. This introduces a large inefficiency in any large scale hadron simulation project. Before this analysis, the muon arms were plagued by a particular background source, hadrons decaying inside the MuTr volume. This background is due primarily to particles which have lower momentum and decay with the daughter particle carrying through to the last gap of the MuID. The kink in the particle trajectory can cause the particle's momentum to be improperly determined. The particle spectra in the muon arms is approximately exponential (more like a power-law) where a drop of approximately five orders of magnitude from a  $p_T$  of 1.0 to 5.0 are observed. Decays from high  $p_T$  particles decaying in the MuTr are suppressed by several orders of magnitude relative

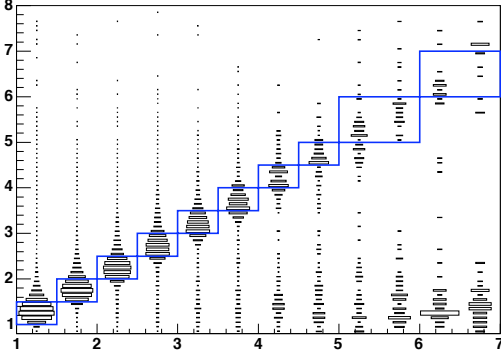


Figure 5.14: Thrown vs. reconstructed  $p_T$  for the hadron cocktail spectra weighted by  $p_T$ , with  $p\delta\theta$  cut NOT applied. A large number of tracks are shown to reconstruct at high  $p_T$  originating from particles with low original  $p_T$ .

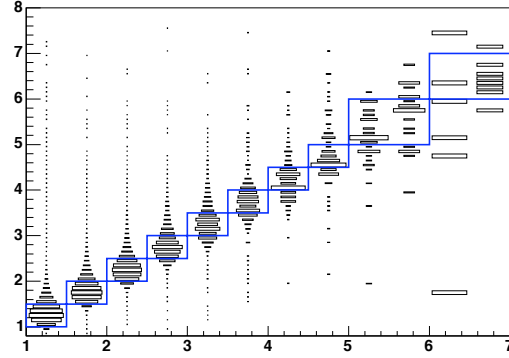


Figure 5.15: Thrown vs. reconstructed  $p_T$  for the hadron cocktail spectra weighted by  $p_T$ , with  $p\delta\theta$  cut applied. The large number of improperly reconstructed tracks high  $p_T$  are eliminated by the  $p\delta\theta$  cut.

to low  $p_T$  particles. However the decay of low  $p_T$  particles that are improperly assigned a larger momentum will have a large effect on the total number of tracks assigned to high  $p_T$  bins.

In order for the hadron cocktail to properly reproduce all physical sources of background in the muon arm, it is necessary to generate a sufficient number of low  $p_T$  hadron cocktail particles which have a chance of decaying and being incorrectly reconstructed. As shown in Figure 5.15, the effect of newly developed analysis cuts (primarily  $p\delta\theta$  and  $\delta Z$ ) has substantially reduced this background fraction in higher  $p_T$  bins to the point where it is justified to “cheat” a little to throw flatter spectra than the true power-law shape observed for pions and kaons. An additional weight of  $p_T^3$  allows us to generate sufficient high  $p_T$  tracks from the hadron cocktail while at the same time still producing orders of magnitude more of the low  $p_T$  particles needed to realistic produce backgrounds in the muon arm.

However, several difficulties exist in the characterization of the hadron flux into the muon arm. No measurements exist of identified or unidentified hadron spectra for  $p+p$  collisions at a rapidity of  $\langle y \rangle = 1.7$ . While the measured rapidity evolution of the  $p_T$  spectra is not known, several models exist which provide a description of hadron spectra at  $\langle y \rangle = 1.7$ . An NLO pQCD prediction has been obtained for the entire muon arm acceptance  $1.0 \leq |\eta| \leq 2.4$  and is used as input for the hadron cocktail [112].

An untuned hadron cocktail consists of the following components:

1. pion and kaon yields drawn from a NLO pQCD prediction
2. full GEANT simulation that takes the appropriate mix of  $\pi$ 's and K's from the theoretical prediction
3. full response and muon software reconstruction (optionally embedded in min bias data)

GEANT input particle distributions are generated by sampling spline fits of the NLO yields of pions and kaons. The NLO pion and kaon invariant cross sections are converted to particle yields in the following way:

$$\frac{d^2 N}{\Delta\eta \Delta p_T} \approx A_{norm} \cdot 2\pi \langle p_T \rangle \cdot E \frac{d^3 \sigma}{dp^3} \quad (5.2)$$

where  $A_{norm}$  is the constant cross section-to-yield conversion. Since it is only the shape of the hadron spectra that is used to generate input particles, the actual value of  $A_{norm}$  is irrelevant in this context. Theoretical predictions are provided for seven pseudo-rapidity bins, each with a width of 0.2 in  $\eta$  bins.

There is an inherent systematic uncertainty associated with the choice of K/ $\pi$  ratio used for the cocktail. The two obvious choices to use is that measured by PHENIX in the central arms. Another option is to use the ratio as reported by the NLO Vogelsang calculations for pions and kaons at  $\langle y \rangle = 1.7$ . Figure 5.16 shows both the PHENIX and the NLO K/ $\pi$  ratios. Figure 5.17 shows the K/ $\pi$  ratio from the NLO calculation as a function of  $p_T$ . The ratios for for each slice of pseudo-rapidity (each 0.2 units of  $\eta$  wide) for which the NLO calculation was made. The ratio's asymptote decreases as the rapidity slice increases. The NLO ratio is about 50% lower than the K/ $\pi$  ratio measured by PHENIX.

### **The role of the hadron interaction packages**

The implementation of a scale factor for the steel cross section, allows the ability to “tune” both FLUKA and GHEISHA such that each package's hadron yields maximally match the observed yields in three gaps of the MuID, Gaps 2, 3 and 4. Since there is  $\sim 10 \lambda_I$  of steel in the flight path from the collision vertex to the deepest gap of the MuID, the use of a full GEANT based monte carlo (MC) “hadron cocktail” with parameterized hadron input is

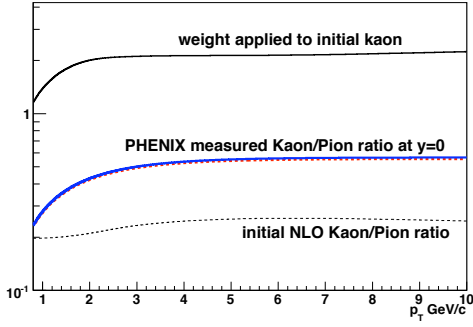


Figure 5.16:  $K/\pi$  values obtained from NLO calculation and the weights required to increase the  $K/\pi$  ratio to that observed by PHENIX at  $y=0$  [112].

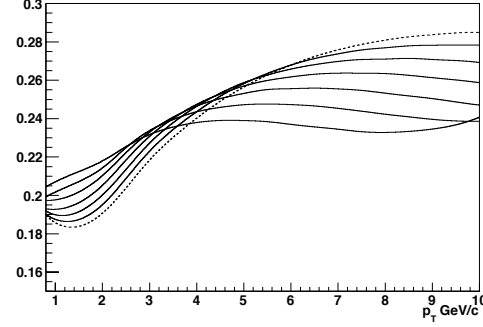


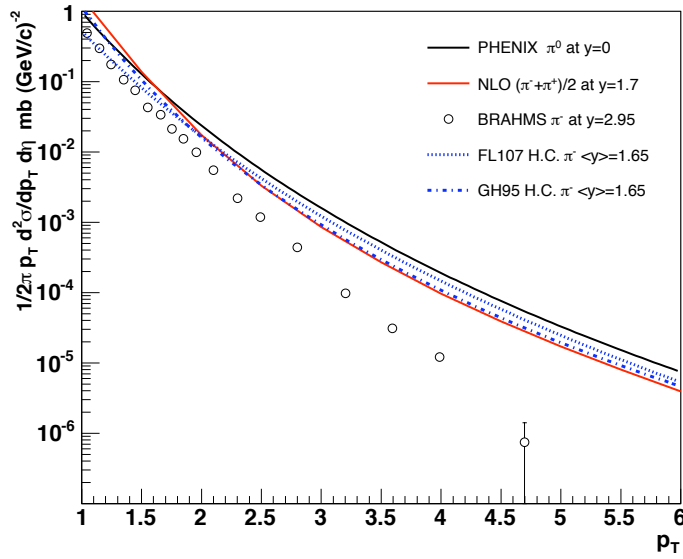
Figure 5.17:  $K/\pi$  ratios as a function of  $p_T$  for  $\eta$  from 1.1 (dashed line) to 2.3 [112]. These ratios are below that observed in PHENIX  $y=0$  measurements.

necessarily dependent on the specific hadron interaction package's ability to accurately propagate the hadrons through steel. Unfortunately, it has already been established that neither hadronic interaction package available in GEANT, FLUKA and GHEISHA, properly estimate hadronic interactions, with differences of a factor of two observed for both packages [42].

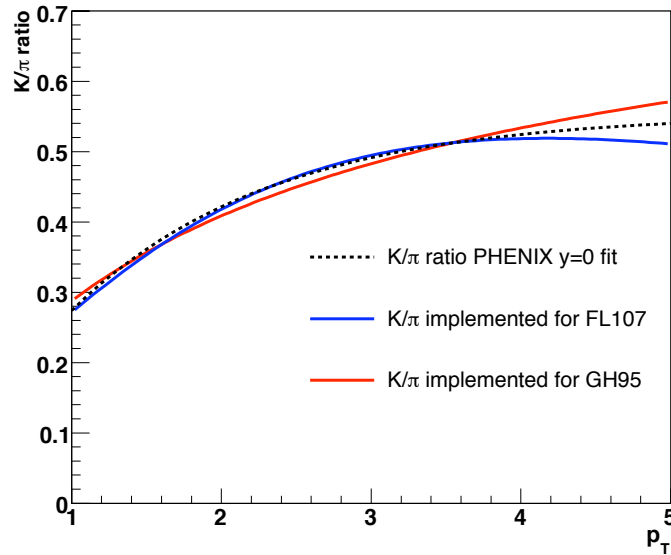
In terms of just the general output of the hadron cocktail, two primary differences are observed concerning FLUKA and GHEISHA. All comparisons made here are for equivalent simulation inputs. Figure 5.18 compares some of the properties of the hadron cocktail to global data measurements.

1. The overall flux of particles propagated for GHEISHA is approximately half of that observed for FLUKA. FLUKA tends to reproduce the particle flux measured in the MuID better than that of GHEISHA. Somewhat at odds with this observation, GHEISHA allows relatively more low  $p_T$  particles below a  $p_T$  of 1.5 GeV/c. This gives the GHEISHA  $p_T$  spectra a peak at this lowest  $p_T$ .
2. GHEISHA tends to allow relatively more kaons than pions through to Gap 4 of the MuID. This is observable in  $z$ -vertex distributions where for identical input  $K/\pi$  ratios, the GHEISHA Gap 4 kaon distributions exceed those of pions by 10 to 20 % (with the amount of kaons increasing slowly with  $p_T$ ), whereas in FLUKA the number of pions and kaons are approximately equal for all  $p_T$ .

The differences are dealt with in the analysis by adjusting the overall GEANT hadron interaction cross section of steel separately for FLUKA and GHEISHA. Changes for the steel



(a) Comparison of hadron cocktail input spectra to BRAHMS and PHENIX measurements. The hadron cocktail (dashed lines) falls in the expected region between the  $y=0$  and  $y=3$  measurements. The same is true for the kaon spectra.



(b) Comparison of  $K/\pi$  ratios for fits to hadron cocktail input ratio and PHENIX  $y=0$  measurement.

Figure 5.18: Pion yields and  $K/\pi$  ratio for hadron cocktail and data determined from PHENIX data (dashed) and two different hadron cocktails (FLUKA 107 and GHEISHA 95).

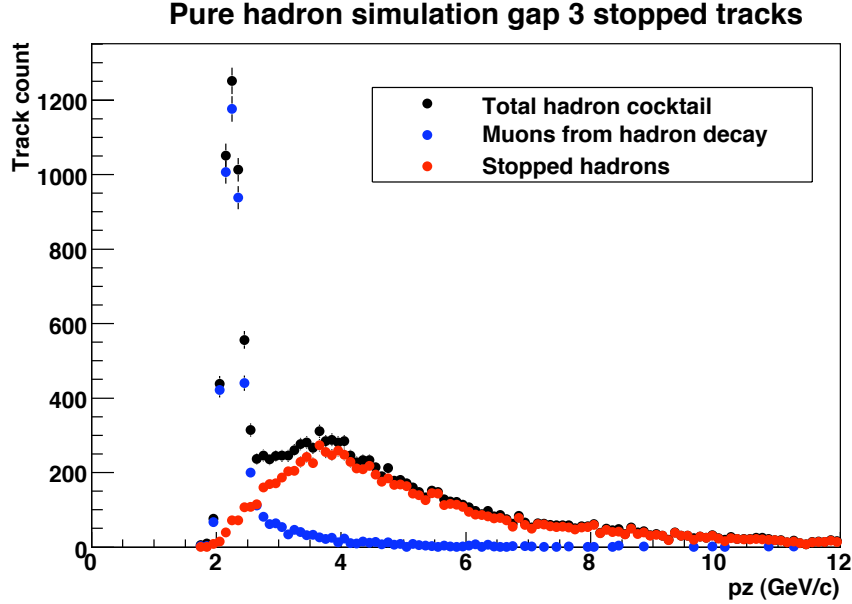


Figure 5.19: Distribution of particles as a function of longitudinal momentum ( $p_z$ ) stopping in a shallow MuID gap (Gap 3).

cross section on the order of 5% can change the overall response of the interaction package by much more than 5%. This is a key step in matching the cocktail for both FLUKA and GHEISHA to data. This subject is discussed in section 5.3.2.

### Hadron cocktail and data yields in Gap 2

The distribution of particles stopping in a shallow MuID gap, such as in figure 5.19, is comprised of those particles ranging out (MIP-like peak) as well as those particles that undergo a strong interaction (the tail). These particles show a characteristic “stopping peak” when plotted as a function of total momentum (or longitudinal momentum). The broad tail of these distributions is comprised of hadrons that have not been reconstructed to the next gap, suggesting a nuclear interaction in the next absorber layer. Hadrons can then be preferentially selected by imposing a cut after the stopping peak and retaining the tracks in the distribution’s tail.

After implementing full acceptance and track quality cuts, including a  $p_z$  cut for Gap 2 and 3 to select stopped hadrons, and after normalizing the yields of the hadron cocktail to data in Gap 3, the Gap 2 hadron cocktail  $p_T$  spectra is compared to that of data (figure 5.20).

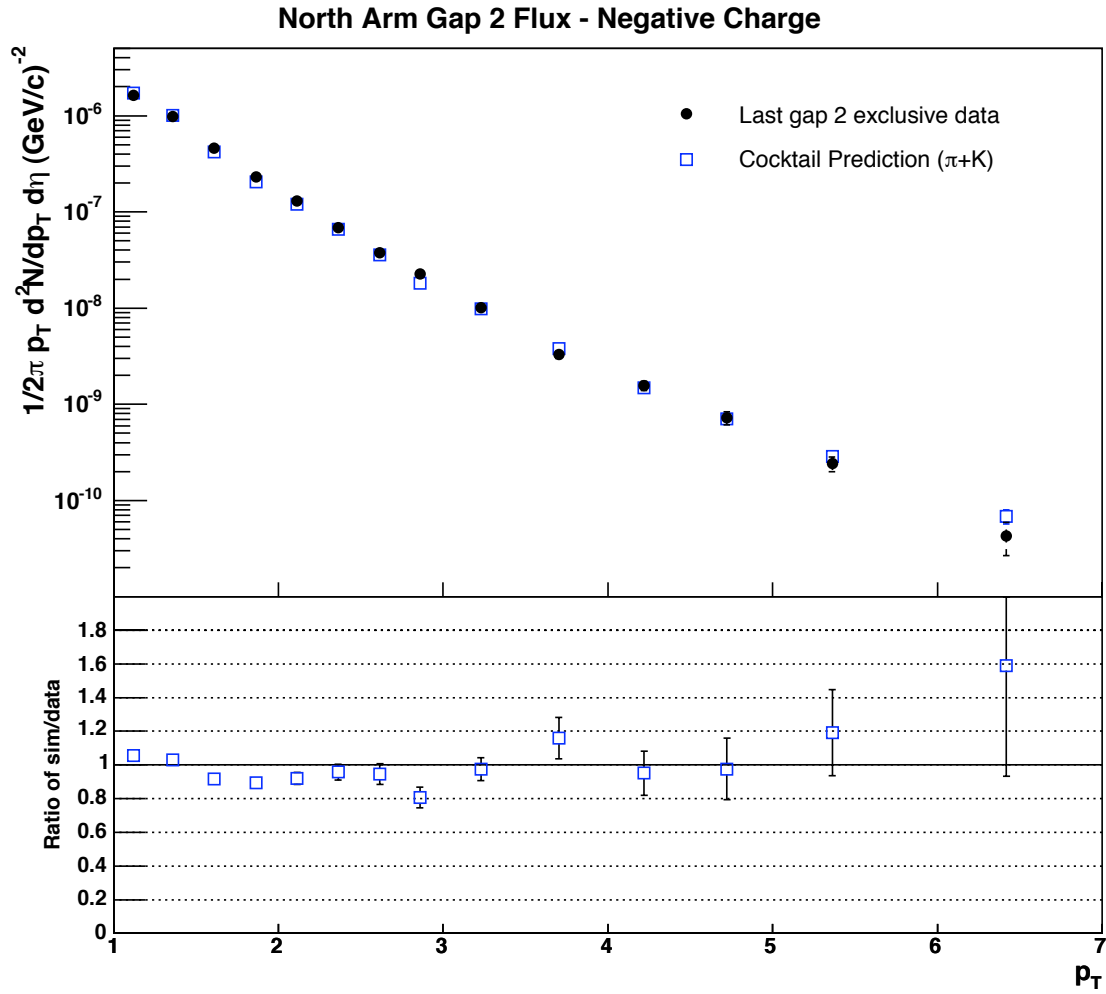


Figure 5.20: MuID Gap 2  $p_T$  spectra for hadron cocktail (blue squares) and data (black circles) for a particular cocktail package after normalizing yields at Gap 3.

## **$z$ -vertex yields in Gap 4**

After normalization of the yield of the hadron cocktail to data in Gap 3 as a function of  $p_T$ , Figure 5.21 shows the subsequent Gap 4  $z$ -vertex distribution of the hadron cocktail and data, for which each panel is an individual  $p_T$  bin. The black points are the inclusive data, of which the heavy flavor signal is a component. The blue points show the total estimate of the hadron cocktail, which is a sum of pion and kaon source particle components. The Gap 4 yield of particles originating from pions is roughly equal to that of kaons, despite the fact that kaons constitute less far less than half of the total input particles. The excess of data over hadron cocktail is an indication of the presence of the single muon signal.

## **Modifying the steel cross section in GEANT**

The previous sections have described the basic approach for taking a particular hadron cocktail version and tuning the input hadron  $p_T$  spectra in Gap 3 to maximize the match to observed data distributions in Gaps 2 and 4. As discussed in section 5.3.2, neither default hadron shower code (FLUKA or GHEISHA) do an adequate job of matching the particle yields observed in the MuID arms. An approach is taken to modify the material interaction cross sections for both FLUKA and GHEISHA to explore to what extent MC can be made to better match yields observed in data. The final  $\chi^2/\text{NDF}$  analysis of an assortment of hadron packages with different settings is described in section 5.6.2.

The CERN libraries (a.k.a. `cernlibs`) used at the GEANT simulation step are modified (Appendix F) to allow a hadron interaction “switch” at the GEANT interface command. The hadron cross section of material, by far and away dominated by steel in the muon arms, are scaled absolutely by percentage by the “switch” command. For example, “switch 9700” would scale the cross section by 0.97 from the default value of 1.0.

A single cocktail data set corresponds to a single hadron interaction cross section setting for a given hadron package. This analysis currently uses seven such cocktail data sets, which are listed in Table 5.1. Figure 5.22 compares the different hadron package yields after normalization to Gap 3 data. A variation of approximately  $\pm 20\%$  is observed for all packages considered in Table 5.1. Not all hadron packages predictions are used to extract the signal. The final process for determining which packages are used is described in Section 5.6 using the calculations described in the next section.

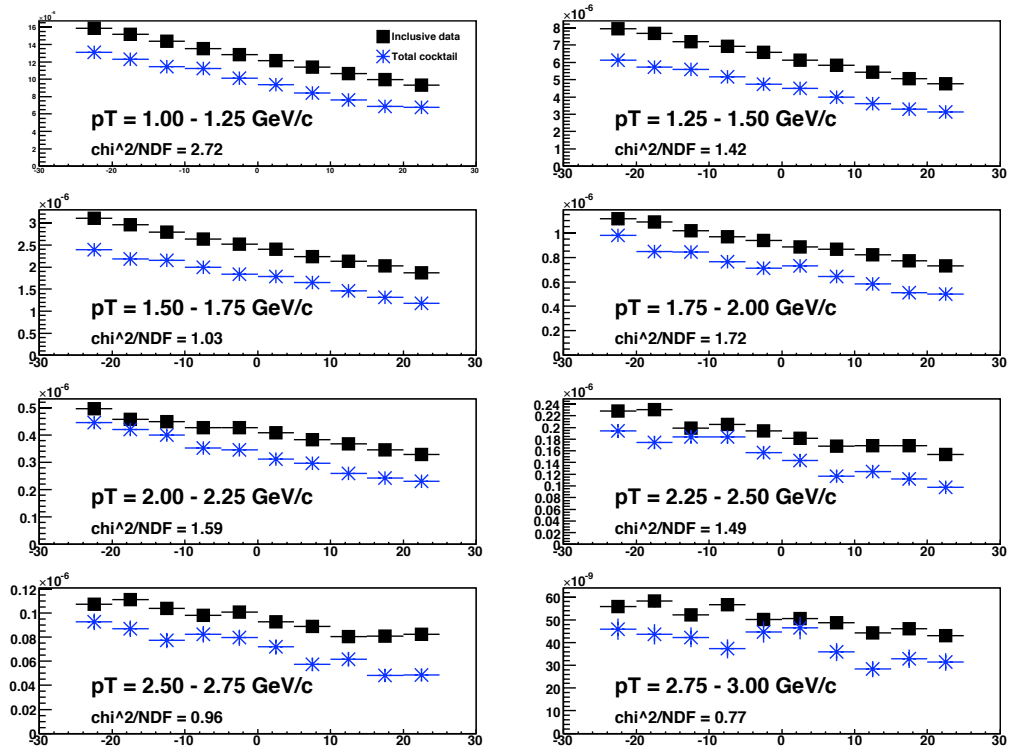


Figure 5.21: MuID Gap 4  $z$ -vertex spectra comparison of hadron cocktail and data.

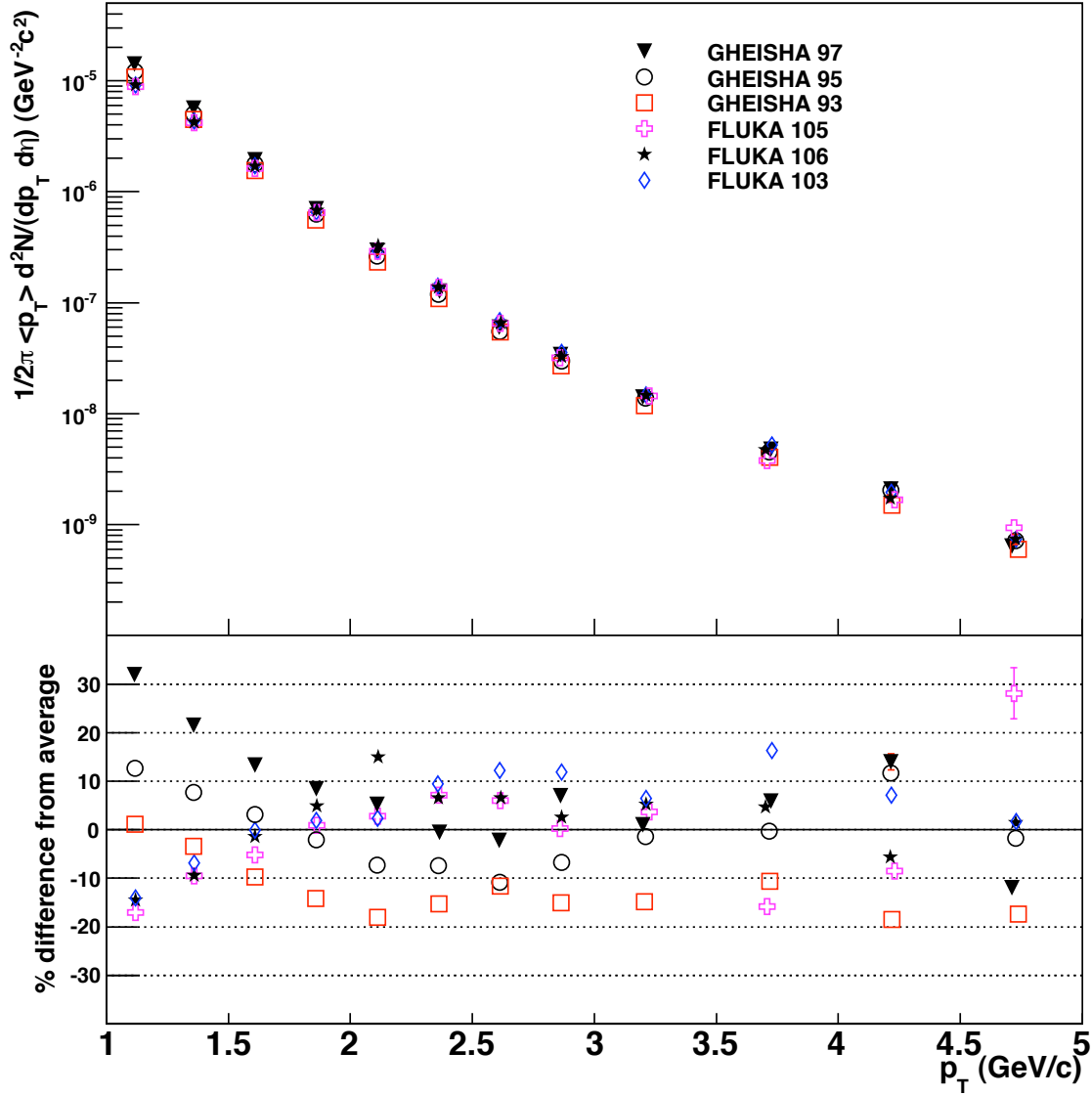


Figure 5.22: Comparisons of different hadron cocktail package predictions as a function of  $p_T$ . The upper panel shows the invariant yields. The lower panel compares the ratio of each package to the mean of all packages. Strong variation at low  $p_T$  in the yields between the different packages is observed.

Table 5.1: Hadron package and steel cross section settings. The numbers indicate the scale value in percent of the hadron interaction cross section (100 is default). Increasing (decreasing) the FLUKA (GHEISHA) cross section reduces (increases) the resulting number of hadrons relative to the default setting.

FLUKA	GHEISHA
107	97
106	95
105	93
103	

### 5.3.3 $\chi^2/\text{NDF}$ evaluation of the hadron cocktail

After forcing the match of data and hadron cocktail gap 3  $p_T$  distributions, the extent of the hadron package's ability to match both the Gap 2  $p_T$  and Gap 4  $z$ -vertex distributions is determined by calculating a  $\chi^2/\text{NDF}$  value for both distributions. The Gap 2  $\chi^2$  values are calculated for each  $p_T$  point according to the following formula:

$$\chi_{\text{Gap } 2}^2(p_T) = \left( \frac{N^{\text{cocktail}}(p_T) - N^{\text{data}}(p_T)}{\sqrt{(\sigma_{\text{Gap } 2}^{\text{cocktail}})^2 + \sigma_{\text{Gap } 3 \text{ match}}^2 + (\sigma_{\text{Gap } 2}^{\text{data}})^2}} \right)^2, \quad (5.3)$$

where  $N^{\text{cocktail}}$  and  $N^{\text{data}}$  are the minimum bias normalized invariant yield  $p_T$  distributions with the associated statistical uncertainties denoted by  $\sigma$ 's. A  $\chi^2/\text{NDF}$  value is calculated for each  $p_T$  bin using the Gap 4  $z$ -vertex distributions. A point-to-point  $\chi^2/\text{NDF}$  determined from the  $z$ -vertex distributions relative to the mean difference between the data and cocktail points is calculating using the following equation:

$$\chi_{\text{Gap } 4}^2(p_T) = \sum_i^{N \text{ } z\text{-bin}} \left( \frac{\delta z_i - \overline{\delta z_i}}{\sqrt{(\sigma_{\delta z_i}^2 + \sigma_{\overline{\delta z_i}}^2)}} \right)^2 \quad (5.4)$$

where the sum is over  $i$   $z$ -bins per  $p_T$  bin,  $\delta z_i$  is the difference between data and cocktail for the  $i^{\text{th}}$  bin, and  $\overline{\delta z_i}$  is the mean difference between the data and cocktail for all  $z$  bins in a single  $p_T$  bin. It should be noted that  $\sigma_{\overline{\delta z_i}} \ll \sigma_{\delta z_i}$  in the denominator of Equation 5.4, so the inclusion of  $\overline{\delta z_i}$  has a negligible effect on the calculated  $\chi^2$  values.

The Gap 2 and Gap 4  $\chi^2/\text{NDF}$  values are summed to determine which package provides

the best combined Gap 2 and Gap 4 match to data. The final determination of hadron package background estimates used to determine the heavy flavor single muon yield is described in Section 5.6.2.

## 5.4 *Non-hadron cocktail high $p_T$ background estimate*

### The observation and likely origin of a high $p_T$ single track background

This section describes a secondary background component other than the primary hadron cocktail that is used in the determination of the heavy flavor single muon yield. The  $p\delta\theta$  distributions (Section 5.2.5) are used as an indicator of track purity since the distribution of the product of the multiple scattering angle  $\delta\theta$  and the momentum  $p$  should have a constant width for muons. In Figure 5.23 the square (red) points in show the “raw”  $p\delta\theta$  distributions binned in  $p_T$ . The clear multiple scattering peak observed at low  $p_T$  expected to remain constant for all  $p_T$  gives way to an increasing fraction of spurious  $p\delta\theta$  values, defined to be those tracks with  $p\delta\theta > 0.2$ . Importantly, the hadron cocktail, which is intended to be the primary estimator of backgrounds in the analysis, fails to reproduce these raw  $p\delta\theta$  distributions. In the initial phase of this analysis, the failure of the hadron cocktail to reproduce the square (red) distribution in Figure 5.23 cast strong doubts on the viability of the analysis for  $p_T$ 's above about 4.0 GeV/c which exhibit significant anomalous  $p\delta\theta$  behavior.

Examination of these high  $p_T$ , high  $p\delta\theta$  tracks eventually revealed a large discrepancy between the event collision vertex measured by the BBC and the event vertex returned by the muon track finding algorithm (the so-called refit Z). Labeling this difference “ $\delta Z$ ” (Section 5.2.5), its distribution is plotted in Figure 5.24 and is characterized by a gaussian peak and non-gaussian tails.

By requiring  $|\delta Z| < 2$  cm for muon track candidates the strong removal of tracks with large  $p\delta\theta$  values is observed and can be seen in in Figure 5.23 by the change in distributions from the squares (red) to the closed circles (black). While it is perhaps not surprising that requiring a common vertex between that measured by the PHENIX vertex detector and that reconstructed, this quantity was not explicitly checked in single muon analyses prior to this discovery. The di-muon analyses that constitute the largest muon analysis effort in PHENIX do require a two-track  $\chi^2$  vertex matching requirement. During the course of this work a single track  $\chi^2$  vertex match was implemented in the tracking algorithm but is not used in

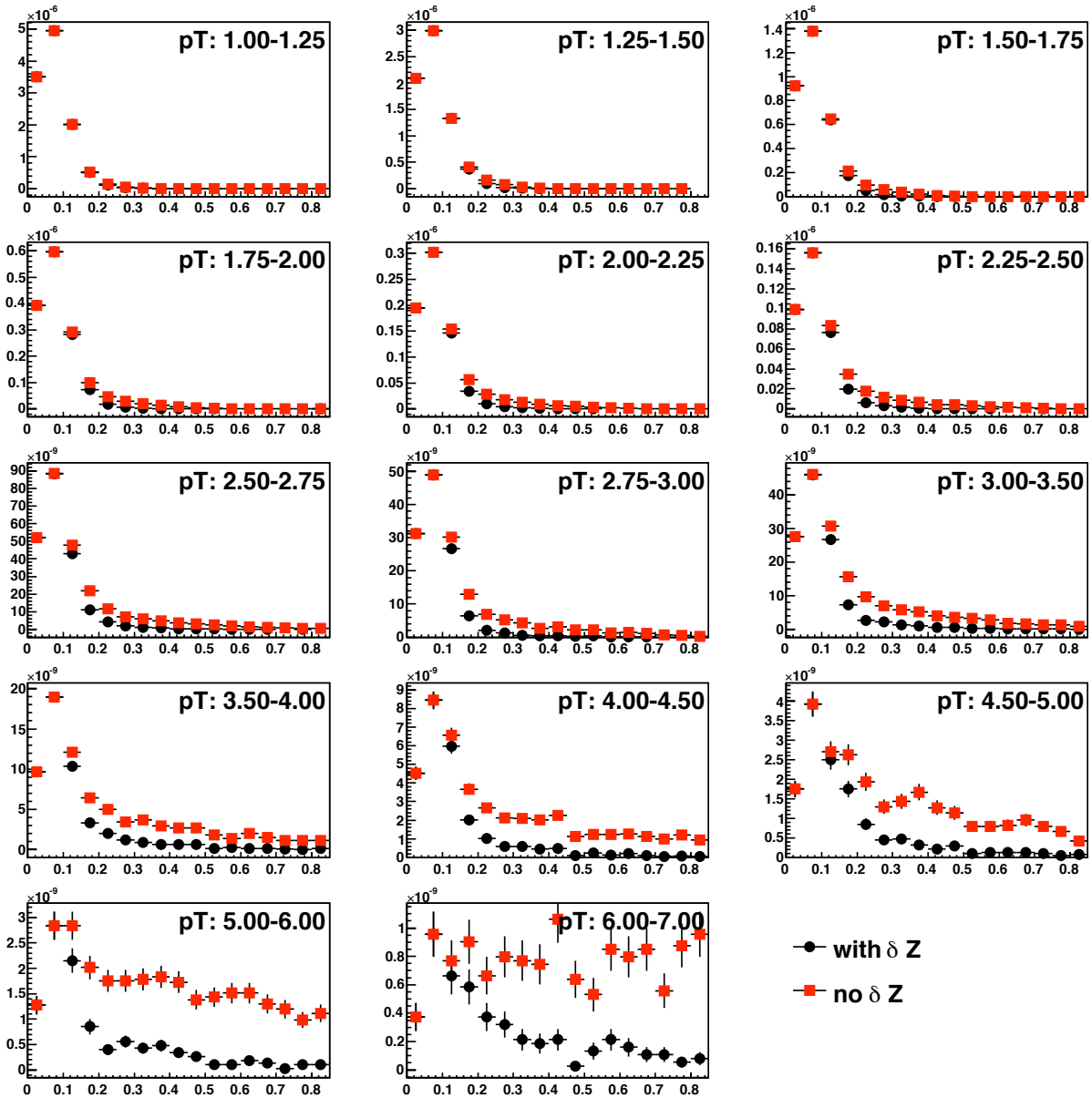


Figure 5.23: Distributions of event normalized  $p\delta\theta$  for inclusive data tracks before and after  $\delta z$  cut. The horizontal axes correspond to the  $p\delta\theta$  variable of units GeV·radians. Particles with  $p\delta\theta > 0.2$  are rejected in this analysis.

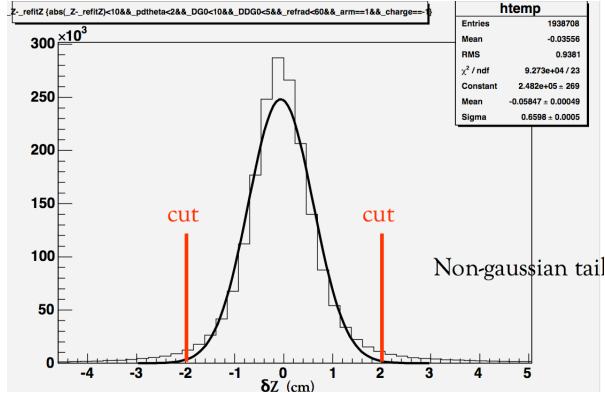


Figure 5.24: Distribution of  $\delta z$  for muon candidate tracks for all  $p_T$ . Tracks outside the labeled cutoff are highly correlated with improperly reconstructed tracks, the fraction of which increases with increasing  $p_T$ .

this work. Future single muon analyses will benefit from this additional information.

The requirement of  $|\delta Z| < 2$  cm is actually a rather crude matching requirement. This is due to the inherent resolution of the BBC in  $p+p$  collisions, which is known to have a resolution of 2 cm in  $p+p$  collisions. After the tracking algorithm completes the track reconstruction in the MuID and MuTr, the track is projected from the shallowest MuTr station (Station 1) through the initial 79 cm of absorber material to the vertex. This projection is crucial in that it takes the momentum determined in the MuTr after the track has passed through initial absorber material and estimates the track’s original  $z$ -vertex and momentum *at this vertex*. It is the momentum from the tracking algorithm that is used in the analysis. If the projected track position is off by more than 2 cm from the  $z$ -vertex measured by the BBC (with an inherent resolution of 2 cm), the tracks exhibit non-physical  $p\delta\theta$  values likely due to incorrect momentum assigned by the tracking algorithm.

The incorrect momentum assignment by the muon tracking algorithm is likely due to the phenomenon of high “local occupancy”. High local occupancy in this context is illustrated in Figure 5.25. This figure shows a highly focused and selective view of the MuTr detector from the muon event display. The individual trapezoids joined on one side are half-octants that form a single octant. Each octant is taken from a MuTr station, with Station 1 on the left, Station 2 the middle, and Station 3 on the right. The (blue) strips in each half-octant correspond to fired cathode strips, and the barely visible (pink) circles represent the MuTr stubs that are used in trying to match tracks within the MuTr stations. The (red) line

crossing through all octants is the final reconstructed MuTr track. The large number of fired cathode strips and the subsequent large number of stubs in Stations 1 and 2 are viewed in a majority of the tracks examined that possess large  $p\delta\theta$  and  $\delta Z$  values.

A full examination of all events that possess large  $p\delta\theta$  and  $\delta Z$  values such as in the (red) square distribution in Figure 5.23 is prohibited by size of the data scale. These events are primarily seen at high  $p_T$  and cumulatively represent several hundred tracks out of a pool of several million. Moreover, these tracks are scattered across the entire data set, with on average no more than one such event per raw data file. A full study of these events with fuller detector information, which is significantly larger in size than the condensed data format used for the analysis, involves access to some large fraction of the total  $\sim 250$  TB of data. It would require a reanalysis of the data which would take several hundred CPU months. Simply put, resolving the issue is not readily accomplished. Alternatively, through painstaking effort, several of these high  $p_T$  events were sifted by hand and viewed in the event display. The strong correspondence between high local occupancy such as in Figure 5.25 and large  $p\delta\theta$  was established. Further study of this issue will be conducted at a latter date to explore possible modification to the tracking algorithm to reduce these aberrant tracks. For the purpose of this analysis, the placement of  $\delta Z$  cuts satisfactorily removes the large  $p\delta\theta$  backgrounds for  $p_T < 5.0$  GeV/c, and the analysis is conducted within this  $p_T$  range. As mentioned, future effort will be placed on extending the analysis for  $p_T > 5.0$  GeV/c.

### **Estimation high $p_T$ background by a two component fit of $p\delta\theta$ distributions**

With the application of the  $\delta z$  cut, the hadron cocktail is highly successful in reproducing  $p\delta\theta$  distributions similar to that observed in data (which is dominated by hadron background). The extent of agreement gradually diminishes as  $p_T$  increases. At  $p_T$  of about 3.0 GeV/c the data begins to exhibit a non-gaussian tail that grows in prominence as  $p_T$  increases. The hadron cocktail also exhibits this non-gaussian tail but to a lesser extent than data.

While the  $p\delta\theta$  cut placed on both the data and hadron cocktail removes the non-gaussian tails which correspond to unphysical tracks. While the correspondence to high local-occupancy and high  $p\delta\theta$  does exist, the exact source of tracks with large  $p\delta\theta$  is not known and therefore can not be strictly eliminated by placing a cut on a particular variable. The phenomena in the data that results in tracks with large  $p\delta\theta$  is not, *a priori* limited to tracks strictly outside of the  $p\delta\theta$  cut implemented in this analysis. Expressing this in terms of the  $p\delta\theta$  distribution

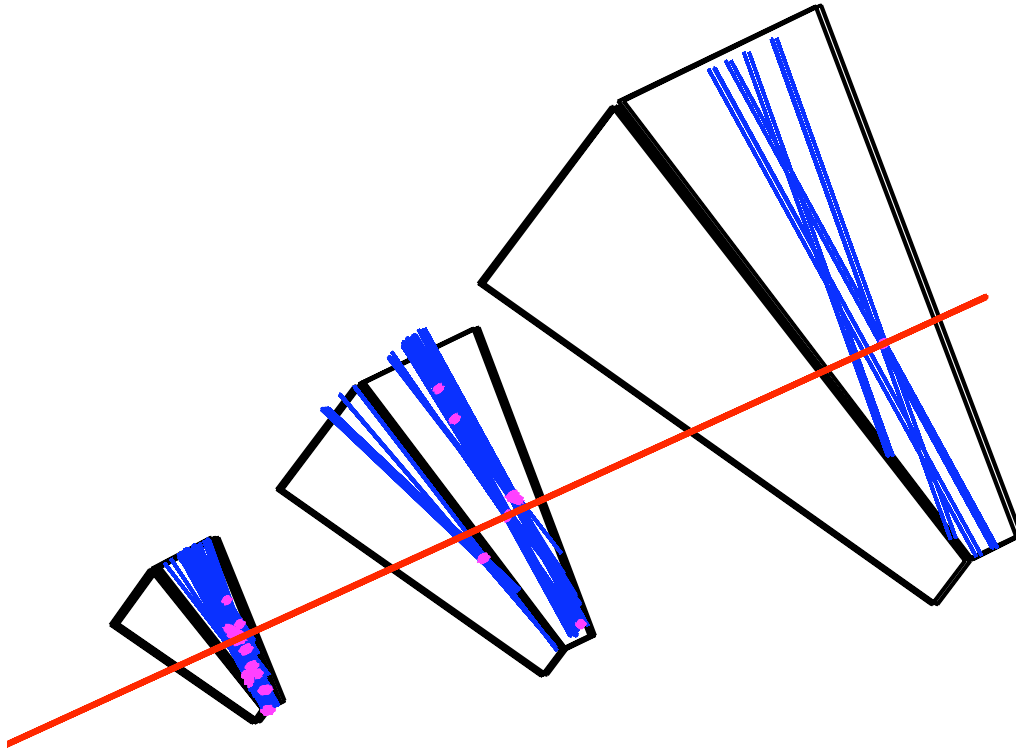


Figure 5.25: High “local” occupancy event. The detector components display are, from left to right, MuTr octants in Stations 1, 2 and 3. The reconstructed  $p_T$  was determined to be 5.8 GeV/c, with a large  $\delta z=8.4$  cm and  $p\delta\theta=0.71$ . A total of 13 stubs are counted in MuTr Station 1.

Table 5.2: Additional two-component background fraction,  $N_{2c}$ .

$p_T$	north arm	south arm	Approx. fraction of inclusive data
1.0-1.25	3.78e-9	1.7e-08	$\ll 0.01$
1.25-1.5	1.23e-8	3.1e-08	$\ll 0.01$
1.5-1.75	3.41e-8	7.1e-09	0.01
1.75-2.0	5.53e-9	4.27e-09	0.01
2.0-2.25	1.09e-8	3.4e-09	0.02
2.25-2.5	2.45e-9	2.3e-09	0.013
2.5-2.75	1.61e-9	1.5e-09	0.016
2.75-3.0	2.07e-9	1.3e-09	0.04
3.0-3.5	1.20e-9	9.6e-10	0.05
3.5-4.0	6.19e-10	3.5e-10	0.08
4.0-4.5	4.73e-10	1.9e-10	0.14
4.5-5.0	2.88e-10	1.4e-10	0.21

itself, it seems likely that the source of the non-gaussian tail “background” tracks will extend inside the  $p\delta\theta$  peak inside the  $p\delta\theta$  cut. Therefore, the extent of this background source, dubbed the “two-component” or  $N_{2c}$ , which is not reproduced by the hadron cocktail, is estimated.

Figure 5.26 shows the  $p\delta\theta$  distribution for data shown in Fig. 5.27 along with a “two component” Gaussian plus linear fit. Exploration of the non-gaussian tail background in the two-dimensional space of  $p\delta\theta$  and  $\delta z$  indicates that the non-gaussian tail likely extends into the peak in a linear fashion. This effect is completely negligible ( $\ll 1\%$ ) until  $p_T > 2.5$  GeV/c. The yield inside the peak is determined by fitting the non-gaussian tail in the region outside the  $p\delta\theta$  cut and extending the linear fit inside the  $p\delta\theta$  cut (Figure. 5.26). The area below the linear fit inside the  $p\delta\theta$  cut region is labeled as a two-component fit background yield,  $N_{2c}$ , and is taken as an additional source of background to be subtracted in the extraction of the single muon yield as described in Equation 5.6 and listed in Table 5.2.

## 5.5 Acceptance $\times$ Efficiency corrections

The measured yield of single muons is subject to finite detector acceptance. The single muon acceptance  $\times$  efficiency correction factor is calculated for the combined reconstruction efficiency, analysis cut efficiency, trigger efficiency, and restricted acceptance. The details of

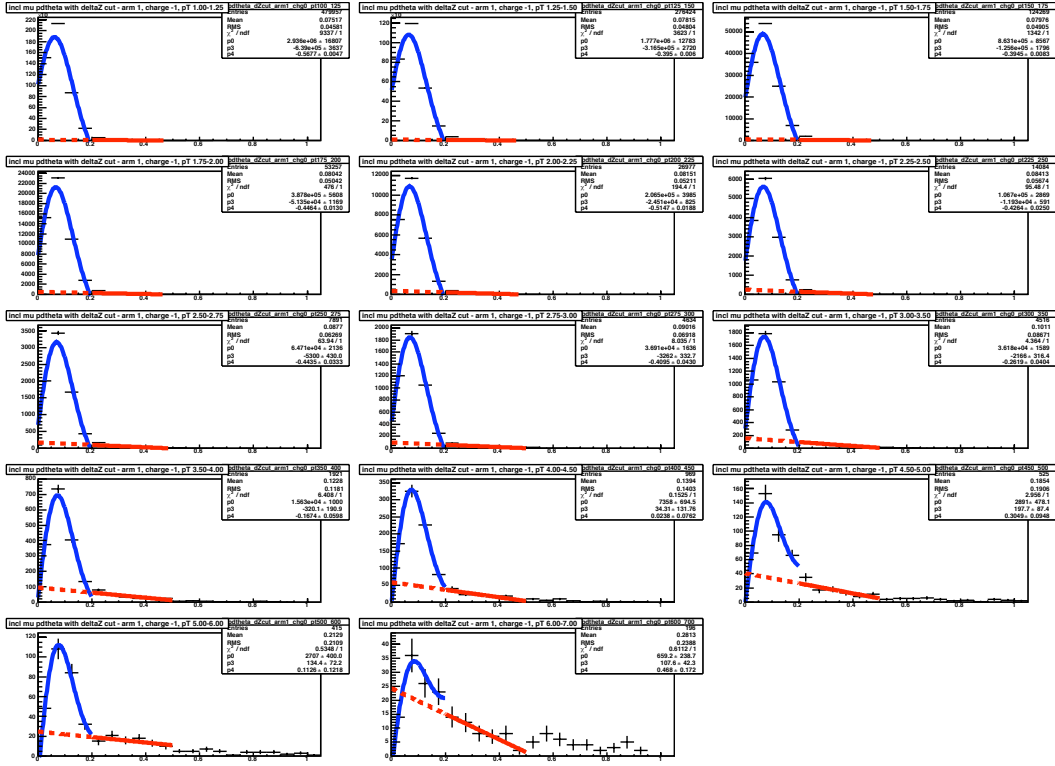


Figure 5.26: Two component fit of  $p\delta\theta$  distributions per  $p_T$  bin. The solid blue line is a gaussian plus linear fit to the  $p\delta\theta$  peak region. The solid red line is a linear fit of the non-gaussian tail, and the dashed red line is a linear extension of the linear fit of the non-gaussian tail. The region inside the peak ( $p\delta\theta < 0.2$  below the dashed red line) is subtracted from both the hadron cocktail and data. This estimated two-component yield,  $N_{2c}$ , is subtracted from data in equation 5.9.

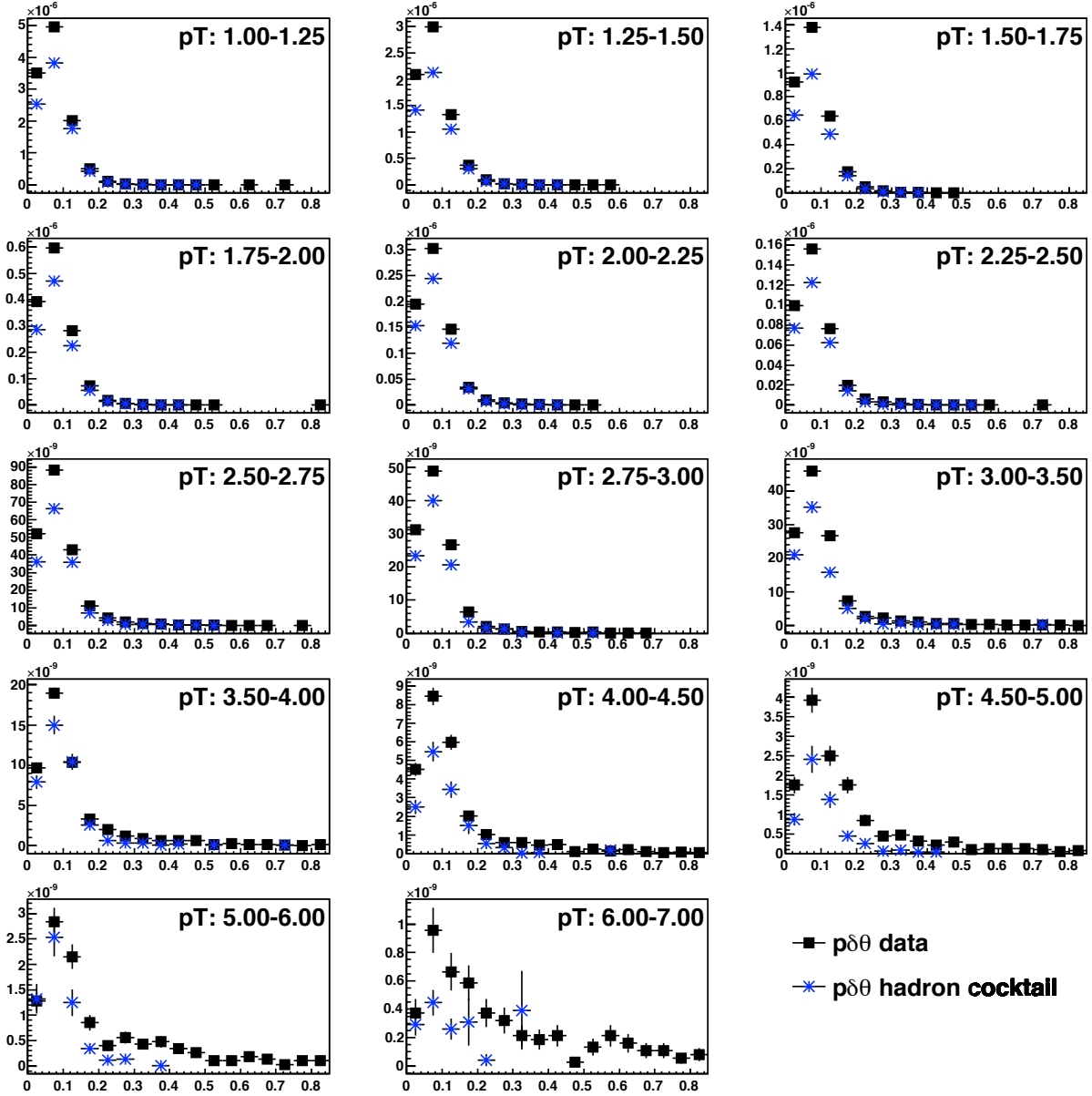


Figure 5.27: Event normalized yields vs.  $p\delta\theta$  distributions for north arm data and hadron cocktail. The excess of data over hadron cocktail inside the  $p\delta\theta$  cut of 0.2 is the single muon yield. The label indicates the  $p_T$  bin in units of GeV/c. The units of  $p\delta\theta$  for the horizontal axis is GeV radians.

the methodology and calculation are now described.

Since the measurement of heavy flavor single muons is accomplished through the statistical subtraction of background quantities, each having potentially different acceptance and efficiencies, care must be taken concerning how and when the acceptance and efficiency corrections are made. The Run 2 single muon analysis subtracted separate corrected quantities of 1) muons from light hadron decay, 2) punch-through hadrons, and 3) “other” background tracks, such as those tracks created from particles decaying inside the muon tracker volume whose decay “kink” leads to a reconstructed track with an inappropriately high  $p_T$ .

In order to subtract individual corrected quantities, it must be known how to separately correct the inclusive, decay, and punch-through components. However, all previous acceptance and efficiency corrections have been applied by using ratios of reconstructed muons to thrown muons. This approach suffers from a few possible problems. Firstly, it is not known to what extent it is valid to use simulated single muons to correct the muons from hadron decay, which dominate the signal at low  $p_T$ , as well as the punch-through hadrons, which begin to dominate the backgrounds at higher  $p_T$ . Secondly, some of track selection cuts have exhibited some degree of  $z$ -vertex dependence. Since ostensibly the  $z$ -vertex distributions of the separate background components are to be extracted by the subtraction of quantities as a function of  $z$ -vertex, the  $z$ -vertex dependence of any track selection criteria would have to be corrected for before any background subtractions can be made.

If instead of subtracting individual corrected background components, a holistic background hadron cocktail can be shown to appropriately account for the different background components in the inclusive track sample, an inclusive uncorrected hadron cocktail could be subtracted from the uncorrected inclusive data sample. The remaining quantity is expected to consist overwhelmingly of single muons from heavy flavor decays. This quantity can then straight forwardly be corrected with single particle muon simulations.

### **Calculated acceptance and efficiencies**

Single muons are simulated over a large portion of the total pseudorapidity acceptance  $\eta$  bin  $1.1 \leq |\eta| \leq 2.1$  for the analyzed region of  $1.4 \leq |\eta| \leq 1.9$  to account for “bleed-over” due to finite detector resolution. Additionally, the simulated muons are thrown according to the

Run 5 BBC  $z$ -vertex event distribution. The acceptance  $\times$  efficiency correction is calculated as a function of  $p_T$  and  $z$ -vertex using;

$$A\epsilon_\mu(p_T, z) = \frac{N_{\text{reconstructed tracks passing cuts}}}{N_{\text{thrown muons in } \eta \text{ window}}} \quad (5.5)$$

Those muons which additionally survive all track selection cuts listed in Section 5.2.5, including kinematic and geometric acceptance, are considered and comprise the “numerator” in Equation 5.5. All muons which were thrown within the  $\eta$  acceptance window are then considered the “denominator.” Since the acceptance  $\times$  efficiency is observed to not depend on the  $z$ -vertex (as expected for muons) as in Figure 5.28, the acceptance  $\times$  efficiency corrections are applied as just a function of  $p_T$ .

As shown in Figure 5.29, muons of realistic (approximately exponentially falling)  $p_T$  spectral shape are sent through the full PHENIX GEANT/ response/ reconstruction chain. Since an exponentially falling muon spectra thwarts obtaining the statistics required for a meaningful acceptance and efficiency at higher  $p_T$ , separate muon simulations of realistic  $p_T$  shape are conducted for each  $p_T$  bin, with the initial  $p_T$  near the low end of the bin being examined. Since the MuTR is estimated to achieve a momentum resolution of  $\sigma_p/p \approx 5\%$  in the studied kinematic range [70], the initial  $p_T$  for each  $p_T$  bin must be thrown with increasingly lower  $p_T$  to account for the bin “bleed over”, those particles with an initial  $p_T$  outside of the  $p_T$  bin being examined. The exponentially falling shaped spectra guarantee that bleed over contributions are substantial from lower  $p_T$  bins. The right column of Table 5.3 shows the range of the thrown realistic single muon  $p_T$  spectra, while the left column shows the  $p_T$  bin for which the corrections numbers are calculated from the right column muon simulation. Due to momentum smearing in the response/reconstruction stage, muons are thrown progressively wider on the lower  $p_T$  side than what is used in the acceptance & efficiency calculation to ensure the full acceptance for a given  $p_T$  bin is accurately determined. Only those particles both thrown and reconstructed inside the  $p_T$  bin are used to determine the final numbers, which are presented for both the north and south arm in the middle columns of Table 5.3.

The consideration of the systematic uncertainty of the acceptance & efficiency calculations are discussed explicitly in section 5.7.2. The acceptance & efficiency corrections are applied per  $p_T$  bin. At higher  $p_T$  where the correction factor is essentially independent of  $p_T$  this approach does not introduce any additional bias. At the lowest  $p_T$  bin where the correction

factor is rising more sharply as a function of  $p_T$ , and considering that the width of the  $p_T$  bin is 250 MeV wide, the application of a single acceptance & efficiency correction for this bin may introduce some bias. The simplest correction to this would be to apply the acceptance & efficiency corrections using a functional form derived from a fit of the correction values as a function of  $p_T$ .

Table 5.3: Average acceptance  $\times$  efficiency corrections as a function of  $p_T$ . These efficiencies are based on single muon simulations of realistic  $p_T$  spectral shape with all analysis cuts imposed, e.g. acceptance, track quality, and trigger emulator,  $-25 \leq z \leq 25$ .

Corrected $p_T$ bin	south	north	Generated $p_T$ range ( $GeV/C$ )
1.0 – 1.25	0.224	0.210	0.8 - 10.0
1.25 – 1.5	0.295	0.334	0.8 - 10.0
1.5 – 1.75	0.325	0.381	1.2 - 10.0
1.75 – 2.0	0.338	0.386	1.2 - 10.0
2.0 – 2.25	0.353	0.395	1.6 - 10.0
2.25 – 2.5	0.367	0.399	1.6 - 10.0
2.5 – 2.75	0.366	0.414	2.0 - 10.0
2.75 – 3.0	0.375	0.407	2.0 - 10.0
3.0 – 3.5	0.368	0.404	2.5 - 10.0
3.5 – 4.0	0.371	0.404	3.0 - 10.0
4.0 – 4.5	0.377	0.404	3.4 - 10.0
4.5 – 5.0	0.377	0.401	3.4 - 10.0

## 5.6 Methodology for signal extraction

### 5.6.1 Subtraction of backgrounds to obtain yield of single muons,

$$N_\mu$$

The yield of heavy flavor single muons is determined with the following equation:

$$N_{H.F.\mu}(p_T) = N_I(p_T) - N_c(p_T) - N_{2c}(p_T), \quad (5.6)$$

where  $N_I$  is the invariant yield of inclusive muon candidates,  $N_c$  is the estimated yield of tracks originating from hadrons estimated by a tuned MC,  $N_{2c}$  is the estimated yield of tracks determined from the two-component fit of the  $p\delta\theta$  distributions.

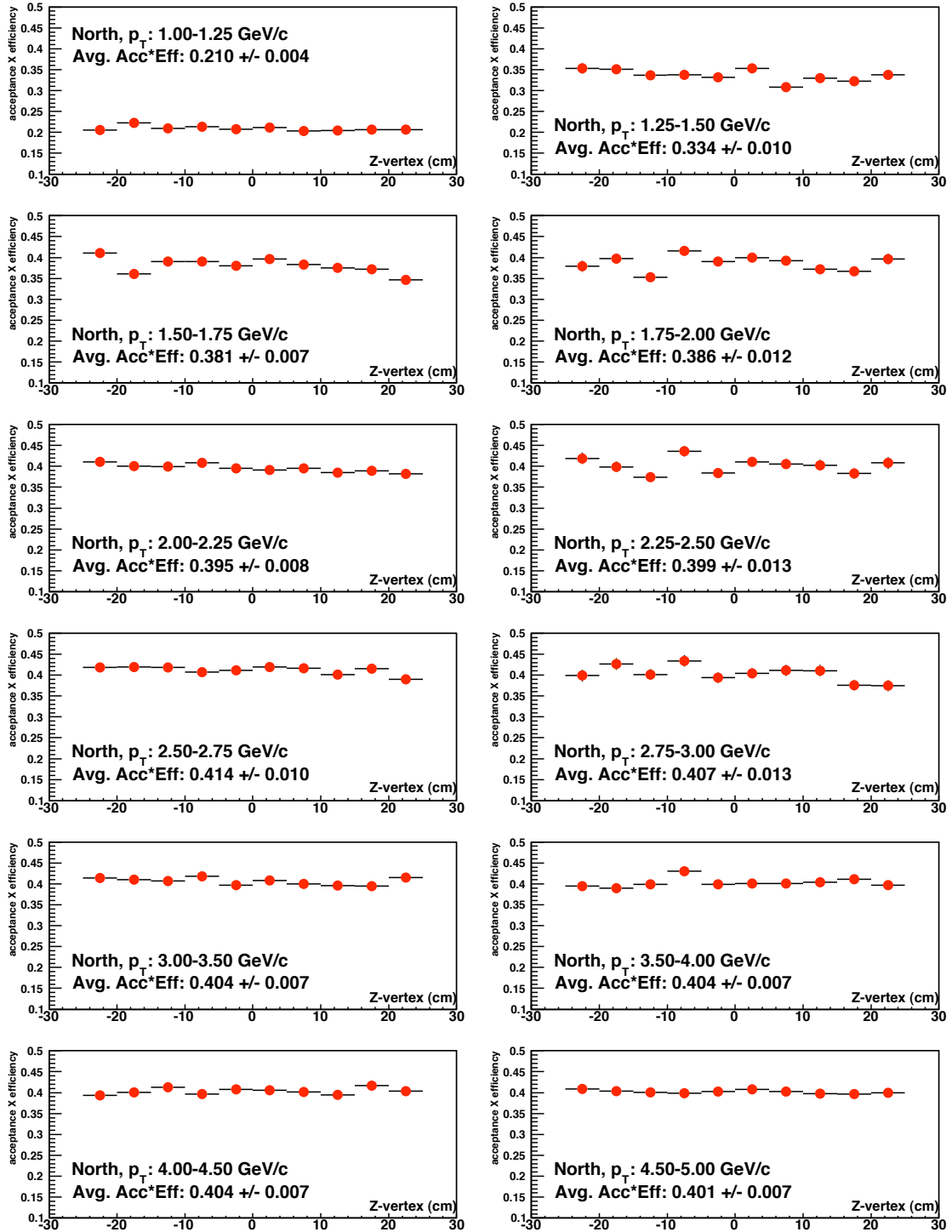


Figure 5.28: North arm calculated  $z$ -vertex dependent Acceptance  $\times$  Efficiency ( $-25 \leq z \leq 25$ ) for  $1.4 \leq |\eta| \leq 1.9$ .

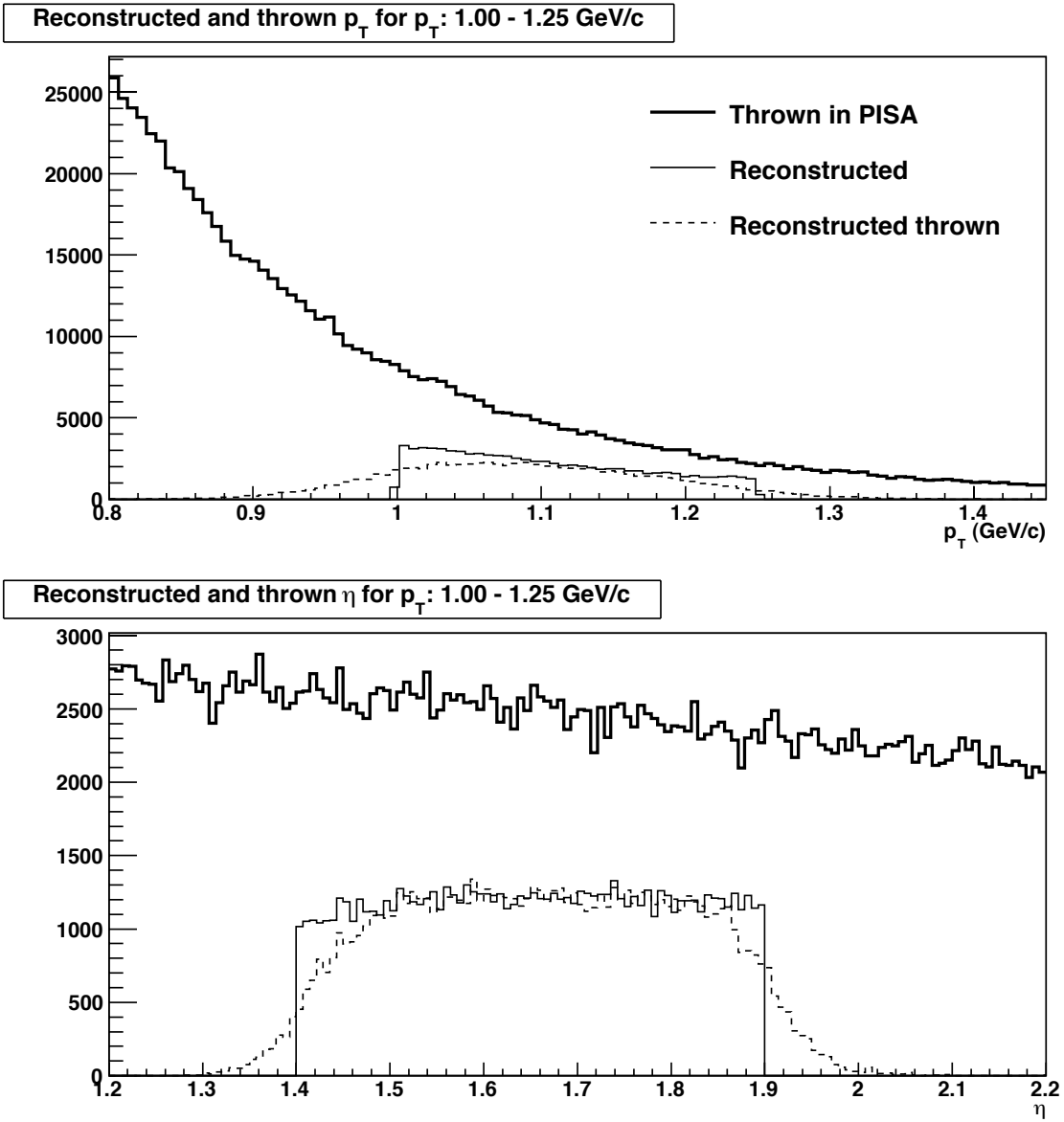
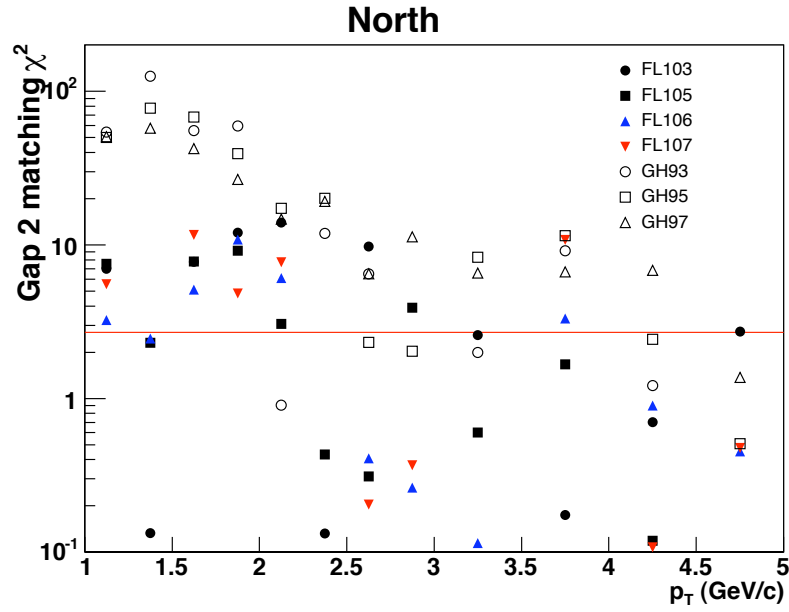


Figure 5.29: Momentum and rapidity smearing for muons considered in the acceptance  $\times$  efficiency corrections. Distributions of  $p_T$  and  $\eta$  are shown for simulated single muons using PISA in the  $p_T$  bin 1.0-1.25 GeV/c and  $\eta$  bin 1.4-1.9 for the original thrown distribution (“Thrown in PISA”), reconstructed in the bin (“Reconstructed”) and the original distributions for those particles reconstructed in the bin (“Reconstructed thrown”). Note: the reconstructed tracks in this figure do not have the full geometric acceptance cuts placed on them, otherwise the acceptance  $\times$  efficiency correction could be derived by dividing the thin solid line by the thick solid line.

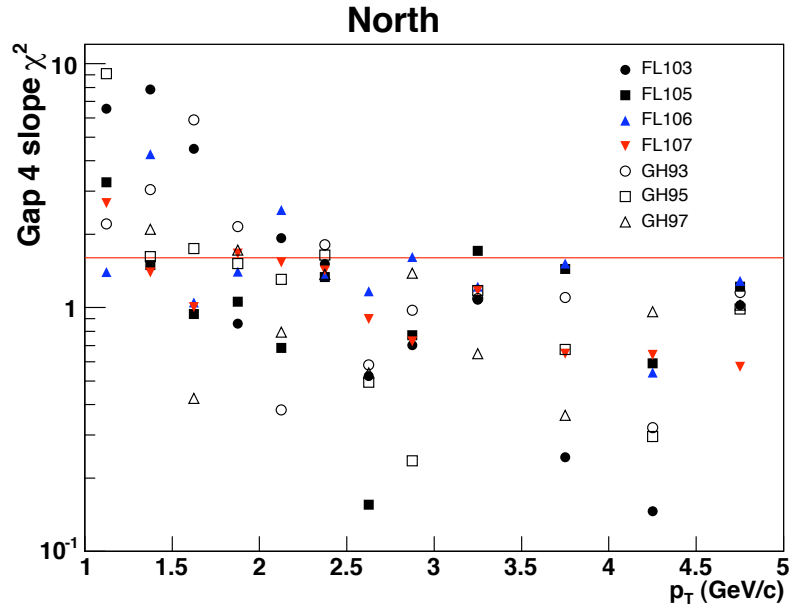
## 5.6.2 Extracting the central values of the single muon yield

The  $\chi^2/\text{NDF}$  is calculated for both the Gap 2  $p_T$  spectra and the Gap 4  $z$ -vertex distribution. The values for different hadron cocktails resulting from individual hadron packages and steel cross section settings (such as GH97 or FL103 ) are plotted for comparison in Figure 5.30. The solid red horizontal line in the plots corresponds to the 90% confidence level for the particular  $\chi^2$  calculation. For  $p_T$  above  $\approx 2.5$  GeV/c several packages from both FLUKA and GHEISHA provide adequate simultaneous hadron cocktail to data matching of Gap 2 and Gap 4 distributions. For this  $p_T$  region (  $> 2.5$  GeV/C ), the average of all hadron cocktail estimates that provide better than the 90% Confidence Level simultaneously for Gap 2 and Gap 4 is used as the central value of the hadron background estimate. It is worth noting that the improvement in the  $\chi^2/\text{NDF}$  values are due in part to the convergence of the overall predictions of the different tuned hadron cocktail predictions, with variations in the yields of each individual tuned prediction diverging less than 10% from the combined mean of all cocktail yields. For  $p_T$  above 2.5 GeV/c the observed linear  $z$ -vertex distributions due to the dominance of muons from hadron decay is waning. At the same time the statistical uncertainties in the hadron cocktail yields are also increasing as less particles are reconstructed with increasing  $p_T$  due to the modified input power law spectral shape that falls off nearly exponentially in  $p_T$ .

For the low  $p_T$  region, none of the single hadron cocktail packages provide adequate simultaneous matching of the Gap 2 and Gap 4 distributions. While several hadron cocktails have fairly good Gap 4  $z$ -vertex  $\chi^2/\text{NDF}$  values, the corresponding Gap 2  $\chi^2/\text{NDF}$  values show GHEISHA over predicting the Gap 2 yields by about 20% (causing very large  $\chi^2/\text{NDF}$  values) and FLUKA under predicting the Gap 2 yields at roughly the 10% level (with less extreme  $\chi^2/\text{NDF}$  values than GHEISHA) . Examination of the input spectra for different tuned hadron cocktail predictions at low  $p_T$  (Figure 5.31) illustrate the nature of the mismatch between the different hadron shower packages (generated at  $y=\langle 1.65 \rangle$ ) as well as their inability to fall inside the reasonable bounds of measured spectra at  $y=0$  and  $y=3$ . Figure 5.31 shows that below  $p_T \approx 2.5$  GeV/c FLUKA hadron yields tend to undershoot the hadron spectra shown by GHEISHA. At even lower  $p_T$  some of the FLUKA yields begin to undershoot the measured hadron spectra at  $y=3$ , while the GHEISHA spectra overshoots the measured PHENIX pion spectra at  $y=0$ .



(a) Gap 2  $\chi^2$ /NDF matching for individual hadron packages



(b) Gap 4  $z$ -vertex  $\chi^2$ /NDF matching for individual hadron packages

Figure 5.30: Single package hadron cocktail  $\chi^2$ /NDF for the north arm. The (red) horizontal lines represent the 90% confidence level for the respective  $\chi^2$  calculation.

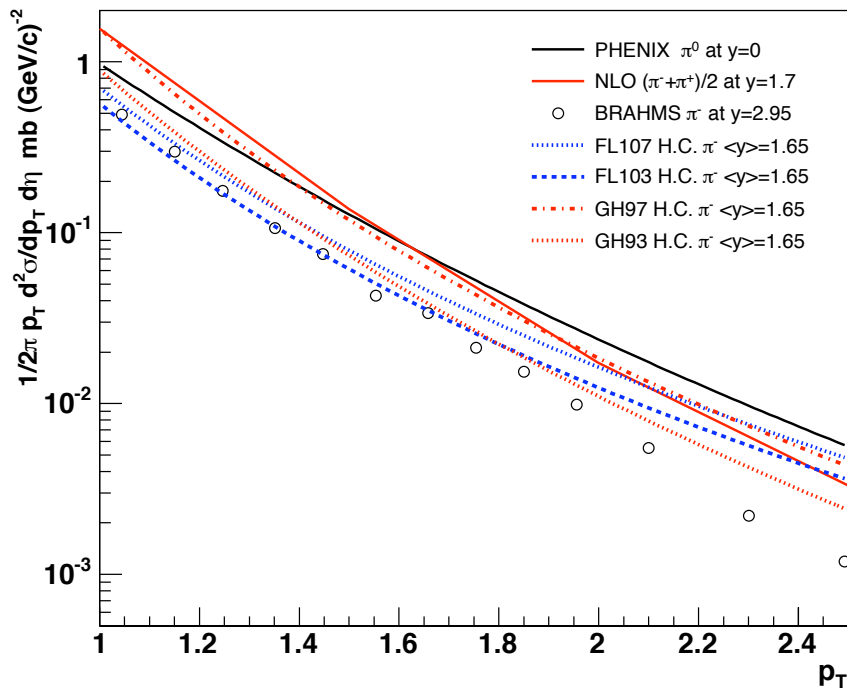


Figure 5.31: Comparison of tuned hadron cocktail input spectra with PHENIX  $y=0$  and BRAHMS  $y=3$  data.

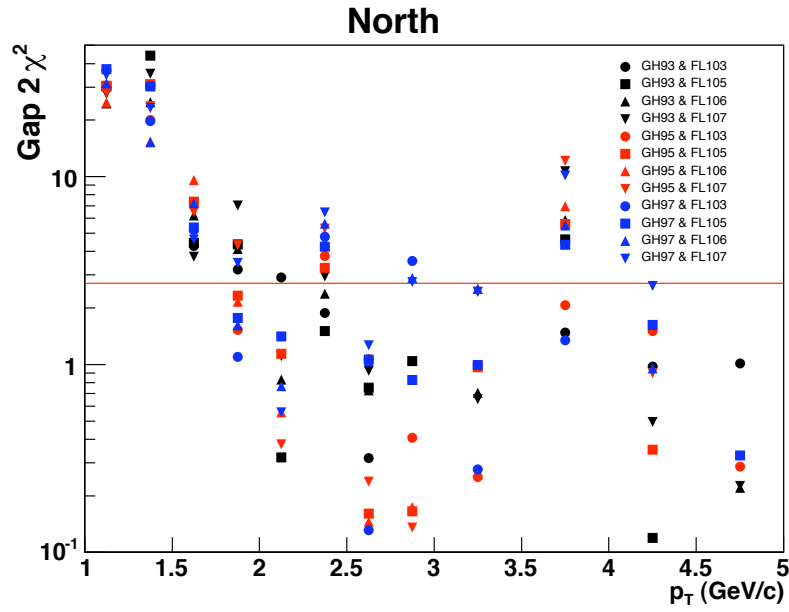
The approach taken for this analysis is that every combination of GHEISHA and FLUKA hadron cocktail yields are averaged in this low  $p_T$  region and the combined 50% FLUKA/50% GHEISHA yields have their Gap 2 and Gap 4 matching  $\chi^2/NDF$  values calculated. Those packages, whose input spectra fall inside the “reasonable” absolute boundaries provided by the PHENIX  $y=0$  and BRAHMS  $y=3$  measurements and whose  $\chi^2/NDF$  values show the best matching are taken as the best estimation of the background hadron yields at low  $p_T$ . Figure 5.32 shows the calculated  $\chi^2/NDF$  plots analogous to Figure 5.30. The combined package Gap 4 matching and Gap 2 matching shows improvement, although the Gap 2  $\chi^2/NDF$  values are large (10 to 11) which correspond to about a 10% mismatch from the data in Gap 2. Since in these low  $p_T$  regions the overall background source is dominated by the Gap 4 yield of decay muons, the Gap 4  $\chi^2/NDF$  matching is considered a more important indicator of the overall background estimate. A 10% error in the Gap 2 yield is expected to most directly reflect on the hadron punch through estimate in Gap 4, which is negligible at the lowest  $p_T$  compared to the decay muon yields.

The choice of using a 50/50 combination of FLUKA and GHEISHA in the low  $p_T$  region is not necessarily the best choice. So long as the input spectra lies inside the absolute bounds of the  $y=0$  and  $y=3$  measurements, we cannot know with any great precision what the true weights should be in mixing the GHEISHA and FLUKA estimates. The uncertainty on the mixed package hadron yields are determined by varying the weights on the linear combination for 0.3 to 0.7 for each FLUKA and GHEISHA. The corresponding variation in the yields for this range of weights is determined to be about 8%.

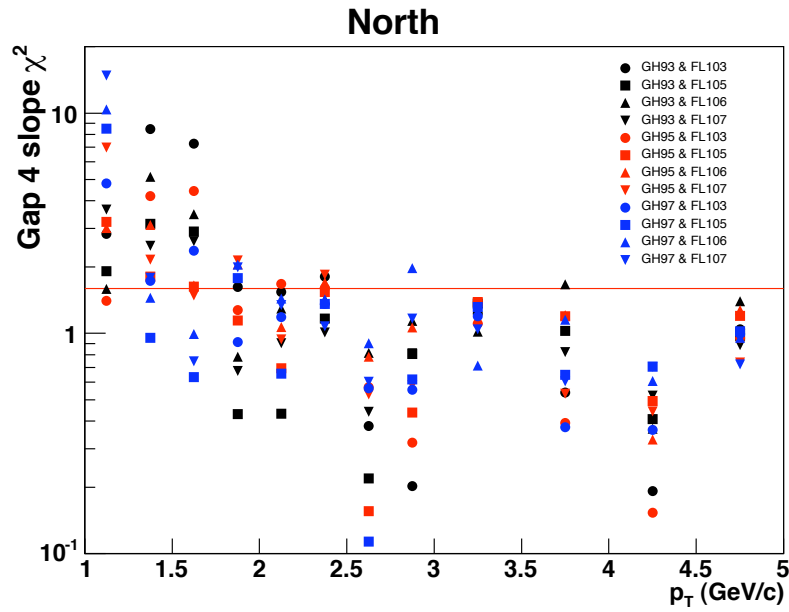
Before publication of these results, this aspect of analysis will be more thoroughly explored. It is expected that using a gaussian functional fit anchored by the measured spectra at  $y=0$  and  $y=3$  can be used to more tightly constrain the overall input spectra which might require a linear combination of FLUKA and GHEISHA with uneven weights.

### 5.6.3 Signal to background

As shown in Equation 5.10, the inverse of the signal to background ratio is a direct multiplier in the determination of the systematic uncertainty in the single muon yield. The signal to background for both north and south arm are shown in Figure 5.33.



(a) Gap 2  $\chi^2/\text{NDF}$  matching for individual hadron packages.



(b) Gap 4  $z$ -vertex  $\chi^2/\text{NDF}$  matching for two-package averaged hadron packages.

Figure 5.32: Two-package averaged hadron cocktail  $\chi^2/\text{NDF}$ . The horizontal (red) lines for both figures represents the 90% confidence level for the given  $\chi^2/\text{NDF}$ .

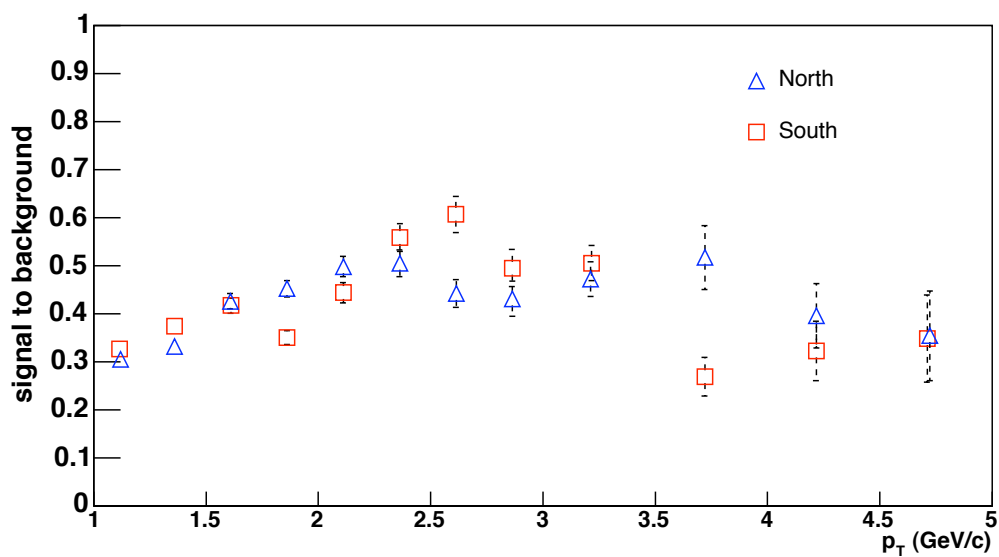


Figure 5.33: Signal/Background ratio for north and south arms including statistical errors. The dip in S/B for south for  $3.5 \leq p_T \leq 4.0$  results from a  $\sim 2.5\sigma$  downward fluctuation in the measured yield in data for this bin.

As mentioned in Section 5.2.5, a near-side  $z$ -vertex cut is placed on the lowest three  $p_T$  bins. The significantly larger amount of hadron decay muons at large  $z$  distances from the detector means that the near-side  $z$ -cut provides approximately a 50% increase in the S/B in the lowest  $p_T$  bin. This cut was applied to the three lowest  $p_T$  bins, which has the effect of raising the S/B values closer to the (approximately) asymptotic value between 0.4 to 0.5 observed in Figure 5.33. The improvement allows for a significant reduction in the systematic uncertainties, since the background-to-signal ratio is a direct multiplier to the uncertainty on  $N_\mu$  (Eq. 5.10).

The general trend of increasing S/B from low  $p_T$  to mid  $p_T$  in Figure 5.33 is expected as the yield of the dominant low  $p_T$  background source, namely of hadron decay muons, begins to wane. The general value of about 0.5 S/B for  $p_T$  above 2.5 GeV/c implies that the combined backgrounds of punch-through hadrons and the diminishing amount of muons from hadron decay equal the expected signal of heavy flavor muons (after all heavy-flavor muon tuned analysis cuts have been applied). Beyond a  $p_T$  of about 3 GeV/c, the S/B begins to drop as the higher  $p_T$  background estimated by the two-component fit ( $N_{2c}$ ) of the  $p\delta\theta$  distributions begins to increase, reaching a level of 15-20% in the highest  $p_T$  bin 4.5-5.0 GeV/c. This is best typified by the north arm curve, for the south arm experiences a  $2\sigma$  level statistical fluctuation in the 3.5-4.0  $p_T$  bin. The fluctuation observed in the south arm S/B in this  $p_T$  bin is due to an upward fluctuation in the south Gap 3 yield of about 10%. The Gap 3 yield is determined from the 1-Shallow triggered (M1S) data set. The M1S data set contains about 1/10 the statistics of the 1-Deep triggered (M1D) data set. Since the hadron cocktail is normalized to match the data yield at Gap 3, the hadron cocktail is normalized “too high.” This results in an over-subtraction, a slightly lower south arm single muon yield, as well as a reduced S/B which increases the associated systematic uncertainties. These effects can be seen in Figure 5.34. If the M1D data set can be used instead for Gap 3 matching, this problem should be eliminated due to the large increase in available Gap 3 statistics. The systematic uncertainty associated with the statistical uncertainty in matching the hadron cocktail to data would also be significantly reduced with the use of the M1D data set for Gap 3 matching.

#### 5.6.4 Comparison of north and south arm results

The double differential single muon cross section is calculated for both the north and south arm using the following equation.

Table 5.4: Combining north and south arm  $p_T$  spectra systematic uncertainties.

Uncert.	Norm.	pt. to pt. uncorr.	pt. to pt. correlated	N/S correlated
$\sigma_{N_\mu}$ , single muon yield uncertainties				
Gap 3 match		X		No
Hadron package			X	Yes
Cocktail input			X	Yes
Gap 4 MuID eff.			X	No
2-component fit			X	Yes
$\sigma_{\sigma_\mu}$ , single muon differential cross section uncertainties				
BBC Lum.	X			Yes
BBC trig bias	X			Yes
$\sigma_{A\epsilon_\mu}$ , acceptance & efficiency uncertainties				
MuTr			X	No
MuID			X	No
Run to run			X	No
Mom. scale			X	No

$$\frac{d^2\sigma_\mu(p_T)}{2\pi p_T dp_T d\eta} = \frac{\sigma_{BBC}^{pp}}{\epsilon_{BBC}^{c\bar{c}\rightarrow\mu}} \cdot \frac{N_\mu}{A\epsilon_\mu} \quad (5.7)$$

The resulting spectra for both muon arms are plotted together in Figure 5.34. BBC normalization systematic uncertainties of  $\approx 10\%$  are shown as a black band on the vertical axis. The arm-correlated uncertainties are plotted separately as the grey band to the right of the data points. Both of these types of systematic uncertainties are separated when comparing the two arms in order to gauge the agreement between the arms. The systematic uncertainty bands associated with non-arm correlated uncertainties are drawn about the north and south arm points. The classification of the different uncertainties into normalization, arm-correlated, and arm non-correlated are summarized in Table 5.4. Following PHENIX data plotting precedent, the lone point-to-point uncorrelated systematic uncertainty is added in quadrature with the statistical error bars on the data points. This is done for each arm independently. The corresponding spectra and assortment of plotted uncertainties for north and south show good agreement, providing a good level of cross check in the analysis method since the measurement for each arm is each the result of an essentially independent analysis.

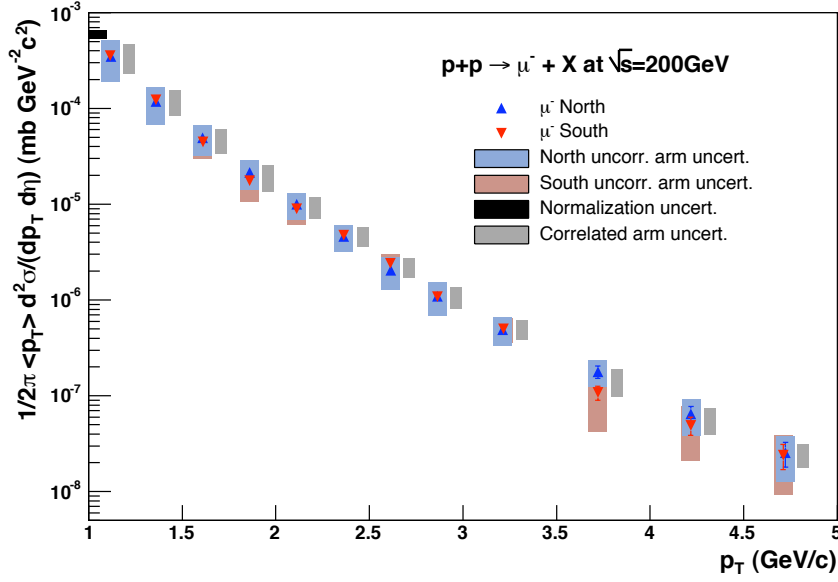


Figure 5.34: Separate north and south single muon spectra.

### 5.6.5 Combining the arms into a single $p_T$ spectrum

Figure 5.35 shows the North/South combined single muon spectrum, and Table 5.5 presents the central values with statistical uncertainties as well as the systematic uncertainties as determined in Section 5.7.

The north and south arm measurements can be combined by averaging the central values, but care must be taken to properly combine the systematic uncertainties. The total combined arm systematic uncertainties,  $\sigma_{\frac{N+S}{2}}$ , can be calculated by taking into account both correlated and uncorrelated uncertainties with the following equation (see Eq. C.11):

$$\sigma_{\frac{N+S}{2}} = \sqrt{\frac{(\sigma_N^{uncor})^2 + (\sigma_S^{uncor})^2}{4} + \left(\frac{\sigma_S^{cor} + \sigma_N^{cor}}{2}\right)^2} \quad (5.8)$$

The derivation of this equation is given in Appendix C.5. The right term in the sum is the average of the correlated errors for each arm. In principle the correlated errors are the same for both arms. While the values do actually differ at some level due to different signal to background values which result in numerically different uncertainty values, we argue it is valid to average the two correlated errors which allows for the straightforward uncertainty

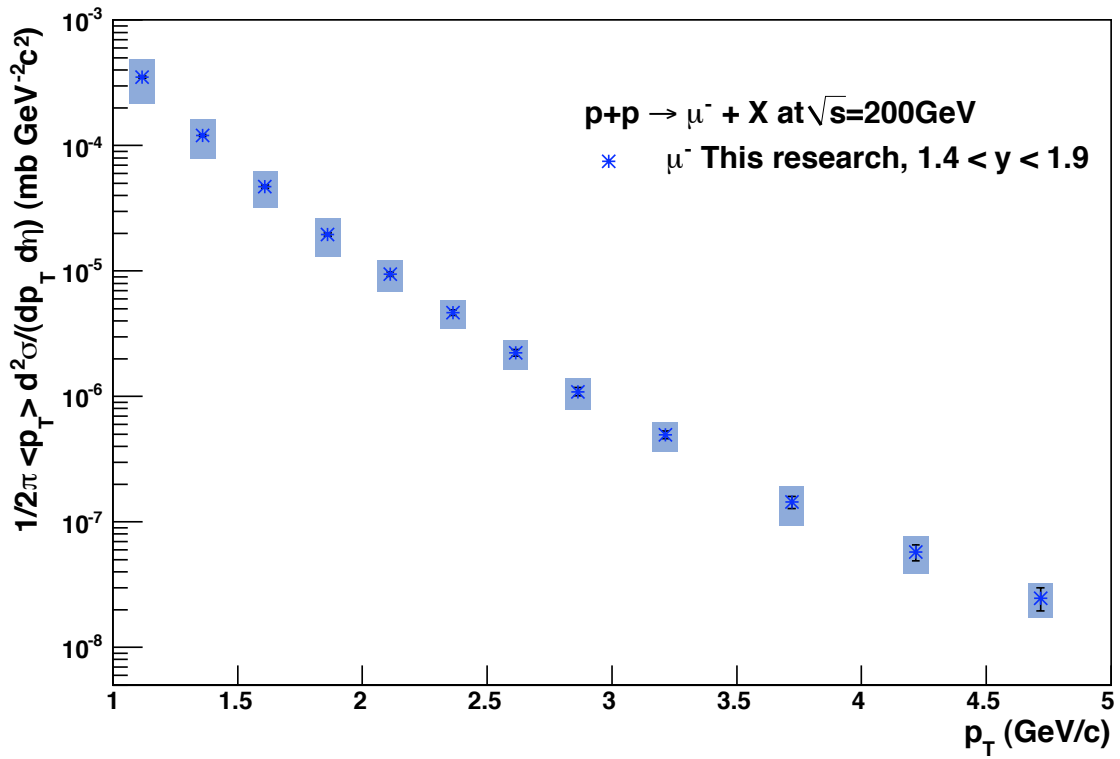


Figure 5.35: Combined arm single muon spectrum.

Table 5.5: Numerical values for Fig. 5.35: arm averaged PHENIX Preliminary heavy flavor single muon (negative charge)  $p_T$  double differential cross section and uncertainties.

$p_T$	Cross section	Stat and pt. to pt. uncorrelated	Sys. uncertainties
1.12	0.000352	6.63e-06	0.000135
1.36	0.000120	2.57e-06	4.15e-05
1.61	4.72e-05	1.31e-06	1.51e-05
1.86	1.97e-05	6.33e-07	6.65e-06
2.11	9.49e-06	3.82e-07	2.69e-06
2.36	4.67e-06	2.30e-07	1.20e-06
2.61	2.23e-06	1.36e-07	5.93e-07
2.86	1.09e-06	8.32e-08	3.10e-07
3.21	4.96e-07	3.39e-08	1.30e-07
3.72	1.43e-07	1.61e-08	5.04e-08
4.22	5.71e-08	8.38e-09	1.89e-08
4.72	2.47e-08	5.12e-09	7.62e-09

propagation suggested by Equation 5.8. The point-to-point uncorrelated uncertainties remain combined with the statistical uncertainty bars, as was done for the individual arm measurements.

## 5.7 Systematic uncertainties in the $p_T$ spectra

Systematic uncertainties are applied to the single muon  $p_T$  spectra in two stages. First, the systematic uncertainties associated with the extraction of the yield of single muons are discussed in Section 5.7.1. Second, the conversion of the single muon yield to an invariant cross section involves a separate set of systematic uncertainties that are explicitly shown in Section 5.7.2. The following shorthand notation for invariant particle yields is used:

$$N_x \equiv \frac{d^2 N_x(p_T)}{2\pi p_T dp_T d\eta}.$$

The details of the exact derivation of the equations are described in Appendix C.

### 5.7.1 Uncertainty on the yield of single muons, $N_\mu$

A systematic uncertainty is associated with the extraction of the single muon yield:

Table 5.6: Uncertainties in  $N_c$  and  $N_{2c}$ . The individual components are added in quadrature to assign the total values of  $\mathcal{F}_{N_c}$  and  $\mathcal{F}_{N_{2c}}$ .

$\mathcal{F}_{N_c}$			
Component		north value	south value
1.	Gap 3 matching hadron cocktail to data	$f(p_T)$ , from 1% to $\approx 20\%$	
2.	FLUKA/GHEISHA hadron package difference	$f(p_T)$ , no more than 10%	
3.	Hadron cocktail input, including K/ $\pi$ uncertainty	7%	
4.	Gap 3 to Gap 4 efficiency matching	6%	9%
$\mathcal{F}_{N_{2c}}$			
1.	Two-component fit and subtraction	taken as 10% for all $p_T$	

$$N_\mu = N_I - N_c - N_{2c} \quad (5.9)$$

where  $N_I$  is the inclusive muon candidate tracks as measured by the PHENIX muon spectrometer.  $N_c$  is the background yield estimate provided by the hadron cocktail as described in section 5.3.  $N_{2c}$  is the yield of particles comprising an additional high  $p_T$  background not estimated by the hadron cocktail (for further details see section 5.4).

The yield of single muons,  $N_\mu$ , is obtained through the subtraction of two different background estimates from the inclusive muon candidate track sample,  $N_I$ , as described in Equation 5.6. These yields are not acceptance and efficiency corrected. Since the inclusive yield of candidate muons,  $N_I$ , is simply the number of candidate muons reaching Gap 4 and surviving analysis cuts, no systematic uncertainty is associated with this yield. The fractional uncertainty<sup>§</sup> on the extracted single muon yield,  $\mathcal{F}_{N_\mu}$ , can then be calculated through a straightforward propagation of errors on  $N_c$  and  $N_{2c}$  (see Eq. C.5 in Appendix C).

$$\mathcal{F}_{N_\mu} = \sqrt{\left(\mathcal{F}_{N_c} \cdot \frac{N_c}{N_\mu}\right)^2 + \left(\mathcal{F}_{N_{2c}} \cdot \frac{N_{2c}}{N_\mu}\right)^2} \quad (5.10)$$

Uncertainties associated with the extraction of  $N_c$  and  $N_{2c}$  are listed in Table 5.6.

---

<sup>§</sup>Fractional in the sense that they can be expressed in terms of a percentage.

Table 5.7: Uncertainties in the single muon differential cross section,  $\sigma_\mu$ . The individual components are added in quadrature to assign the total value of  $\sigma_{\sigma_\mu}$

$\sigma_{\sigma_\mu}$		
Component		Value
$\sigma_{N_\mu}$	uncertainty in single muon yield	as determined in Table 5.6
$\sigma_{\sigma_{BBC}}$	Uncertainty in $\sigma_{BBC}^{pp}$	9.6%
$\sigma_{\epsilon_{BBC}}$	Uncertainty in BBC trigger bias	2.5%
$\sigma_{A\epsilon_\mu}$	Acceptance and efficiency correction	as determined in Table 5.8

### 5.7.2 Uncertainty on the single muon differential cross section

A systematic uncertainty is calculated for the single muon double differential cross section from the following equation:

$$\frac{d^2\sigma_\mu(p_T)}{2\pi p_T dp_T d\eta} = \frac{\sigma_{BBC}^{pp}}{\epsilon_{BBC}^{c\bar{c}\rightarrow\mu}} \cdot \frac{N_\mu}{A\epsilon_\mu} \quad (5.11)$$

where  $\sigma_{BBC}^{pp}$  is the cross section of the BBC trigger for  $p+p$  interactions and  $\epsilon_{BBC}^{c\bar{c}\rightarrow\mu}$  is the efficiency of the BBC trigger for events in which a charm quark is created and decays into a muon.  $A\epsilon_\mu$  is the acceptance times efficiency correction factor for muons reaching Gap 4 of the MuID (Section 5.5).

Once  $N_\mu$  is determined, the systematic uncertainty on the single muon differential cross section is determined by propagating uncertainties in equation 5.11.

$$\sigma_{\sigma_\mu} = \sqrt{\sigma_{N_\mu}^2 + \sigma_{\sigma_{BBC}}^2 + \sigma_{\epsilon_{BBC}}^2 + \sigma_{A\epsilon_\mu}^2}. \quad (5.12)$$

#### Determination of $\sigma_{A\epsilon_\mu}$

As indicated in Table 5.7, the systematic uncertainty associated with the acceptance and efficiency corrections is the quadratic sum of the four components given in Table 5.8. For this uncertainty the same values are used for both arms.

Table 5.8: Uncertainties in the acceptance and efficiency corrections. The individual components are added in quadrature to assign the total value of  $\sigma_{A\epsilon}$

$\sigma_{A\epsilon}$		
Component		Value
$\sigma_{MuTR}$	$\phi$ -distributions for MuTR station data/MC comparison	8%
$\sigma_{MuID}$	MuID Gap 4 efficiency uncertainty	4.5%
$\sigma_{run\ to\ run}$	Run to run variation	2%
$\sigma_{p-scale}$	$J/\Psi$ mass peak	1.5%

## 5.8 Integrating single lepton spectra for $p_T > 1.0$ GeV/c

This section describes how the single lepton data is integrated, with the results shown in Figure 6.6. The procedure is outlined with some detail since it is also used in the exploration of the nature of the theoretical uncertainty ultimately assigned to  $d\sigma^{c\bar{c}}/dy$  located in Section 5.10.4.

### 5.8.1 General notes on the integration of the $p_T$ lepton spectra

All integrations performed in this analysis are over discrete arrays of finite bin width. The points used in the integration of the data spectra is determined by the measured  $p_T$  bins. The integration of theoretical curves is determined strictly by the theoretical points made available to me. Two classes of theoretical curves are used in this analysis. The first class is comprised of the central, upper bound, and lower bound FONLL curves which are calculated with a  $p_T$  bin width of 0.05 GeV/c from infinity (around 10.0 GeV/c to zero). This first class of curves are the theoretical calculations used to extract the integrated charm quark cross section as well as the theoretical uncertainty component used in the determination of the upper and lower systematic uncertainties on the charm quark estimate. A second set of “non-standard” FONLL curves corresponding to a collection of different theoretical parameters were obtained. These curves are used to explore the impact of theoretical parameter choices on the predicted spectral shape and are discussed further in Section [refsec:vogtcurves].

### 5.8.2 How much of the integrated cross section is sampled for $p_T > 1.0 \text{ GeV}/c$ ?

The single lepton  $p_T$  spectra measured by PHENIX at both mid and forward rapidity is measured above some lower bound in transverse momentum. The minimum  $p_T$  sampled in the muon arms is higher than that of the central arms ( $p_T=1.0 \text{ GeV}/c$  versus  $p_T=0.35 \text{ GeV}/c$ ) due to the large amount of steel (more than one meter) in between the interaction point and the deepest sensitive layer of the Muon Identifier. The PHENIX mid-rapidity single electron analyses measure as low as  $p_T = 0.35 \text{ GeV}/c$ , while the single muon analysis measures muons with a  $p_T$  as low as  $1.0 \text{ GeV}/c$ . Due to the exponentially falling shape of the curves, the total integral of the single lepton cross section is dominated by the low  $p_T$  portion of the curve. This effect is shown in Figure 5.36 which depicts a one minus the cumulative distribution normalized to a total integral of one. The FONLL central curve at  $\langle y \rangle = 1.65$  is used to make the comparison because the points can be extended to  $p_T$  zero.

An integral from infinity (which for all intents and purposes can be taken to be  $p_T = 5.0 \text{ GeV}/c$ ) will contain 100% of the curve's integral. To approximate the fraction of the total lepton cross section sampled in the single muon measurement, we integrate over the  $p_T$  region 1.0 to  $\infty \text{ GeV}/c$ , which amounts roughly to 6% (large, red dotted line in Figure 5.36). This can be compared to the roughly 50% fraction sampled in the single electron measurement from  $p_T$  region 0.35 to  $\infty \text{ GeV}/c$  (fine black dashed line in Figure 5.36).

### 5.8.3 Integration of the lepton spectra

Two methods are used to cross check the integration of the  $p_T$  binned spectra. Simpson's method and a piecewise fit over a sub-region of the  $p_T$  spectra are used. Once the accuracy of the fitting technique was verified to match the results obtained via Simpson's method ( $\ll 1\%$  match), the fitting technique was used to integrate both the data and theory curves using the same algorithm.

The numerical integration of the discrete spectra points is performed using Simpson's rule which uses smooth quadratic interpolation to perform integration:

$$\int_{p_T^a}^{p_T^b} f(p_T) dp_T \approx \frac{p_T^b - p_T^a}{6} \left[ f(p_T^a) + 4f\left(\frac{p_T^b + p_T^a}{2}\right) + f(p_T^b) \right] \quad (5.13)$$

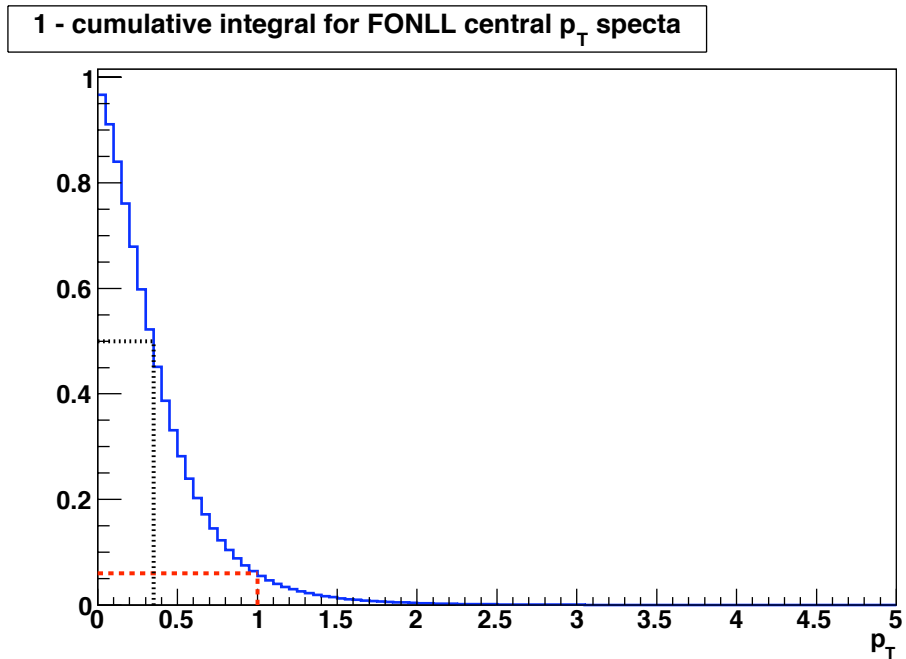


Figure 5.36: One minus the cumulative integral distribution for FONLL central charm curve [20]. This curve illustrates the fraction of the integrated  $p_T$  spectra sampled from infinity to some minimum  $p_T$ . The dashed (red) line corresponds to the single muon acceptance for  $p_T > 1.0$  GeV/c and the dotted (black) line corresponds to the PHENIX single electron measurement for  $p_T > 0.35$  GeV/c.

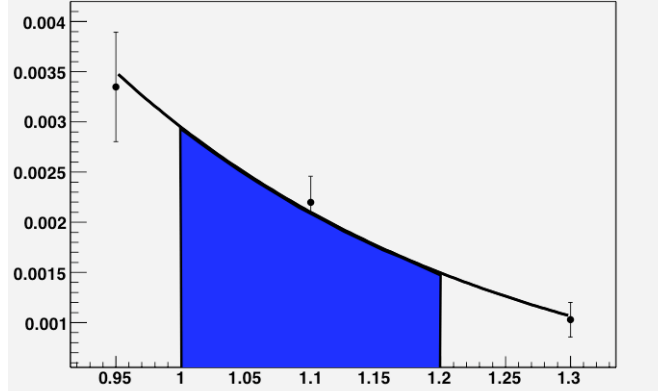


Figure 5.37: Example of piecewise fit of exponential to a sub-region of the  $p_T$  spectra. The solid blue region illustrates the region used to estimate the integral in the given  $p_T$  region.

where  $a$  and  $b$  effectively represent two successive  $p_T$  bins. The choice of the term  $f(\frac{p_T^b + p_T^a}{2})$  is perhaps the only ambiguous aspect of this method. For functions that fall as steeply as the power-law type functions, taking the average between the two data points may not be sufficient. Using a fit over a sub-region of the data points and using the fit function to provide the term  $f(\frac{p_T^b + p_T^a}{2})$  results in a Simpson's Rule integral estimate that matches the integral obtained by an exponential fit over sub-regions of the data as described in the next.

This technique is verified by integrating with a piecewise exponential fit over sub-regions in  $p_T$ . The integrals of each of the  $p_T$  bins are then evaluated and summed to provide the total integral. Figure 5.37 illustrates an example fit. The fit is performed using a two parameter exponential function. For data where statistical errors are present they are used in the fit procedure, where for the theoretical curves no errors are used in the fit. The choice of fitting  $p_T$  sub-regions is motivated by the difficulty in fitting a power-law  $p_T$  spectra with a single function over a large region in  $p_T$ . Figure 5.37 shows the fit and integration for the single electron  $1.0 \leq p_T \leq 1.2$  region, which has larger statistical errors at  $p_T \approx 1.0$  GeV/c than at higher  $p_T$  due to the lower converter run sampled luminosity used at low  $p_T$ .

#### 5.8.4 Statistical errors on the integrated lepton spectra

The statistical errors assigned to the integrated cross section are calculated by summing the statistical errors of each data bin in quadrature. This summed statistical error can be stated in terms of a fractional error. The same statistical fractional error is then assigned to the value of the integral determined from the successive fit of  $p_T$  bins, as described in the

previous section. Other approaches to assigning the integral's statistical errors such as using the error associated with the integral (based on the fit function errors) were dabbled with but ultimately abandoned due to possible bin-to-bin correlations in the error since each  $p_T$  point is used in up to three fits.

### 5.8.5 Systematic uncertainties of the $p_T > 1.0$ GeV/c integrated lepton spectra

The systematic uncertainties in the integrated lepton spectra are the sum of systematic uncertainties for all  $p_T$  bins included in the integration multiplied by the width of the particular  $p_T$  bin in question.

## 5.9 Methodology for the extraction of $d\sigma_{c\bar{c}}/dy |_{y=1.65}$

Results from this section are discussed in Section 6.2.  $d\sigma_{c\bar{c}}/dy$  from heavy flavor single leptons is determined using the following formula:

$$d\sigma_{c\bar{c}}/dy = \frac{1}{BR(c \rightarrow \mu)} \cdot \frac{1}{C_{e/D}} \cdot \frac{d\sigma_{\mu}}{dy}. \quad (5.14)$$

$BR(c \rightarrow \mu)$  is the total muon branching ratio of charm. This number is fixed in the FONLL scheme to be 0.103.  $C_{e/D}$  is a kinematical correction factor to account for the different in the rapidity distributions of leptons and  $D$  mesons.  $d\sigma_{\mu}/dy$  is the integrated cross section of single leptons over all  $p_T$  that is extrapolated from the lowest measured  $p_T$  to 0 GeV/c using a model (FONLL in this case). Details for the determination of  $d\sigma_{\mu}/dy$  are described in Section 5.9.1. The  $BR$  is determined from measured data, though the value used by FONLL for this analysis differs slightly from the standard value<sup>¶</sup>, and  $C_{e/D}$  is determined as described in Section 5.9.3.

For the single muon rapidity window of  $1.4 \leq |y| \leq 1.9$ , the mean rapidity is  $\langle y \rangle = 1.65$ . The single muon  $p_T$  spectra used in this analysis is combined from separate single muon measurements at both forward and backward rapidity. While the single muons are measured at both  $y=1.65$  and  $y=-1.65$  this combined spectra is used to determine a single value of  $d\sigma/dy$ . As a convention we plot the  $y=-1.65$  point as a solid point and the  $y=1.65$  as a

---

<sup>¶</sup>See for instance [15].

hollow point to serve as a reminder that the muons are measured in two rapidity bins but the value is determined from a single source.

### 5.9.1 Extrapolating the measurement for $p_T < 1.0$ GeV/c

This section describes the procedure used to integrate the single muon  $p_T$  spectra at  $y=1.65$ . This technique can be described using a single formula:

$$d\sigma_{c\bar{c}}/dy \Big|_i^{PHENIX} = d\sigma_{c\bar{c}}/dy \Big|_i^{FONLL} \cdot Scale_i^{FONLL} \quad (5.15)$$

where the  $i^{th}$  FONLL case corresponds to a particular  $p_T$  spectra obtained from a choice of theoretical parameters<sup>||</sup>. The FONLL  $p_T$  spectra (in  $E \frac{d^3\sigma}{dp^3}$  form), is fit to data to determine the value of  $Scale^{FONLL}$ . The value of  $d\sigma_{c\bar{c}}/dy \Big|_i^{FONLL}$  (taken from the distribution in Figure 2.8) for the particular FONLL case is then multiplied with the  $Scale^{FONLL}$  to determine  $d\sigma_{c\bar{c}}/dy \Big|_i^{PHENIX}$ . While the procedure is straightforward, for clarity we step through a single example using a test FONLL case. The bottom component is currently ignored in this analysis. Inclusion of the bottom component in this analysis will decrease the extracted cross charm cross section by just a few percent based on some initial studies.

#### Determination of a particular scale factor, $Scale_i^{FONLL}$

The data (Fig. 5.35) and FONLL central charm points are plotted together in the top panel of Figure 5.38. The basic spectral shape observed in the data approximately matches that of FONLL charm, with the data curve lying roughly a factor of four above the FONLL central charm prediction. The lower panel of Figure 5.38 shows the ratio of data to FONLL charm, with a constant fit to the data to FONLL charm ratio, which in this particular case corresponds to a constant factor of 4.22. The observed spectral shape agreement after scaling is on the order of 10% over all  $p_T$ , with 5% agreement for  $p_T < 2.0$  GeV/c. The final scale factors used to determine the charm cross section are listed in Table 5.9.

### 5.9.2 Procedure for determination of $d\sigma_{c\bar{c}}/dy$ at $y=1.65$

The invariant  $E \frac{d^3\sigma}{dp^3}$  spectra of single muons is now converted to an integrated charm quark cross section,  $\frac{d\sigma_{c\bar{c}}}{dy} \Big|_{y=1.65}$ . Theoretical curves  $\frac{d\sigma}{dp_T dy}$  are used to extrapolate the lepton spectra for  $0.0 p_T < p_T^{min}$ , and the resulting integrated lepton spectra can then be used to determine

---

<sup>||</sup>This includes quark mass, normalization and factorization scales, parton distribution functions, fragmentation schemes.

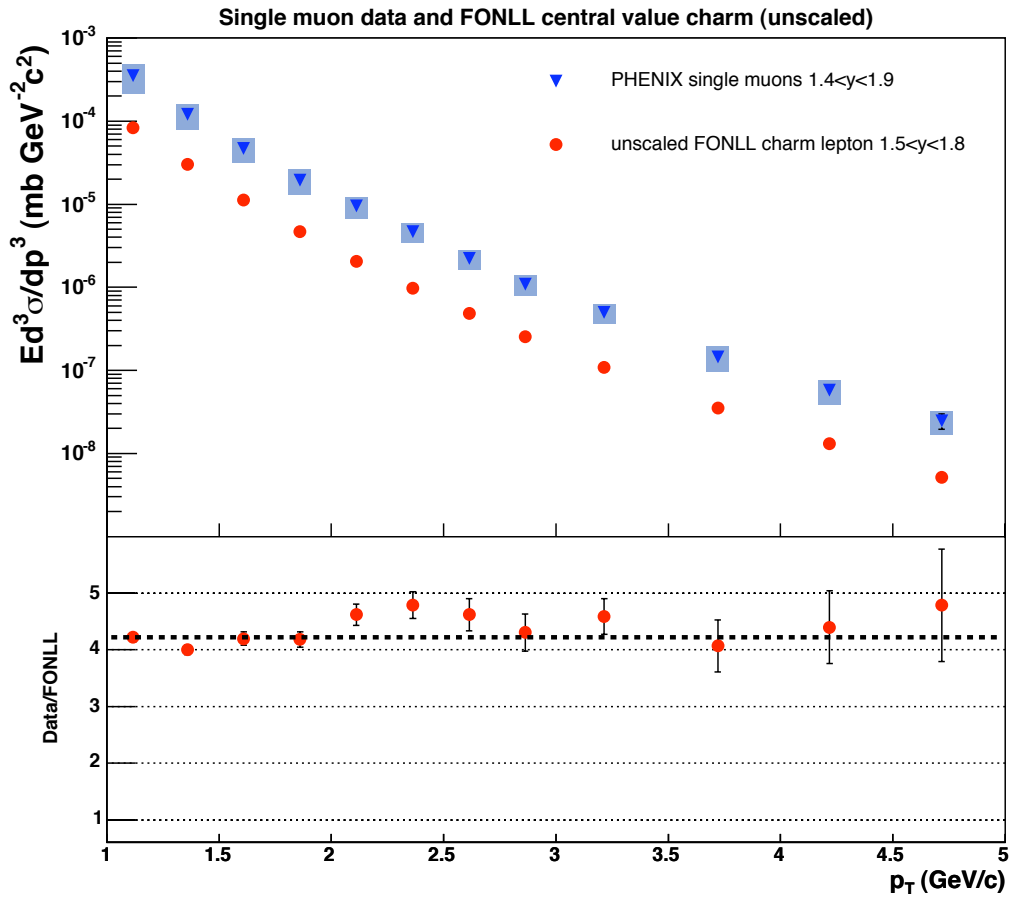


Figure 5.38: Data (Fig. 5.35) and unscaled FONLL charm spectrum only (upper panel); ratio of Data to FONLL with constant fit (lower panel). See text for additional details.

Table 5.9: Derived FONLL normalization scales that fit the FONLL lepton spectra to data for  $y=0$  and  $y=1.65$ .

$y$	central FONLL scale	upper FONLL scale	lower FONLL scale
0	1.44	0.80	2.43
1.65	3.57	1.77	7.11

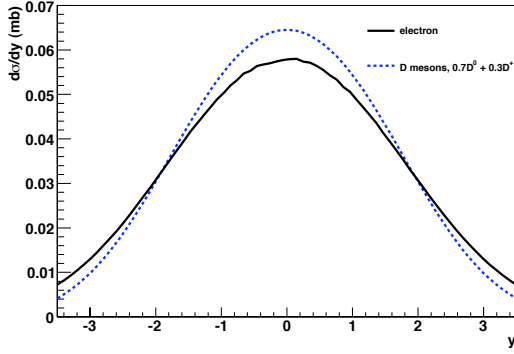
$\frac{d\sigma}{dy} |_{y=1.65}$  for charm quarks.

The particular extrapolation technique from the minimum measured transverse momentum,  $p_T^{min}$ , to zero can be performed a few different ways. The integration is performed over  $p_T$ , converting the  $d\sigma/(dp_T dy)$  spectral distribution over a certain  $p_T$  and rapidity window to a single  $d\sigma/dy$  point which corresponds to the  $\langle y \rangle$  of the rapidity window. The following steps describe the particular extrapolation procedure performed in this analysis. Since at this point the discussion assumes the identification of single muons, the experimentally determined  $\eta$  is now equated to  $y$ .

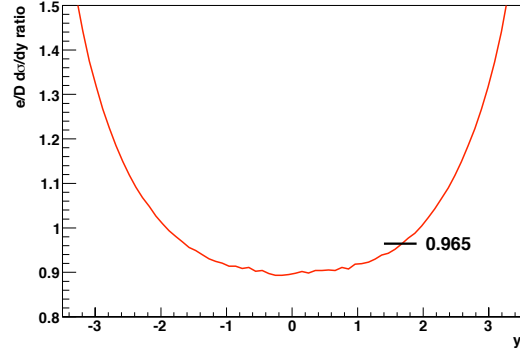
1. The  $p_T$  data points above a certain minimum is converted from an invariant differential cross section,  $E \frac{d^3\sigma}{dp^3}$  into a cross section of the form  $\frac{d\sigma}{dp_T dy} |_{p_T > 1.0}$  by multiplying each point by  $2\pi \langle p_T \rangle$ . For the single muon spectra used in this note,  $dy=0.5$  since the analysis measures muons with  $1.4 \leq |y| \leq 1.9$ .
2. The  $\frac{d\sigma}{dp_T dy} |_{p_T > 1.0}$  is extrapolated to a  $p_T$  of zero using a theoretical curve. Since the spectral shapes of the data and theory show good agreement but with a sizable difference in overall normalization, the theory curve is fit to data to obtain a normalization scale factor,  $Scale^{theory}$ .
3. For a particular theoretical  $Scale^{theory} \cdot \frac{d\sigma}{dy} |_{y=1.65}$  provides the predicted charm quark cross section. The details of the fragmentation used in the calculation along with the branching ratio of C to D is provided by the particular theoretical curve and its corresponding value of  $\frac{d\sigma}{dy}$ .

### 5.9.3 The rapidity broadening of leptons from D mesons

Relative to light quark fragmentation, heavy flavor quark fragmentation is harder, meaning that the resulting heavy flavor mesons retain a large fraction of the momentum of the original heavy quark [15]. Single leptons that result from the heavy flavor meson decay, such as



(a) *Lepton* and *D* rapidity distributions.



(b) *Lepton* and *D* FONLL rapidity distribution ratio.

Figure 5.39: FONLL *lepton*/*D* ratio vs.  $y$  [113].

$D \rightarrow K\mu\nu_\mu$  for instance, share the momentum fraction with the sibling light hadrons (and neutrinos). As a consequence of this indirect observation of heavy flavor mesons, the measured momentum of the single leptons is reduced relative to the parent  $D$ , and the rapidity distribution of the leptons relative to the parent  $D$  is broader. While it is not experimentally possible to compare these distributions from data, they can be made using FONLL (or PYTHIA, etc.) as seen in Figure 5.39 [113]. For the mass scale of the calculation, the electron and muon mass are negligible and are treated as equivalent “leptons”.

A clear broadening of the lepton rapidity distribution (solid line) relative to that of the  $D$ -meson distribution (dashed line) is shown in the left plot. The ratio of *lepton*/ $D$  of the two distributions, shown in Figure 5.39(b), shows that on average in this analysis’ rapidity region of  $1.4 \leq |y| \leq 1.9$ , electrons have a slightly smaller rapidity value than  $D$ ’s in the same region (black line at 0.965). To extract an integrated charm cross section from a single lepton  $p_T$  spectra in a particular rapidity bin, this kinematic factor,  $C_{e/D}=0.965$  should be applied to the final  $d\sigma_{c\bar{c}}/dy$  value to account for the difference in the shape of the measured distribution and the expected charm meson distribution. Due to the uncertainty in the generation of leptons (which is based on electron spectra) in FONLL, this rapidity broadening correction is not applied in the presented results, but this correction should be applied at some future date.

## 5.10 Systematic uncertainties on $d\sigma_{c\bar{c}}/dy$

Two systematic uncertainties are considered for the  $d\sigma_{c\bar{c}}/dy|_{y=1.65}$  points: data systematic uncertainties and theoretical (FONLL) uncertainties. These two quantities are then added in quadrature to represent the systematic uncertainty in the extracted  $d\sigma_{c\bar{c}}/dy$  value.

### 5.10.1 Data systematic uncertainties

The data associated systematic uncertainty for  $d\sigma_{c\bar{c}}/dy|_{y=1.65}$  is obtained from the single muon  $p_T$  spectrum systematic uncertainties as described in Section 5.7. These systematic uncertainties are determined for the  $d\sigma_{c\bar{c}}/dy|_{y=1.65}$  by fitting the upper and lower **data** systematic uncertainty bounds of the  $p_T$  spectrum with the FONLL central value spectrum. The variation in the extracted fit scale value due to data systematic uncertainties amounts to approximately 35%.

### 5.10.2 Theoretical systematic uncertainties

Both the FONLL  $d\sigma^{lepton}/dp_T$  and  $d\sigma_{c\bar{c}}/dy$  curves are provided with both upper and lower theoretical uncertainty bands. As understood from a reading of FONLL papers, the uncertainty bands take into account scale and mass variation. Other uncertainties such as fragmentation and parton distribution functions (PDFs) are small in comparison to the dominant scale and mass choice uncertainties. These theoretical uncertainty bands then represent the envelope of upper and lower bounds achieved by varying the scale and mass choice as described in [114]. While not strictly correct, these upper and lower uncertainty bands are used in this analysis as corresponding to 1- $\sigma$  errors. The choice of using the FONLL uncertainty bands as 1- $\sigma$  errors has been shown to be slightly more conservative than an alternative approach explored in this analysis that uses different FONLL spectra “cases” calculated from differing parameter sets. This side study is described in Section 5.10.4.

### 5.10.3 Total systematic uncertainty of $d\sigma_{c\bar{c}}/dy$ at $y=1.65$

The final systematic uncertainty used in the results is assigned by adding in quadrature both the data and theoretical systematic uncertainties as determined in the previous two sections:

$$\sigma_{sys.total} = \sqrt{\sigma_{data.sys.}^2 + \sigma_{theo.sys.}^2}. \quad (5.16)$$

Based on the scale factors in Table 5.9 of the FONLL spectrum fit the measured single muon spectrum (shown in Figure 5.38), the value for  $d\sigma_{c\bar{c}}/dy|_{y=1.65}$  is determined to be  $0.145 \pm 0.0016$  (stat.)  $^{+0.062}_{-0.072}$  (syst.) mb, or in terms of percentages the uncertainties are  $\pm 1.1\%$  (stat.)  $^{+42.7\%}_{-49.8\%}$  (syst.).

#### 5.10.4 Exploring the theoretical systematic uncertainty by variations in FONLL parameters

*Disclaimer:* Any cross sections or plots derived in this section do not contribute directly to any results presented in this dissertation. However, this section does present a study that investigates the systematic uncertainty in the FONLL theoretical curves not taken directly from the provided upper and lower systematic uncertainty bounds.

The upper and lower FONLL theoretical bounds on the central  $d\sigma^{lepton}/dp_T$  correspond to an envelope of spectra predictions resulting from a matrix of different FONLL calculations, with each calculation “case” corresponding to a particular choice of calculation parameters. The upper and lower theoretical bounds are constructed in this fashion primarily because there is not a single “best” choice of parameters. Ultimately, the “best” choice to evaluate a given FONLL parameter set with would be a precise measurement, the best currently available being the PHENIX single electron measurement with systematic uncertainties of about 10% averaged across all  $p_T$ . Regardless, there still remains some uncertainty in parameter choices, particularly in the quark mass, a direct input to the calculation, as well as the calculation scale choices ( $\mu_R$  and  $\mu_F$ ).

This unavoidable uncertainty in calculation parameter choices can be further understood by taking the example of two different FONLL calculations resulting from two different scale choices (all other parameters being the same for both). It is possible that the two scale choices result in  $d\sigma^{lepton}/dp_T$  curves that cross one another at some  $p_T$ . It is possible that neither of the theoretical spectra will match the data at all  $p_T$ . One curve may best match the data at high  $p_T$ , while the other curve matches best at low  $p_T$ . While not currently available, it is possible that a higher order calculation beyond the existing FONLL (NLO +NLL) would shed some light on the best possible choice of theoretical parameters to use to provide a “best” single theoretical curve. The list of possible modifiable parameters in the context of the FONLL calculation are listed in Table 5.10.

Table 5.10: Modifiable parameters in FONLL with the range of upper and lower values used in this study of 11 FONLL “cases”. Note:  $\mu_0 = m_T = \sqrt{m^2 + p_T^2}$ .

parameter	central value	variation	comment
quark mass	1.5 GeV	1.3 -1.7 GeV	smaller mass $\rightarrow$ more produced
bottom mass	4.75 GeV	4.5 -5.0 GeV	not included in current analysis
$\mu_F$	$\mu_0$	$\mu_F < 2\mu_0$	require: $1/2 < \mu_R/\mu_F < 2$
$\mu_R$	$\mu_0$	$\mu_R > \mu_0/2$	require: $1/2 < \mu_R/\mu_F < 2$
PDF	CTEQ6M	$n/a$	not currently varied
Frag. Func.	default	$n/a$	not currently varied

It is also important to distinguish between real physics inputs, such as quark mass, from more artificial parameters such as the scale choices because each parameter may differently effect  $d\sigma/dp_T$  and  $d\sigma/dy$ . The mass choice matters less at high  $p_T$  than at low  $p_T$ , so possessing a measurement of only some region of  $p_T$  will prohibit constraining the mass at all  $p_T$ .

For a matrix of FONLL  $d\sigma^{leptons}/dp_T$  curves at  $y=1.65$ , such as those listed in Table 5.11, each of the cases will have a corresponding  $d\sigma_{c\bar{c}}/dy$ . The same procedure using Equation 5.15 of scaling each FONLL spectra to fit data could be performed to arrive at a  $d\sigma_{c\bar{c}}/dy$  for each case. This would provide a comprehensive mapping of the associated systematic uncertainties.

### Some caveats on the curves used in this study

A basic assumption of this methodology is that each FONLL case would have a corresponding  $Scale^{FONLL}$  and  $d\sigma_{c\bar{c}}/dy|^{FONLL}$  which are consistent with one another. The exact choice of which FONLL cases/ parameter sets to used in the analysis was determined by Romona Vogt, who provided the calculations in a private communication. Additionally, several calculations were also provided by Matteo Cacciari through private communication to assist in this analysis.

The  $d\sigma^{lepton}/dp_T$  curves used in this study have a minimum  $p_T$  of 0.25 (our request of curves that extend to  $p_T=0.0$  GeV/c is pending). In terms of a cumulative integral plot this corresponds to approximately 75% of the total integral in  $p_T$ . In order to use these FONLL lepton curves they must be extrapolated to  $p_T=0.0$  GeV/c in some way in order to produce the needed  $d\sigma^{lepton}/dy$  curve that is used to obtain the  $d\sigma_{c\bar{c}}/dy$  value. A central FONLL

Table 5.11: FONLL “cases” at  $y=1.65$ . The derived  $d\sigma_{c\bar{c}}/dy$  are plotted collectively in Figure 5.42.

number	Norm. scale to data	$d\sigma^{lepton}/dy$ (mb)	$d\sigma_{c\bar{c}}/dy$ (mb)	comments
0	3.58	4.09e-3	0.142	central, $\mu_0, m_c=1.5$
1	6.87	1.44e-3	0.096	lower envelope bound
2	1.69	1.05e-2	0.172	upper envelope bound
3	5.04	2.67e-3	0.130	$\mu_0, m_c=1.7$
4	2.41	6.33e-3	0.148	$\mu_0, m_c=1.3$
5	2.17	5.52e-3	0.117	$\mu_R = \mu_F = 0.5\mu_0$
6	4.45	1.90e-3	0.082	$\mu_F = 0.5\mu_0, \mu_R = \mu_0$
7	1.79	1.01e-2	0.175	$\mu_F = \mu_0, \mu_R = 0.5\mu_0$
8	5.24	3.27e-3	0.166	$\mu_R = \mu_F = 2\mu_0$
9	3.27	5.56e-3	0.177	$\mu_F = 2\mu_0, \mu_R = \mu_0$
10	5.74	2.34e-3	0.131	$\mu_F = \mu_0, \mu_R = 2\mu_0$

$d\sigma^{lepton}/dp_T$  calculation was obtained with  $\Delta p_T=0.05$  GeV/c that extends to  $p_T=0.0$  GeV/c. This curve is used to extrapolate all eleven test curves to zero. The integral below  $p_T=0.25$  GeV/c for the  $i^{th}$  curve, denoted as  $N_i^{p_T<0.25}$ , is estimated the following way:

$$N_i^{p_T<0.25} = \frac{f_i(p_T = 0.25)}{f_0(p_T = 0.25)} \cdot N_0^{p_T<0.25} \quad (5.17)$$

where  $f_i$  is the value of the particular  $d\sigma^{lepton}/dp_T$  curve,  $N_0$  and  $f_0$  denote the integral and value of the central  $d\sigma^{lepton}/dp_T$  curve, respectively. This approach is vulnerable to differences in the shape of the different  $d\sigma^{lepton}/dp_T$  curves below  $p_T=0.25$  GeV/c. If a 30% error in the extrapolation of the integral for  $p_T < 0.25$  is possible, and the corresponding fraction of the total integral for  $p_T < 0.25$  is approximately 30%, then the expected error on the extrapolation is 9%. While an error of this size is not negligible, it is small enough to proceed with this exploratory analysis with the expectation that additional  $d\sigma^{lepton}/dp_T$  curves that extend to zero will be obtained. It is also hoped that additional curves that vary PDF and fragmentation functions can also be obtained. For the present analysis, three theoretical parameters are varied, mass,  $\mu_F$ , and  $\mu_R$ , and even for these parameters the mass is not varied for each choice of  $\mu_F$  and  $\mu_R$ . Nonetheless, this procedure will still be able to explore some meaningful portion of the FONLL uncertainty phase space, since the parameter choices presented correspond closely to those used by the FONLL authors to define the upper and lower FONLL uncertainty bounds.

## Results from the examination of 11 different FONLL cases

Figure 5.40 plots each of the FONLL  $d\sigma^{lepton}/dp_T$  vs.  $p_T$  (in units of GeV/c) distributions relative to the central FONLL distribution. Each panel corresponds to a different parameter set (with the curve number starting at zero in the upper left plot and increasing moving to the right). The ratio of each curve relative to the central FONLL curve is shown in the lower plot of each panel. The absolute variation in the normalization and shape of the  $p_T$  spectra is observed to vary by as much as a factor of 2.5.

The different FONLL  $d\sigma^{lepton}/dp_T$  parameter sets are listed in Table 5.11.

Figure 5.42 shows the derived  $d\sigma_{c\bar{c}}/dy$  for each of the FONLL parameter sets. The variation in the distribution of these points corresponds approximately to the upper and lower FONLL points (curves 1 and 2). Based on the  $p_T$  spectral shape matching observed in Figure 5.41,

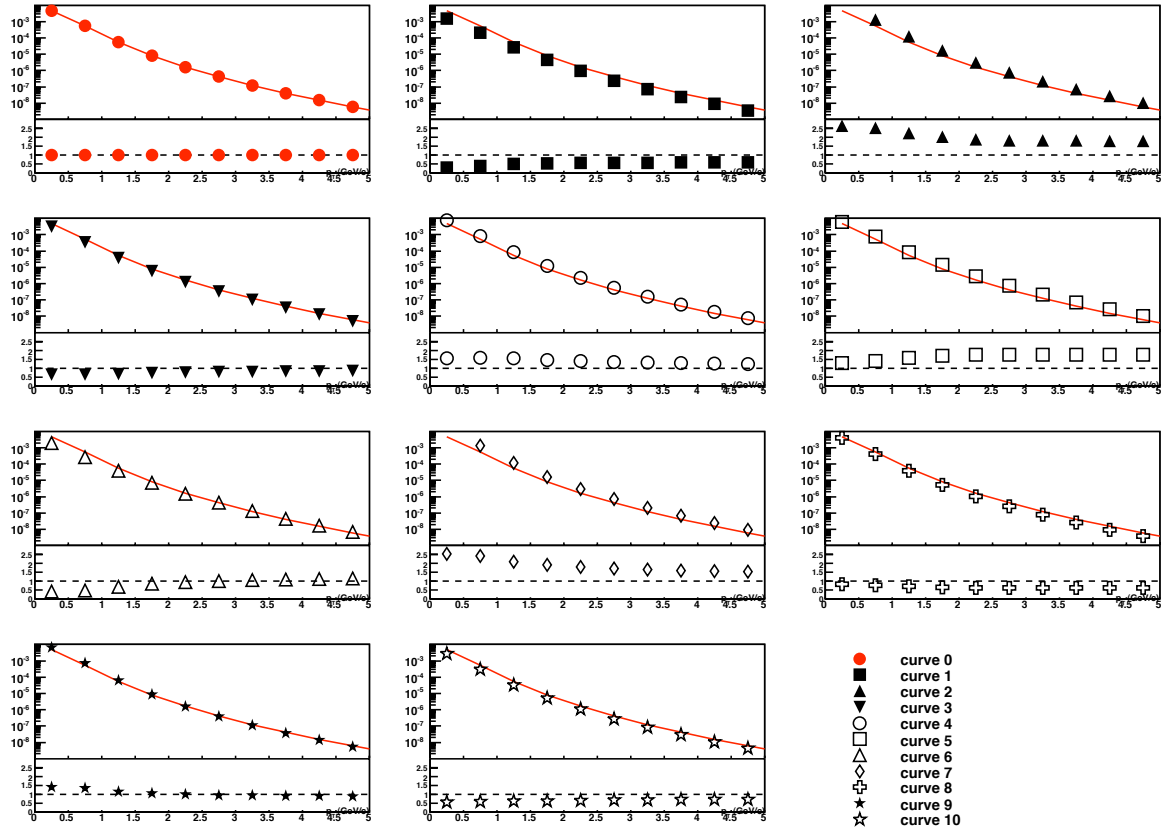


Figure 5.40: Variation of the different FONLL  $d\sigma^{lepton}/dp_T$  vs.  $p_T$  (in units of GeV/c) distributions relative to the central FONLL prediction.

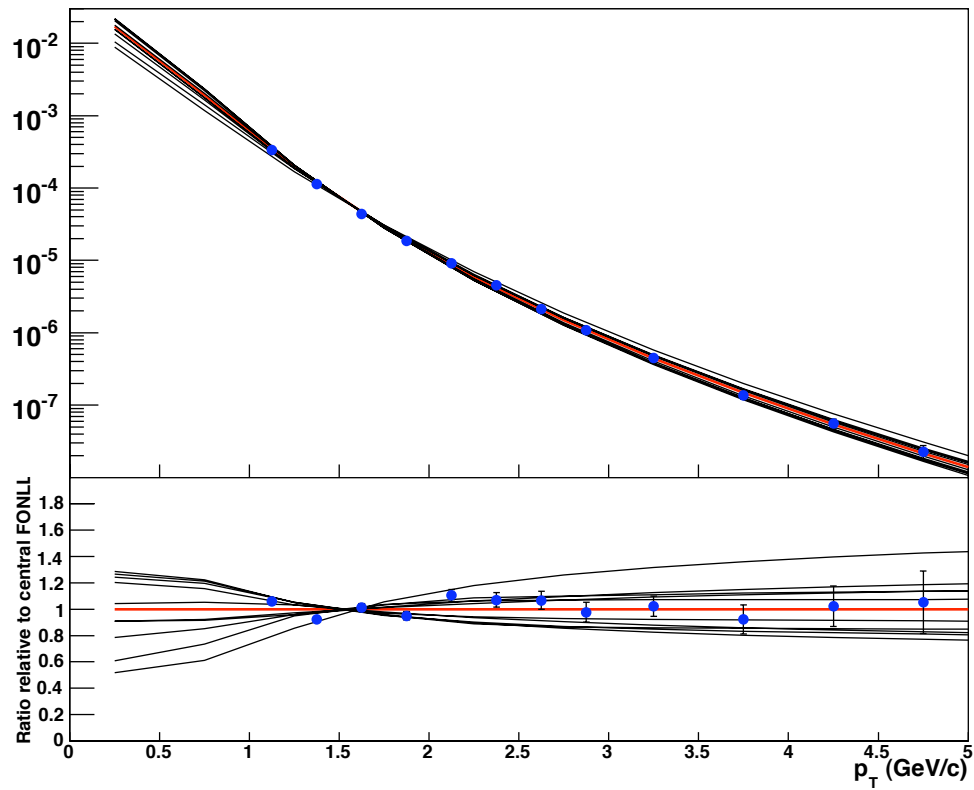


Figure 5.41: Upper panel: Each FONLL curve corresponding to a particular parameter set (Table 5.11) is scaled according to the data matching normalization scale determined by fit. The data is also plotted (blue points). Lower panel: The ratio of each FONLL case is plotted relative to the central FONLL curve (red line). The ratio of the data to the FONLL central curve is also plotted.

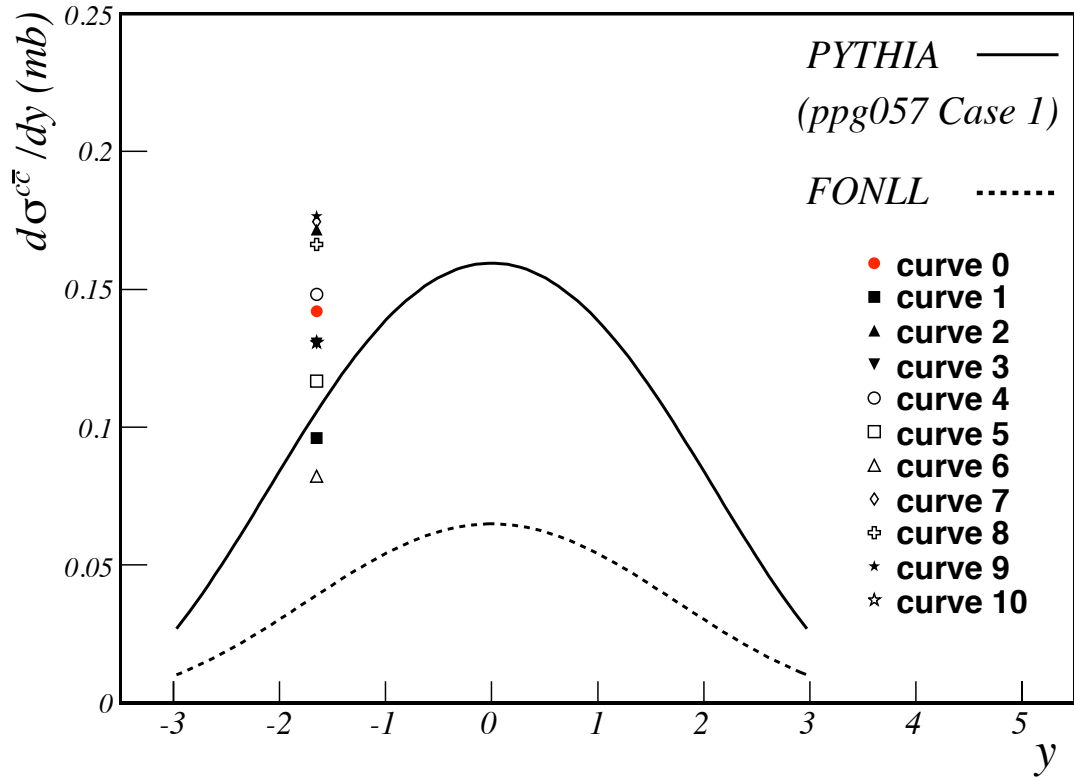


Figure 5.42: Extracted  $d\sigma/dy$  from the 11 different FONLL calculations (see “curves” in Figure 5.40). The spread in the variation of the quark masses and scale choices matches to a great extent the spread in the “standard” upper and lower FONLL theoretical bounds. The central FONLL point is the solid (red) point corresponds to curve 0 and has a  $d\sigma_{c\bar{c}}/dy$  of 0.142 mb.

taking the upper and lower FONLL bounds to serve as  $1\text{-}\sigma$  uncertainty bands to the FONLL central curve is determined to be a reasonable approach, if not absolutely rigorous.

# Chapter 6

## Results and Discussion

There are two primary physics results from this research: 1) the heavy flavor single muon  $p_T$  spectra at  $y=1.65$ , and 2) the integrated charm cross section,  $d\sigma_{c\bar{c}}/dy$ , calculated from the measured  $p_T$  spectra. These two single muon results address multiple issues in the context of the RHIC charm program, which indeed follow-through on the goals and ideals listed in Section 1.1:

- This research has produced a coherent framework for PHENIX to make single muon measurements with substantially reduced and better understood levels of background. It has opened the door to multiple PHENIX single muon measurements that are now nearing completion. In addition, a robust, compact software and data format have been developed to enable this analysis. This framework has now been adopted by multiple colleagues within PHENIX. Analysis techniques developed in the course of this research have been used for analyses of unpolarized  $p + p$  data, polarized  $p + p$  “spin” results,  $Cu + Cu$  data, and  $Au + Au$  data. This research is the first PHENIX analysis and the first dissertation (of a least several to come) to employ these extensive developments. In the development of this analysis method, numerous pitfalls and oversights in past methods were identified and remedied. Multiple technical notes and internal presentations and maintenance of the code in a versioning system have documented and archived these developments for colleagues.
- This measurement provides a test of pQCD calculations for charm production at forward rapidity and large  $\sqrt{s}$  —a relatively unexplored region of phase space where little other experimental data is available. Theoretical understanding of charm, and to a lesser extent, bottom production is plagued by currently irreducible uncertainties

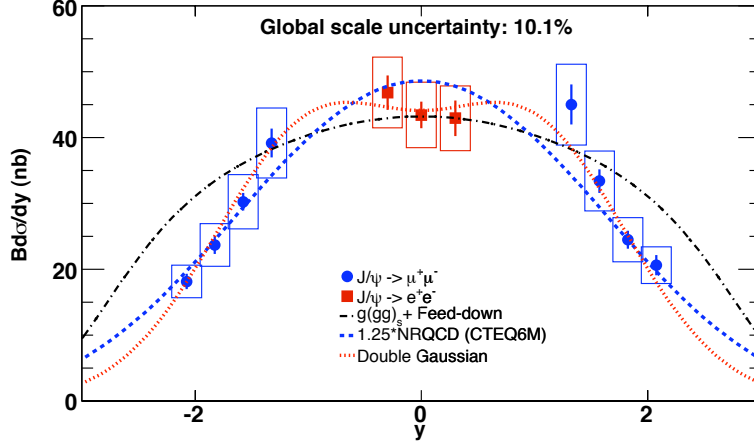


Figure 6.1: PHENIX  $J/\Psi$  rapidity evolution for  $p+p$  collisions at  $\sqrt{s}=200$  GeV for electrons of  $y < 1.5$  and muons of  $y > 1.5$  [115]. An analogous plot for open charm is one of the goals of the single muon measurement.

due in part to renormalization and factorization scale dependences and uncertainties in gluon parton densities. While charm rapidity cross sections are expected to follow a Gaussian distribution, the exact nature of the total charm cross section is unknown. The rapidity evolution for charmonium ( $J/\Psi$ ) has been measured by PHENIX at both mid and forward rapidity (Figure 6.1) [115]. The observed charmonium rapidity distribution is not reproduced by a non-relativistic QCD model (dashed curve) or a pQCD calculation (dash-dot curve) and is best described by a double Gaussian (dot-dot curve) that is not well motivated theoretically\*. The charmonium cross section represents roughly 1% of the total charm cross section. Also of great interest is the rapidity distribution observed for the total charm cross section, which is better studied through open charm measurements that constitute the bulk of the total charm cross section. This research provides a test of the FONLL predictions, and has provided useful feedback to a particular FONLL calculation framework.

- This measurement provides a further test with different techniques and observables to address the current discrepancy between the measured charm cross sections of PHENIX and STAR, which currently differ by *a factor of two*. The discrepancy has persisted for several years over multiple measurements. The large uncertainties in the theoretical predictions preclude theory from clarifying this issue, and the protracted discrepancy has cast a pall, in general, over the charm measurements at RHIC. A PHENIX single

\*References to the specific models in the Figure can be found in [115].

muon measurement with sufficiently small systematic uncertainties could help resolve what has become by 2008 an experimental impasse.

- This single muon measurement in  $p + p$  collisions provides a critical baseline measurement for heavy-ion collisions, such as  $Au+Au$  and  $Cu+Cu$  which explore “hot” nuclear matter, as well as in asymmetric  $d+Au$  collisions which permit the study of so-called “cold” nuclear matter effects. Future PHENIX single muon measurements in these collision systems will form a nuclear modification factor,  $R_{AA}$ , plots (see Equation 1.5 and Figure 1.6) using the  $p+p$  single muon spectra presented in this dissertation to normalize the distributions. Deviations of  $R_{AA}$  from unity in both hot and cold nuclear matter for charm production will provide further insight into the nuclear environment at RHIC.
- This single muon measurement can impose (still quite loose) constraints on recombination models. The potential suppression of the  $J/\Psi$  in a deconfined state of matter (QGP) was one of the driving physics signals in the early RHIC program. To date, experimental results have not provided a clear understanding of possible  $J/\Psi$  suppression. In models [116, 117] for  $J/\Psi$  dissociation and recombination in heavy-ion collisions, the magnitude of  $J/\Psi$  recombination is controlled by the total charm cross section in  $p+p$  collisions.
- This research extends the  $p_T$  reach of the first PHENIX single muon heavy flavor measurement [70] from 3.0 to 5.0 GeV/c with significantly improved statistics (factor of  $\sim 100$ ) and reduced systematic uncertainties ( $\sim 30\%$  smaller).

The discussion is broken into two sections, first for the  $p_T$  spectra and then for the integrated spectra.

## 6.1 Single muon $p_T$ spectra in p+p collisions

After background subtraction and applying the necessary correction factors described in Chapter 5, the invariant cross section,  $E d^3\sigma_\mu/dp^3$ , as a function of  $p_T$  for  $1.0 \leq p_T \leq 5.0$  GeV/c (Figure 5.35) single muons resulting from the semi-leptonic decay of heavy flavor mesons is found. A comparison plot to the Run 2 single muon result can be found in Appendix B.

Figure 6.2 shows a comparison of the Run 5 p+p PHENIX single muon spectra (blue solid

points) to a FONLL calculation [20] (solid black line) with  $\langle y \rangle = 1.65$  averaged over the bin  $1.4 \leq |y| \leq 1.9$ . The charm and bottom components of FONLL are shown (dashed blue and red lines, respectively). Systematic uncertainty in the data is represented with solid blue bands, and in the lower plot, the FONLL uncertainty is indicated by the upper and lower theoretical uncertainty bands (solid lines).

As discussed in Chapter 2, the central FONLL curve is determined by a certain parameter choice for the renormalization/factorization scales and quark mass in the context of a NLO + Next-to-Leading-Log pQCD calculation. The upper and lower theoretical uncertainty bands do not represent Gaussian errors, rather the envelope of possible curves obtained through a systematic variation of the quark mass and the renormalization and factorization scales. The band represents an approximately flat probability region with a high probability of containing the correct calculation [43]. While the uncertainty band defined by the upper and lower theoretical bounds are possibly more conservative than an expected  $1\text{-}\sigma$  uncertainty on the parameter choices. It should also be noted that the FONLL upper and lower limits exclude variations due to fragmentation and parton distribution function choices, which are expected to contribute relatively less theoretical uncertainty than the mass and scale choices [67].

In the comparison between the measured single muon spectra and FONLL shown in Figure 6.2, the data lies a factor of  $\sim 3.5$  to 4 above the central FONLL curve at low  $p_T$ , with the difference decreasing to a factor of two above for  $p_T > 3.0$  GeV/c, which happens to correspond to the charm to bottom crossover region. While the single muon data points lie clearly above the theory, the uncertainties in both the data points (30-40%) and in the theory band ( $\sim 50\%$ ) are such that this single muon measurement is consistent with the theoretical calculation at almost a  $1\sigma$  level. However, the size of the systematic uncertainties preclude this single muon measurement from resolving the STAR/PHENIX single electron discrepancy. The extent of the systematic uncertainties also do not allow this measurement to constrain any of the pQCD parameter choices used in the FONLL calculation, such as the charm quark mass or the renormalization or factorization scale choices.

The observed ratio in the lower plot of Figure 6.2 between the single muon spectra and FONLL calculation is greatest for  $p_T < 3.5$  GeV/c. There are two possible reasons for the increased discrepancy at  $p_T < 3.5$  GeV/c, one experimental and one theoretical. Firstly, as shown in the top panel of Figure 6.2, below this  $p_T$  the contribution from charm dominates that of bottom. While the theoretical footing of bottom production is quite solid, [81, 83]

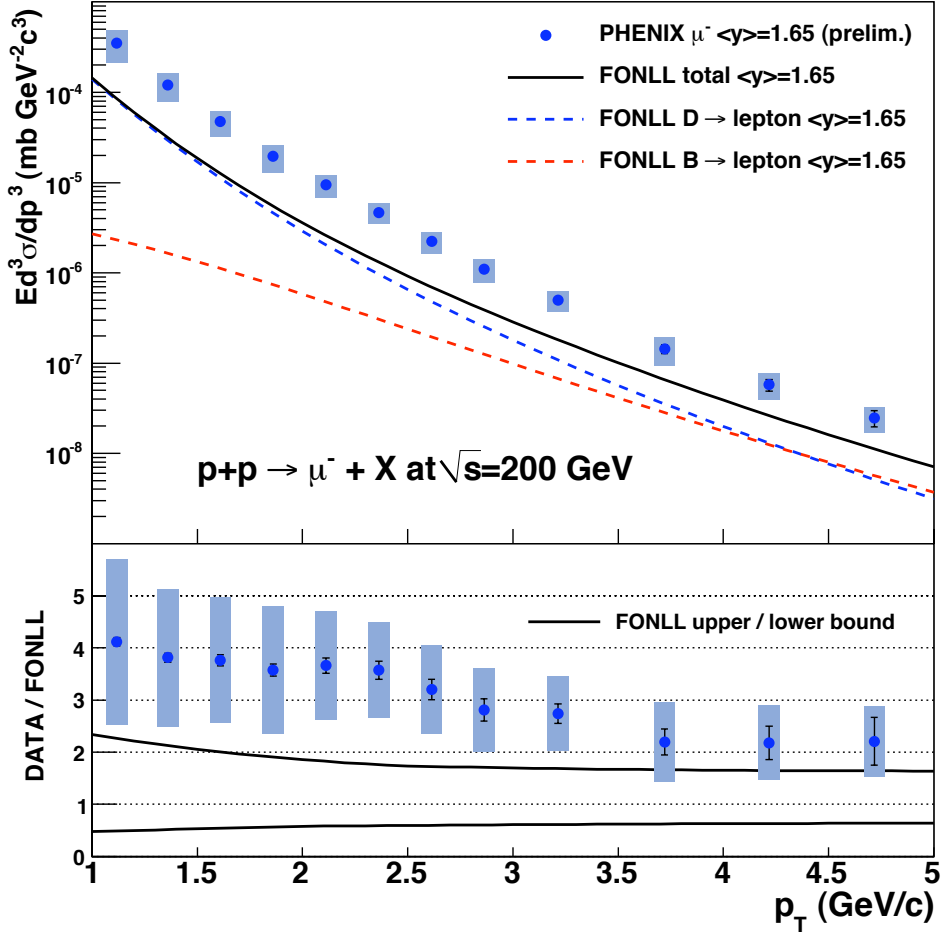


Figure 6.2: Upper plot: invariant differential cross sections of muons from heavy-flavor decay for  $\langle y \rangle = 1.65$ . The error bars (bands) represent the statistical (systematic) errors. The curves are FONLL calculations. Lower plot: ratio of data and FONLL calculation. The upper (lower) curves represent the FONLL upper (lower) limits.

charm production retains large theoretical uncertainties. If one assumes that the bottom production is sufficiently described in pQCD, fixing the bottom contribution and allowing the charm contribution to change can accommodate some of the observed discrepancy, though the size of the uncertainties on the data precludes drawing precise conclusions from such an exercise.

The second likely reason for the increase in the difference between the single muon and FONLL  $p_T$  spectra at low  $p_T$  is strictly related to the data analysis. With a signal/background (S/B) ratio between 0.3 and 0.4 in this  $p_T$  region, just a 10% underestimation of the true background component will result in a mistaken increase of the extracted signal by about one-third. This is the single greatest contributor to the systematic uncertainty bands shown Figures 6.2 and 6.4, where the inverse of the S/B enters as a direct multiplier in determination of the final systematic uncertainties. While both explanations may contribute to the observed difference between FONLL and data at low  $p_T$ , the experimental uncertainties must be reduced in order to provide better theoretical constraints. Suppressing all reducible systematic uncertainties associated with this single muon analysis and improving the S/B at low  $p_T$  through an optimization of the “near-side z-vertex” may permit an overall reduction to  $\sim 25\%$  at lower  $p_T$ . From experience, this number represents the rock-bottom possible uncertainties with the given detector configuration. Even with these reduced uncertainties of order 25%, it is unclear how much constraint this idealized measurement would provide to theoretical inputs, such as renormalization/factorization scale choices. Nonetheless, comparisons of this single muon spectra to other single-lepton heavy flavor measurements at RHIC can also shed some light onto the current experimental situation. It is also of note that planned detector upgrades for both PHENIX and STAR will, if successful, provide dramatic improvements over the existing capabilities for heavy flavor measurements starting in 2011-2012.

The most precise charm measurement at RHIC to date is the PHENIX single electron measurement [26] at  $|y| \leq 0.35$ . With clear electron identification and the measurement of the primary background source of electrons from photon conversion, heavy flavor “non-photonic” electrons are measured over  $0.3 \leq p_T \leq 9$  GeV/c with an average systematic uncertainty on the order of 15%. This spectra is compared to FONLL in Figure 6.3. The data points are shown as circles (red) with yellow systematic uncertainty bands. The measured single electron spectra resides within the FONLL uncertainty bands for  $p_T < 2$  GeV/c and rides along the upper edge of the uncertainty band for higher  $p_T$ . Within the experimental and

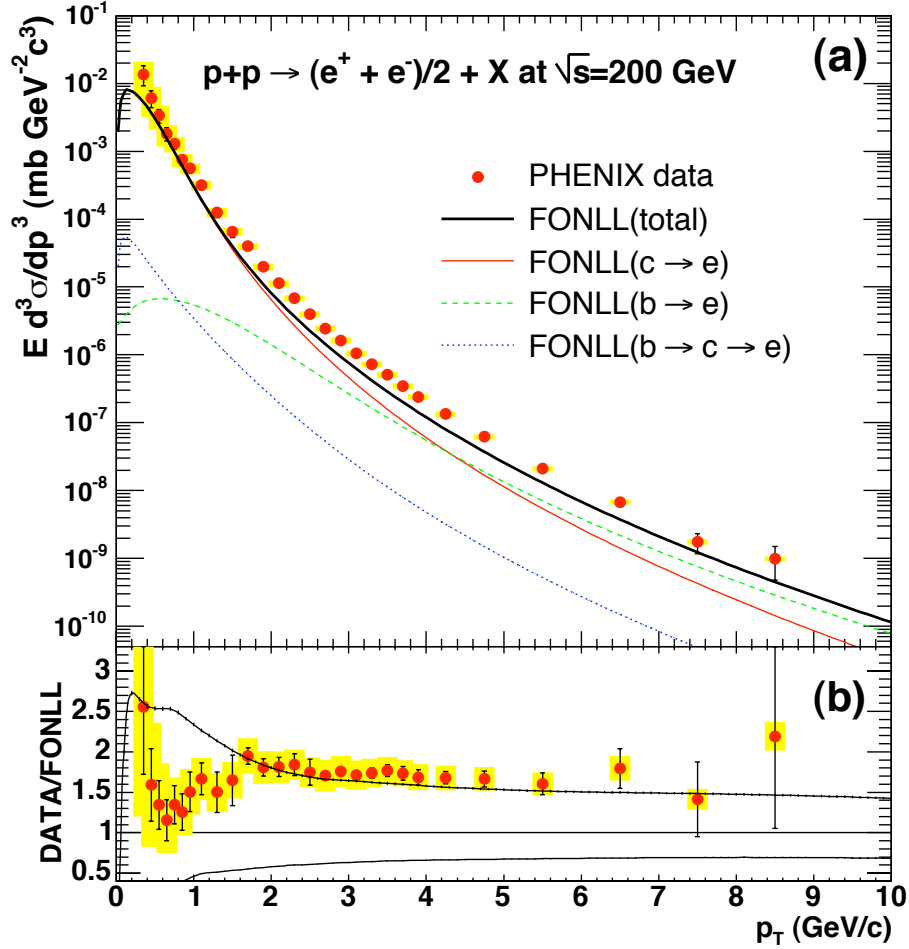


Figure 6.3: Upper plot: invariant differential cross sections of electrons from heavy-flavor decays [26]. The error bars (bands) represent the statistical (systematic) errors. The curves are FONLL calculations. Lower plot: ratio of the data to the FONLL calculation. The upper and lower curves represent the upper and lower limits of the FONLL uncertainty band. An overall normalization uncertainty of 10% is *not shown*.

theoretical uncertainties the PHENIX single electron spectra is consistent with the FONLL curve, though systematically higher by a fit-to-constant value of  $\sim 1.7$ .

In comparing two  $p_T$  spectra, one at mid-rapidity and one at forward rapidity, two trends are expected. First, if one chooses to take the  $p_T$  spectra defined as  $d\sigma/dp_T d\eta$  and integrate over  $p_T$  to obtain  $d\sigma/d\eta$  distributions, the distribution is expected to be Gaussian, reflecting the expected charm distribution. With this standard assumption  $p_T$  spectra at forward rapidity should be *below* an equivalent measurement at forward rapidity. Second, owing to kinematic reasons, the  $p_T$  spectra at  $y=1.65$  are expected to be softer than the  $y=0$  spectra. Figure 6.4 highlights both of these trends.

In the top plot of Figure 6.4, the single muon spectra (blue stars) at  $y=1.65$  is compared to the PHENIX single electron spectra (open circles) at  $y=0$ . The  $y=1.65$  spectra does exhibit the expected softening relative to the  $y=0$  spectra. In the bottom plot of Figure 6.4 the ratio for  $d\sigma/dp_T$  of  $y=1.65/y=0$  is shown for the measured spectra (closed circles) as well as for the predicted FONLL lepton spectra (pink band). Here the behavior of the  $y=1.65$  spectra runs counter to naive expectations, with values at low  $p_T$  exceeding the  $y=0$  spectra and for  $p_T > 3.0$  GeV the data  $y=1.65/y=0$  ratio is closer to the rapidity evolution predicted by FONLL.

Chapter 3 already discussed some of the STAR heavy flavor results measurements at mid-rapidity, including direct measurements of  $D$  mesons and single electrons [27,88]. Figure 3.7 taken from [88] compares the STAR single electron spectra and  $D$  spectra to the PHENIX single electron spectra using FONLL as the common baseline reference. The discrepancy between PHENIX and STAR single electron spectra is well known, with the STAR measurement effectively a factor of two above that of PHENIX for all  $p_T$ . A combined straight line fit to the STAR  $D$  and single electron measurements results in a fit-to-constant value of  $5.5 \pm 0.8(\text{stat.}) \pm 1.7(\text{sys.})$  above the central FONLL prediction.

Figure 6.5 adds this dissertation’s single muon result at  $\langle y \rangle = 1.65$  to the data comparisons made previously to FONLL calculations in Figure 3.7. The FONLL calculation used here [113] differs from that in the published comparison in Figure 6.3. The difference between the two calculations concerns how the fragmentation is done [118]. The fragmentation in [20] circa 2005 differs from the current FONLL implementation in that the fragmentation of the charm quark now uses “ $p_T$ -scaling” rather than “ $p$ -scaling”. The difference manifests itself

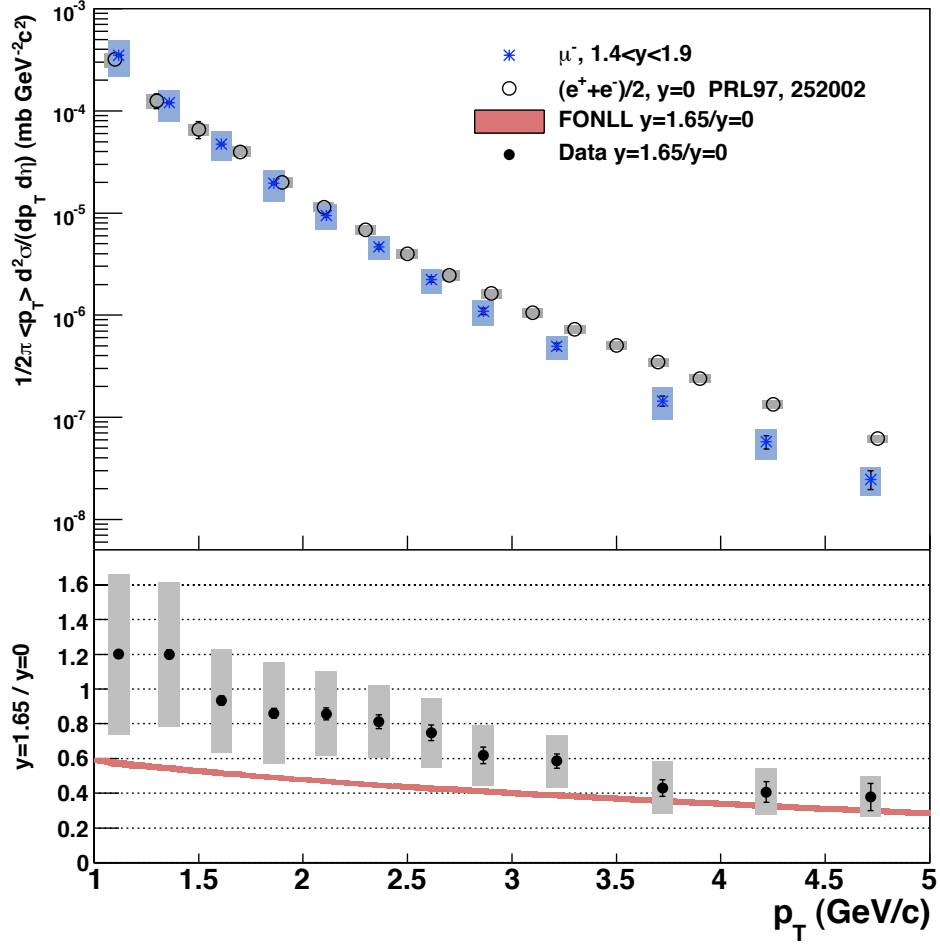


Figure 6.4: Upper plot: invariant differential cross sections of muons from heavy-flavor decay at  $\langle y \rangle = 1.65$  (this work) and electrons at  $\langle y \rangle = 0$  [26]. The expected softening of the spectra at forward rapidity is apparent. Lower plot: ratio of the forward muon spectra to that of electron spectra. The solid red line is the  $y=1.65/y=0$  ratio expected from the FONLL calculation. In both panels, the 10% normalization uncertainty is included in the data systematic uncertainties.

in the rapidity distribution of the charm meson. Where before the p-scaling approach caused the charm mesons to have a *more narrow* rapidity distribution than the charm quarks, the  $p_T$ -scaling results in the charm mesons having essentially the same rapidity distribution as the quarks, which is certainly a more physical result since the charm mesons will have a broader rapidity distribution due to momentum “smearing” in the fragmentation process. The effect of this change on the  $p_T$  spectra can be seen by comparing the original PHENIX single electron ratio to FONLL in Figure 6.3 and Figure 6.5 which is to harden the FONLL calculation at large  $p_T$  while slightly suppressing the spectra for  $p_T < 1.0$  GeV/c. This overall flattening of ratio of the PHENIX data to FONLL raises slightly the fit-to-constant ratio to about 2.0 from 1.7 but does not change the conclusion that the PHENIX single electron spectra is in agreement with the FONLL bands.

Figure 6.5 ignores the STAR D meson results shown in Figure 3.7 which are obtained directly through invariant mass reconstruction of hadron decay channels. Examination of just the STAR single electron data shows that the fit-to-constant in the ratio to FONLL is 4.4 and is relatively flat in  $p_T$ .

The difference between the PHENIX and STAR single electron measurements is at the heart of perhaps the largest experimental discrepancies in the RHIC experimental program, so it is worth some discussion. The most striking feature of Figure 6.5 is the size of the uncertainties on the data points. Above  $p_T > 1.0$  GeV/c, the PHENIX single electron points have an average systematic uncertainty of about 15%, which is significantly smaller than the 35% average on the STAR points. Taking these uncertainties as a reflection of the overall of precision of the given analysis technique, the PHENIX single electron points can be taken as the most precise open heavy flavor measurement at RHIC.

As discussed in Chapter 2, in the realm of  $p_T \sim m_{charm}$ , theoretical calculations must contend with a calculation scheme change and increasing uncertainties due to increasing sensitivity to  $\mu_R$  and  $\mu_F$  variation as  $m_{charm} \rightarrow p_T$ . For  $p_T \gg m_{charm}$ , FONLL treats charm as an active parton ( $n_{lf}=4$ ) in terms of the perturbative calculation and is considered the most rigorous theoretical treatment available [43, 60]. It is in the region of  $4.0 \leq p_T \leq 8.0$  GeV/c, where statistical errors are not too large that the disagreement between the STAR and PHENIX is not easily reconciled. This is also the region where bottom contribution is known to dominate and FONLL has been shown to match measurements in  $p + \bar{p}$  collisions by CDF at the Tevatron to a factor of 1.7 [87]. In this region, the PHENIX single electrons essentially

match the observed cross sections in [87] which is consistent with FONLL and is at a  $2\sigma$  disagreement with the STAR spectrum.

Inclusion of this single muon result into the Figure 6.5 comparison does not immediately clarify the existing STAR/PHENIX single electron discrepancy at low  $p_T$ . At high  $p_T$  ( $p_T > 3.0$  GeV/c) the single muon measurement is consistent with the PHENIX single electron result (Figure 6.5) and also exhibits the expected rapidity evolution of the  $p_T$  spectra as seen in Figure 6.4. The most noticeable feature of the single muon data is that counter to both the STAR and PHENIX single electron data, it does not obviously trend as a constant in  $p_T$  relative to FONLL. Rather, a strong (factor of 2) systematic effect is at work that takes the single muon data from an upper factor of 4 to a lower factor of 2 above FONLL, as  $p_T$  increases. Unrelated experimental and theoretical effects may be at work to produce this trend. Experimentally, as already mentioned, the S/B is decreases from  $\sim 0.5$  to  $\sim 0.3$  from  $p_T=5.0$  GeV/c to  $p_T=1.0$  GeV/c, which greatly increases the sensitivity to the estimated backgrounds. At the same time, between the two primary single muon background sources of muons from hadron decay and punch-through hadrons, the relative background mix is increasingly dominated by muons from hadron decay. At the lowest  $p_T$  the muon decay contribution is a factor of  $\sim 2$  larger than the punch-through component. Tuning of the hadron cocktail to match the MuID gap 4  $z$ -vertex distributions resulted in the largest  $\chi^2$  matching values. It is expected that when the analysis is performed with a improved hadron cocktail implementation a more sophisticated matching scheme than the  $z$ -vertex matching will be improved. This is the single most likely step that can be taken to clarify the trend observed in the single muon data in Figure 6.5.

Theoretically, shifting from a  $p_T=5.0$  GeV/c to  $p_T=1.0$  GeV/c takes the calculation from the case where  $p_T \gg m_{charm}$  which is dominated by bottom quark production to the regime dominated by charm quark production that is subject to large uncertainties in the FONLL prediction due to the relatively low charm quark mass that exacerbates the uncertainties due to  $\mu_R$  and  $\mu_F$  choices. The large uncertainty on both experimental and theoretical fronts leads to the following question: what is the nature of both the experimental and theoretical uncertainties, and how much can those uncertainties be reduced in the near future? On the theoretical side, useful “rule(s) of thumb” concerning perturbative order cross sections and uncertainties can be described as follows [67]:

- A leading order (LO) calculation provides a rough estimate of the cross section.

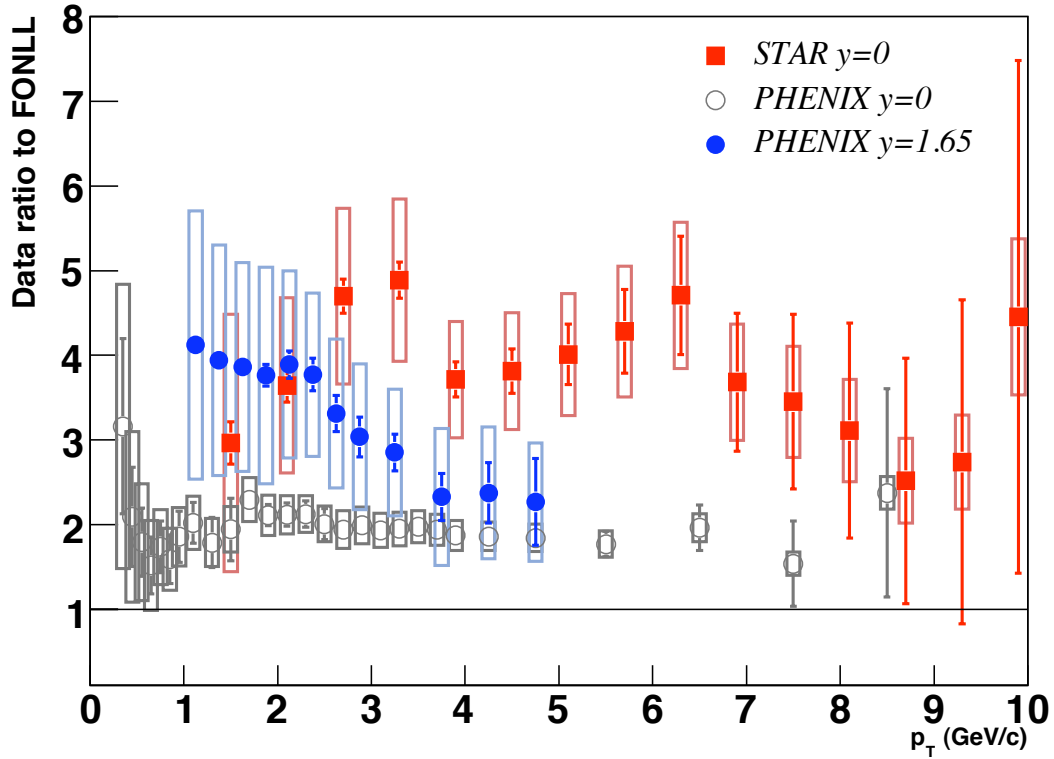


Figure 6.5: Forward single muon results compared to mid-rapidity PHENIX and STAR spectra. The ratio is taken to the appropriate FONLL  $y=0$  or  $y=1.65$  calculation combining charm and bottom. The single muon measurement for this dissertation are the solid circle points labeled PHENIX  $y = 1.65$ .

- A next-to-leading order (NLO) calculation provides a good estimate of the cross section and a rough estimate of the uncertainty.
- A next-to-next-to-leading (NNLO) order calculation provides a good estimate of the uncertainty.

In practice, since a NNLO calculation is not available, the independent variation of both  $\mu_R$  and  $\mu_F$  effectively explores the uncertainties due to truncated higher order terms beyond NLO in the FONLL calculation. As was discussed in Section 2.2.2, the variation of  $\mu_R$  and  $\mu_F$  is the single largest source of theoretical uncertainty in FONLL, with the effect of mass variation the second largest contributor to the uncertainties and uncertainties due to parton distribution and fragmentation relatively small by comparison. Although a FONLL style calculation to one higher order may be several years off (from present day 2008), it is clearly expected to contribute positively to the existing FONLL spectra on the order of 20-30% which will provide better matching than the current level of 1.7-2.0 [43]. Without additional calculations to orders beyond NLO, the only way to constrain the choice of scales is through better precision measurements than what have been made to date, including the single muon measurement presented in this work.

## 6.2 Integrated cross section

### Integrated lepton cross sections

The single lepton production cross sections measured as functions of  $p_T$  discussed up to this point (and referred to as just “ $p_T$  spectra”) are distributions represented in the functional form  $A \times d\sigma/dp_T dy$ , where  $A$  is a constant correcting for finite phase space acceptance and  $dy$  represents the narrow region of measured rapidity. Integration of this  $d\sigma/dp_T dy$  distribution over all measured  $p_T$  above the minimum  $p_T^{min}$  provides a single cross section value for the measured leptons,  $d\sigma_{leptons}/dy |_{p_T > p_T^{min}}$ . Single lepton cross sections of this form are obtained for  $p_T^{min} > 1.0$  GeV/c, which coincides with the minimum measured  $p_T$  in the single muon analysis, for both PHENIX heavy flavor single electrons and muons. These points are plotted at their respective  $\langle y \rangle$  values in Figure 6.6 along with a FONLL single lepton  $d\sigma/dy$  distribution obtained from charmed mesons. While the single electron analysis measures down to a  $p_T$  of 0.35 GeV/c, it is integrated from the same  $p_T^{min}$  as used by the muon analysis to permit an equivalent comparison. The  $p_T$  integrated lepton contribution from bottom relative to charm is  $\sim 1\%$  and is neglected in this plot.

As expected from the  $d\sigma/dp_T dy$  distributions in Figure 6.4, where the muon points exceed the electron points for  $p_T < 1.5$  GeV/c, the  $p_T$  integrated  $d\sigma/dy$  distribution of muons exceeds that of electrons by about 10%. The tabulated values with statistical and systematic uncertainties are located in Table 6.1. This comparison, free of any model dependence, shows straightforwardly that the measured single muon cross section is larger than expected when compared to the published single electron result. However, the large systematic uncertainties of order 40% also accommodate potential agreement with the upper uncertainty band of the FONLL distribution in Figure 6.4, especially in recalling the discussion that the FONLL uncertainties are not Gaussian in nature but essentially a flat probability region for containing the “correct” theoretical value.

### Integrated charm cross sections

The measured  $d\sigma/dp_T dy$  distributions can be used to extract integrated and total charm quark cross sections. Total heavy quark cross sections can be calculated in pQCD, but they are rarely measured because of the requirement of measuring heavy flavor mesons or single leptons down to  $p_T = 0$  GeV/c, which is extremely challenging experimentally. At RHIC, measurements of  $D^0$ 's have been made by the STAR collaboration down to  $p_T \sim 0.1$  GeV/c [27], and measurements of heavy flavor single electrons have been made by the PHENIX collaboration down to  $p_T \sim 0.3$  GeV/c [26]. The experimental uncertainties on both measurements are non-negligible, especially at the lowest values of  $p_T$  which include most of the integrated cross section.

The rapid fall-off of the measured  $p_T$  spectra described approximately by a power-law shape means that even at these low  $p_T$ 's only a fraction of the total cross section is being measured:  $\sim 50\%$  for  $p_T > 0.3$  GeV/c and  $\sim 5\%$  for  $p_T > 1.0$  GeV/c as shown in Figure 5.36. In addition to integrating the  $d\sigma/dp_T dy$  distributions above the minimum measured  $p_T$ , the distribution

Table 6.1: Integrated lepton cross section. Note forward and backward points at  $y=1.65$  are derived from combined forward/backward  $p_T$  spectra.

$y$	Cross section (mb)	$\sigma_{stat.}$ (mb)	$\sigma_{sys.}$ (mb)
0	0.00101	6.98e-5	1.43e-4
1.65	0.00110	1.75e-5	4.04e-4

Table 6.2: Integrated charm quark cross section results. Note forward and backward points at  $y=1.65$  are the same. The total systematic uncertainty assigned is the systematic uncertainty due to the data added in quadrature with the systematic uncertainty inherent in the theory curves.

y	FONLL scale	$c\bar{c}$ cross section (mb)	$\pm$ Stat.	+ Sys.	- Sys.
1.65	3.75	0.145	1.59e-3 1.1%	6.19e-2 42.7%	7.22e-2 49.8%

can be extrapolated in the region from  $0 \text{ GeV}/c \leq p_T \leq p_T^{min}$  by some means. With the availability of a new generation of theoretical pQCD calculations that can produce not only charm and charm hadron spectra, but single lepton spectra as well, the reliance on PYTHIA for this extrapolation has diminished, being replaced by calculations such as FONLL.

As discussed in Chapter 5, the extrapolated lepton spectra can be converted into an integrated charm cross section using the predicted fragmentation of the charm quark, e.g.  $c \rightarrow D$  from a model (such as FONLL) and the known branching ratios to leptons, e.g.  $D \rightarrow lepton$ . Implementations of the quark fragmentation, branching ratios, the extrapolation to  $p_T = 0.0 \text{ GeV}/c$ , and the full phase space correction from the limited detector acceptance all introduce additional systematic uncertainties in the final extracted total cross section which serves to obscure comparisons between theoretical and experimental results, especially in comparisons when the experimental cross section is compared to the model used to derive the cross section. But, due primarily to the limited number of predictions to compare against, this is precisely the situation that is often found (as in this dissertation).

The full procedure used to obtain the charm cross section from the combined-arm single muon  $p_T$  spectrum is described in Chapter 5, where the FONLL spectrum is fit to the measured single muon spectrum in Figure 6.2. The  $d\sigma_{c\bar{c}}/dy$  of the FONLL charm distribution at  $\langle y \rangle = 1.65$  is 0.0386 mb. Multiplying  $d\sigma_{c\bar{c}}/dy|_{y=1.65}^{FONLL}$  by the scale factor (of 3.75) to match the data and FONLL  $p_T$  spectra yields a  $d\sigma_{c\bar{c}}/dy|^{PHENIX}$  of  $0.145 \pm 0.0016$  (stat.)  $^{+0.062}_{-0.072}$  (syst.) mb, shown in Figure 6.7 and listed in Table 6.2. The upper and lower FONLL  $p_T$  spectra uncertainty bands are also fit to data with the resulting scale value and integral used to extract an upper and lower theoretical point  $d\sigma_{c\bar{c}}/dy$ . The resulting normalization scale factors are listed in Table 5.9. The difference between the upper and lower  $d\sigma_{c\bar{c}}/dy$  points are added in quadrature with the data systematic uncertainty (which is about 36% having

also been determined by fitting the FONLL spectra to data) to quote the final  $d\sigma_{c\bar{c}}/dy$  systematic uncertainty. The systematic uncertainty plotted on the  $\langle y \rangle = 1.65$  points includes data and theoretical uncertainties that are at least partially correlated, since the theoretical uncertainty has been folded into the systematic uncertainty boxes assigned to the  $\langle y \rangle = 1.65$  point using the upper and lower FONLL bounds.

As observed in the integrated lepton spectra comparison in Figure 6.6, the single muon point at  $\langle y \rangle = 1.65$  exceeds the extracted  $\langle y \rangle = 0$  point from PHENIX single electron data, as well as that expected from the FONLL distribution. Assuming a Gaussian form for the  $d\sigma/d\eta$  distribution, the FONLL ratio  $\langle y \rangle = 1.65 / \langle y \rangle = 0$  suggests a Gaussian with  $\sigma = \sim 1.7$  which is slightly narrower than the PYTHIA charm distribution used in [70] to extract the integrated charm cross section. While a slightly narrower FONLL distribution would result in the extracted  $\langle y \rangle = 1.65$  point being slightly higher relative to the theoretical curve, however, as indicated in the figure, this effect pales in size with respect to the systematic uncertainties present in both the theoretical and experimental quantities. The total charm cross section determined from the PHENIX  $\langle y \rangle = 0$  single electron measurement is determined to be  $\sigma_{c\bar{c}} = 567 \pm 57^{stat} \pm 224^{sys} \mu b$ . The uncertainties on the single muon point are too large at this time to constrain the rapidity shape of the charm cross section.

As was the case in the discussion of the  $p_T$  spectra, the presence of the STAR charm measurement adds a quantity of intrigue to the state of charm measurements at RHIC. The STAR charm result at  $y=0$  is determined by scaling the central FONLL value by  $5.5 \pm 0.8$  (stat.)  $\pm 1.7$  (sys.), in accordance to the values published by the STAR collaboration [88]. In so much as the expected rapidity distribution is Gaussian, the Run 5 single muon points are consistent with both the PHENIX and STAR  $y=0$  points when considering the  $1\sigma$  systematic uncertainties.

Figures 6.8(a) and 6.8(b) shows two plots, one with the FONLL central curve scaled to the STAR  $\langle y \rangle = 0$  point (scale value of 5.5) and the other scaled to match the PHENIX  $\langle y \rangle = 0$  point (scale value of about 1.9). The FONLL curve scaled to the STAR  $\langle y \rangle = 0$  result, as in Figure 6.8(a), shows that the theoretical curve is observed to pass through the upper tip systematic uncertainty band for the  $\langle y \rangle = 1.65$  muon result. Alternatively, the FONLL curve scaled to the PHENIX  $\langle y \rangle = 0$  result is observed to pass through the lower tip of the  $\langle y \rangle = 1.65$  muon result. The magnitude of the systematic uncertainties associated with the muon result (nearing 50%) do not permit a statement regarding the large discrepancy between the

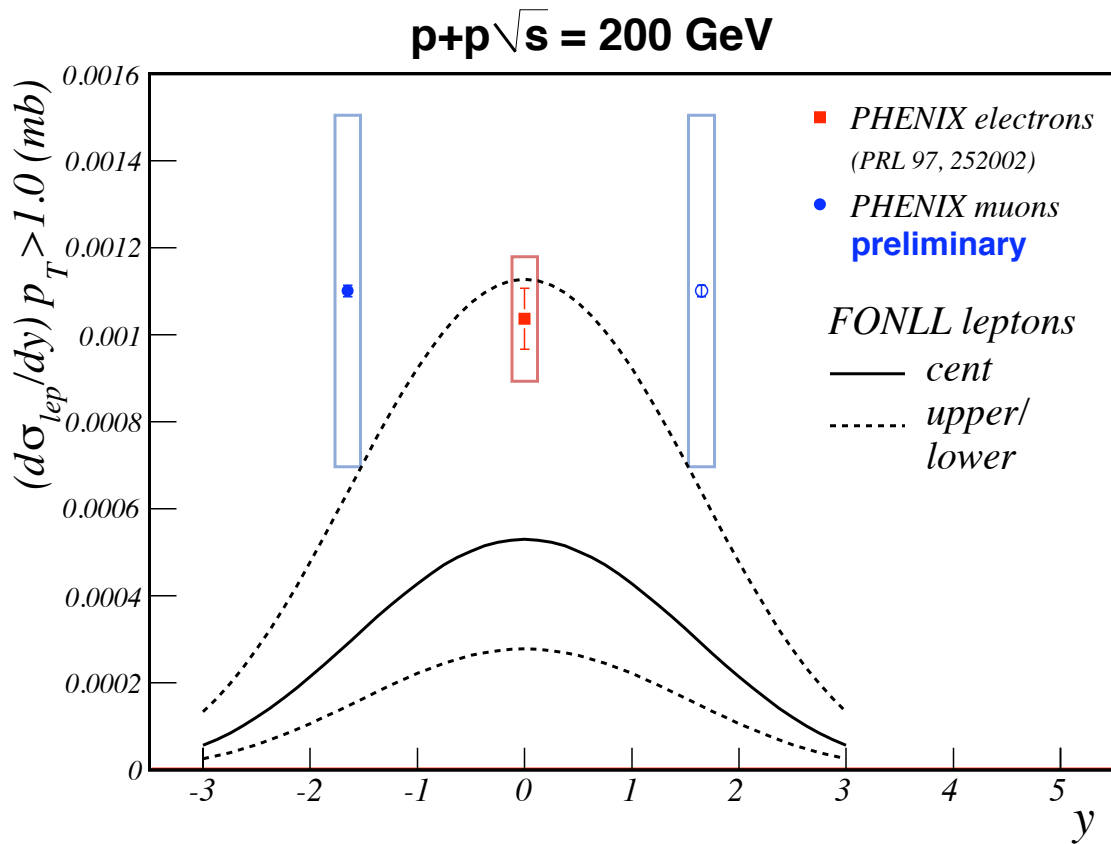


Figure 6.6: PHENIX lepton spectra integrated for  $p_T > 1.0$  GeV/c. Single electrons at  $\langle y \rangle = 0$  and single muons at  $\langle y \rangle = 1.65$ . A 10% global normalization uncertainty due to luminosity determination is not shown for the electron point but is included in the muon uncertainty.

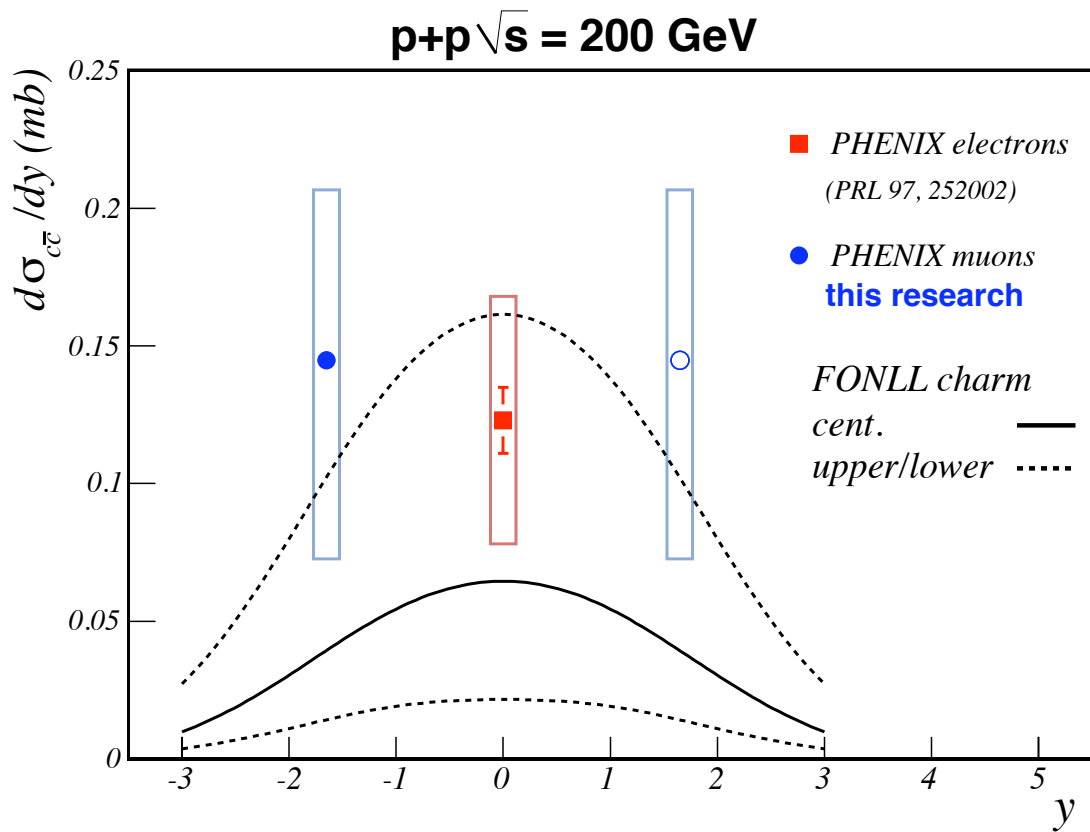
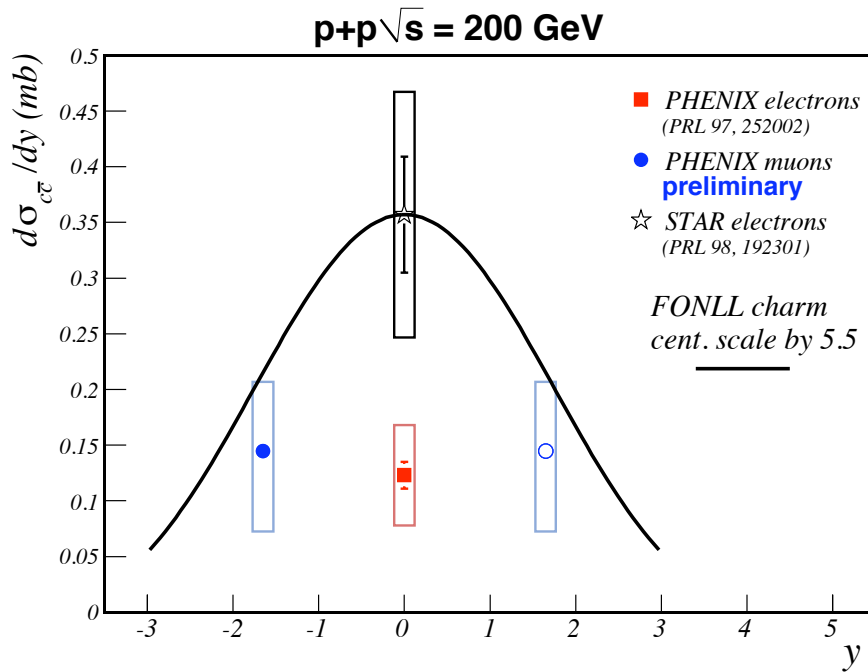
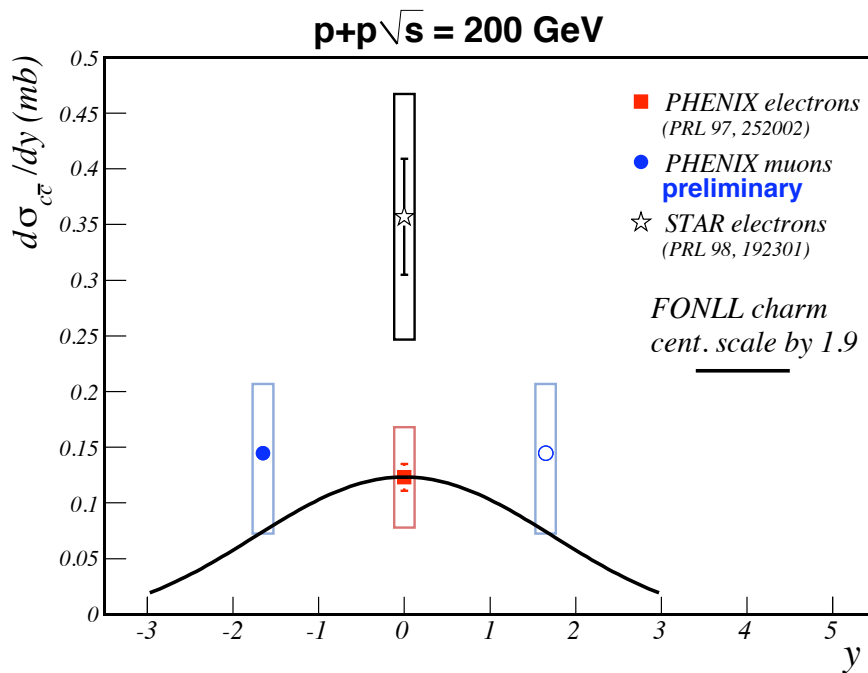


Figure 6.7: Integrated  $d\sigma_{c\bar{c}}/dy$  and  $y=0$  and  $y=1.65$ . Since the collision environment is symmetric, a single value for  $d\sigma_{c\bar{c}}/dy$  is used for  $\langle y \rangle = 1.65$  and  $\langle y \rangle = -1.65$ . The open circle at  $\langle y \rangle = 1.65$  reflects this fact.



(a) FONLL scaled to STAR  $\langle y \rangle = 0$  charm measurement.



(b) FONLL scaled to PHENIX  $\langle y \rangle = 0$  charm measurement.

Figure 6.8: FONLL scaled to PHENIX  $\langle y \rangle = 0$  charm measurement.

PHENIX and STAR results.

Figure 6.9 plots the extracted  $d\sigma_{c\bar{c}}/dy$  at  $\langle y \rangle = 1.65$  along with other relevant results, including the PHENIX single electron extracted point at  $\langle y \rangle = 0$ , the previous single muon point at  $\langle y \rangle = 1.65$ , and the STAR charm estimate [88]. The Run 5 single muon  $d\sigma_{c\bar{c}}/dy$  at  $\langle y \rangle$  point is consistent with the previous Run 2 single muon point, with the Run 5 result sitting at the lower end of the Run 2 1- $\sigma$  systematic uncertainty band. In comparison to the previous Run 2 single muon  $d\sigma_{c\bar{c}}/dy$  point, two observations can be made: 1) the extracted  $d\sigma_{c\bar{c}}/dy$  value has shifted from 0.243 to 0.145 mb (40% reduction), 2) the systematic uncertainty has been reduced. Additional details concerning the downward shift in the extracted single muon charm cross section from Run 2 to Run 5 is discussed in Appendix B.

In general, the reduction in the Run 5 result's charm cross section systematic uncertainties relative to the Run 2 result is due to two effects: 1) reduced systematic uncertainty in the measured single muon spectra, 2) reduced theoretical systematic uncertainty relative to PYTHIA. In regards to the second item, multiple parameter cases of PYTHIA were used in the Run 2 analysis to determine the PYTHIA systematic uncertainty. As discussed in [70], the Run 2 analysis conservatively takes the maximum range in different parameter cases to determine the systematic uncertainty. A few of the PYTHIA parameter choices produces spectra that would be rejected by the Run 5 data but can not be rejected by the Run 2 data due to the larger errors associated with the Run 2 analysis. The use of min bias PYTHIA on the Run 5 analysis to obtain  $d\sigma_{c\bar{c}}/dy$  results in a value of 0.168 mb, 30% below the Run 2 result.

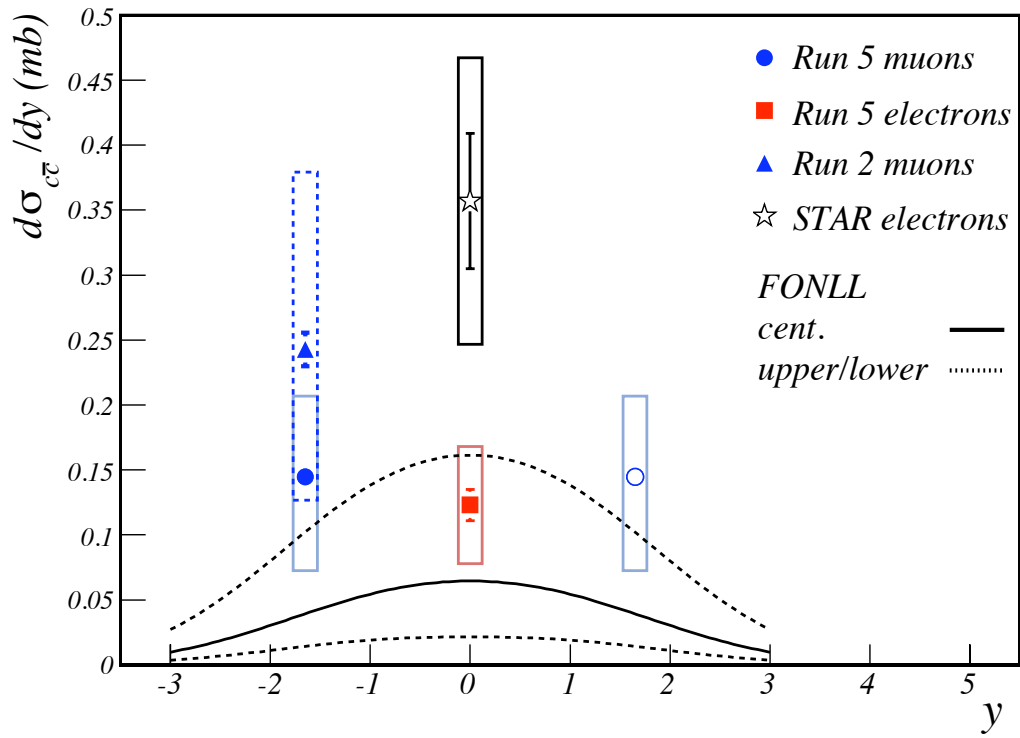


Figure 6.9: Integrated  $d\sigma_{c\bar{c}}/dy$  and  $\langle y \rangle = 0$  and  $\langle y \rangle = 1.65$  for both STAR and PHENIX plotted with the central FONLL curve.

# Chapter 7

## Epilogue

The single muon cross sections presented in this dissertation fall into the regime of measurements not originally envisioned in the planning stage of PHENIX. While some goals, such as the measurement of the  $\phi$  and  $\Upsilon$  at forward rapidity have not really materialized\*, the measurement of single muons in a detector not optimized for their measurement does potentially open up some interesting physics topics for study. The work presented in this measurement follows two previous efforts in measuring single muons in PHENIX. The first result which has been published from the Run 2 data set [70], has been discussed and compared to the results of this dissertation (Appendix B). The second result from the Run 3  $d+Au$  data set using a modified analysis approach to that done in [70] achieved PHENIX preliminary status but has not been published. Ongoing single muon analyses (benefitting from the techniques developed here) in  $Cu+Cu$  and  $Au+Au$  should produce results before 2009 that will allow plots of  $R_{AA}$  for both species to be made which will contribute toward the understanding of the medium produced at RHIC in heavy-ion collisions. On going PHENIX spin analyses to measure both  $A_N$  and  $A_{LL}$  are underway which take advantage of this work, although due to the challenging nature of the analysis, it is not clear whether theoretically restrictive measurements will result from these efforts.

Bypassing the discussion of upgrades in the planning and development stage, it is worth asking what else can be done with the existing data and detector. The work presented in this dissertation has reached PHENIX preliminary status, having been shown at multiple conferences and workshops and has been published in conference proceedings. Before pursuing publication by PHENIX, additional work will be done to extend this analysis in

---

\*There is a PHENIX preliminary result that potentially uncovered about a twenty  $\Upsilon$ 's in the Run 5 data.

both  $p_T$  reach and in the rapidity binning. Since the limitations of this measurement are presently systematic rather than statistical, the extension of the measurement, possibly up to 7.0 GeV (as included in some of the plots in this work), will be pursued. While the acceptance (shown in Appendix I) of the PHENIX muon spectrometer for  $\langle y \rangle = 1.65$  based on minimum ionization energy loss in the muon arm steel is nominally  $p_T = 1.0$  GeV/c, a statistically significant yield of low  $p_T$  heavy flavor muons stop in the second-to-last MuID Gap 3. As shown in Figure I, the muon arm acceptance extends  $p_T < 1.0$  GeV/c. The novel approach of measuring heavy flavor single muons very well may extend the  $p_T$  reach to 0.8 GeV/c, or even lower. One of the most interesting contributions from a heavy flavor single muon measurement is the constraint of the rapidity evolution of the total charm quark production cross section. Future results based on this work will be obtained for multiple data points over the range  $1.4 \leq y \leq 2.0$ . Despite the inherent  $\pm 30\%$  uncertainties on these measurements, some indication of the charm rapidity distribution should be observable.

Several other details of a PHENIX single muon analysis were uncovered in the course of this work and in the parallel work that has commenced for the Cu+Cu single muon analysis. Consideration of these details will modify the measured single muon cross section presented in this work and are briefly mentioned here for completeness. Only time will tell what the final effects of these “details” will have on the final published result. In the “response” stage of the hadron simulations a flaw has been uncovered in how neutral particles are treated. It is possible for neutral particles leaving the absorber material preceding a MuID detector gap to create a charged particle that can deposit a hit in a MuID tube. The simulations used in this work are blind to this effect. After study, the application of a correction is thought to be likely to *increase* the final single muon yield by less than 10%.

Another effect that potentially will *increase* the measured cross section of single muons is the inclusion of positive hadrons. The present work used only negatively charged hadrons to extract the background estimate for negatively charged single muons. Since positive hadrons can result in negative secondaries in the muon arm (and vice-versa for negative hadrons) the effect was originally thought to cancel out when analyzing separately for negative and positive muons. However, an overall charge imbalance does exist in the muon arm where more positive tracks are observed. This imbalance arises from two sources, 1) a measured global charge asymmetry for K’s [119], and 2) a significant difference in the interaction cross section between  $K^+$  and  $K^-$  that leads to significantly more  $K^+$  relative to  $K^-$  reaching the deepest gap of the MuID. Keeping in mind the difference between the  $c\tau$  of K’s and  $\pi$ ’s that leads to

approximately half of the deepest tracks in the hadron background estimate tracks having originated from K's. As a result of this fact and the charge imbalance, it is now realized to be very important to include oppositely charged initial particles in the hadron background estimate.

In this dissertation's single muon measurement the effect of the light vector mesons (primarily  $\eta$ ,  $\rho$ , and  $\omega$ ) has been ignored. Figure 2.9 shows that the expected yield of single muons with  $p_T > 0.9$  GeV/c (from a PYTHIA calculation) resulting from light vector mesons is 13% of the total single muons. Any contribution of these light vector mesons add directly to the measured single muon signal. Figure 2.10 shows that the relative fraction of light vector mesons is more significant at lower  $p_T$ . Recent PHENIX mesons measurements [29] that demonstrate a sort-of universal  $m_T$  scaling parameterization for the light meson yields can be used to provide estimates of the the expected contributions that are included in the present heavy flavor single muon yield. If the estimates provided by PYTHIA are accurate, the expected single muon cross section should be reduced by 10%.

The existing disagreement between STAR and PHENIX is an unfortunate accident of history to which the "lightness" of charm compounds the situation by ensuring existing theoretical calculations can not clearly weigh in. It was clear at the Quark Matter 2008 Conference in Jaipur, India, that this discrepancy is perhaps the largest remaining experimental discrepancy that should not be, for heavy quarks are understood to be clear signals, not sources of controversy themselves. But as pointed out in Chapter 3, discrepancies in charm production between both experiments and theoretical calculations have always existed and eventually resolved themselves. If successfully implemented, both of the PHENIX and STAR upgrades program will greatly enhance both of the remaining RHIC experiments' abilities to measure heavy flavor. I am confident that these upgrades will eventually achieve peace on this subject.

# Bibliography

# Bibliography

- [1] E. Shuryak, Phys. Rept. **61** (1980).
- [2] K. Rajagopal, Nucl. Phys. **A661**, 150 (1999).
- [3] J. Peter *et al.*, arXiv:0705.1930 (2007).
- [4] B. Muller and J. L. Nagle, Annual Review of Nuclear and Particle Science **56**, 93 (2006).
- [5] K. Adcox *et al.*, Nuclear Physics A **757**, 184 (2005).
- [6] F. Karsch, Progress of Theoretical Physics , 106 (2004).
- [7] F. Karsch, E. Laermann, and A. Peikert, Nuclear Physics B **605**, 579 (2001).
- [8] F. Karsch, Nucl. Phys. **A698**, 199 (2002).
- [9] J. Cleymans, H. Oeschler, K. Redlich, and S. Wheaton, Physical Review C (Nuclear Physics) **73**, 034905 (2006).
- [10] P. Braun-Munzinger, K. Redlich, and J. Stachel, nucl-th/0304013 (2003).
- [11] A. Bickley, *Charged Antiparticle to Particle Ratios Near Midrapidity in d+Au and p+p Collisions at sqrt(sNN)=200GeV*, PhD thesis, University of Maryland, 2004.
- [12] J.-P. Blaizot, Nuclear Physics A , 3 (1999).
- [13] G. Kane, *Modern Elementary Particle Physics, The Fundamental Particles and Forces?* (Westview Press, 1993).
- [14] M. Guidry, *Gauge Field Theories, An Introduction with Applications* (John Wiley and Sons, Inc., 1991).
- [15] W. Yao and others (Particle Data Group), Journal of Physics G: Nuclear and Particle Physics **33**, 1 (2006).
- [16] I. Aitchison and A. Hey, *Gauge Theories in Particle Physics. Volume 2: QCD and the Electroweak Theory* (Taylor and Francis, 2005).

- [17] W.-K. Tung, *Perturbative qcd and the parton structure of the nucleon*, 2001.
- [18] C.-Y. Wong, *Introduction to High-Energy Heavy-Ion Collisions* (World Scientific, 1994).
- [19] A. Adare *et al.*, *Phys. Rev.* **D76**, 051106 (2007).
- [20] P. N. M. Cacciari and R. Vogt, *Phys. Rev. Lett.* **95**, 122001 (2005).
- [21] R. Vogt, *Uncertainties in the charm production cross section*, Heavy Quark Workshop at LBNL, 2007.
- [22] J. A. Appel, *Annual Review of Nuclear and Particle Science* **42**, 367 (1992).
- [23] G. Bunce, N. Saito, J. Soffer, and W. Vogelsang, *Annual Review of Nuclear and Particle Science* **50**, 525 (2000).
- [24] F. Halzen and A. Martin, *Quarks and Leptons: An Introductory Course in Modern Particle Physics* (John Wiley and Sons, 1984).
- [25] R. Vogt, *Int. J. Mod. Phys.* **E12**, 211 (2003).
- [26] A. Adare *et al.*, *Phys. Rev. Lett.* **97**, 252002 (2006).
- [27] J. Adams *et al.*, *Phys. Rev. Lett.* **94**, 062301 (2005).
- [28] Y. Morino, *Measurement of charm and bottom production in p+p collisions at  $\sqrt{s} = 200$  GeV at RHIC-PHENIX*, arXiv:0805.3871, 2008.
- [29] A. Adare *et al.*, arXiv:0802.0050 (2008).
- [30] J. Rak and D. Kim, *Heavy quarks and heavy quarkonia as a probe of a new state of matter*, Lecture, 2007.
- [31] M. L. Miller, K. Reygers, S. J. Sanders, and P. Steinberg, *Glauber modeling in high energy nuclear collisions*, nucl-ex/0701025, 2007.
- [32] J. W. Cronin *et al.*, *Physical Review D* **11** (1975).
- [33] S. Adler *et al.*, *Phys. Rev. Lett.* **94**, 232301 (2005).
- [34] PHENIX, A. Adare *et al.*, *Phys. Rev.* **D98**, 172301 (2007).
- [35] M. Bedjidian *et al.*, hep-ph/0311048 (2004).
- [36] Y. Dokshitzer and D. Kharzeev, *Phys. Lett.* **B519**, 199 (2001).
- [37] Z. A., arXiv:0710.0314 (2007).
- [38] M. Bishai and t. C. Collaboration, *Journal of Physics: Conference Series* **9**, 95 (2005).

- [39] J. A. Appel *et al.*, Phys. Rev. Lett. **33**, 722 (1974).
- [40] D. Buchholz *et al.*, Phys. Rev. Lett. **36**, 932 (1976).
- [41] E. Cornell, *Calorimeter/Absorber Optimization for a Relativistic Heavy Ion Collider Dimuon Experiment*, PhD thesis, Vanderbilt University, 1994.
- [42] E. W. Cornell *et al.*, Nuclear Instruments and Methods in Physics Research Section A: Accelerators, Spectrometers, Detectors and Associated Equipment **350**, 150 (1994).
- [43] M. Cacciari, J. Phys. **G34**, 479 (2007).
- [44] M. Gell-Mann, Physical Review **125**, 1067 (1962).
- [45] R. P. Feynman, Physical Review Letters **23**, 1415 (1969).
- [46] B. Povh, K. Rith, C. Scholz, and F. Zetsche, *Particles and Nuclei, An Introduction to the Physical Concepts*, 2nd ed. (Springer, 1999).
- [47] V. Gribov and L. Lipatov, Soviet Journal of Nuclear Physics **15**, 438 (1972).
- [48] G. Altarelli and G. Parisi, Nuclear Physics B **126**, 298 (1977).
- [49] Y. Dokshitzer, Soviet Physics JETP **46**, 641 (1977).
- [50] A. D. Martin, R. G. Roberts, W. J. Stirling, and R. S. Thorne, Eur. Phys. J. **C4**, 463 (1998).
- [51] S. Kretzer, H. L. Lai, F. I. Olness, and W. Tung, Phys. Rev. **D69**, 114005 (2004).
- [52] W. K. Tung *et al.*, JHEP **02**, 053 (2007).
- [53] B. Melic, B. Nizic, and K. Passek, Eur. Phys. J. **C36**, 453 (2004).
- [54] J. C. Collins, D. E. Soper, and G. Sterman, Adv. Ser. Direct. High Energy Phys. **5**, 1 (1988).
- [55] J. C. Collins, D. E. Soper, and G. Sterman, Nuclear Physics B **263**, 37 (1986).
- [56] J. A. Appel, Annual Review of Nuclear and Particle Science , 367 (1992).
- [57] P. Nason, S. Frixione, and G. Ridolfi, hep-ph/9510253 (1995).
- [58] J. C. Collins, Phys. Rev. **D58**, 094002 (1998).
- [59] R. Demina *et al.*, hep-ph/0005112 (1999).
- [60] R. Vogt, The European Physical Journal - Special Topics **155**, 213 (2008).
- [61] P. Nason, S. Dawson, and E. R.K., Nuclear Physics B **303** (1988).

- [62] N. Kidonakis and R. Vogt, Eur. Phys. J. **C36**, 201 (2004).
- [63] P. Nason, S. Dawson, and E. R.K., Nuclear Physics B **327** (1989).
- [64] M. G. Matteo Cacciari and P. Nason, Journal of High Energy Physics , 007 (1998).
- [65] M. Cacciari and P. Nason, Phys. Rev. Lett. **89**, 122003 (2002).
- [66] M. Artuso *et al.*, Phys. Rev. **D70**, 112001 (2004).
- [67] M. Cacciari, Heavy quark production: Prediction of uncertainties and uncertainty of predictions, Heavy Quark Workshop at LBNL, 2007.
- [68] M. Cacciari, FONLL calculation, private communication concerning D meson decay to leptons, 2008.
- [69] T. Sjostrand, L. Lonnblad, and S. Mrenna, hep-ph/0108264 (2001).
- [70] S. Adler *et al.*, Phys. Rev. **D76**, 092002 (2007).
- [71] K. Adcox *et al.*, Physical Review Letters **88**, 192303 (2002).
- [72] M. Gell-Mann, Phys. Lett. **8**, 214 (1964).
- [73] S. Glashow, J. Iliopoulos, and L. Maiani, Phys. Rev. D. , 1285 (1970).
- [74] F. W. Busser *et al.*, Nuclear Physics B **113**, 189 (1976).
- [75] M. J. Tannenbaum, Heavy ion Physics **4**, 139 (1996).
- [76] G. Goldhaber *et al.*, Physical Review Letters **37**, 255 (1976).
- [77] S. P. K. Tavernier, Reports on Progress in Physics **50**, 1439 (1987).
- [78] J. Yoh *et al.*, Phys. Rev. Lett. **39**, 252 (1977).
- [79] C. Albajar *et al.*, Phys. Lett. **B**, 237 (1987).
- [80] C. Albajar *et al.*, Phys. Lett. **B**, 121 (1991).
- [81] M. Cacciari, hep-ph/0407187 (2004).
- [82] S. Frixione, M. L. Mangano, P. Nason, and G. Ridolfi, Adv. Ser. Direct. High Energy Phys. **15**, 609 (1998).
- [83] M. L. Mangano, AIP Conf. Proc. **753**, 247 (2005).
- [84] G. A. Alves *et al.*, Physical Review Letters **77**, 2388 (1996).
- [85] B. Abbott *et al.*, Phys. Rev. Lett. **84**, 5478 (2000).

- [86] D. Acosta *et al.*, Physical Review D **65**, 052005 (2002).
- [87] D. Acosta *et al.*, Phys. Rev. Lett. **91**, 241804 (2003).
- [88] B. I. Abelev *et al.*, Phys. Rev. Lett. **98**, 192301 (2007).
- [89] Y. Zhang, Overview of charm production at RHIC, arXiv:0806.0079, 2008.
- [90] Y. Zhang, *Measurement of charm production cross-section and leptons from its semi-leptonic decay at RHIC*, PhD thesis, University of Science and Technology of China, 2007.
- [91] X. Dong, *Single Electron Transverse Momentum and Azimuthal Anisotropy Distributions: Charm Hadron Production at RHIC*, PhD thesis, University of Science and Technology of China, 2005.
- [92] E. L. Berger *et al.*, Physical Review Letters **86**, 4231 (2001).
- [93] H. Hahn *et al.*, Nuclear Instruments and Methods in Physics Research Section A: Accelerators, Spectrometers, Detectors and Associated Equipment **499**, 245 (2003).
- [94] M. Harrison, T. Ludlam, and S. Ozaki, Nuclear Instruments and Methods in Physics Research Section A: Accelerators, Spectrometers, Detectors and Associated Equipment **499**, 235 (2003).
- [95] P. Steinberg, Hotter, denser, faster, smaller... and nearly-perfect: What's the matter at RHIC?, 410th BNL Lecture, 2005.
- [96] K. Adcox *et al.*, Nuclear Instruments and Methods in Physics Research Section A: Accelerators, Spectrometers, Detectors and Associated Equipment , 469 (2003).
- [97] M. Allen *et al.*, Nuclear Instruments and Methods in Physics Research Section A: Accelerators, Spectrometers, Detectors and Associated Equipment , 549 (2003).
- [98] S. Adler *et al.*, Nuclear Instruments and Methods in Physics Research Section A: Accelerators, Spectrometers, Detectors and Associated Equipment , 593 (2003).
- [99] S. Adler *et al.*, Nuclear Instruments and Methods in Physics Research Section A: Accelerators, Spectrometers, Detectors and Associated Equipment , 560 (2003).
- [100] H. Akikawa *et al.*, Nuclear Instruments and Methods in Physics Research Section A: Accelerators, Spectrometers, Detectors and Associated Equipment , 537 (2003).
- [101] X. Wang, PHENIX muon arm x range for charm, PHENIX Analysis Note 412, 2005.
- [102] A. M. Glenn, *Single Muon Production and Implications for Charm in 200 GeV Au+Au Collisions*, PhD thesis, University of Tennessee, 2004.

- [103] V. Cianciolo *et al.*, Run 5 MuID efficiency results and technical details, PHENIX Analysis Note 501, 2006.
- [104] J. Lajoie, Symset trigger logic, Private communication.
- [105] R. Brun and F. Rademakers, ROOT - An object oriented data analysis framework, <http://root.cern.ch/>.
- [106] R. J. Newby, *J Psi Production in Au+Au Collisions at 200 GeV*, PhD thesis, University of Tennessee, 2003.
- [107] H. P. D. Costa, Offline track finding algorithm in the phenix muon arms, Private communication.
- [108] PHENIX, MUTOO: PHENIX Muon tracker analysis framework, <http://www.phenix.bnl.gov/phenix/WWW/publish/hpereira/doc/mutoo/html/index.html>.
- [109] Geant 3.2.1 manual (1994), CERN W5013, 1994.
- [110] Run 5 p+p 200 gev phenix dimuon analysis webpage, <https://www.phenix.bnl.gov/WWW/p/draft/bickleya/pp200/>.
- [111] W. Leo, *Techniques for Nuclear and Particle Physics Experiments*, Second ed. (Springer-Verlag, 1995).
- [112] W. Vogelsang, Light hadron NLO pQCD calculation, private communication.
- [113] M. Cacciari, Fonll numerical results, Private communication, 2008.
- [114] M. Cacciari, S. Frixione, M. L. Mangano, P. Nason, and G. Ridolfi, *JHEP* **07**, 033 (2004), hep-ph/0312132.
- [115] A. Adare *et al.*, *Physical Review Letters* **98**, 232002 (2007).
- [116] A. Capella *et al.*, arXiv:0712.4331 (2007).
- [117] E. L. Bratkovskaya, W. Cassing, and H. Stoecker, *Phys. Rev.* **C67** (2003).
- [118] Y. Akiba *et al.*, Phenix run 5 single electron analysis note, PHENIX analysis note, 2006.
- [119] I. Arsene *et al.*, *Phys. Rev. Lett.* **98**, 252001 (2007).
- [120] J. K. Pope, *Light-Isotope Production in Relativistic Au-induced Nucleus-Nucleus Reactions*, PhD thesis, Yale University, 1998.
- [121] LANL, Lanl muon arm design, [http://www.phenix.bnl.gov/WWW/muon/design\\_books](http://www.phenix.bnl.gov/WWW/muon/design_books), 1999.

- [122] K. Read, The phenix experiment, 15th Winter Workshop on Nuclear Dynamics, 1999.
- [123] V. Cianciolo, Muon range in mud, private communication, 2000.

# Appendices

# Appendix A

## Glossary of selected terms

This is intended to provide some basic definitions.

1. **Rapidity,  $y$ :** The dimensionless kinematic variable rapidity,  $y$ , of a particle is defined in terms of the energy,  $E$ , and longitudinal momentum,  $p_z$ , of a particle:

$$y = \frac{1}{2} \ln \left( \frac{E + p_z}{E - p_z} \right) \quad (\text{A.1})$$

$y$  can be either positive or negative, depending on the orientation of positive  $p_z$ . Since  $y$  requires knowledge of a particle's full energy, particle identification is required. Rapidity is a convenient variable for describing kinematic properties of particles in high-energy reactions for a couple of reasons. First, due to its properties under a Lorentz transformation, the rapidity of a particle in a moving frame,  $y'$  is equal to the rapidity of the rest frame,  $y$  minus the rapidity of the moving frame,  $y_\beta$  [18]:

$$y' = y - y_\beta.$$

To change between a frame reference at rest to the frame of reference of a particle can be accomplished through a simple addition/subtraction. The second reason for the convenience of using rapidity to describe particle kinematics is its relation to a variable referred to as pseudo-rapidity,  $\eta$ .

2. **Pseudo-rapidity,  $\eta$ :**

$$\eta = -\ln \left[ \tan \left( \frac{\theta}{2} \right) \right]$$

In the limit of  $|\mathbf{p}| \sim E$ , then  $\eta \approx y$ , and  $\eta$  can be substituted into Equation A.1. Since  $\theta$  is often measured experimentally, access to  $\eta$  is “straightforward”, and for sufficiently relativistic particles, which is the case at RHIC with a high degree of accuracy,  $\eta$  provides experimental access to  $y$ .

# Appendix B

## Additional comparison of results

Comparison to the previous PHENIX single muon result [70]

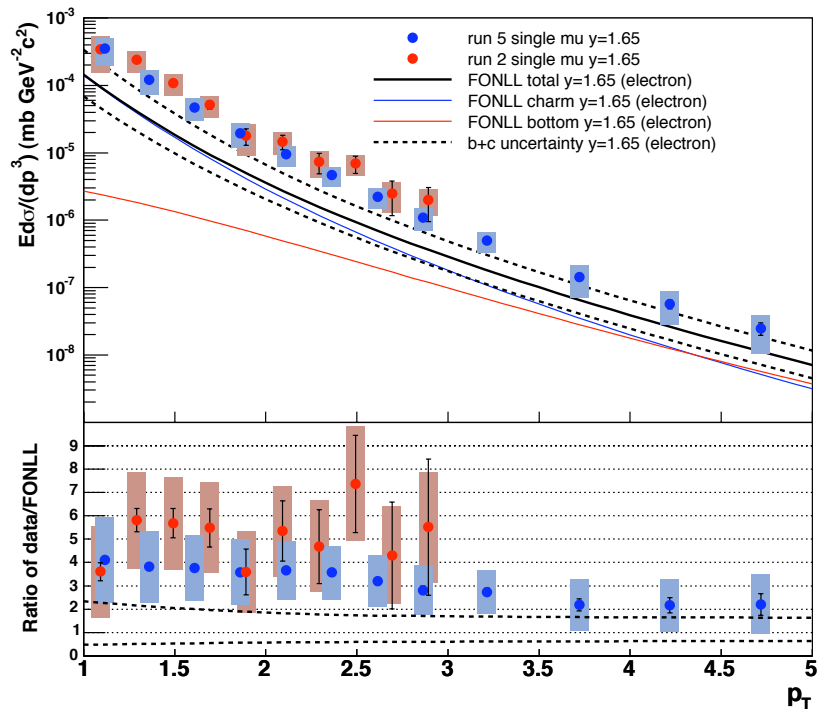


Figure B.1: Run 5 spectra (this work) comparison to the published Run 2 result [70].

Table B.1: PYTHIA tuning parameters, Case 1

Parameter	Value	Meaning
MSEL	2	Minimum bias events
MSTP(32)	4	Hard scattering scale, $Q^2 = \hat{s}$
MSTP(33)	1	Use $K$ -factor
MSTP(52)	2	Use PDF libraries
MSTP(51)	4046	Select CTEQ5L PDF libraries
MSTP(91)	1	Use Gaussian distribution for intrinsic $k_T$
PARP(31)	3.5	$K$ -factor
PARP(93)	5.0	Maximum $k_T$
PMAS(4,1)	1.25	$m_c$ (GeV/c)
$D^+/D^0$	0.32	Default charm chemistry ratio

### Spectra comparison to PYTHIA

$\sqrt{s}=200$  GeV p+p minimum bias collisions were generated in PYTHIA (version 6.205), with the PYTHIA parameters listed in Table B.1. These parameters allow PYTHIA to reproduce the measured charm production at  $y=0$  at SPS and FNAL as well as single electron data at the PHENIX. As opposed to running with PYTHIA MSEL=4 where a heavy quark is produced every collision, running MSEL=2 is the “inefficient” way of obtaining charm and bottom.

### Integrated cross section comparisons with PYTHIA

PYTHIA was used in the charm cross section extraction in [70] (Run 2 PHENIX single muon analysis) and at one point was considered for use in this study. However, a “tuned” PYTHIA has been abandoned in favor of exclusive use of FONLL which is an NLO pQCD calculation. Regardless, for comparison and as a bit of nostalgia, Figure B.3 shows the extracted charm cross section obtained using both PYTHIA (MSEL=2) and FONLL  $p_T$  spectra, illustrating that this current method is consistent with the use of PYTHIA as in [70]. PYTHIA was not used to extract any results presented in this dissertation.

### The reason for the reduced charm cross section from the Run 5 result relative to the published Run 2 result in Figure B.3.

As described in [70], the Run 2 point uses the same basic spectral fitting methodology to extract the charm cross section. In this Run 2 analysis the PYTHIA spectra was produced

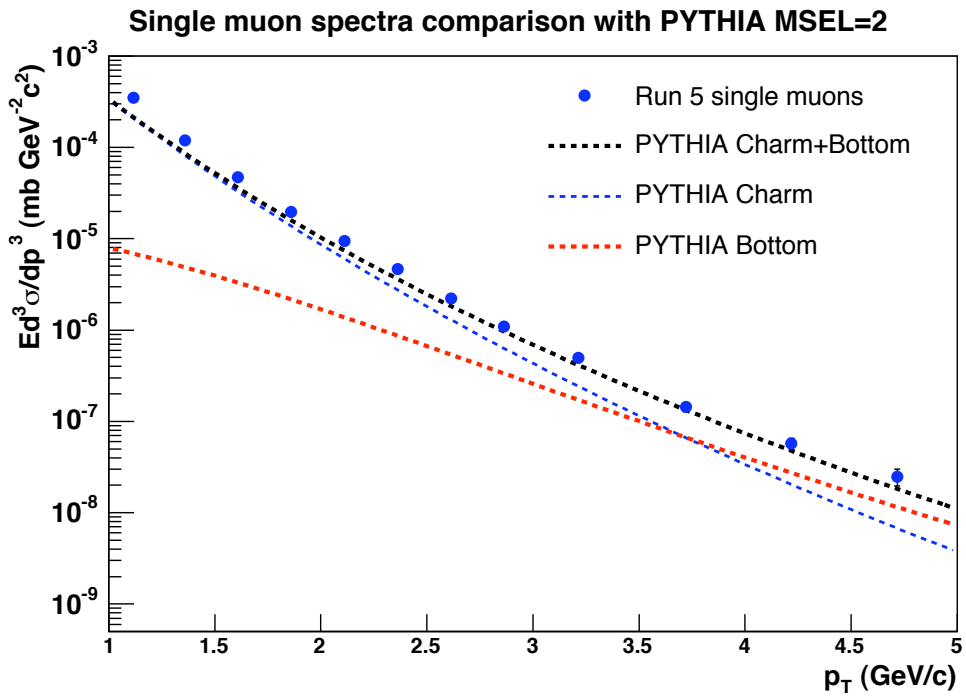


Figure B.2: Comparison with PYTHIA tuned with parameters in Table B.1.

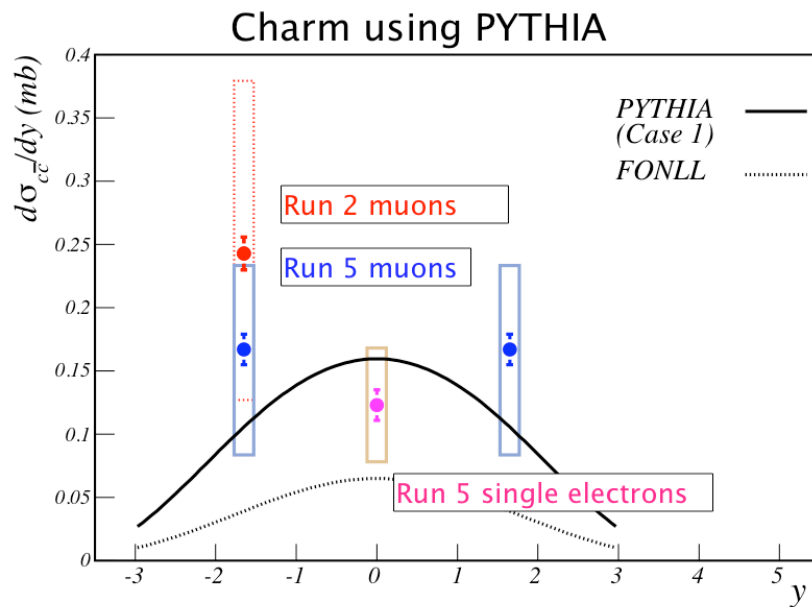


Figure B.3: Comparison plot: Determining  $d\sigma/dy$  at  $y=1.65$  for charm using PYTHIA. The central point determined using Case 1 PYTHIA parameters from [70] and Table B.1 is 0.168 mb, approximately 30% lower than the Run 2 single muon result and about 15% above the  $d\sigma/dy$  determined for Run 5 (not shown) using FONLL.

with the charm heavy quark (HQ) production turned on for every event (MSEL=4). Large differences in the PYTHIA HQ lepton spectra exist between the using MSEL values of 2 (minimum bias) or 4. The HQ lepton spectra produced in the minimum bias events is harder, and the overall cross section is larger. This means that when the minimum bias PYTHIA spectra is used to fit the data instead of the HQ spectra that the overall normalization scale factor needed to match data is lower which results in a lower extracted  $d\sigma_{c\bar{c}}/dy$ . The reason minimum bias PYTHIA was not used in the Run 2 analysis is the large cpu time required to run the multiple parameter sets used to extract the PYTHIA “theoretical” systematic uncertainty. The single min bias PYTHIA parameter set used in this note (Figure B.3) for comparison took two weeks of dedicated running on the ORNL cluster (22 cpu’s). Eighteen different PYTHIA parameter sets were used in the final Run 2 analysis.

# Appendix C

## Derivation of systematic uncertainties

### C.1 From which the errors spring

Using the following notation for invariant yields:

$$N_x \equiv \frac{d^2 N_x(p_T)}{2\pi p_T dp_T d\eta},$$

the yield of single muons as an implicit function of  $p_T$  is determined by the equation:

$$N_\mu = N_I - N_c - N_{2c} \tag{C.1}$$

where  $N_I$  is the yield of inclusive muon candidate tracks,  $N_c$  is the hadron cocktail background yield estimate, and  $N_{2c}$  is the additional yield of particles removed in the two-component fit of the  $p\delta\theta$  distributions. Once the single muon yield is determined, the differential cross section is determined using the following equation:

$$\frac{d^2 \sigma_\mu(p_T)}{2\pi p_T dp_T d\eta} = \frac{\sigma_{BBC}^{pp}}{\epsilon_{BBC}^{c\bar{c} \rightarrow \mu}} \cdot \frac{N_\mu}{\epsilon_{A\epsilon}} \tag{C.2}$$

where  $\sigma_{BBC}^{pp}$  is the cross section of the BBC trigger for p+p interactions and  $\epsilon_{BBC}^{c\bar{c} \rightarrow \mu}$  is the efficiency of the BBC trigger for events in which a charm quark is created and decays into a muon, and  $\epsilon_{A\epsilon}$  is the acceptance times efficiency correction factor for muons reaching gap 4 of the MuID (see Section 5.5 on how  $\epsilon_{A\epsilon}$  is determined).

## C.2 Uncertainty on the yield of single muons assuming an error on $N_I$

The purpose of this section is to develop Eq. 5.10 (see Eq. C.5). For clarity,  $\mathcal{F}$ 's are used to signify fractional uncertainties and  $\sigma$ 's are used to signify absolute uncertainties, meaning explicitly that  $\mathcal{F} = \sigma/N_I$ . Multiplying equation C.1 by  $N_I/N_I$ :

$$N_\mu = N_I \left( \frac{N_I - N_c - N_{2c}}{N_I} \right)$$

The uncertainties on this equation can be propagated as:

$$\mathcal{F}_{N_\mu} = \frac{\sigma_\mu}{N_\mu} = \sqrt{\left( \frac{\sigma_{N_I}}{N_I} \right)^2 + \left( \frac{\sigma_{N_I - N_c - N_{2c}}}{\frac{N_I - N_c - N_{2c}}{N_I}} \right)^2} \quad (\text{C.3})$$

Using  $N_\mu = N_I - N_c - N_{2c}$ , the systematic uncertainty on the muon yield can now be expressed as:

$$\mathcal{F}_{N_\mu} = \frac{\sigma_\mu}{N_\mu} = \sqrt{\left( \frac{\sigma_{N_I}}{N_I} \right)^2 + \frac{\sigma_{N_c}^2 + \sigma_{N_{2c}}^2}{\left( \frac{N_\mu}{N_I} \right)^2}}$$

$\sigma_{N_I}$ ,  $\sigma_{\frac{N_c}{N_I}}$ , and  $\sigma_{\frac{N_{2c}}{N_I}}$  are now rewritten in terms of fractional uncertainties:

$$\mathcal{F}_{N_\mu} = \sqrt{\mathcal{F}_{N_I}^2 + \left[ \left( \mathcal{F}_{\frac{N_c}{N_I}} \cdot \frac{N_c}{N_I} \right)^2 + \left( \mathcal{F}_{\frac{N_{2c}}{N_I}} \cdot \frac{N_{2c}}{N_I} \right)^2 \right] \cdot \left( \frac{N_I}{N_\mu} \right)^2}$$

Reducing terms provides:

$$\mathcal{F}_{N_\mu} = \sqrt{\mathcal{F}_{N_I}^2 + \left( \mathcal{F}_{\frac{N_c}{N_I}} \cdot \frac{N_c}{N_\mu} \right)^2 + \left( \mathcal{F}_{\frac{N_{2c}}{N_I}} \cdot \frac{N_{2c}}{N_\mu} \right)^2}$$

The fractional uncertainties,  $\mathcal{F}_{\frac{N_c}{N_I}}$  and  $\mathcal{F}_{\frac{N_{2c}}{N_I}}$ , are:

$$\mathcal{F}_{\frac{N_c}{N_I}} = \sqrt{\mathcal{F}_{N_c}^2 + \mathcal{F}_{N_I}^2}$$

$$\mathcal{F}_{\frac{N_{2c}}{N_I}} = \sqrt{\mathcal{F}_{N_{2c}}^2 + \mathcal{F}_{N_I}^2}$$

so that the uncertainty can be written as:

$$\mathcal{F}_{N\mu} = \sqrt{\mathcal{F}_{N_I}^2 + \left( \sqrt{\mathcal{F}_{N_c}^2 + \mathcal{F}_{N_I}^2} \cdot \frac{N_c}{N_\mu} \right)^2 + \left( \sqrt{\mathcal{F}_{N_{2c}}^2 + \mathcal{F}_{N_I}^2} \cdot \frac{N_{2c}}{N_\mu} \right)^2}. \quad (\text{C.4})$$

Equation C.4 is used to determine the uncertainty on the yield of single muons. The expected behavior of increasing uncertainty in the yield with decreasing signal background ( $N_\mu/N_c$  and  $N_\mu/N_{2c}$ ) is reflected in this equation.

### C.3 Uncertainty on the yield of single muons assuming no error on $N_I$

If the error on  $N_I$  is considered to be negligible ( $\sigma_{N_I} \rightarrow 0$ ), then the uncertainty in the muon yield reduces to:

$$\mathcal{F}_{N\mu} = \sqrt{\left( \mathcal{F}_{N_c} \cdot \frac{N_c}{N_\mu} \right)^2 + \left( \mathcal{F}_{N_{2c}} \cdot \frac{N_{2c}}{N_\mu} \right)^2}. \quad (\text{C.5})$$

In this case the fractional uncertainties,  $\mathcal{F}_{\frac{N_c}{N_I}}$  and  $\mathcal{F}_{\frac{N_{2c}}{N_I}}$ , are equivalent to the fractional uncertainties on the background sources ( $\mathcal{F}_{N_c}$  and  $\mathcal{F}_{N_{2c}}$ ) since no intrinsic systematic uncertainty is assigned to  $N_I$ .

### C.4 Uncertainty on the single muon differential cross section

The total systematic uncertainty associated for the single muon differential cross section is the quadratic sum of the uncertainties on the four components to the differential cross section (Eq. 5.11)

$$\sigma_{\sigma_\mu} = \sqrt{\sigma_{N_\mu}^2 + \sigma_{\sigma_{BBC}}^2 + \sigma_{\epsilon_{BBC}}^2 + \sigma_{\epsilon_{Ac}}^2}. \quad (\text{C.6})$$

## C.5 Combining North and South muon arm systematic uncertainties with correlated and uncorrelated errors

This subsection explains how equation 5.8 was derived. The standard propagation of errors equation for averaging the north and south arm single muon measurements that possess both correlated and correlated errors is:

$$\sigma_x^2 = \sigma_N^2 \left( \frac{\partial x}{\partial N} \right)^2 + \sigma_S^2 \left( \frac{\partial x}{\partial S} \right)^2 + 2\sigma_{NS}^2 \left( \frac{\partial x}{\partial S} \right) \left( \frac{\partial x}{\partial N} \right) \quad (\text{C.7})$$

where  $x = (N + S)/2$  and  $\sigma_{NS}$  is the covariance term representing the correlated north and south uncertainties. Rewriting  $\sigma_{NS}$  as  $\sigma_{N\&S}^{cor}$ , Eq. C.7 can be written as:

$$\sigma_{\frac{N+S}{2}}^2 = \frac{(\sigma_N^{total})^2 + (\sigma_S^{total})^2}{4} + \frac{(\sigma_{N\&S}^{cor})^2}{2} \quad (\text{C.8})$$

where the last term is the covariance term. The total uncertainties can be divided into the uncorrelated (arm independent) components as well as the correlated components:

$$\sigma_{\frac{N+S}{2}}^2 = \frac{(\sigma_N^{uncor})^2 + (\sigma_{N\&S}^{cor})^2}{4} + \frac{(\sigma_S^{uncor})^2 + (\sigma_{N\&S}^{cor})^2}{4} + \frac{(\sigma_{N\&S}^{cor})^2}{2} \quad (\text{C.9})$$

which reduces immediately to

$$\sigma_{\frac{N+S}{2}} = \sqrt{\frac{(\sigma_N^{uncor})^2 + (\sigma_S^{uncor})^2}{4} + (\sigma_{N\&S}^{cor})^2}. \quad (\text{C.10})$$

In practice,  $\sigma_{N\&S}^{cor} = 1/2(\sigma_N^{cor} + \sigma_S^{cor})$ , so that Equation C.10 can be written as:

$$\sigma_{\frac{N+S}{2}} = \sqrt{\frac{(\sigma_N^{uncor})^2 + (\sigma_S^{uncor})^2}{4} + \left( \frac{\sigma_S^{cor} + \sigma_N^{cor}}{2} \right)^2} \quad (\text{C.11})$$

which is Eq. 5.8.

# Appendix D

## Notes concerning yields and cross section expressions, and how to convert from one to the other

Measurements of single-particle production are discussed in terms of the number of particles per event, per unit of Lorentz-invariant momentum space, referred to as invariant yield or invariant multiplicity [120]:

$$E \frac{d^3 N}{d^3 p} = N(\vec{p}) \frac{E}{\Delta^3 p} \quad (\text{D.1})$$

where  $N(\vec{p})$  is the number of particles per event measured in a bin in momentum space centered at the Energy,  $E$ , and momentum of the produced particle,  $\vec{p}$  in the  $\Delta^3 p$  phase-space volume of the bin. As shown below, a unit of Lorentz-invariant momentum space can be written in terms of the variables  $y$ ,  $p_T$ , and  $\phi$ . Since experimentally the full three-dimensional phase space is not measured,  $\Delta\phi$  is integrated over  $2\pi$  (since the muon arms cover the full  $2\pi$  in acceptance), and the exact form of measured yields is expressed in the double-differential form:

$$\frac{1}{2\pi p_T \Delta p_T} \frac{d^2 N}{dy dp_T} = \frac{1}{2\pi p_T \Delta p_T \Delta y} \cdot N(y, p_T) \quad (\text{D.2})$$

$N(y, p_T)$  is the number of tracks per event in the  $\Delta y$ ,  $\Delta p_T$  bin covered by  $p_T \pm \Delta p_T/2$  and  $y \pm \Delta y/2$ .

## A different derivation of the invariant yield formula

The yield of particles,  $N$ , detected over a finite volume of momentum space  $1/dp^3$ :

$$\begin{aligned}\frac{d^3 N}{dp^3} &= \frac{d^3 N}{dp_x dp_y dp_z} \\ &= \frac{d^3 N}{p_T dp_T d\phi dp_z}\end{aligned}$$

using  $dp_x dp_y = p_T dp_T d\phi$  for change to cylindrical coordinates. Integrating over the full azimuth in  $d\phi$ :

$$\frac{d^3 N}{dp^3} = \frac{d^2 N}{2\pi p_T dp_T dp_z}$$

then using  $p_z = m_T \sinh(y)$  [18]:

$$\frac{d^3 N}{dp^3} = \frac{d^2 N}{2\pi p_T dp_T d(m_T \sinh(y))}$$

and taking the derivative in the denominator:

$$\frac{d^3 N}{dp^3} = \frac{d^2 N}{2\pi p_T dp_T m_T \cosh(y) dy}$$

and using  $E = m_T \cosh(y)$ , and the invariant yield is ...

$$E \frac{d^3 N}{dp^3} = \frac{d^2 N}{2\pi p_T dp_T dy} \tag{D.3}$$

For the case of the PHENIX muon arm where a number of tracks,  $N$ , is measured in a particular pseudo-rapidity bin, say  $\Delta y \sim \Delta\eta = 1.9 - 1.4 = 0.5$ , and in a particular  $p_T$  bin of a particular width  $\Delta p_T$ , then the invariant yield is formed according to Equation D.3.

### Converting $d\sigma/dp_T$ to $E \frac{d\sigma}{dp^3}$

Theoretical curves have been provided in primarily two ways that must be converted in order to compare to data in the form of  $E \frac{d\sigma}{dp^3}$ . FONLL  $p_T$  spectra have been provided in the form of  $d\sigma/dp_T$  integrated over a particular  $d\eta$  range. In this case, to numerically convert

(c.f. Eq. D.3)  $d\sigma/dp_T$  values to  $E \frac{d\sigma}{dp^3}$ , one need only multiply by the so-called “phase-space factor”,  $1/(2 \pi d\eta dp_T)$ :

$$E \frac{d^3\sigma}{dp^3} = \frac{1}{2\pi d\eta dp_T} \cdot \frac{d\sigma}{dp_T} \quad (\text{D.4})$$

# Appendix E

## Bin shift corrections

This appendix describes the method of bin-shift correction used in this analysis. The magnitude of the corrections are in fact quite small and are only mentioned for completeness. This information is adapted from internal PHENIX sources and is listed here for reference. Data which is distributed along exponential curves, such as particle yields as a function of  $p_T$ , will experience a non-negligible error when binned in  $p_T$ . The exponential drop-off is significant inside a single bin such that the center of the bin (in  $p_T$ ) will not correspond to the average  $p_T$  of the data in that bin. There are two ways to approach this issue:

1. Move the data point vertically and leave the  $p_T$  of the data point unchanged, i.e. use the bin centers to represent the  $p_T$  points.
2. Move the data point along the  $p_T$ -axis and leave the yield unchanged. The average value of  $p_T$  for that particular bin is used for plotting and in all calculations involving invariant yields, etc.

### Method 1

The method 1 correction depends on approximating the spectra with some function. When fitting entire exponential or power-law distributed data points, the fits tend to match the data well at low  $p_T$  but not at high  $p_T$  due to the several orders of magnitude drop of in the value of the data. In order to side-step this issue, the data distributions can be accurately approximated with an exponential or power-law function over several subranges of the full distribution. Each function can then be evaluated in its particular fit sub-region, which is what Figure 5.37 is essentially showing.

The corrected yield in a given  $p_T$  bin is calculated in the following way:

$$dN/dp_T |_{corrected} = \frac{dN/dp_T |_{uncorrected}}{R}. \quad (\text{E.1})$$

Where  $R$  is the ratio of the average yield in the bin to the value of the function at the bin center  $p_T^c$ .  $R$  is defined as:

$$R = \frac{\frac{1}{\Delta} \int_{p_T^c - \Delta/2}^{p_T^c + \Delta/2} f(p_T) dp_T}{f(p_T^c)}. \quad (\text{E.2})$$

Where  $\Delta$  is the bin width. This approach is equivalent to just evaluating the fitting function at the bin center and taking the value of  $f(p_T)$  provided that:

$$dN/dp_T |_{uncorrected} = \frac{1}{\Delta} \int_{p_T^c - \Delta/2}^{p_T^c + \Delta/2} f(p_T) dp_T \quad (\text{E.3})$$

## Method 2

The method 2 correction is achieved in this work by calculating the average  $p_T$  value for every histogram bin in every instance. This method has the advantage in that it is easy to use numerically and program, but it does suffer from the fact that it makes any subsequent comparisons less straightforward since not all  $p_T$  points exactly correspond.

Most of the work done in this analysis, including the results are presented using method 2, although some final comparisons are made instead with Method 1 corrections.

Table E.1: Method 1 bin-shift correction factors for single muon data points

Average $p_T$ (GeV)	Bin center (GeV)	R
1.118	1.125	1.054
1.360	1.375	1.063
1.610	1.625	1.071
1.860	1.875	1.043
2.112	2.125	1.035
2.363	2.375	1.038
2.614	2.625	1.057
2.863	2.875	1.012
3.214	3.25	1.103
3.720	3.75	1.062
4.218	4.25	1.034
4.717	4.75	1.089

# Appendix F

## Details on the modification of the hadronic package cross sections in the CERN libs

The analysis methodology established in this dissertation depends upon the ability to “tune” the simulation response to hadrons by altering the interaction cross sections of the hadron shower packages available in GEANT 3. In April 2006, during his postdoctoral tenure at the University of Tennessee, Youngil Kwon performed a basic modification to both the FLUKA and GHEISHA hadron shower packages. The hadron interaction cross sections do possess some momentum dependence, but as a basic attempt, the interaction cross section of material was scaled by a simple constant. Since the GEANT 3 implementation of the PHENIX muon arms is rather basic and dominated by the large amount of steel material, the approximation of scaling the hadron cross sections for all materials was used.

The 2005 CERN libraries were used, and the scaling of the material cross sections are performed in the following two files:

for FLUKA: */src/geant321/fiface/fldist.F*

for GHEISHA: */src/geant321/giface/ghesig.F*

The modification to FLUKA is presented verbatim below:

```
kwon We modify FLUKA! =====  
ckwon decide scale factor based on switch
```

```

        if(iswit(6).eq.0) then
ckwon   Case we don't change hadron interaction cross section
        CrossXScaleFactor = 1
    else
        if(iswit(10).eq.0) then
ckwon   Case we scale cross section uniformly
        CrossXScaleFactor = iswit(6)/10000.0
        if(firstcall.eq.1) then
            print *,'*****
            print *,'***** Modified FLUKA for muon analysis *****
            print *,'***** Version 1.00 *****
            print *,'*   Date : Apr. 24th, 2006                               *
            print *,'*   Iinitial work : Y. Kwon                               *
            print *,'*       iswit( 6) = ',iswit(6)
            print *,'*       We scale hadron cross section by ',
+ CrossXScaleFactor
            print *,'*****
        endif
    else
ckwon   Case we scale PI/K- cross section and K+ cross section
        if(firstcall.eq.1) then
            print *,'*****
            print *,'***** Modified FLUKA for muon analysis *****
            print *,'***** Version 1.00 *****
            print *,'*   Date : Apr. 24th, 2006                               *
            print *,'*   Iinitial work : Y. Kwon                               *
            print *,'*       iswit( 6) = ',iswit(6)
            print *,'*       iswit(10) = ',iswit(10)
            print *,'*       We scale PI/K- cross section by ',
+ iswit(6)/10000.0
            print *,'*       We scale      K+ cross section by ',
+ iswit(10)/10000.0
            print *,'*****
        endif
        CrossXScaleFactor = 1

```

```

        if(IPART.eq.8.or.IPART.eq.9.or.IPART.eq.12) then
            CrossXScaleFactor = iswit(6)/10000.0
        endif
        if(IPART.eq.11) then
            CrossXScaleFactor = iswit(10)/10000.0
        endif
    endif
endif
firstcall = 0

SINE = CrossXScaleFactor*SINE
SELA = CrossXScaleFactor*SELA

ckwon    print *, ' (YKWONF) IPART,CrossXScaleFactor ',
ckwon    + IPART,CrossXScaleFactor

ckwon =====

```

# Appendix G

## Run 5 MuID efficiency plots

Run 5 MuID tube efficiency plots are shown in Figure G.1 and Figure G.2 and are taken from [103].

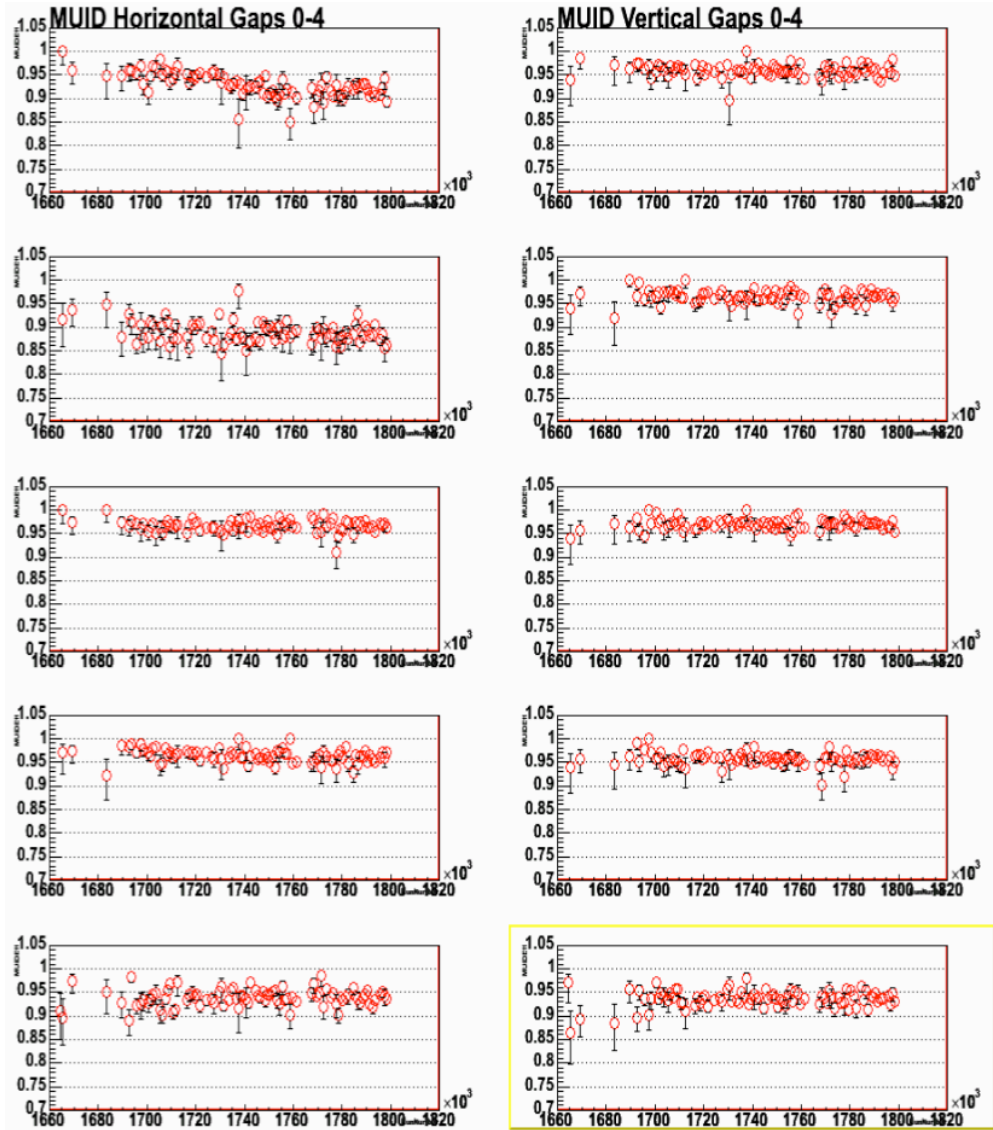


Figure G.1: MuID efficiencies versus run, north muon arm.

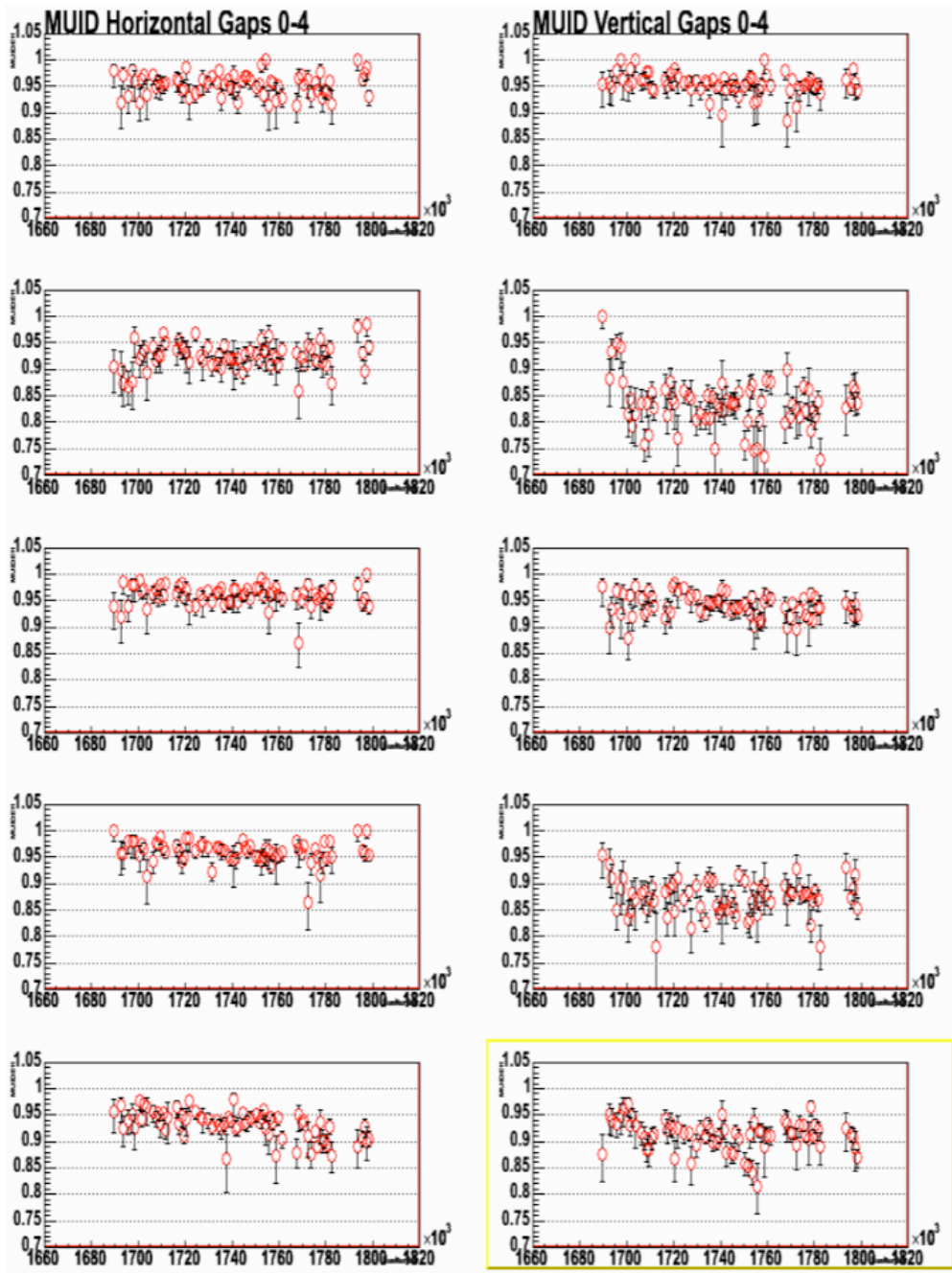


Figure G.2: MuID efficiencies versus run, south muon arm.

# Appendix H

## Design specifications and performance of the PHENIX muon spectrometer

The PHENIX muon spectrometers design specifications were driven by the following physics requirements [121] [122]:

1. Resolve  $\phi$  (1.02 GeV) from  $\rho$  (0.77 GeV) and  $\omega$  (0.78 GeV) and optimize signal to background.
2. Resolve  $J/\Psi$  (3.097 GeV) from  $\Psi'$  (3.686 GeV) and optimize signal to background.
3. Resolve  $\Upsilon(1S)$  (9.46 GeV) from  $\Upsilon(2S+3S)$  (10.02+10.36 GeV) over all rapidity (including central rapidity).
4. Have low enough occupancy to be able to reconstruct tracks efficiently in central  $Au + Au$  events (with a particle multiplicity of about 1000 particles).
5. High performance in lower occupancy/ higher event rate  $p + p$  and  $d + Au$  events.

In order to meet these design goals the muon tracking chambers are required to be able to provide 100  $\mu m$  resolution in particle trajectory measurement. Physics simulations (circa 1999) conducted assuming this resolution performance and test-bench measurements of production chambers and electronics provided the following expected mass resolutions as follows:  $\phi \approx 80 \text{ MeV}/c^2$ ,  $J/\Psi \approx 110 \text{ MeV}/c^2$ , and  $\Upsilon \approx 200 \text{ MeV}/c^2$ . Absent from this list of physics goals is measuring heavy flavor single muons as performed in this work.

The following sections describe the muon spectrometer used for this research, installed in

1999-2000 and operated in essentially the same configuration through the RHIC Run 5 period (2005) when the data taken for this particular work was recorded. Since 2006 PHENIX has engaged in an ongoing detector upgrades program that is introducing new and/or upgraded subsystem detectors annually. Upgrades to the muon arm's electronics, trigger capabilities, and a forward silicon vertex detector are currently planned for 2009-2010 and after. These upgrades are under way largely as an effort to enhance the  $W$  detection capability in a future  $\sqrt{s}=500$  GeV  $p+p$  run, but these upgrades may also significantly improve PHENIX's ability to measure heavy flavor single muons.

### **Performance of the PHENIX muon spectrometer with regards to design specifications**

We will briefly run through the list of physics goals for the PHENIX muon arms previously listed.

1. Resolve the  $\phi$  meson. Due to larger than expected backgrounds, the  $\phi$  has not been measured in any collision environment.
2. Resolve the  $J/\Psi$  meson. The PHENIX muon arms have measured the  $J/\Psi$  in all recorded collision environments. Figure H.1 shows the separate  $J/\Psi$  peaks for the North and South muon arms measured during the same run period of this dissertation's single muon measurement ( $p+p$  at  $\sqrt{s} = 200$  GeV). The mass resolution as determined from a gaussian fit to the  $J/\Psi$  are about 180 MeV, larger than the design resolution of 110 MeV, but still good enough to provide a rich collection of physics results.
3. Resolve  $\Upsilon(1S)$ . A dimuon pair analysis on the same 2005  $p+p$  data set resulted in a total of 27  $\Upsilon$  events *in both arms* (15 North and 12 South) [PHENIX AN401]. Relative to  $J/\Psi$  dimuons, dimuons in  $\Upsilon$ s are higher momentum muons that experience less multiple scattering in the ample absorber material. The primary limitations in the  $\Upsilon$  mass resolution are associated with MuTr position resolution and alignment errors. Based on these effects the expected mass resolution for  $\Upsilon$  is about a three times  $J/\Psi$  resolution, about 500 MeV. While this analysis provided a first look at  $\Upsilon$  in the PHENIX muon arm, increased luminosity, future upgrades, and improved understanding of high momentum background are needed to achieve this particular physics goal.
4. Efficient reconstruction of central Au+Au events. While the combinatoric background levels are high, PHENIX has successfully measured  $J/\Psi$  in central Au+Au events.

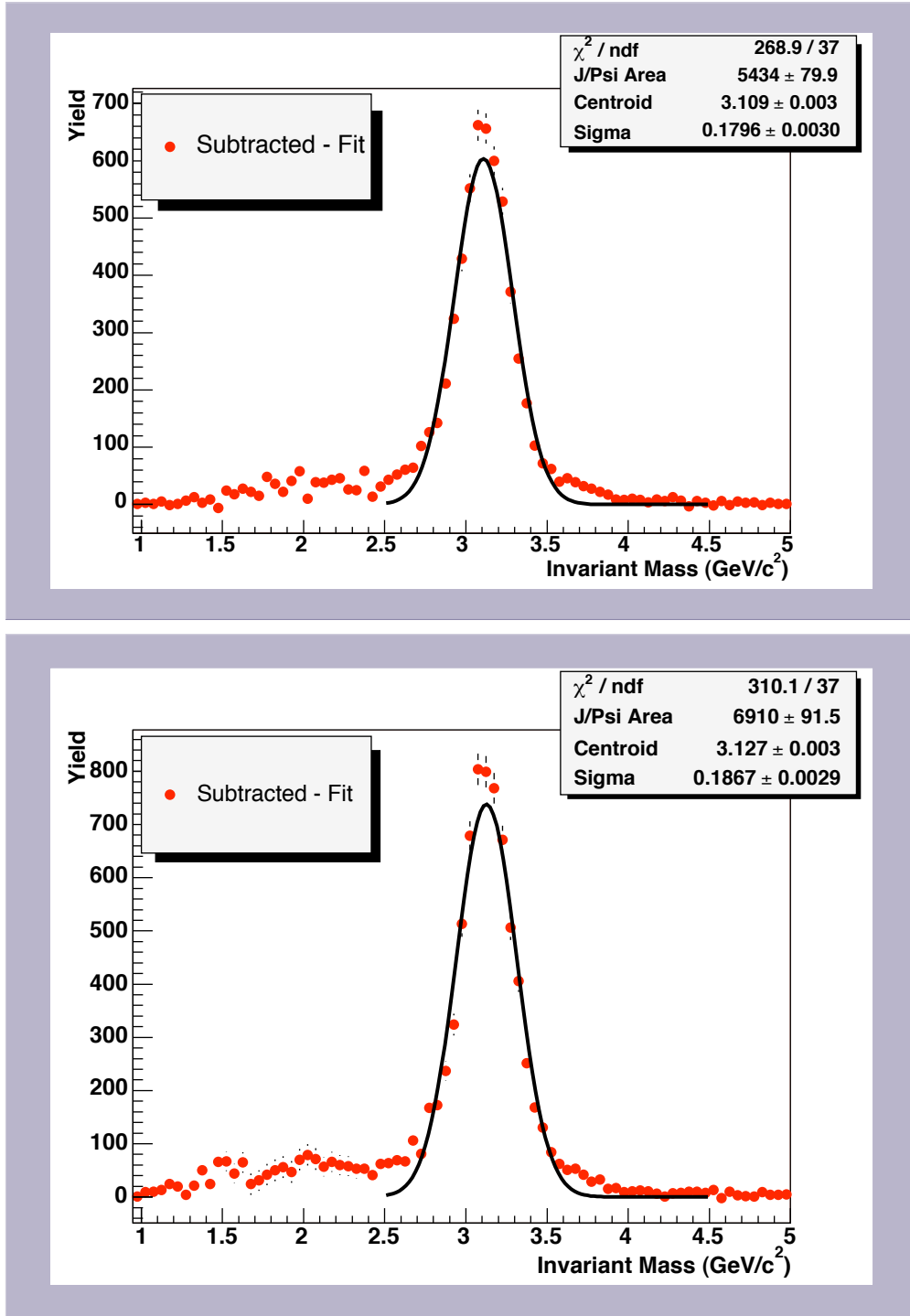


Figure H.1: J/ $\Psi$  peaks for both the North and South PHENIX muon arms from the 2005  $\sqrt{s} = 200$  GeV  $p + p$  run. The mass resolution can be taken as the Sigma from the fit. The north and south arms have about a 10 MeV difference in mass resolution. Plots obtained from [110].

The tracking challenge associated with central Au+Au events is unprecedented, and the level of efficiency achieved is an achievement in and of itself.

5. High performance in lower occupancy/ higher event rate p+p and d+Au. The performance has been sound if slightly less than hoped for originally.

The original design and the stated goals of the muon spectrometer were made for a new accelerator and an unknown collision environment, so it is understandable that not all goals were achieved. Shortfalls in performance are due to a few different reasons, but they are all essentially related to the topic of unanticipated “backgrounds”. Backgrounds from the beam itself were realized during the first RHIC physics run in 2002 (Run 2). Before Run 3, additional shielding was installed in both the square hole (Figure 4.10) and on the *outside* of the last MuID gap in order to minimize an initially unexpected, large non-collision related background from beam “scraping” on the magnets and beam-pipe both upstream and inside the PHENIX experimental hall.

# Appendix I

## Optimal muon acceptance in $(p_T, \eta)$

This section considers the  $p_T$  vs.  $\eta$  acceptance for muons in the PHENIX muon arms. High energy muons passing through the large amount of absorber material between the collision vertex and the muon arm detector lose energy primarily as a minimum ionizing particle (MIP). This energy loss is characterized by the well known Bethe-Bloch formula and can be applied to the PHENIX muon arms in order to determine the minimum  $p_T$  that should be considered for a given choice of pseudorapidity (angle from the beam-line) acceptance. The impact of software reconstruction efficiencies on this issue are not considered and are applied at the last step of the analysis. Based solely on the function  $p_T(\eta)$ , for a lower acceptance bound of  $\eta=1.4$ , it is found that muons of  $p_T \geq 1.2$  GeV and  $p_T \geq 1.3$  are capable of penetrating to Gap 4, for south and north arms respectively.

Minimum penetration momenta for muons has been tabulated [123] by integration of the Bethe-Bloch formula and are show in tables 1 and 2. Since this calculation there has been a small decrease (from 20 cm to 19 cm) in material of both arms' copper nose cone absorber, decreasing slightly the energy needed to penetrate to a given gap. This change is ignored in the following plots.

An analytical expression  $p_T(\eta)$  is determined in order to graph the minimum penetration  $p_T$  vs.  $\eta$  for a given gap. The value  $p_{min}(\theta)$  is defined as:

$$p_{min}(\theta) = \frac{p_{min}(0^0)}{\cos(\theta)} \tag{I.1}$$

Gap	Intervening Material	Cumulative Material (Fe cm-equivalents)	$p_{min}(0^\circ)$ GeV/c
1	20 cm Cu, 90 cm Fe	112	1.63
2	10 cm Fe	122	1.76
3	10 cm Fe	132	1.90
4	20 cm Fe	152	2.18
5	20 cm Fe	172	2.45

Table 1:  $p_{min}(0^\circ)$  for North Arm gaps.

Gap	Intervening Material	Cumulative Material (Fe cm-equivalents)	$p_{min}(0^\circ)$ GeV/c
1	20 cm Cu, 80 cm Fe	102	1.49
2	10 cm Fe	112	1.63
3	10 cm Fe	122	1.76
4	20 cm Fe	142	2.04
5	20 cm Fe	162	2.31

Table 2:  $p_{min}(0^\circ)$  for South Arm gaps.

Figure I.1: Tabulated energy loss for a MIP in the PHENIX muon arms. Tables taken from [123].

where  $P_{min}(0^0)$  are the tabulated values. In discussing minimum penetration momentum,  $p_{min}(0^0) = p_z$  and  $p_{min}(\theta) = p_{total}$ . Then,

$$p_T(\theta) = p_{min}(\theta) \cdot \sin(\theta). \quad (\text{I.2})$$

Using the following standard expression for pseudorapidity,

$$\eta = -\ln \left[ \tan\left(\frac{\theta}{2}\right) \right] \quad (\text{I.3})$$

and eliminating  $\theta$  in favor of  $\eta$ , an expression of  $p_t(\eta)$  is found:

$$p_T(\eta) = p_{min}(0^0) \cdot \tan[2 \tan^{-1}(e^{-\eta})]. \quad (\text{I.4})$$

The distributions that follow in Fig. I are created using Eq. I.4.

In considering the lower bound for  $\eta$  acceptance one should consider the Gap 4 distribution. For a lower bound of  $\eta=1.4$  muons of  $p_T \geq 1.2$  GeV penetrate to Gap 4 in the south arm. For the north arm the value is  $p_T \geq 1.3$  GeV.

For a lower bound of  $\eta=1.5$  as used in the run 2 analysis, Figures I.2(a) and I.2(b) suggest that muons of minimum energies of  $p_T \geq 1.1$  GeV are capable of penetrating to Gap 4. For the north arm the value is approximately  $p_T \geq 1.15$  GeV.

These distributions show that shifting the lower  $\eta$  bound by 0.1 by going from 1.5 to 1.4 raises the threshold of muons penetrating to Gap 4 by about 0.1 GeV. Barring other restricting issues, such as reconstruction inefficiencies, these distributions also suggest that it is possible to extend  $p_T$  acceptance range to below a minimum  $p_t = 1.5$  GeV. This can be accomplished by either pushing the  $\eta$  acceptance to above 1.8 or possibly incorporating Gap 3 in the calculation of the decay muon yield.

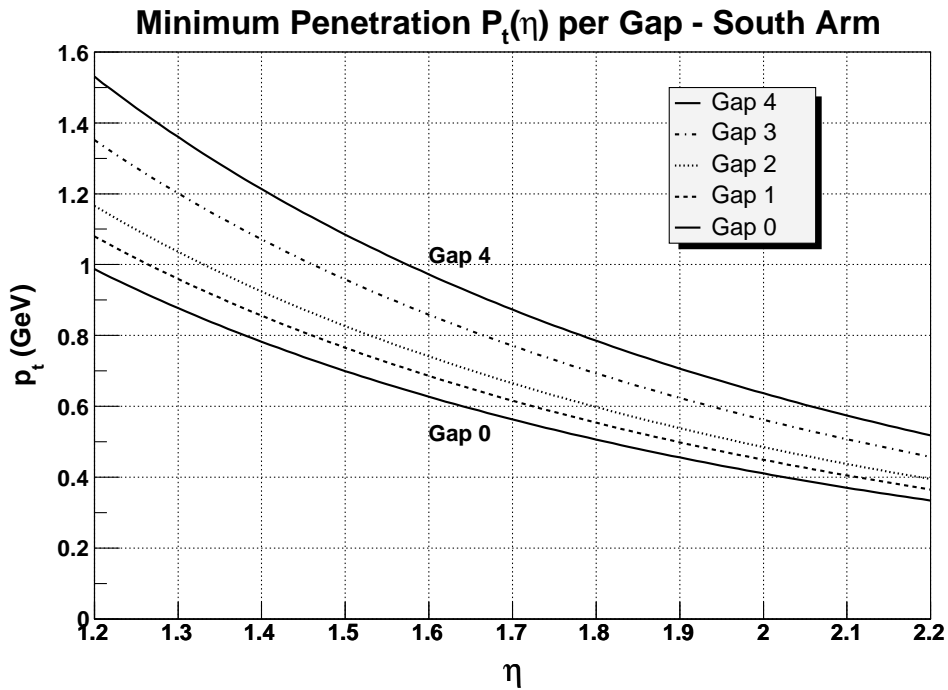
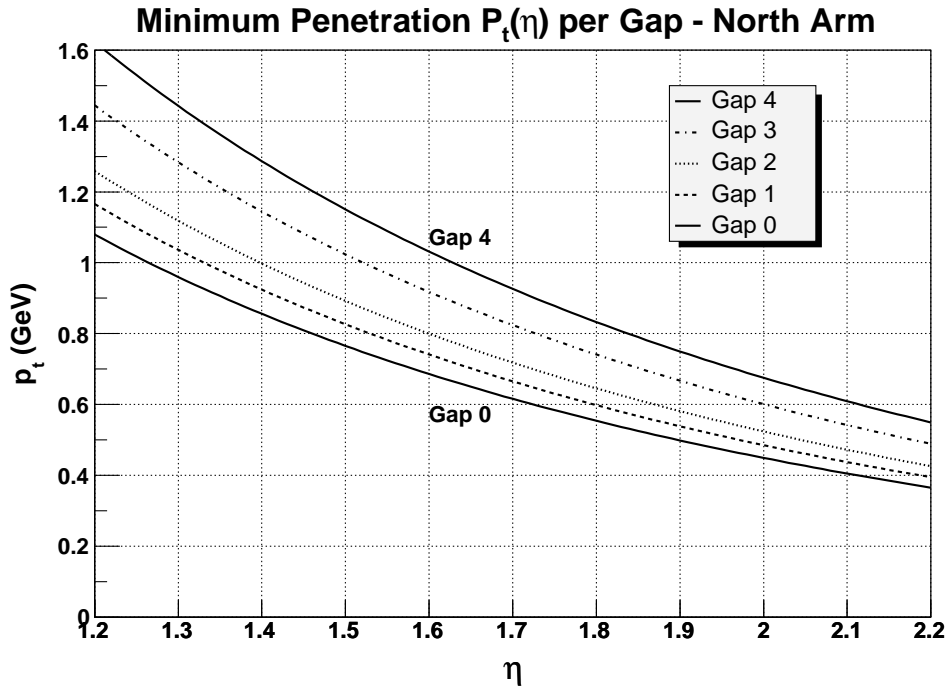


Figure I.2: Minimum penetration  $p_T$  in GeV as a function of  $\eta$  for the PHENIX north and south muon arms.

# Vita

Donald Eric Hornback was born on November 19, 1973 in St. Louis, Missouri. He spent his childhood in the St. Louis area, Ormond Beach, Florida, and lastly in Houston, Texas where he graduated from high school in May 1991. After spending one year at Vanderbilt University as an engineering student, he enlisted in the United States Air Force and learned Arabic at the Defense Language Institute in Monterey, California. From 1994 to 1998 Donald was stationed in the United Kingdom serving as an airborne cryptological linguist flying reconnaissance missions out of RAF Mildenhall in Suffolk, England, Souda Bay, Crete and Riyadh, Saudi Arabia.

Upon leaving the Air Force in November 1998, Donald moved to northern California where he began his studies to be an oceanographic researcher at Humboldt State University in Arcata, California. However, the dream of “swimming with the dolphins” was soon cast aside after he took his first physics course taught by Dr. Richard L. Thompson. Two years later Donald transferred to the University of Tennessee, completing his B.S. in Physics in December 2002 and began his post-graduate physics studies in January 2003 at the same university.

Donald performed his doctoral research in experimental high-energy nuclear physics with Dr. Ken Read as advisor on the PHENIX experiment at Brookhaven National Laboratory. After completion of his Ph.D. in August 2008, he began his post-doctoral work at Oak Ridge National Laboratory. Of far and away more importance, he is also lucky enough to be happily married and to have two amazing sons.